Numerical Modeling of Tsunami Bore Attenuation and Extreme Hydrodynamic Impact Forces Using the SPH Method

Steffanie Piché

Thesis submitted to the
Faculty of Graduate and Postdoctoral Studies
In partial fulfillment of the requirements for the degree of
Master of Applied Science in Civil Engineering

Academic Advisors: Dr. Ioan Nistor and Dr. Tad Murty

Department of Civil Engineering
University of Ottawa
2014

Abstract

Understanding the impact of coastal forests on the propagation of rapidly advancing onshore tsunami bores is difficult due to complexity of this phenomenon and the large amount of parameters which must be considered. The research presented in the thesis focuses on understanding the protective effect of the coastal forest on the forces generated by the tsunami and its ability to reduce the propagation and velocity of the incoming tsunami bore. Concern for this method of protecting the coast from tsunamis is based on the effectiveness of the forest and its ability to withstand the impact forces caused by both the bore and the debris carried along by it. The devastation caused by the tsunami has been investigated in recent examples such as the 2011 Tohoku Tsunami in Japan and the Indian Ocean Tsunami which occurred in 2004.

This research examines the reduction of the spatial extent of the tsunami bore inundation and runup due to the presence of the coastal forest, and attempts to quantify the impact forces induced by the tsunami bores and debris impact on the structures. This research work was performed using a numerical model based on the Smoothed Particle Hydrodynamics (SPH) method which is a single-phase three-dimensional model. The simulations performed in this study were separated into three sections. The first section focused on the reduction of the extent of the tsunami inundation and the magnitude of the bore velocity by the coastal forest. This section included the analysis of the hydrodynamic forces acting on the individual trees. The second section involved the numerical modeling of some of the physical laboratory experiments performed by researchers at the University of Ottawa, in cooperation with colleagues from the Ocean, Coastal and River Engineering Lab at the National Research Council, Ottawa, in an attempt to validate the movement and impact forces of floating driftwood on a column. The final section modeled the movement and impact of floating debris traveling through a large-scale model of a coastal forest.

Acknowledgments

First, I would like to express my gratitude and appreciation to my supervisor, Dr Ioan Nistor, for his continued support and encouragement of my endeavors - without his devotion none of this would have been possible. Additional thanks goes to Dr Tad Murty for his recommendations and support during my work and presentations. I would also like to thank Phil St-Germain and Safinaz El-Solh, the University of Ottawa SPH team, for sharing their knowledge and taking the time to answer my questions.

I would like to acknowledge Taofiq Al-Faesly for providing me with the necessary data required to use in this research. On a similar note, I would to thank the Civil Engineering professors and staff for their guidance and help and getting me to where I am today.

I would like to sincerely thank my family for putting up with me and for giving me their unconditional love and support in this and in all aspects of my life: my mother and father, Ann and Rey and my sister Lise. I would like to thank all of my friends for their encouragement when times got tough, and for their company as I worked. Most of all I would like to thank Nick for all the sacrifices he made for me and for his love and support throughout my studies.

Table of Contents

List of Figures

List of Tables

List of Symbols

Roman Letter Symbols

B	Pressure constant in Tait's equation of state
c	Speed of sound in water (m/s)
c_0	Reference speed of sound in water at the reference density ρ_0 (m/s)
c_i	Speed of sound at particle i (m/s)
C	Wave celerity (m/s)
C_I	SPS constant = 0.00066
C_S	Smagorinsky constant = 0.12
dA	Tributary area of sampling region (m)
D_i	Density of particle i ($d\rho_i/dt$)
e_i	Density of energy for particle i
E_i	Density of energy for particle i (de_i/dt)
f_i	Internal and external forces per unit mass
F_{debris}	Force acting on the debris (N)
F_i	Corrected debris impact force (N)
$\boldsymbol{F_i}$	Momentum for particle i ($d\boldsymbol{u}_i/dt$)
F_X	Horizontal force acting streamwise on the column (N)
$f(\boldsymbol{x})$	Scalar function at position $\boldsymbol{x}$
$\boldsymbol{f(x)}$	Vector function at position $\boldsymbol{x}$
g	Gravitational acceleration (m/s²)
$\boldsymbol{g}$	Gravitational acceleration vector (m/s²)
h	Smoothing length or water surface elevation (m)
H	Wave height (m)
$\boldsymbol{L}_{ij}$	Correction matrix for gradient correction
m_i	Mass (kg)
$\dot{m}$	Momentum
N	Total number of particles within the influence domain
N_{vol}	Total number of water particles within a sampling volume

$\boldsymbol{n}$	Unit vector normal to the solid boundary
n	Time step (subscript)
P	Fluid pressure (Pa)
r_c	Radius of the circular column
S	Surface of influence domain Ω (m^2)
dS	Infinitesimal surface of the influence domain Ω (m^2)
S_{ij}	Favre-filtered rate of strain
S_s	Wave board stroke (m)
t	Time (s)
t_f	Stroke duration (s)
u	X component of velocity vector $\boldsymbol{u}$ (m/s)
$\boldsymbol{u}$	Velocity vector (m/s)
$\boldsymbol{u_f}$	Final velocity vector at time step (m/s)
$\boldsymbol{u_i}$	Initial velocity vector at time step (m/s)
$\boldsymbol{U_i}$	Velocity contribution from particle i
v	Y component of velocity vector $\boldsymbol{u}$ (m/s)
w	Z component of velocity vector $\boldsymbol{u}$ (m/s)
W	Smoothing kernel
W_{ij}	Smoothing kernel evaluated for particles i and j
∇W_{ij}	Corrected kernel gradient
$\tilde{\nabla} W_{ij}$	Corrected kernel gradient
x	Position along x-axis (m)
$\boldsymbol{x}$	Position vector (m)
x_{ij}	Distance separating two particles i and j (m)
$\boldsymbol{x_{ij}}$	Vector separating two particles i and j (m)
X_o	Wave board displacement (m)
y	Position along y-axis (m)
z	Position along z-axis (m)

Greek Letter Symbols

α_{time}	Time step CFL coefficient
α_{visc}	Artificial viscosity coefficient
α_{sound}	Speed of sound coefficient
α_{smooth}	Smoothing length coefficient
γ	Specific weight of water (N/m^3) or exponent for equation of state
δ	Dirac delta function
ε	XSPH coefficient
η	Water surface profile
Θ_v	Angle corresponding to the arc of the tributary area
κ	Scaling factor or wave number
ν	Kinematic viscosity of laminar flow (m^2/s)
ν_t	Turbulence eddy viscosity
Π_{ij}	Viscosity condition for particles *i* and *j*
ρ	Water density (kg/m^3)
ρ_0	Reference water density (kg/m^3)
$\boldsymbol{\tau}$	Sub-particle scale shear stress tensor (N/m^2)
Ω	Influence domain of smoothing kernel
$d\Omega$	Infinitesimal volume of influence domain Ω (m^3)

1 Introduction

1.1 Objective and Research Needs

The main objective of the present study is to examine the effect of coastal forests in reducing the inundation and velocity of a tsunami-induced bore and its impact on the propagation of tsunami-moved debris.

The generation of tsunami waves is caused by the vertical displacement of seawater by the ocean bottom in a vertical direction during large under-ocean earthquake events. Underwater landslides or meteors can also generate tsunamis, but they are typically caused by large subduction earthquakes occurring along the submarine fault lines. The displacement of the ocean seafloor, caused by the motion of the fault line, results in a localized vertical displacement of the water level which then propagates outward from the source as one or several successive tsunami waves. In deeper water the generated tsunami wave will have relatively small amplitude, less than 1m, having at the same time a large period and travelling at very high speeds which may reach up to 900 km/hour [Ward, 2002]. As tsunami waves propagate onto shallower coastal regions their wave length and wave velocity begin to reduce, while their amplitude begins to increase. Depending on the localized bathymetry, the tsunami waves will break in water depth roughly equal to that of its amplitude and will form a hydraulic bore which will then advance onshore. The hydraulic bore is characterized by its rapid advancement at the shoreline and by its steep turbulent bore front. The propagation of a tsunami bore inland can result in substantial damage to infrastructure and may cause significant casualties and injuries.

While tsunami events have been recorded throughout history, the last decade has seen numerous events which have resulted in large economic damage and loss of life, such as the 2004 Indian Ocean Tsunami, the 2010 Chilean Tsunami, and the 2011 Tohoku Tsunami. Examples of the destruction caused by these tsunamis are shown in Figures 1.1 and 1.2. Table 1.1 shows estimates of the damage and casualties caused by significant tsunamis during the last decade [NOAA, 2013].

Figure 1.1 - Damage to Sukuiso, Japan, one week after the 2011 Japan Tsunami [NOAA (D. McCord, U.S. Navy)]

Figure 1.2 - Damage at Velankanni, India, after the 2004 Indian Ocean Tsunami [NOAA (Trainor, University of Delaware)]

Table 1.1- Recent major tsunamis - economic damage and loss of life [NOAA, 2013]

Location	Date	Cause	Economic Loss (US dollars)	Loss of Life/ Missing (person)
Indian Ocean	2004/12/26	9.1 Earthquake	10 billion	226,898
Java	2006/07/17	7.7 Earthquake	55 million	802
Samoa Islands	2009/09/29	8.0 Earthquake	275 million	192
Chilean	2010/02/27	8.8 Earthquake	30 billion	156
Tohoku Japan	2011/03/11	9.0 Earthquake	210 billion	19,057

To try reducing the damage caused by tsunami events, coastal communities sometimes deploy a number of coastal protection measures whose function is either to halt the advance of the tsunami inundation or reduce its extent. These protection measures can be man-made structures such as seawalls and breakwaters or naturally occurring features such as hills and/or coastal forests.

The design and implementation of the man-made coastal protection systems depends on knowledge of historical tsunami events as the magnitude of future events is difficult to predict. As such, it is possible that the protection may not be sufficient to withstand large tsunami waves and the systems may fail due to the overtopping of the protection structures or due to its inability to resist the large impact forces resulting from the fast moving tsunami bores. The failure of protection structures may result in damage to the community or, even worse; it may contribute to the damage as parts of it may become debris moving with the incoming bore. Figures 1.3 and 1.4 show examples of a tsunami-protection seawall being overtopped and the complete structural failure of a breakwater, respectively.

Figure 1.3 - Seawall overtopping in Miyako, Japan [Asahi Shimbun, 2010]

Figure 1.4 - Failed breakwater in Kamaishi, Japan [Sasaki, 2011]

The development of coastal communities, partly to accommodate a growing population, can also increase the level of damage caused by large tsunami bores. Often, the removal of the local vegetation, which would normally provide coverage and protection from storms and tsunami, requires the construction of man-made protection systems. This is required to offset the increased exposure to the tsunami inundation and velocity due to the absence of the coastal vegetation. An example of the removal of the forest and mangrove in Burma's Irrawaddy Delta, which can ensure protection against coastal inundation due to storm surge, is shown in Figure 1.5.

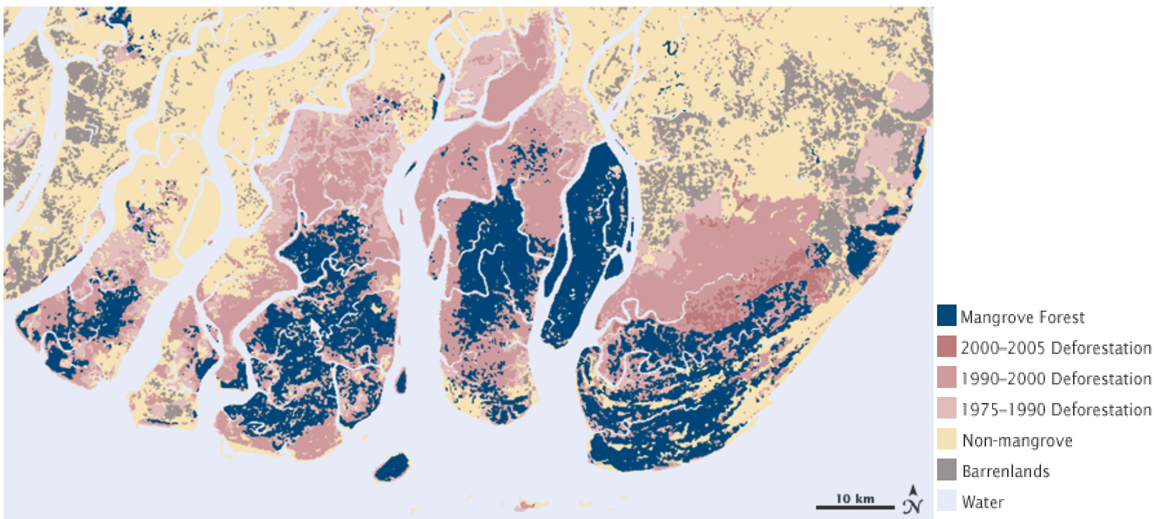

Figure 1.5 - Reduction in the mangrove forests in the Irrawaddy Delta, Burma [adapted by Robert Simmon from Giri *et al.*, 2008]

While coastal forests may not be fully effective against coastal flooding, particularly when associated with successive, non-breaking tsunami waves, they have been found to be capable of limiting the extent of the tsunami inundation. Mature, well-designed forests are deemed potentially capable of offering complete protection from a large tsunami wave of 8m or even 10m in height [Forbes and Broadhead, 2007]. An example of the effectiveness of coastal forests in reducing economic damage is shown in Figure 1.6 for the 2011 Tohoku Tsunami. This figure shows, circled in red, a group of residences which appear to have withstood the tsunami while the majority of the town was destroyed. The survival of these houses was attributed to their location behind a thick coastal forest which remained relatively intact.

Figure 1.6 - Protection of houses by a coastal forest during the 2011 Tohoku Tsunami – images before and after the event [Google Earth, 2011]

Key parameters in the forests' ability to reduce the inundation and velocity of the tsunami bore include factors such as the forest belt width, the age of the trees and their diameter, as well as the density of the trees. While each of these factors may have a significant impact on the tsunami inundation alone, the relation between the different factors has been found to be complex.

Additional benefits from coastal forests include the protection it may provide in the form of preventing the propagation of debris, such as shipping tankers from moving inland and impacting into coastal communities. However, coastal forests also have the potential to become hazards should the trees be unable to withstand the tsunami waves and debris impact forces. Should the trees become uprooted or the tree branches break from the trees, they would become debris which can result in large damage to the local coastal communities.

1.2 Scope

The numerical work performed in this research examined the impact forces of the tsunami bore on the individual trees in the coastal forest and the bores' propagation and runup through the forest for different initial still-water levels. The numerical tsunami bores were generated as solitary waves in a rectangular flume with a sloped "beach" profile, which propagated through and impacted trees simulated as cylindrical piers. The coastal forest band width, density and layout were varied for the different still-water levels in order to observe the full effect of the initial still-water depth in relation to these key parameters.

The impact forces generated by the debris as it propagated through the forest was also investigated. This was validated using a "dam-break" wave, carrying debris, which impacted a free-standing cylindrical column. Numerical results were compared to the experimental ones of Al-Faesly *et al.* [2013].

1.3 Contributions

The novelty of the this research resides in the use of a novel, improved numerical SPH model to investigate the interaction of a tsunami-induced hydraulic bore with a simulated coastal forest and in the examination of the impact forces on the forest caused by the tsunami-moved debris.

While the influence of a coastal forest on the attenuation of a tsunami-induced bore has been investigated in other studies, the effect of the initial still-water level on the spatial extent of the inundation and the bore velocity, in addition to the variation in inundation extent caused by the presence of small forests has not been investigated. Furthermore, the impact forces of the tsunami-born debris on the coastal forest have not been investigated.

The findings presented in this thesis will allow for a better understanding of the coastal forests' ability to protect coastal communities from tsunami-induced bores and debris when employing various forest configurations in terms of forest size and density. These findings may also be applied to other coastal disaster scenarios, such as the flooding induced by hurricane storm surges along coastlines.

1.4 Outline

This thesis has been organized into 8 chapters and a general description of these chapters is presented below.

Chapter 1 – An introduction into the research topic and the scope, main objectives and main contributions of the research work.

Chapter 2 – An introduction into the background of the Smoothed Particle Hydrodynamics (SPH) method and its application to the field of computation fluid dynamics (CFD). This includes a description of the governing equations and basic formulations of the method and contains also a description of the different model parameters used in this work.

Chapter 3 – A detailed literature review with reference to the propagation of solitary wave runup and bore propagation, the interaction of the tsunami-induced bore and coastal vegetation, and the impact forces of tsunami-moved debris.

Chapter 4 – Detailed description of the numerical setup of the different models, including the computational domains utilized in the research. This chapter also includes a sensitivity analysis on the different SPH parameters used and a description of the methodology used in the extraction of data for post-processing.

Chapter 5 – An examination on the effect of different still-water levels on the attenuation of the tsunami-induced bores by the coastal forest. The analysis of the reduction in the bore runup velocity and the wave impact forces are included for the propagation of the bore up the shoreline.

Chapter 6 – An analysis of the water surface elevation and the hydrodynamic and debris forces on a cylindrical column for the validation of the impact forces using experimental results.

Chapter 7 – An investigation of the impact of initial debris location on its movement through a coastal forest and its impact on the trees on the runup of a tsunami-induced bore.

Chapter 8 – Summary of the research findings and conclusions, as well as recommendations for future studies in this field.

2 The SPH Method

2.1 Introduction

This chapter presents the background and the theory behind the Smoothed Particle Hydrodynamic (SPH) method. Presented first is the background of the method with its development, its applications and its basic principles. Presented second are the core concepts and governing equations pertaining to the model. The final sections of this chapter include a description of the formulations implemented in the code and a basic explanation of the model selected for this research.

2.2 SPH Background

The SPH method was initially introduced by Gingold and Monaghan [1977] and Lucy [1977] for modeling continuum physics in order to avoid the limitations brought on by finite difference models. Since the inception of this method it has expanded to include the modeling of dynamic flow and material problems. Specific applications in the field of computational fluid dynamics (CFD) include investigations into incompressible flows [Monaghan, 1994; Morris *et al*., 1997], gravity currents [Monaghan, 1996], free-surface flows [Monaghan and Kos, 1999], breaking waves, wave impact [Lo and Shao, 2002] and sediment transport and suspension [Zhou and Dalrymple, 2006].

The SPH method is a Lagrangian mesh-free particle-based method which represents the fluid as a set of arbitrarily distributed particles that are assigned individual properties such as mass, velocity and density. As the particles travel in space their properties are adjusted with time based on the information of the surrounding particles, which have an influence on them.

The advantages of this method are its ability to capture the free surface of the fluid and its interaction with both fixed and moving boundary particles. It is able to model the variation at the fluid-air interface with great accuracy when compared to grid-based methods and is capable of handling large deformations in the fluid surface. As the model requires smoothing of the particles at each time step it has the potential to become computationally intensive for large-scale problems. However, recent advancements in the development of the individual models and in computer technology have greatly reduced this issue.

2.3 SPH Theory

The basic principle of the SPH method is the numerical discretization of the model which results from the combination of the function/kernel approximation and the particle approximation. The governing equations used in this method are conservation of momentum and mass.

2.3.1 Function Approximation

The function approximation applied in the SPH method involves the representation of a vector function $\boldsymbol{f(x)}$, and its derivative within a local domain of influence, Ω, such that:

[2.1] $$\boldsymbol{f}(\boldsymbol{x}) = \int_{\Omega} \boldsymbol{f}(\boldsymbol{x}')\delta(\boldsymbol{x}-\boldsymbol{x}')d\Omega$$

where $\boldsymbol{x}$ is the position vector at the location where the function $\boldsymbol{f}$ is being approximated, $\boldsymbol{x'}$ is the position vector for the surrounding locations where the function $\boldsymbol{f}$ is being evaluated and $\delta(\boldsymbol{x}-\boldsymbol{x'})$ is the Dirac delta function which is represented by:

[2.2] $$\delta(\boldsymbol{x}-\boldsymbol{x}') = \begin{cases} 1 & \boldsymbol{x} = \boldsymbol{x}' \\ 0 & \boldsymbol{x} \neq \boldsymbol{x}' \end{cases}$$

The Dirac delta function can be replaced by a scalar smoothing function W, which is also known as the weighting or smoothing kernel, which gives the integral representation of Eq. 2.1:

[2.3] $$f_i(\boldsymbol{x}) = \int_{\Omega} f(\boldsymbol{x}')W(\boldsymbol{x}-\boldsymbol{x}', h)d\boldsymbol{x}'$$

where the value of the smoothing length, h, controls the size of the domain of influence for the smoothing kernel. Generally, the value of h must be larger than the initial particle separation and the smoothing kernel must satisfy the following conditions:

1. Positivity Condition

[2.4] $W(\boldsymbol{x}-\boldsymbol{x}') \geq 0$ inside the domain Ω

This condition requires that the smoothing function be positive within the support domain. While this condition is not a mathematical necessity it is integral in ensuring the stability and meaningful representation of the physical phenomena.

2. Compact Support

[2.5] $W(\boldsymbol{x}-\boldsymbol{x}') = 0, \text{ for } |\boldsymbol{x}-\boldsymbol{x}'| > \kappa h$

The dimension of the compact support is defined by the smoothing length and by the scaling factor κ, where κ determines the spread of the smoothing function. This condition allows for the transformation of the SPH approximation from a globalized to a localized operation, which eases the computational effort.

3. Normalization

[2.6] $\int_{\Omega} W(\boldsymbol{x}-\boldsymbol{x}', h)d\boldsymbol{x}' = 1$

The smoothing function is required to be normalized over its support domain; this ensures that the integral of the smoothing function is equal to one over the support domain.

4. Delta Function Behavior

[2.7] $\lim_{h\to 0} W(\boldsymbol{x}-\boldsymbol{x}', h) = \delta(\boldsymbol{x}-\boldsymbol{x}')$

The delta function behavior should be satisfied as the smoothing function tends to zero. This condition ensures that as the smoothing length gets smaller, the approximation value begins to approach the function value.

5. Decay

The particles' smoothing function is required to be monotonically decreasing as the distance from the particle increases. This is based on the consideration that particles with closer proximity to each other should have a larger influence than particles which are further apart.

6. Symmetric Property

The symmetric property dictates that the smoothing function should be an even function. This ensures that particles that are equidistant apart, but on different planes, will have an equal influence on the particle of interest. This requirement is not rigid and is occasionally ignored in methods which provide a higher consistency.

7. Smoothness

The smoothing function is required to be sufficiently smoothed in order to obtain a more accurate approximation. Additionally, the smoothing function is required to be sufficiently continuous in order to obtain accurate results for the approximation of the function and its derivative. Smoother functions tend to provide better results as they are less sensitive to particle disorder.

The function approximation of the spatial derivative is obtained by replacing the term ***f(x)*** from Eq. 2.3 with the term $\nabla \cdot f(\boldsymbol{x})$ which gives:

[2.8] $$\langle \nabla \cdot f(\boldsymbol{x}) \rangle = \int_{\Omega} [\nabla \cdot f(\boldsymbol{x}')] W(\boldsymbol{x} - \boldsymbol{x}', h) d\boldsymbol{x}'$$

When considering the function,

[2.9] $$[\nabla \cdot f(\boldsymbol{x}')] W(\boldsymbol{x} - \boldsymbol{x}', h) = \nabla \cdot [f(\boldsymbol{x}') W(\boldsymbol{x} - \boldsymbol{x}', h)] - f(\boldsymbol{x}') \cdot \nabla [W(\boldsymbol{x} - \boldsymbol{x}', h)]$$

Eq. 2.8 can be modified to:

[2.10] $$\nabla \cdot f(\boldsymbol{x}) = \int_{\Omega} \nabla \cdot [f(\boldsymbol{x}')W(\boldsymbol{x}-\boldsymbol{x}',h)]d\boldsymbol{x}' - \int_{\Omega} f(\boldsymbol{x}') \cdot \nabla[W(\boldsymbol{x}-\boldsymbol{x}',h)]d\boldsymbol{x}'$$

The first integral on the right hand side of Eq. 2.10 can be converted to an integral over the domain of influence; however, as the smoothing function is generally defined to have compact support (Eq. 2.5) the value of the surface integral will be zero in the SPH method. Therefore, the function approximation of the derivative can be reduced to:

[2.11] $$\langle \nabla \cdot f(\boldsymbol{x}) \rangle = -\int_{\Omega} f(\boldsymbol{x}') \cdot \nabla[W(\boldsymbol{x}-\boldsymbol{x}',h)]d\boldsymbol{x}'$$

2.3.2 Particle Approximation

The particle approximation is the second stage of the SPH method, which involves the representation of the numerical domain as a set of arbitrarily distributed particles, as shown in Figure 2.1. The particle approximation enables the model to estimate the different variables for the set of particles.

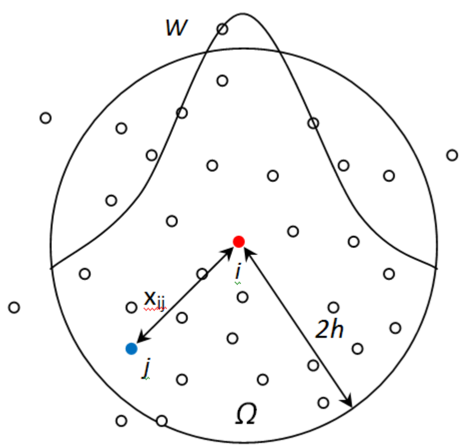

Figure 2.1 - Particle approximation for particle *i* over the domain of influence *Ω* with surface *S*, and with smoothing function *W*

Once the computational domain has been represented by a set of arbitrarily distributed particles, the continuous form of Eq. 2.3 can be expressed as the summation of all the neighboring particles:

[2.12] $$\langle f_i(\boldsymbol{x})\rangle = \sum_{j=1}^{N} f\left(\boldsymbol{x}_j'\right) W(\boldsymbol{x}-\boldsymbol{x}_j', h)\frac{m_j}{\rho_j}$$

where N is the number of particles within the influence domain of particle $\boldsymbol{x}$, and m_j and ρ_j are the mass and density of the neighboring particle j, respectively. The particle approximation of the derivative can be determined based on an approach similar to that shown in Section 2.3.1, for the kernel approximation, resulting in:

[2.13] $$\langle \nabla \cdot f(\boldsymbol{x})\rangle = -\sum_{j=1}^{N} f\left(\boldsymbol{x}_j'\right) \cdot \nabla_i W(\boldsymbol{x}-\boldsymbol{x}_j', h)\frac{m_j}{\rho_j}$$

where the gradient, ∇W is evaluated at particle j.

2.3.3 Governing Equations

The governing equations of the SPH method are based on the principles of conservation of mass and momentum.

Conservation of Mass

The conservation of mass principle for a compressible fluid can be represented in its Lagrangian form as:

[2.14] $$\frac{1}{\rho}\frac{D\rho}{Dt} = -\nabla \cdot \boldsymbol{u}$$

As the equation must be discretized for use in the SPH method, both sides of the equation are multiplied by the smoothing kernel and integrated over the domain of influence:

[2.15] $$\int_\Omega W(\boldsymbol{x}-\boldsymbol{x}', h)\left(\frac{1}{\rho}\frac{d\rho}{dt}\right) d\Omega = -\int_\Omega W(\boldsymbol{x}-\boldsymbol{x}', h)\, \nabla \cdot \boldsymbol{u} d\Omega$$

Due to the nature of the smoothing kernel, the left-hand side of the equation can be represented as $\frac{d\rho}{dt}/\rho$ and the right-hand side can be represented by the identity:

[2.16] $$-\int_\Omega [\nabla \cdot (W(\boldsymbol{x}-\boldsymbol{x}', h)\boldsymbol{u}) - \boldsymbol{u} \cdot \nabla W(\boldsymbol{x}-\boldsymbol{x}', h)]\, d\Omega$$

where the gradient is applied to $\boldsymbol{x'}$. Based on Guass's theorem:

[2.17] $$\int_{\Omega} \nabla \cdot \boldsymbol{f} d\Omega = \int_{S} f \cdot \boldsymbol{n} dS$$

where the right-hand side is an integral over the surface which encloses the domain, S and $\boldsymbol{n}$ is normal to the surface. Using Eq. 2.16 and 2.17, Eq. 2.15 becomes:

[2.18] $$\frac{1}{\rho}\frac{D\rho}{Dt} = -\int_{S} W(\boldsymbol{x}-\boldsymbol{x}', h)\, \boldsymbol{u} \cdot \boldsymbol{n} dS + \int_{\Omega} \boldsymbol{u} \cdot \nabla W(\boldsymbol{x}-\boldsymbol{x}', h) d\Omega$$

Should the surface be far from the particles, then the integrand in the first integral would be zero as the smoothing function tends to zero rapidly. Only the last term would remain, leaving:

[2.19] $$\frac{1}{\rho}\frac{D\rho}{Dt} = \int_{\Omega} \boldsymbol{u} \cdot \nabla W(\boldsymbol{x}-\boldsymbol{x}', h) d\Omega$$

The discretized form of this equation, used in the SPH method, when evaluated at particle $\boldsymbol{x_i}$ is:

[2.20] $$\left(\frac{1}{\rho}\frac{D\rho}{Dt}\right)_i = \sum_j \frac{m_j}{\rho_j} \boldsymbol{u}_j \cdot \nabla_j W\left(\boldsymbol{x}_i - \boldsymbol{x}_j\right)$$

where $W(\boldsymbol{x}_i - \boldsymbol{x}_j) = W_{ij}$.

Due to the symmetrical property of the smoothing function, its gradient $-\nabla_j W\left(\boldsymbol{x}_i - \boldsymbol{x}_j\right)$ is equal to $\nabla_j W\left(\boldsymbol{x}_i - \boldsymbol{x}_j\right)$. Therefore Eq. 2.20 can be expressed as:

[2.21] $$\left(\frac{1}{\rho}\frac{D\rho}{Dt}\right)_i = -\sum_j \frac{m_j}{\rho_j} \boldsymbol{u}_j \cdot \nabla_j W_{ij}$$

A second method of defining this equation can be determined by examining the expression for a gradient, which states that the gradient of a constant is zero:

[2.22] $$0 = \sum_j \frac{m_j}{\rho_j} \boldsymbol{u}_j \cdot \nabla_j W_{ij}$$

By multiplying Eq. 2.22 by $\boldsymbol{u}_i$, the zero sum can be added to the previous form of the conservation equation resulting in:

[2.23] $$\left(\frac{D\rho}{Dt}\right)_i = \rho_i \sum_j \frac{m_j}{\rho_j} (\boldsymbol{u}_i - \boldsymbol{u}_j) \cdot \nabla_j W_{ij}$$

Conservation of Momentum

The equation for the conservation of momentum, with no viscosity, in a continuum field can be represented with:

[2.24] $$\frac{D\boldsymbol{u}}{Dt} = -\frac{1}{\rho} \nabla P + \boldsymbol{g}$$

where $\boldsymbol{g}$ is the acceleration due to gravity, P is the pressure, ρ is the density, and $\boldsymbol{u}$ is the velocity. The viscosity term was not represented in Eq. 2.24 due to the different viscosity formulations available in the SPH model used.

By multiplying Eq. 2.24 with the density and the smoothing kernel and integrating over the domain, the equation becomes:

[2.25] $$\left(\frac{D\boldsymbol{u}}{Dt}\right)_i = -\frac{1}{\rho_i} \sum_j \frac{m_j}{\rho_j} P_j \nabla_i Wij + \boldsymbol{g}$$

Subtracting the zero sum, $\frac{P_i}{\rho_i}\left(\sum_j \frac{m_j}{\rho_j} \nabla_i W_{ij}\right) = 0$, from Eq. 2.25 results in:

[2.26] $$\left(\frac{D\boldsymbol{u}}{Dt}\right)_i = -\sum_j m_j \left(\frac{P_i + P_j}{\rho_i \rho_j}\right) \nabla_i W_{ij} + \boldsymbol{g}$$

Eq. 2.26 can also be represented as:

[2.27] $$\left(\frac{D\boldsymbol{v}}{Dt}\right)_j = -\sum_j m_j \left(\frac{P_i}{\rho_i^2} + \frac{P_j}{\rho_j^2}\right) \nabla_i W_{ij} + \boldsymbol{g}$$

2.4 SPH Implementation

This section presents the numerical formulations for the SPH model. The formulations included are those implemented in the DualSPHysics model [Crespo *et al.*, 2011; Gómez-Gesteira *et al.*, 2010, 2012a, 2012b], which is based on the SPH model SPHysics. This model is designed to run on either the computers central processing unit (CPU), as in the original model, or on the graphics processing unit (GPU) which significantly improves the computational time of the calculations. The SPH theory implemented in the DualSPHysics model is the same as that available in the SPHysics model; however, not all of the formulations are available in the newer model.

2.4.1 Time Stepping

The SPH model time step is controlled by three conditions: the Courant Fredrich-Levy (CFL) condition, the viscosity condition [Monaghan, 1989], and the magnitude of the internal and external forces affecting the particles.

Both the CFL and viscosity conditions require that the time step to be less than or equal to the duration of a waves movement between two adjacent particles, and that the time step be smaller than the time scale of the viscous phenomenon. These conditions are expressed in combination as:

[2.28] $$\delta t_{CV} = \min_i \left(\frac{h}{c_i + \sigma_i} \right)$$

where the variable c_i corresponds to the speed of sound at particle *i* and σ_i is given by:

[2.29] $$\sigma_i = \max_j \left| \frac{h \boldsymbol{u}_{ij} \cdot \boldsymbol{x}_{ij}}{\boldsymbol{x}_{ij}^2} \right|$$

where the maximum is over all of the particles which contribute to the velocity of the particle *i*.

The internal and external force condition ensures that the particles do not get too close during the duration of their movement [Morris *et al*, 1997]:

[2.30] $$\delta t_{forces} = \min_i \sqrt{\frac{h}{f_i}}$$

where f_i is the sum of the internal and external forces per unit mass associated to the particle *i*.

The time step is then determined based on the smaller of the force and CFL/viscosity conditions, where the time stepping coefficient, α_{time} is usually taken to be 0.3, but can range from 0.1 to 0.5:

[2.31] $$\delta t = \alpha_{\mathrm{time}} \min_i(\delta t_{forces}, \delta t_{CV})$$

In this model the time step can be progressed based on two different methods: the Verlet algorithm [Verlet, 1967], and the symplectic algorithm [Leimkuhler *et al.*, 1996].

Verlet Algorithm

The Verlet algorithm is a common time integration scheme which utilizes two sets of equations based on a third-order Taylor expansion for the momentum, density, position and density of energy. The first set is shown in Eq. 2.32 to Eq. 2.35:

[2.32] $$\boldsymbol{u}_i^{n+1} = \boldsymbol{u}_i^{n-1} + 2\Delta t \boldsymbol{F}_i^n = \boldsymbol{u}_i^{n-1} + 2\Delta t \frac{d\boldsymbol{u}_i{}^n}{dt}$$

[2.33] $$\rho_i^{n+1} = \rho_i^{n-1} + 2\Delta t D_i^n = \rho_i^{n-1} + 2\Delta t \frac{d\rho_i{}^n}{dt}$$

[2.34] $$\boldsymbol{x}_i^{n+1} = \boldsymbol{x}_i^n + \Delta t \boldsymbol{U}_i^n + 0.5\Delta t^2 \boldsymbol{F}_i^n = \boldsymbol{x}_i^n + \Delta t \frac{d\boldsymbol{x}_i{}^n}{dt} + 0.5\Delta t^2 \frac{d\boldsymbol{u}_i{}^n}{dt}$$

[2.35] $$e_i^{n+1} = e_i^{n-1} + 2\Delta t E_i^n = e_i^{n-1} + 2\Delta t \frac{de_i{}^n}{dt}$$

These equations are evaluated at each time step; however, a second set of equations (Eqs. 2.36 to 2.39) are evaluated every *M* time steps, where *M* is in the order of 50. This prevents the time integration from diverging as the equations are no longer coupled.

[2.36] $$\boldsymbol{u}_i^{n+1} = \boldsymbol{u}_i^n + \Delta t \boldsymbol{F}_i^n = \boldsymbol{u}_i^n + \Delta t \frac{d\boldsymbol{v}_i}{dt}^n$$

[2.37] $$\rho_i^{n+1} = \rho_i^n + \Delta t D_i^n = \rho_i^n + \Delta t \frac{d\rho_i}{dt}^n$$

[2.38] $$\boldsymbol{x}_i^{n+1} = \boldsymbol{x}_i^n + \Delta t \boldsymbol{V}_i^n + 0.5\Delta t^2 \boldsymbol{F}_i^n = \boldsymbol{x}_i^n + \Delta t \frac{d\boldsymbol{x}_i}{dt}^n + 0.5\Delta t^2 \frac{d\boldsymbol{u}_i}{dt}^n$$

[2.39] $$e_i^{n+1} = e_i^n + \Delta t E_i^n = e_i^n + \Delta t \frac{de_i}{dt}^n$$

Symplectic Algorithm

The symplectic algorithm is time-reversible in the absence of friction or of viscous effects. This scheme calculates the values of the density and particle motion during the middle of the time step based on:

[2.40] $$\rho_i^{n+1/2} = \rho_i^n + \frac{\Delta t}{2} \frac{d\rho_i^n}{dt}$$

[2.41] $$\boldsymbol{x}_i^{n+1/2} = \boldsymbol{x}_i^n + \frac{\Delta t}{2} \frac{d\boldsymbol{x}_i^n}{dt}$$

where *n* denotes the time step and *t* = *nΔt*. After the initial stage, $\frac{d(\omega_i \rho_i \boldsymbol{u}_i)^{n+1/2}}{dt}$ is applied to calculate the velocity and therefore the position of the particles at the end of the time step:

[2.42] $$(\omega_i \rho_i \boldsymbol{u}_i)^{n+1} = (\omega_i \rho_i \boldsymbol{u}_i)^{n+1/2} + \frac{\Delta t}{2} \frac{d(\omega_i \rho_i \boldsymbol{u}_i)^{n+1/2}}{dt}$$

[2.43] $$\boldsymbol{x}_i^{n+1} = \boldsymbol{x}_i^{n+1/2} + \frac{\Delta t}{2} \boldsymbol{u}_i^{n+1}$$

At the end of the time step, $d\rho_i^{n+1}/dt$ is used to calculate the updated values of the velocity and position [Monaghan, 2005].

2.4.2 Smoothing Kernel

The smoothing kernel determines the intensity of the interaction between adjacent particles by calculating the weighted sums of the fluid particles at a point. The kernel functions available in the model are the cubic spline kernel [Monaghan and Lattanzio, 1985] and the quintic Wendland kernel [Wendland, 1995]. As remarked in Section 2.3.1 the smoothing kernel is required to satisfy conditions such as positivity and normalization.

Cubic Spline Kernel

The cubic spline kernel is a widely used function as it resembles a Gaussian function while having a narrower compact support. This offers an advantage as it reduces the numerical computations. Monaghan and Lattanzio [1985] proposed the cubic spline function which is expressed as follows:

[2.44] $$W(\boldsymbol{x},h) = \alpha_D \begin{cases} 1-\frac{3}{2}q^2+\frac{3}{4}q^3 & 0 \le q \le 1 \\ \frac{1}{4}(2-q)^3 & 1 \le q \le 2 \\ 0 & q \ge 2 \end{cases}$$

with $q = x_{ij}/h$. The dimensional factor, α_D, is $15/(7\pi h^2)$ in two dimensions and $3/2(\pi h^3)$ in three dimensions. The cubic spine and its first derivative with respect to q are shown in Figures 2.2 and 2.3, respectively.

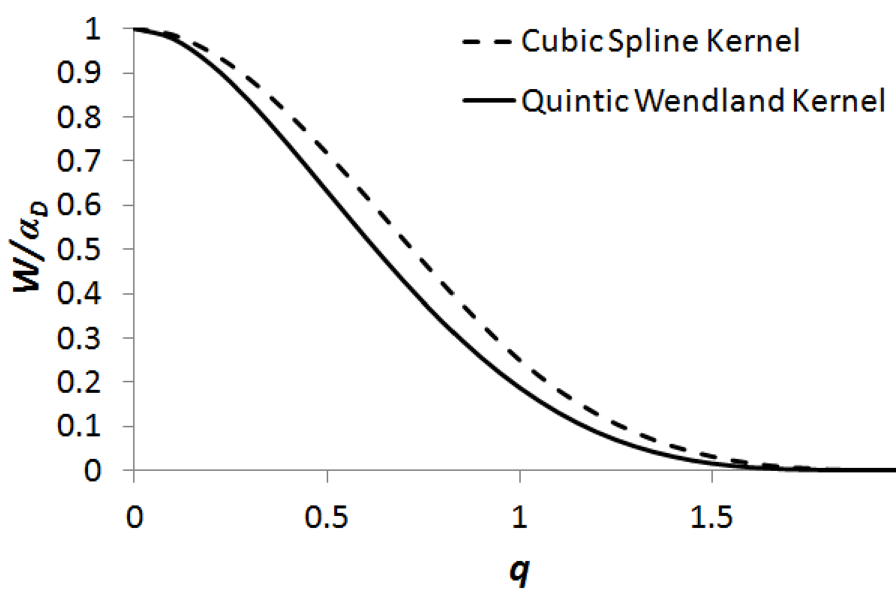

Figure 2.2- Cubic spline and quintic Wendland smoothing kernels

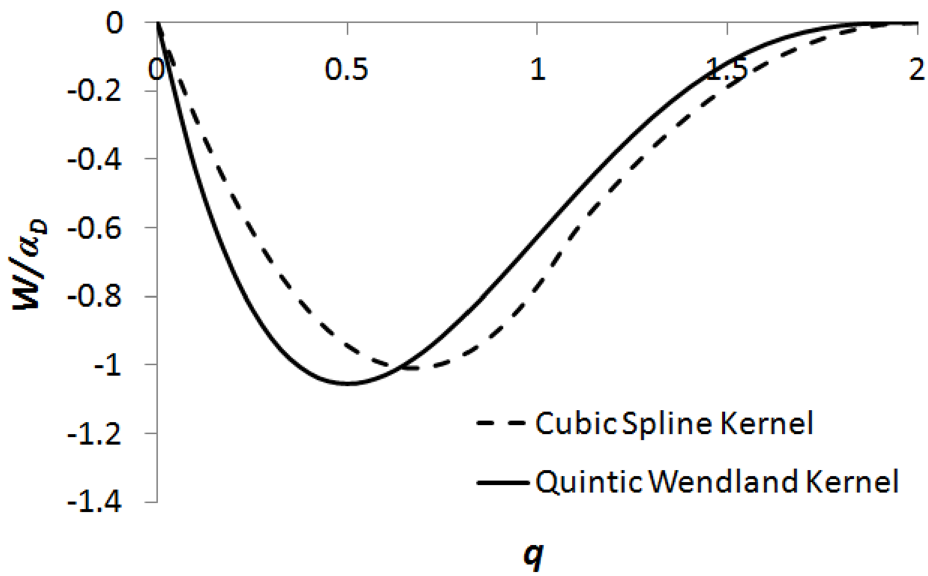

Figure 2.3- First derivative of the cubic spline and quintic Wendland smoothing kernels

Quintic Wendland Kernel

The quintic Wendland smoothing kernel is considered a good compromise between accuracy and the computational time cost. The kernel function is given by:

[2.45] $$W(\boldsymbol{x}, h) = \propto_D \left(1 - \frac{q}{2}\right)^4 (2q + 1) \qquad 0 \leq q \leq 2$$

where the dimensional factor is $7/(4\pi h^2)$ in two dimensions and $7/(8\pi h^3)$ in three dimensions. The quintic kernel and its first derivative can be seen in Figures 2.2 and 2.3. It is generally found that results using the quintic wendland kernel have better stability and a smoother property estimate then with the cubic spline [Zhu et al, 1999]; however, this results in a higher computational time.

2.4.3 Correction Schemes

There are several correction schemes available in the SPH method. These schemes are required in order to keep the simulation accurate and stable. These include the kernel correction and the shepherd density filter.

Kernel Correction

The kernel correction is a periodic correction which adjusts the truncated smoothing function for particles located near boundaries or the free surface, as at these locations the conditions of consistency and normalization fail.

The kernel gradient correction involves modifying the kernel gradient in order to produce a corrected kernel gradient, $\tilde{\nabla} W_{ij}$. This corrected gradient is used to calculate the forces in the equation of motion as opposed to the uncorrected gradient. This correction is accomplished by introducing a correction matrix $\boldsymbol{L}$ to the original gradient, which gives:

[2.46] $$\tilde{\nabla} W_{ij} = \boldsymbol{L}_{ij} \nabla W_{ij}$$

where the correction matrix is equal to M_i^{-1}:

[2.47] $$M_i = \sum_j^{num} \frac{m_j}{\rho_j} \nabla W_{ij} \otimes (\boldsymbol{x}_i - \boldsymbol{x}_j)$$

This correction ensures that the gradient of any linear velocity field is evaluated.

Density Filter

The Shepard density filter [Panizzo, 2004] is used to increase the stability of the model; however, it is only available while using the Verlet time stepping algorithm. The filter is applied every M time steps, with M on the order of 30, and is represented by

[2.48] $$\rho_i = \frac{\sum_j \rho_j \bar{W}_{ij} V_j}{\sum_j \bar{W}_{ij} V_j}$$

where the kernel has been corrected using a zeroth-order correction:

[2.49] $$\bar{W}_{ij} = \frac{W_{ij}}{\sum_j W_{ij}\frac{m_j}{\rho_j}}$$

Moving the Particles

Particles are moved in the model using the XSPH variant [Monaghan, 1989]:

[2.510] $$\frac{d\boldsymbol{x}_i}{d_t} = \boldsymbol{u}_i + \epsilon \sum_j \frac{m_i}{\bar{\rho}_{ij}} (\boldsymbol{u}_j - \boldsymbol{u}_i) W_{ij}^*$$

where ε is a constant whose value ranges from 0 to 1, with 0.5 being the most commonly used. The XSPH variant is used to modify the momentum equation to ensure that particles which are in close proximity will travel with similar velocities. This variant allows for the conservation of linear and angular momentum to be conserved exactly and enables the particles to be better organized. The use of this variant aides in the avoidance of particle penetration for high velocity fluids.

2.4.4 Viscosity and Turbulence

The viscosity term in the momentum equation had the original purpose of representing both the viscosity of the particles and to prevent the penetration of the particles. Furthermore, it had the benefit of keeping the numerical scheme stable for problems relating to free-surface flows. Unfortunately, the viscosity term can be overly dissipative which may affect the shear forces in the fluids, which can be detrimental in the case of turbulent structures.

The model contains two formulations that are available to describe the diffusive term in the momentum equation: artificial viscosity and laminar viscosity with a sub-particle scale (SPS) turbulence model.

Artificial Viscosity

The artificial viscosity formulation was proposed by Monaghan [1992] and is often utilized due to its simplicity. The artificial viscosity does not function like actual viscosity, but is designed to allow for shock phenomena to be simulated and is used to increase the stability of the model. The artificial viscosity can be obtained by rewriting the momentum equation as:

[2.51] $$\frac{d\boldsymbol{u}_i}{dt} = -\sum_j m_j \left(\frac{P_i}{\rho_i^2} + \frac{P_j}{\rho_j^2} + \Pi_{ij}\right) \nabla_i W_{ij} \ + \mathbf{g}$$

The pressure gradient tern in symmetrical form can be expressed in the SPH notation as:

[2.52] $$\left(-\frac{1}{\rho}\nabla P\right)_i = -\sum_j m_j \left(\frac{P_i}{\rho_i^2} + \frac{P_j}{\rho_j^2}\right) \nabla_i W_{ij}$$

The viscosity term Π_{ij} is given by:

[2.53] $$\Pi_{ij} = \begin{cases} \frac{-\alpha_{visc} c_{ij} \mu_{ij} + \beta \mu_{ij}^2}{\rho_{ij}} & \boldsymbol{u}_{ij} \cdot \boldsymbol{x}_{ij} < 0; \\ 0 & \boldsymbol{u}_{ij} \cdot \boldsymbol{x}_{ij} > 0; \end{cases}$$

with, $\mu_{ij} = \frac{h\boldsymbol{u}_{ij} \cdot \boldsymbol{x}_{ij}}{\boldsymbol{x}_{ij}^2 + \eta^2}$. When $\boldsymbol{u}_{ij} \cdot \boldsymbol{x}_{ij}$ is greater than zero there is no viscosity in the system.

The constant α_{visc} is a free parameter which is user-defined and will vary between different problems, the constant β is in the order of $\eta^2 = 0.01h^2$. It should be noted that for the current version of the model, the implementation of floating objects can only be performed using the artificial viscosity formulation.

Laminar Viscosity + SPS Turbulence

The sub-particle scale (SPS) approach to modeling turbulence was introduced by Gotoh *et al.* [2001]; this formulation was designed to represent the effect of turbulence in a moving particle semi-implicit (MPS) model. The laminar viscosity and SPS turbulence formulation can be expressed as:

[2.54] $$\frac{d\boldsymbol{u}}{dt} = -\frac{1}{\rho}\nabla P + \boldsymbol{g} + \frac{1}{\rho}(\nabla \cdot \rho \nu_o \nabla)\boldsymbol{u} + \frac{1}{\rho}\nabla\boldsymbol{\tau}$$

where $\boldsymbol{\tau}$ is the sub-particle scale stress tensor element, as shown below:

[2.55] $$\boldsymbol{\tau}_{ij} = \rho\left(2\nu_t\boldsymbol{S}_{ij} - \frac{2}{3}\boldsymbol{S}_{kk}\delta_{ij}\right) - \frac{2}{3}\rho C_I \Delta^2 \delta_{ij}$$

C_I can be approximated as 0.00066 [Blinn *et al*., 2002]. The Favre-filtered rate of strain, $\boldsymbol{S}_{ij}$ from Eq. 2.55 can be expressed as:

[2.56] $$\boldsymbol{S}_{ij} = -\frac{1}{2}\left(\frac{\partial \boldsymbol{v}_i}{\partial \boldsymbol{x}_j} + \frac{\partial \boldsymbol{v}_j}{\partial \boldsymbol{x}_i}\right)$$

and the turbulence eddy viscosity, ν_t is calculated using the standard Smagorinsky model [Smagorinsky, 1963]:

[2.57] $$\nu_t = (C_s\Delta)^2|S|$$

where the Smagorinsky constant, C_S is equal to 0.12. The laminar aspect of the viscosity equation can be simplified to [Lo and Shao, 2002]:

[2.58] $$(\nu_0\nabla^2\boldsymbol{u})_i = \sum_j m_j\left(\frac{4\nu_0\boldsymbol{x}_{ij}\nabla_i W_{ij}}{(\rho_i+\rho_j)|\boldsymbol{x}_{ij}|^2}\right)\boldsymbol{v}_{ij}$$

where υ_0 is the kinetic viscosity of laminar flow with a value of 10^{-6} m/s. The laminar and SPS turbulence can then be discretized in SPH notion [Dalrymple and Rogers, 2006] as:

[2.59] $$\frac{D\boldsymbol{u}_i}{Dt} = -\sum_j m_j\left(\frac{P_j}{\rho_j^2} + \frac{P_i}{\rho_i^2}\right)\nabla_i W_{ij} + \boldsymbol{g} + \sum_j m_j\left(\frac{4\nu_0\boldsymbol{x}_{ij}\nabla_i W_{ij}}{(\rho_i+\rho_j)|\boldsymbol{x}_{ij}|^2}\right)\boldsymbol{u}_{ij} + \sum_j m_j\left(\frac{\boldsymbol{\tau}_j}{\rho_j^2} + \frac{\boldsymbol{\tau}_i}{\rho_i^2}\right)\nabla_i W_{ij}$$

2.4.5 Equation of State

The SPH model used for this study is a weakly compressible model, which means it uses an equation of state to calculate the pressure. The Tait equation of state [Monaghan, 1994; Batchelor, 1974] enforces very low density variations by neglecting atmospheric pressure, which can be added separately as a constant pressure term. The Tait equation is given by:

[2.60] $$P = B\left(\left(\frac{\rho}{\rho_0}\right)^{\gamma} - 1\right)$$

where $\gamma = 7$ and $\rho_o = 1000.0$ Kg/m^3; for lower Reynolds numbers γ may be approximated as 1 which would provide more accurate pressure estimates [Morris, 1997]. The pressure constant *B* governs the fluctuation of the relative density and affects the speed of sound, c_0. The speed of sound can be determined by the square root of the derivative of the equation of state:

[2.61] $$c^2(\rho) = \frac{\partial P}{\partial \rho} = \frac{B\gamma}{\rho_o}\left(\frac{\rho}{\rho_o}\right)^{\gamma-1} = \frac{B\gamma}{\rho_o^{\gamma}}\rho^{\gamma-1}$$

[2.62] $$c_0^2 = c^2(\rho_0) = \frac{\partial P}{\partial \rho}_{|\rho=\rho o} = \frac{B\gamma}{\rho_0}$$

where $c(\rho_0)$ is the speed of sound at the reference density. Eq. 2.63 can also be written as:

[2.63] $$B = \frac{C_0^2\rho_0}{\gamma}$$

where it sets a limit for the maximum change in the density. It should be noted from Eq. 2.60 that small fluctuations in density could result in large variations in pressure. The speed of sound is greatly reduced so that the time step remains reasonable; typically the speed of sound should be roughly 10 times the flow velocity.

2.4.6 Boundary Condition

Boundary particles are used in the model to create a repulsive force which acts to prevent the fluid particles from exiting the limits of the computational domain, or from going through solid objects. The dynamic boundary condition [Crespo *et al.*, 2007] functions by using dynamic particles which are governed by the same governing equations and equation of state as the fluid particles. Unlike the fluid particles though, the dynamics particles are given an imposed location and their position remains unchanged over the course of the simulation, or they are moved based on an externally imposed function. An advantage with this boundary condition is its computational simplicity, as the particles are evaluated in the same loop as the fluid particles. This boundary condition may also be considered advantageous when using complex model boundaries.

The boundary particles are organized in a staggered configuration, see Figure 2.4. The separation between the different particles is $dx = dz$.

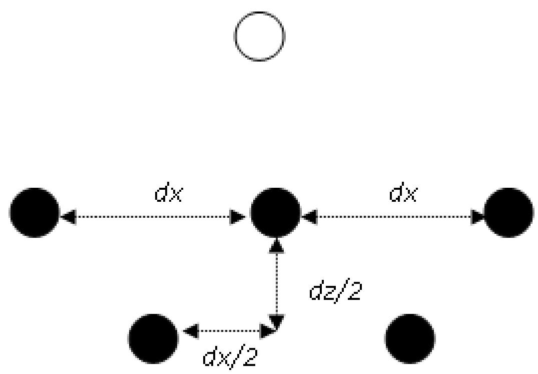

Figure 2.4- Spacing between boundary particles (black)

When approached by a fluid particle the density of the boundary particle increases resulting in a pressure increase. This increases the force exerted on the fluid particle. When the distance between the boundary and fluid particle is smaller than $2h$ the density, pressure and force is increased enough to generate a repulsion mechanism.

The dynamic boundary particles may also have additional applications inside the computational domain as solid objects with an imposed motion. This has been used for the simulation of wave mitigating dikes [Crespo *et al.*, 2007], and for wave generators [Crespo *et al.*, 2008].

2.5 Open Source Code

As previously mentioned in Section 2.4, the model utilized in this study was the DualSPHysics model, which is an open source model developed by the University of Vigo, the University of Manchester and Johns Hopkins University. This model was designed to address problems with the computational cost found in previous SPH models by allowing the model to be run on both the graphics processing unit (GPU) and the CPU or only on the CPU, as shown in Figure 2.5.

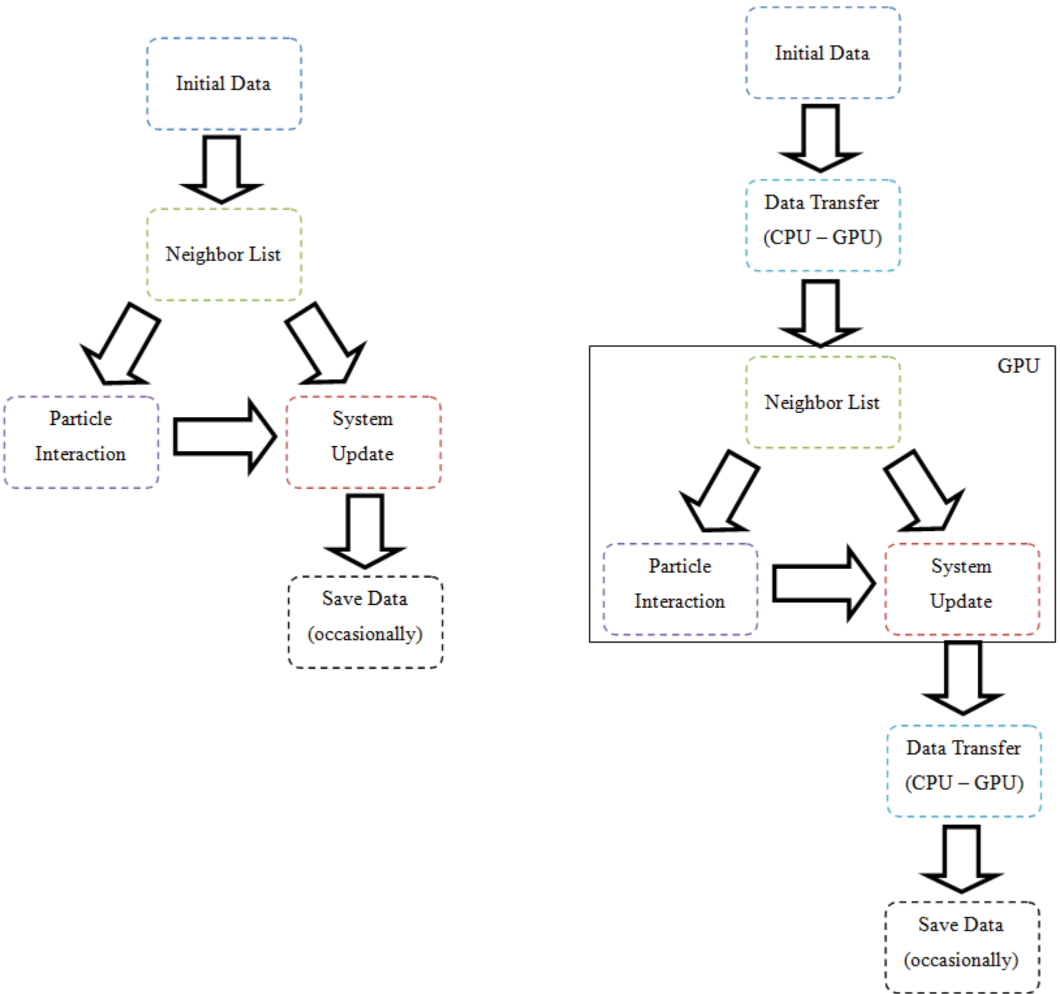

Figure 2.5 - Flow diagram of the CPU (left) and total GPU (right) implementation [adapted from Crespo *et al.* 2011]

3 Literature Review

3.1 Introduction

The literature review presented in this chapter focuses on previous authors' research and their observations and results. The first section examines studies which investigated modeling the generation and propagation of tsunami waves and hydraulic bores using analytical, physical and numerical modeling methods. The second section investigates the effects of the coastal forest on tsunami attenuation and velocity, while the final section investigates the impact forces on structures caused by tsunami-moved debris. Each of these sections looks at various analytical, physical and numerical models. The objective of this literature review is to provide a background on the concepts related to tsunami generation and propagation and debris movement, as well as to provide a reference for the research presented in the current study.

3.2 Modeling of Tsunami Waves and Hydraulic Bores

Prior to modeling the propagation of the tsunami waves and hydraulic bores it is integral to understand the way that actual tsunami waves behave as they approach the coastline. As observed in previous tsunamis, the behavior of the wave or bore is greatly influenced by the local geographic features.

Tsunami waves are commonly modeled as solitary waves due to their ability to represent the important aspects of the tsunami; while the hydraulic bores are typically modeled using a "dam-break" style bore. Solitary waves may be modeled as either breaking or non-breaking waves, both of which are examined in this chapter. The propagation of the breaking wave is considered to be a function of the method of breaking undergone by the wave.

Solitary Waves

One method of analyzing the runup of a solitary wave on a plane beach was presented by Synolakis [1987]. Synolakis proposed an approximate theory to calculate the runup for a non-breaking wave. This theory was used to derive results which are applicable to the maximum runup of a solitary wave, and was validated through a series of laboratory experiments.

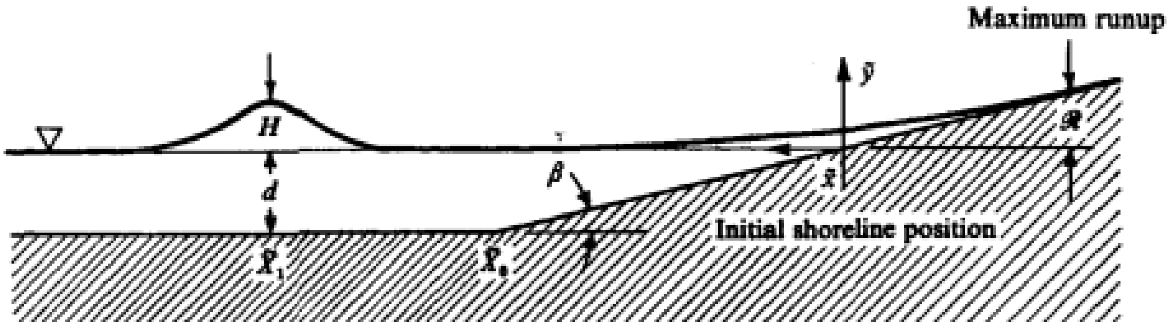

Figure 3.1 - Definition sketch for a solitary wave on a sloping beach [Synolakis, 1987]

The time of the maximum runup can be approximated using the function:

[3.1] $$t_{max} = \frac{1}{c}\left(X_1 + X_0 - \frac{0.366}{\gamma}\right)$$

where $\gamma = \left(\frac{3H}{4d}\right)^{\frac{1}{2}}$. The following expression can be approximated as the "Runup law":

[3.2] $$\frac{\mathcal{R}}{d} = 2.831(\cot\beta)^{\frac{1}{2}}\left(\frac{H}{d}\right)^{\frac{5}{4}}$$

where $\mathcal{R}$ is the maximum value of the runup. This expression is formally correct when $\left({}^{H}/_{d}\right)^{\frac{1}{2}} \gg 0.288 tan\beta$. The experimental validation of this equation, shown in Figure 3.2, indicates that the equation is able to approximate the runup height of non-breaking waves with some accuracy, but is not capable of approximating those of breaking waves. It can also be seen from this figure that the accuracy of the approximation decreases as H/d increases, based on the definition sketch in Figure 3.1.

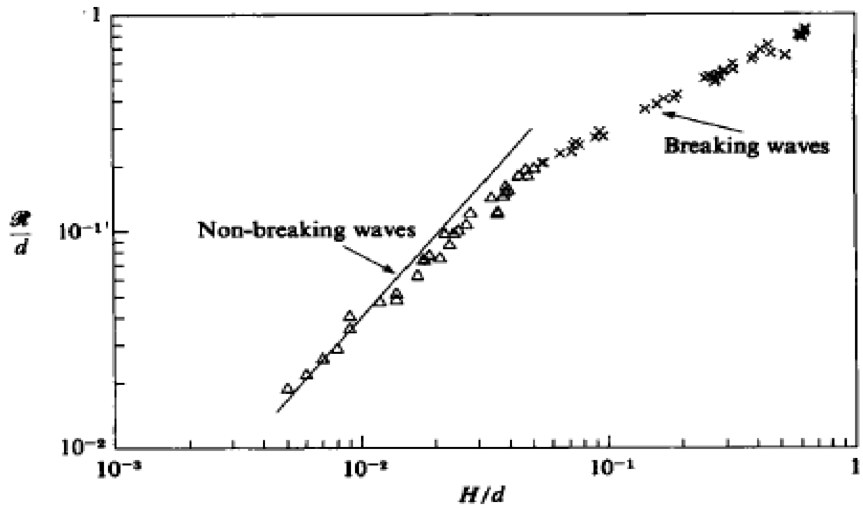

Figure 3.2 - Normalized maximum runup of a solitary wave. *x*, breaking wave; Δ, non-breaking wave; – , runup law [Synolakis, 1987]

An analysis of the three-dimensional runup of a solitary wave was performed by both Briggs *et al.* [1995] and by Liu *et al.* [1995] on a circular island. The laboratory experiments performed by Briggs *et al.* used a 7.2m diameter conical island, as shown in Figure 3.3, solitary waves with a height-to-depth ratio, *H/d*, of 0.05 to 0.2 and a "source" length ranging from 0.3 to 7.14 island diameters for water depths, *d*, of 32 and 42cm. The runup on the island was found to be roughly symmetrical, with the runup at the back of the island being slightly larger. This was believed to be due to the refraction and diffraction of the wave, which caused the wave to bend around the island. As the wave and island were symmetrical, the wave diffracted evenly around the island producing a larger runup along the back of the island. When the wave source was offset from the islands center, the runup was found to be largest on the island quadrant closest to the source.

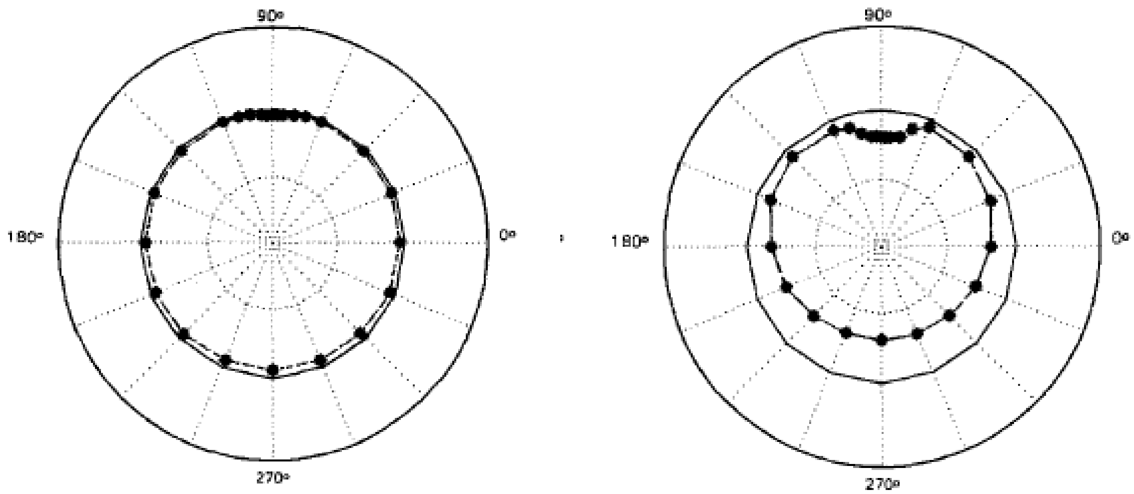

Figure 3.3- Maximum runup measured for H = 0.05 and 0.20, module = 4 and d = 32cm [Briggs *et al*., 1995]

The study performed by Liu *et al.* examined the same model setup using a numerical model based on the nonlinear shallow-water equations. The numerical model results obtained were then compared to those obtained in the experimental study. The comparison of the normalized runup height distribution around the island for different values of ε, where $\varepsilon = A/h$ and h is the still-water depth, are shown in Figure 3.4.

It was found in this study that when the solitary wave did not break on the front of the island, then the numerical and experimental results were in good agreement. Additionally, it was observed that the velocity tended to be relatively strong nearshore, which could result in significant sediment transport for sandy beaches. The analysis of the runup patterns were deemed comparable to those observed in Briggs *et al.* [1995].

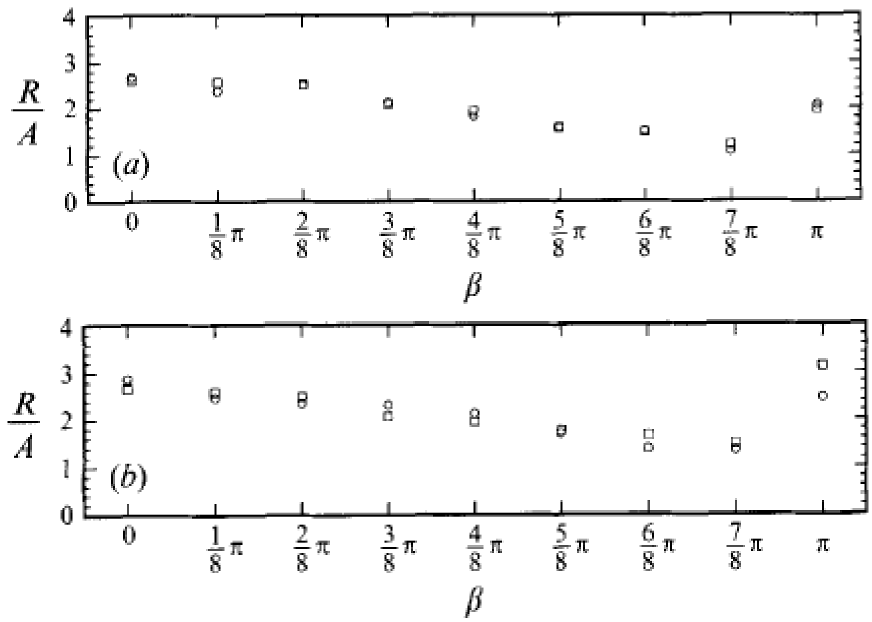

Figure 3.4 - Comparisons of normalized runup height: (a) *ε = 0.05*, **(b)** *ε = 0.05*: **□, experimental; ○ numerical [Liu *et al.*, 1995]**

The study of a solitary wave runup on non-plane beaches, conducted by Pelinovsky *et al.* [2008] was analyzed both analytically and numerically for a parabolic beach, shown in Figure 3.5.

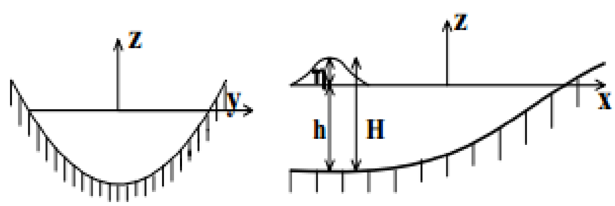

Figure 3.5 - Cross-section and longitudinal projection of the parabolic bay [Pelinovsky *et al.*, 2008]

The analytical formula for the vertical displacement of the water level on the shore was presented as:

[3.3] $$R(t) = -\frac{2\sqrt{6}L}{\sqrt{gh_0}}\frac{d\eta_{in}(t-\tau)}{dt}$$

where τ is the wave travel time from a fixed point to the shore. This analytical formulation was compared with that of Synolakis [1987] in order to determine the maximum runup for the two beach geometries with a beach slope of $\alpha = 0.1$. From the results shown in Figure 3.6, it can be seen that the runup on a parabolic beach is larger due to the concentration of the wave energy near the beach.

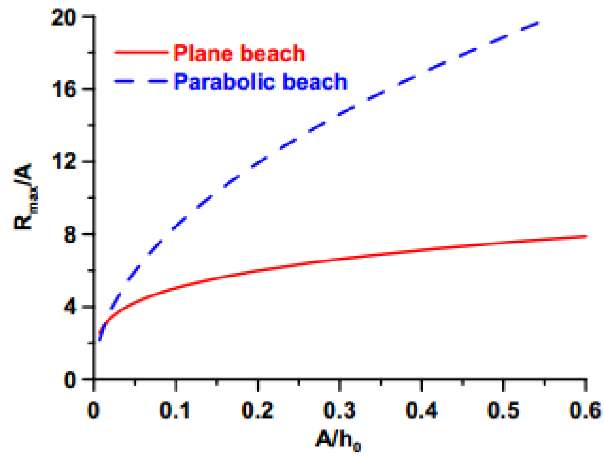

Figure 3.6 - Runup of a solitary wave on a plane and parabolic beach [Pelinovsky *et al*., 2008]

The final paper reviewed analysed the runup and rundown of a solitary wave propagating over a sloped beach backed with a vertical wall. Monaghan and Kos [1999] utilized this setup for their study which was designed to mimic the coastline on the northern coast of Crete which is characterized by narrow coastal plains that are backed by steep mountains. The solitary wave was generated for this study by dropping a heavy box to the bottom of the tank, shown in Figure 3.7. As the solitary wave propagated it became asymmetrical in the shallower depths and did not break.

This experiment was then replicated using an SPH model, and the runup results were compared to those of the physical experiment and with results obtained by the MAC calculations of Chan and Street [1970]. These results, shown in Figure 3.8, show good agreement for the normalized runup value.

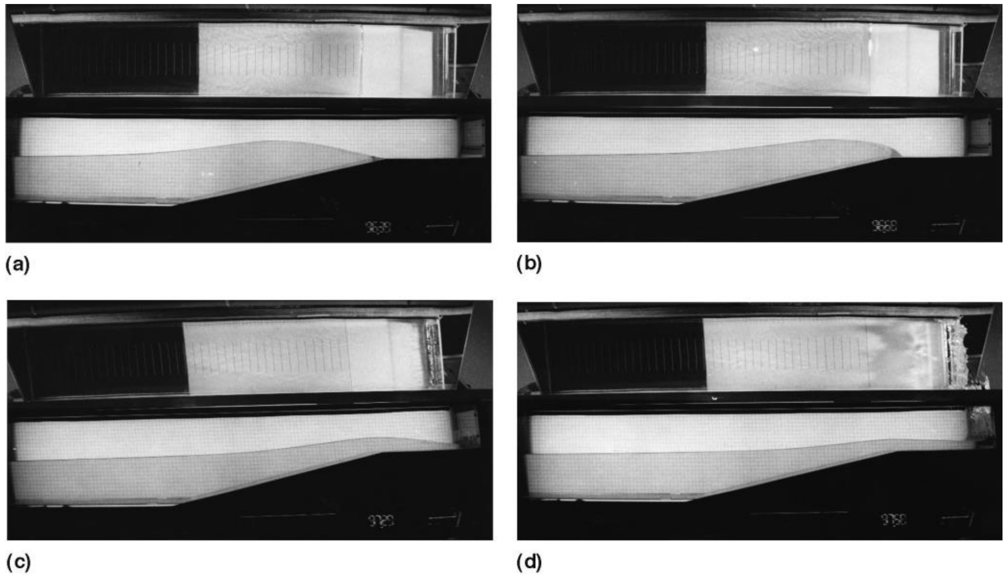

Figure 3.7 - Evolution of a solitary wave [Monaghan and Kos, 1999]

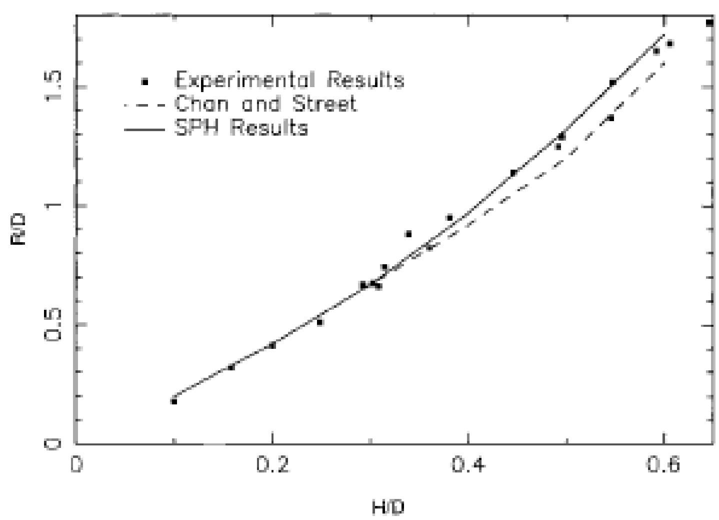

Figure 3.8 - Solitary wave runup using SPH, MAC and experimental results [Monaghan and Kos, 1999]

Additionally, it was found in this study that the initial tsunami wave was laminar; but, upon impacting the vertical wall the flow ran down the shore as a turbulent bore with velocities similar to those seen in the runup.

Hydraulic Bores

The modeling of hydraulic bores is typically performed as a "dam-break" style bore, in which a water reservoir of height, H_0, is released into a dry or wet flume to create a turbulent bore. The schematic of the dam-break bore is shown in Figure 3.9.

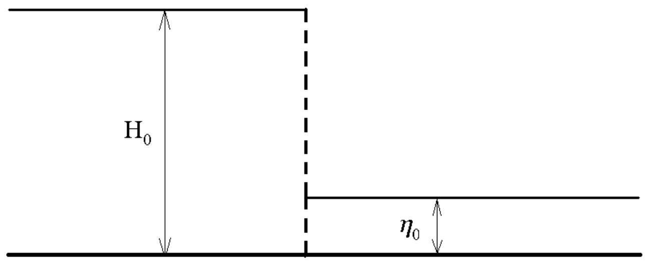

Figure 3.9 - Schematic of a dam-break problem [Shugan *et al*., 2010]

The first paper assessed did not generate the hydraulic bore using the typical "dam-break" method, instead using the setup shown in Figure 3.10. This report, by Chanson *et al.* [2000] examined the propagation of a hydraulic bore over a sloped beach for both dry and wet initial conditions.

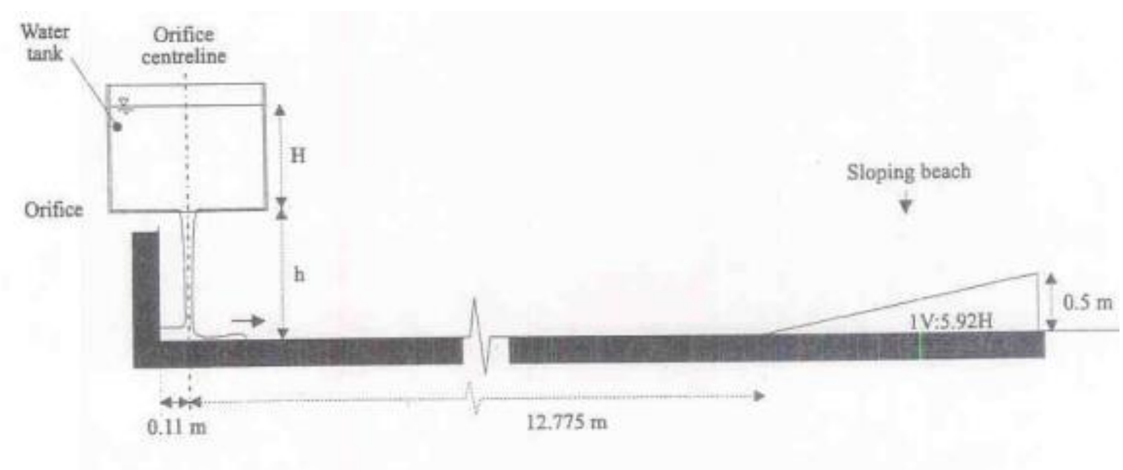

Figure 3.10 - Bore propagation for dry bed condition on a sloped beach [Chanson *et al.*, 2000]

This study resulted in consistently greater wave front celerity for the dry bed condition than predicted in traditional dam-break analysis at the initial stage of propagation, which was then followed by deceleration due to the bottom friction and the dissipation of the energy due to turbulence. However, it was found that further downstream the bore would propagate at similar speeds to that of the theoretical "dam-break" bore. It was found that the experimental data was best correlated by:

[3.4] $$\frac{C_S}{V_i} = \frac{0.598}{1-0.0336\frac{x}{d_o}+0.00237\left(\frac{x}{d_o}\right)^2}$$

where V_i is the initial jet impact velocity, C_s is the wave front velocity, x is the horizontal longitudinal coordinate and d_o is the equivalent dam break reservoir depth. For the scenario with an initial wet bed, the experimental results indicated greater wave front celerity than for the analytical equation. Downstream it was found that the data was consistent with the momentum principle. Chanson *et al.* found that the experimental data was best represented using:

[3.5] $$\frac{C_S}{V_i} = \frac{0.598}{1-0.0263\frac{x}{d_o}+0.00117\left(\frac{x}{d_o}\right)^2}$$

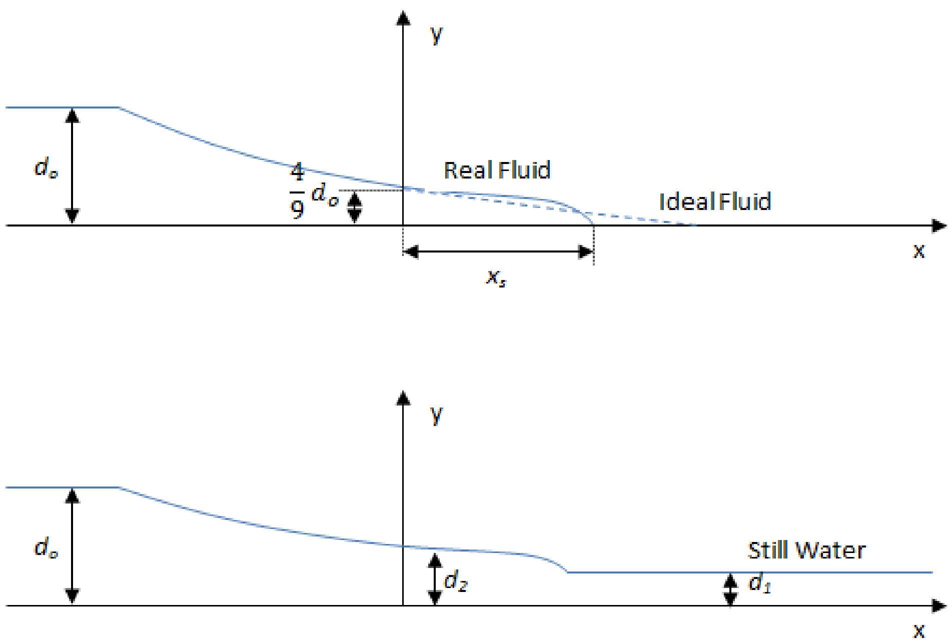

Figure 3.11 - Bore propagation for dry and wet bed conditions [adapted from Chanson *et al.*, 2000]

A second method of calculating the bore celerity and propagation was suggested by Stoker [1957]. For a dry bed condition Stoker proposed that the velocity of the bore water tends to $\frac{2}{3}c_o$ as time progresses, where c_o is equal to $\sqrt{gd_o}$ based on the definition sketch shown in Figure 3.11. When considering an initial setup with a wet bed of uniform depth, Stoker separated the bore into four sections for any time $t = t_0$, see Figure 3.12.

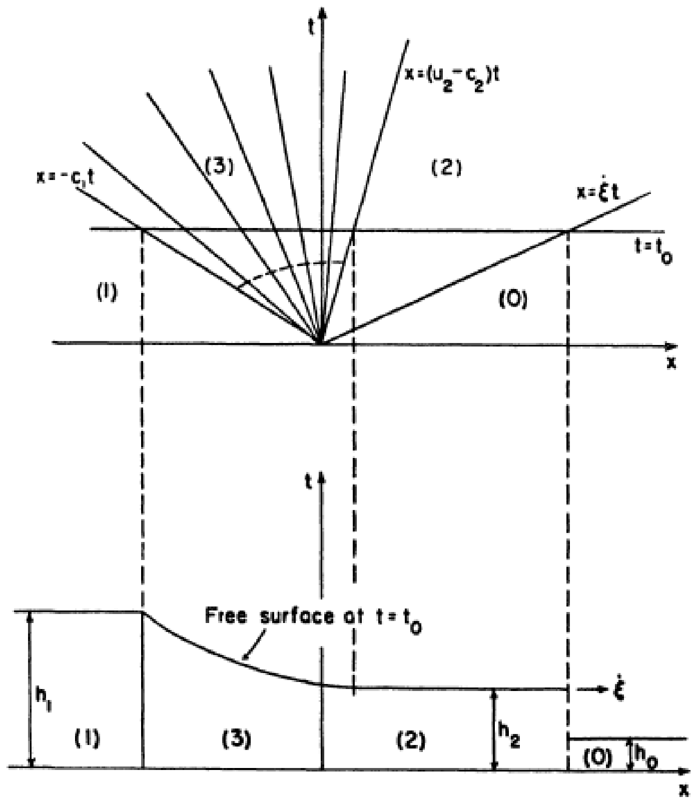

Figure 3.12 - Dam break [Stoker, 1957]

Zone (0) is represented as the still-water downstream of the bore; zone (2) is the bore front and is in constant state but is not at rest. Zone (3) is the centered simple wave which connects the constant state (2) with the constant state (1) of the undisturbed upstream water. Stoker represents the wave celerity for the transition from state (0) to state (2) as:

[3.6] $$\frac{c_2}{c_0} = \left\{\frac{1}{2}\left(\sqrt{1 + 8\left(\dot{\xi}/c_0\right)^2} - 1\right)\right\}^{\frac{1}{2}}$$

The velocity in zone (3) can be calculated using the same method as for the dry bed condition:

[3.7] $$u = \frac{2}{3}(c_1 + \frac{x}{t})$$

and the wave celerity can be obtained using:

[3.8] $$c_2 = \frac{1}{9}(2c_1 + \frac{x}{t})^2$$

Another study of tsunami runup on dry and wet coastlines was performed by Chanson *et al.* [2003]. The experiments were completed in a horizontal steel flume with a sloped beach where the bore was generated by the vertical release of the water. The flow patterns for this study found that there was a high level of turbulence of the surge and the wave front was highly aerated. The maximum runup height on the sloping beach was measured; it was found that the initial wave runup height for the dry channel could be approximated as:

[3.9] $$\frac{H_r}{H_1+h} \approx 0.215$$

Where H_1 was the head above the orifice and h was the fall height between the orifice and the channel bed. When run with a wet bed condition, the beach was overtopped by the first runup.

3.3 Influence of Coastal Forests on Tsunami Propagation

The coastal forest acts as a barrier that absorbs the impact of the tsunami and delays and reduces the tsunami flow. These natural structures act as a permeable barrier which partially reflects and partially transmits the tsunami wave [Forbes and Broadhead, 2000], see Figure 3.13. Additionally, further energy is lost as the tsunami propagates through the forest.

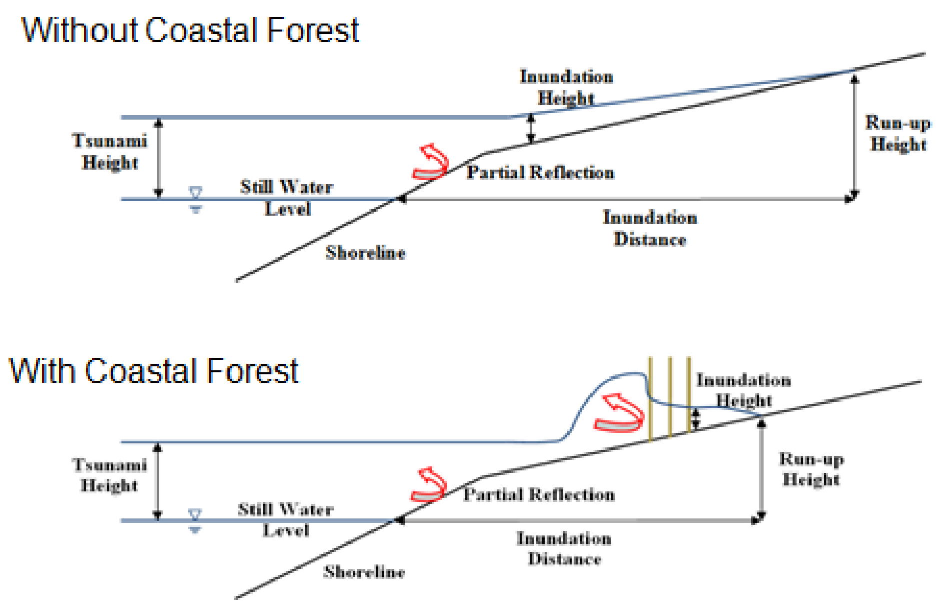

Figure 3.13 - Effect of coastal forest on tsunami wave runup [adapted from Forbes]

There is a large body of research investigating the influence of coastal forests on the propagation and attenuation of tsunami waves and bores. This research focuses primarily on the changes in the bore attenuation due to the presence of a coastal forest for various forest, bathymetric and tsunami parameters. Research has also been conducted into the effectiveness of different forest layouts and the impact of gaps in the forest, such as roads, on the tsunami propagation and velocity. Additional studies have examined the reduction in tsunami force as it propagates through the coastal forest. This section presents a summary of the analytical, physical and numerical analyses which have examined these phenomena.

3.3.1 Analytical Modeling of Tsunami Attenuation by Coastal Forests

The influence of the forests' structure, for a mangrove forest, on the attenuation of waves was examined by Bao [2011] for two regions in Vietnam. This study examined the relationship between the forest structures, wave height and forest band width with the intent of developing a function to describe the attenuation. The research found that the effect of the forest band width on the sea wave height could be expressed as an exponential function:

[3.10] $$W_h = a \times e^{b \times B_w}$$

where W_h is the sea wave height behind the forest, B_w is the forest band width, a is the intercept and b is the slope coefficient. Additionally, Boa examined the minimum mangrove forest width required to protect from sea waves, assuming wave heights to be less than 300 cm, which allowed a classification index to be made based on the forest characteristics (V), see Figure 3.14, where high V values correspond to tall and dense trees.

Levels	V index	Required band width [m]	Name of levels
I	< 0.005	> 240	very weak prevention
II	0.005–0.010	120–240	weak prevention
III	0.010–0.015	80–120	moderate prevention
IV	0.015–0.028	40–80	strong prevention
V	> 0.0280	< 40	very strong prevention

The maximum wave height is assumed to be 300 cm.

Figure 3.14 - Classification of mangrove forest widths for protection against sea waves [Boa, 2011]

The impact of tree morphology and tree growth were examined by Asano [2008a, 2008b] in order to assess the fluid resistance of the individual tree components and the temporal change of the tree diameter and forest density for a self-thinning forest.

The effect of the tree morphology, including the trunk, branches and leaves was assessed by Asano [2008a] using a mathematical model which separated the tree into two regions, the tree/crown and the trunk/branch. This model was used to a conduct a sensitivity analysis on wave and tree parameters which affect the attenuation coefficient k. From this analysis it was found that the attenuation coefficient increased for larger wave amplitudes and forest densities, and went down for increased tsunami periods and water depths.

The forest growth model completed by Asano [2008b] assessed the forests ability to attenuate a tsunami based on temporal changes in the tree diameter and stand density under self-thinning conditions as would be present in reality. This model also included a tree throw-down effect and a trunk distribution based on the Weibull distribution. The self-thinning condition took into consideration the upper limit of tree density due to competition for sunlight, and was used to develop an accurate forest growth model. By considering this and the trunk diameter distribution, greater accuracy in the attenuation of the tsunami was found. Additionally, it was found that due to the distribution of the tree diameters the tree throw-down effect only affected certain trees which resulted in a continuous attenuation of the wave as opposed to the complete failure of the forest stand.

3.3.2 Physical Modeling of Tsunami Attenuation by Coastal Forests

Several researchers have examined the effect of tree stand densities on the attenuation of the tsunami bore. Iimura and Tanaka [2012] completed both experimental and numerical work on the effect of stand density by comparing forest stands with various uniform densities to that of a combined forest with both sparse and dense sections. The experimental and numerical results indicated that as the stand density increased so too did the reduction in water level and velocity for both uniform and combined arrangements. Additionally, the runup of the tsunami on the trees as described by Figure 3.13 was found to be noticeable for both experimental and numerical models and became more profound for the denser arrangements. Finally, it was noted that the reduction in attenuation was only marginally larger for the combined arrangement when the model was denser in the back of the stand then in the front. Irtem *et al.* [2009] performed similar experiments, examining rectilinear, staggered and dense rectilinear forest configurations for different tree types, artificial pine trees and cylindrical trees, using different distances between the forest and the still-water level. The results indicated that the dense rectilinear forest provided the largest reduction in run-up for the artificial pine trees, while the staggered layout provided the best reduction for the cylindrical trees; it should be noted however that the dense rectilinear method was not tested for this tree type. Additionally, Irtem *et al.* found that the distance between the forest and the still-water level did not have an effect on the attenuation for the cylindrical timber trees, but that there was a decrease in the run-up for smaller distances using the artificial pine trees.

The correlation between the wave runup and the Iribarren number, as defined by Iribarren and Nogales [1949] was analyzed by Noarayanan *et al.* [2012] for cnoidal and regular waves using differing tree diameters and spacing, and various wave heights and periods. This study utilized flexible trees in order to simulate the natural movement of the trees when impacted by a wave. Noarayanan *et al.* found that there was a positive correlation between the wave runup and the Iribarren number; additionally, by using non-dimensional parameters to examine the runup it was concluded that high degrees of reduction were possible for sparser forests provided that the forest belt was wider.

A comparison between the effectiveness of coastal forests and other wave protection barriers was performed by Hiraishi and Harada [2003]; this study compared a tsunami coastal forest model with trunk and leaf components (S1), a uniform greenbelt model (S2), a wave dissipating block dike (S3), a ruble breakwater (S4), and a house (S5). Figure 3.15 shows the variation in the dimensionless measured tsunami height, current and pressure for the various porous barriers.

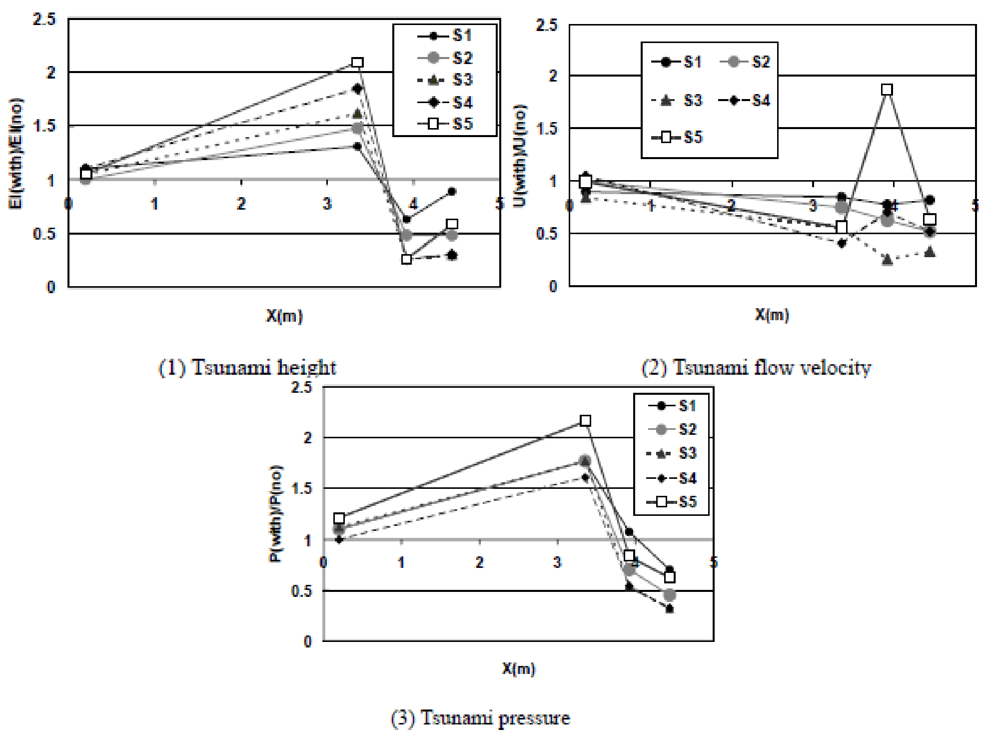

Figure 3.15 - Variation of tsunami height, current and pressure for porous barriers [Hiraishi and Harada, 2003]

The results indicated that the greenbelt increased the offshore tsunami wave height due to the wave reflection, but caused a reduction in the water level, current velocity and wave pressure behind the greenbelt. It was found that the tsunami reduction effect of the greenbelt was smaller than that of the breakwater with wave dissipating blocks but was similar to a comparably sized rubble mound breakwater.

To analyze the propagation of both broken and non-broken waves in the form of solitary waves and hydraulic bores a complex mangrove model was utilized by Struksińska-Correia *et al.* [2013] that contained exposed root systems. This research was unique in its use of fully-exposed mangrove roots as opposed to more traditional submerged systems, Figure 3.16.

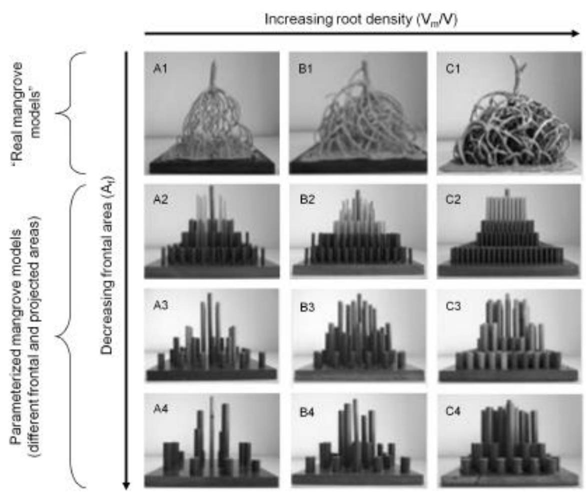

Figure 3.16 - Parameterized mangrove models of varying frontal and root densities [Struksińska-Correia *et al.*, 2013]

For the solitary waves it was found that the wave height reduction was higher for lower water depths and wider forests due to the waves' interaction with the root system. Additionally, it was found that the lowest transmission rate occurred for the non-breaking wave conditions indicating relatively poor forest damping performance. For the tsunami bore it was found that there was a similar minimum wave transmission despite the larger forces exerted by the tsunami bores as there was larger interaction with the root system. This study determined that the location of wave breaking is crucial for the evaluation of the forests effectiveness due to the additional energy dissipation caused by the breaking event.

3.3.3 Numerical Modeling of Tsunami Attenuation by Coastal Forests

A study into the effectiveness of different tree species in the reduction of the water depth and current velocity was performed by Nandasena *et al.* [2008a]. This study examined the bore reduction for varying ground slopes and vegetation positions, see Figure 3.17, for two different tree species.

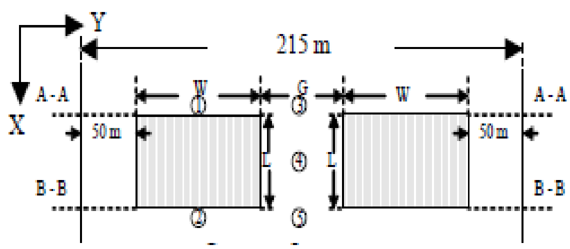

	L = 50 m	W = 25 m	G = 65 m	Remarks
Case 1	L	W	G	Wide gap - small patches
Case 2	L	2W	3G/13	Narrow gap - small patches
Case 3	2L	W	G	Wide gap - big patches
Case 4	2L	2W	3G/13	Narrow gap - big patches

Figure 3.17 - Sketch of vegetation placement and dimensions [Nandasena *et al.*, 2008a]

The study findings indicated that the species of tree had a small effect on the forests' ability to withstand the tsunami event. It was found that as the ground slope steepened, the reduction of the maximum water depth behind the vegetation was lessened and changing the forest arrangement had minimal effect. This is a result of the increased gravitational effect seen for the steeper slopes. For milder slopes it was found that increases in forest size reduced the run-up length. In respect to the forest gaps it was found that narrow gaps between the forest patches could result in an increase in the maximum current velocity at the gap outlet.

A second study by Nandasena [2008b] also examined the effect of variations in ground slope, as well as forest width and tsunami period for vegetation of a species commonly found in the South Asian coast. The findings indicated that the capability of the vegetation to reduce the water depth behind the forest was minimal for relatively steep slopes, but was increased as the ground slope became milder. It was also clearly found that widening the vegetation belt increased the reduction of the maximum water depth behind the forest belt. Contrary to the water depth, the current velocity had a larger decrease for the steeper slopes than for milder slopes. The findings for the variations in the wave period indicated minimal influence on the percentage of reduction in the horizontal run-up when compared to bare land.

Additional studies on the effect of the forest width on attenuation were performed by Ohira *et al.* [2012], Yanagisawa *et al.* [2009], and Harada and Imamura [2005]. Ohira *et al.* examined the damping effect of a coastal forest in Yogyakarta, Indonesia for varying forest widths. The water level change behind the forest belt was found to have increased negatively behind the wider forests as the depth was reduced significantly, while the water level increased positively in front of those forests due to the wave reflection, Figure 3.18. The findings of the study indicated that the damping effect of the forest was 2-dimensional and that the relationship between the forest widths and reduction in inundation could be expressed by an exponential relationship.

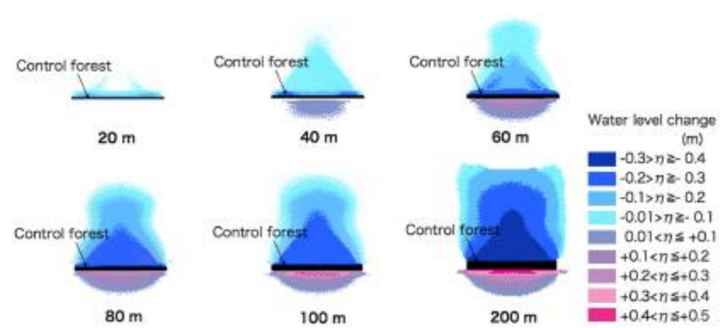

Figure 3.18 - Inundation depth change around coastal forest (With - Without) [Ohira *et al.*, 2012]

Yanagisawa *et al.* conducted field investigations in Pakarang Cape in Pang Nga Province, Thailand in order to validate their numerical model. The model was used to examine the bending height, stress and pressure of the trees in order to calculate a fragility function to estimate the damage probability, shown in Figures 3.19 and 3.20. The reduction rate of the inundation depth and pressure based on different mangrove forest widths using the damage probability was also examined. The conclusions of the study indicated that there was a large increase in the reduction rate corresponding to an initial increase in forest width, which then began to slowly level off once the forest reached a certain width.

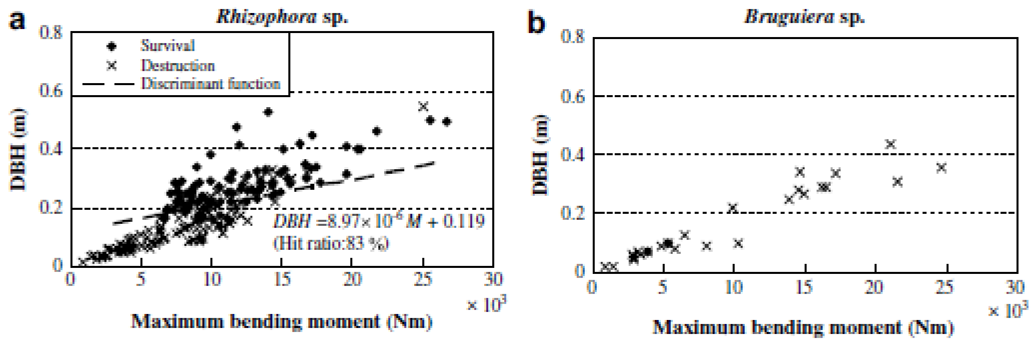

Figure 3.19 - Maximum bending moment for different breast height diameters (DBH) [Yanagisawa *et al*., 2009]

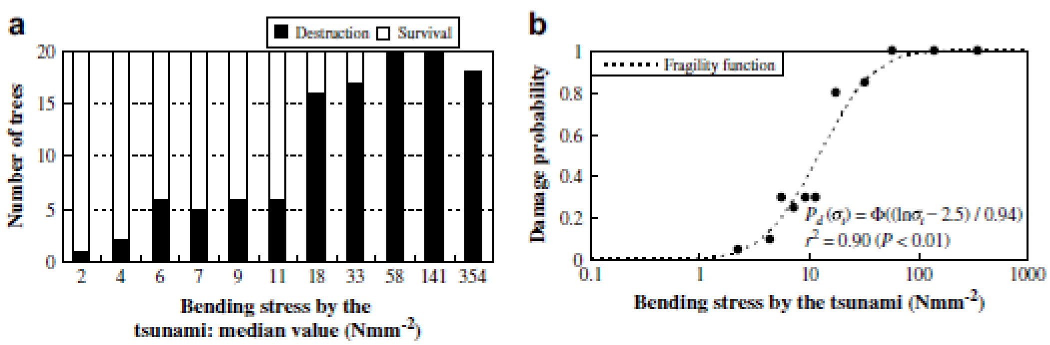

Figure 3.20 - Bending stress and damage probability [Yanagisawa *et al*., 2009]

The final study examining the effect of the forest width was by Harada and Imamura [2005] who assessed the forest effect under different densities, trunk diameters, wave periods and wave heights. Similar to the previous studies mentioned it was found that the forest width had a significant effect on the reduction of the inundation depth, current and wave force. In terms of the tsunami period it was found that as the tsunami period increased, the forests reduction effect became smaller for the inundation depth but did not have a large effect on the current velocity or the hydraulic forces, except for the smaller forests. Finally, the forest density was seen to have an effect on the inundation, current and force, as there was an increase in the reduction effect as the density increased.

Included in the study completed by Hiraishi and Harada [2003], shown in Section 3.3.2 was a numerical analysis examining the variation in the maximum water level and flow pressure for different greenbelt densities. The results of the study indicated that the maximum water level was exponentially decreased for increasing forest densities, as was the maximum flow pressure estimated on the ground.

The maximum bending moment on a coastal forest was examined by Nandasena *et al.* [2012] with their numerical model using the local geography of Misawa, and Hachinohe, Japan. In addition to the bending moment, these models examined the reduction in flow depth and flow velocity at different locations in the model for both real and hypothetical protection scenarios. For the location in Misawa, the coastal forest was located atop a dune, and it was found through the model that the dune provided most of the protection from the tsunami wave as opposed to the coastal forest. In the case of Hachinohe, the coastline was protected by both a coastal forest and partially by a seawall. In this scenario it was found that the seawall resulted in more damage to the coastal forest due to the diffraction of the tsunami wave around the barrier. This was examined further by comparing the bending moment of the vegetation for the different scenarios, Figure 3.21, where much larger bending moments were seen to be caused by the seawall. In both scenarios significant improvement on the reduction of the flow depth and velocity was seen for the coastal forest when compared to no vegetation; however, it was seen that the combination of dune and coastal forest provided the best results.

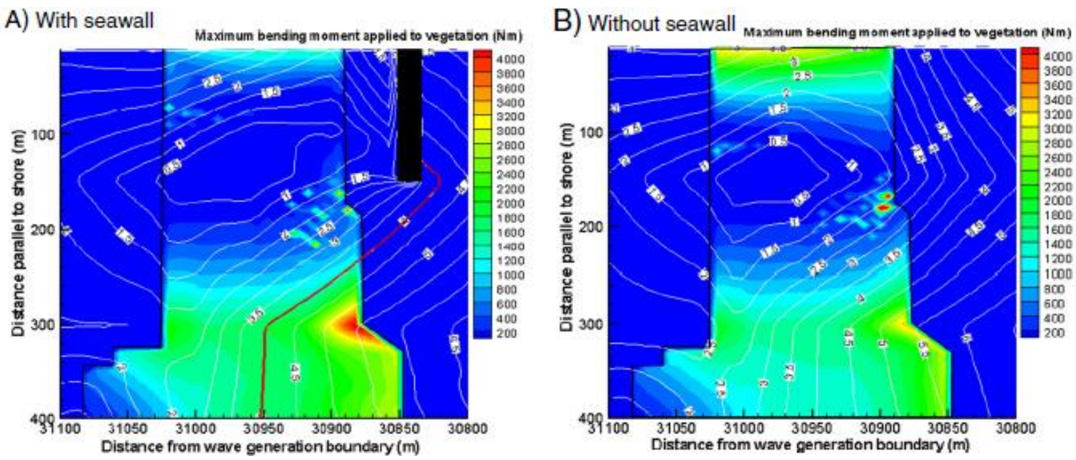

Figure 3.21 - Bending moment for coastal forest in Hachinohe, Japan [Nandasena *et al.*, 2012]

The final study, by Gelfenbaum *et al*. [2007] examined the erosion, deposition caused by a tsunami wave based on field measurements obtained from Sumatra using the Delft3D model. It was found that the sediment transport and morphological changes caused by the tsunami would have a large effect on tsunami defense structures such as coastal forests and sand dunes. The conclusions of the study indicated that experiments utilizing fixed bed models were not capable of capturing these morphological changes which may have an impact on the perceived usefulness of the defense structures.

3.4 Impact Forces of Tsunami-Moved Debris

The impact of debris on structures and on trees can result in large amounts of damage as the impact forces caused by the debris are not fully understood. This is due in part to the complex nature in which the debris and structure can interact.

Based on FEMA P-646 [2008], the debris impact force can be considered as a dominant cause for building damage. It was recommended that the debris impact force could be estimated based on:

[3.11] $$F_i = C_m u_{max} \sqrt{km}$$

where C_m is the added mass coefficient, u_{max} is the maximum flow velocity carrying the debris at the site, and *m* and *k* are the mass and effective stiffness of the debris. This equation was modified for FEMA P-646 [2012] to be:

[3.12] $$F_i = 1.3 u_{max} \sqrt{k m_d (1 + c)}$$

where *c* is the hydrodynamic mass coefficient which represents the effect of the water in motion with the debris. This force loading assumes that the impact acts locally on a single member of the structure at the elevation of the water surface, Figure 3.22.

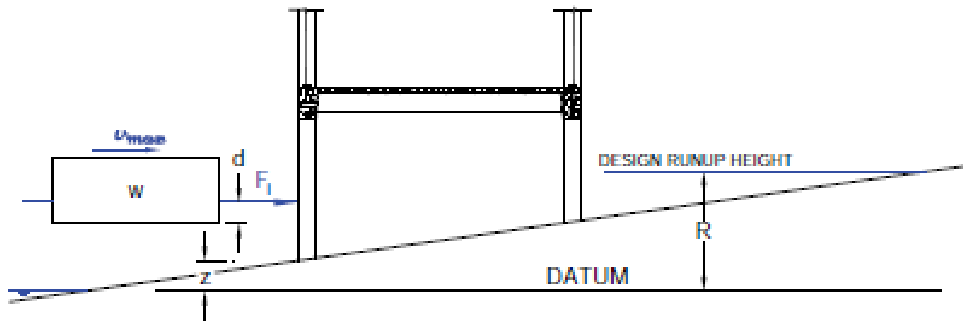

Figure 3.22 - Waterborne impact debris forces [FEMA P-646, 2012]

From FEMA P-55 [2011] the debris impact load can be calculated based on:

[3.13] $$F_i = WVC_D C_B C_{str}$$

where *W* is the weight of the object (lb), *V* is the water velocity (ft/sec), C_D is the depth coefficient, C_B is the blockage coefficient, and C_{str} is the building structure coefficient.

Research completed by Al-Faesly *et al.* [2013] compared Eq. 3.12 and Eq. 3.13 with experimentally found impact forces for cylindrical columns for different bore sizes and debris masses. This study indicated that the FEMA P-55 impact force equation greatly underestimates the impact force, see Figure 3.23, while that of FEMA P-646 [2012] is much more accurate. It is interesting to note the relatively large range of forces that can be obtained using the analytical equations depending on the choice of *c* and C_{str} values.

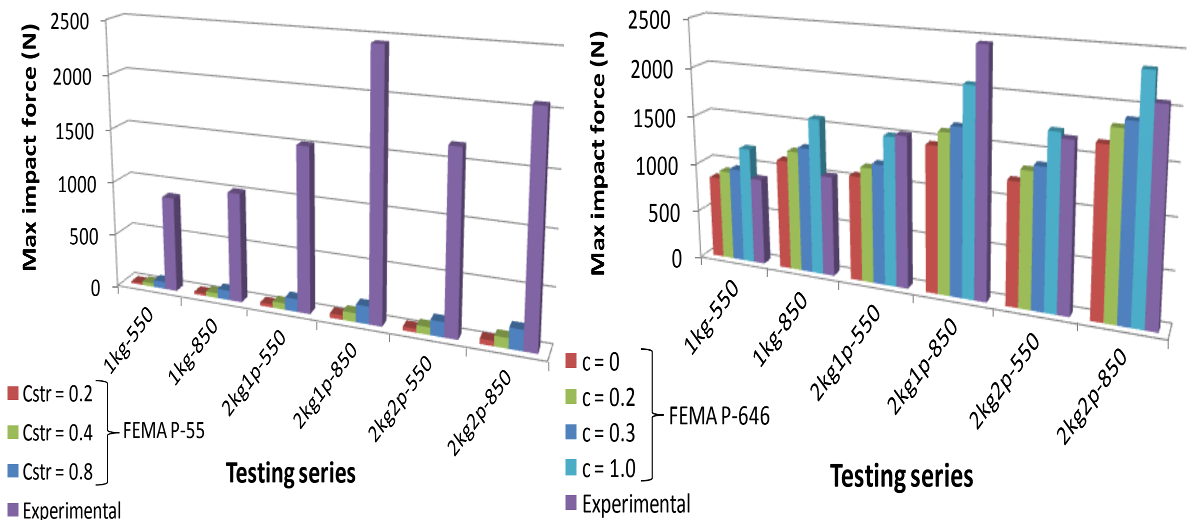

Figure 3.23 – Experimental debris impact force comparison with FEMA P-55 and FEMA P-646 [Al-Faesly *et al.*, 2013]

A separate method for calculating the impact force of debris was proposed by Matsutomi [1999], as summarized in FEMA P-646. This study investigated the experimental impulse force of driftwood for a small-scale experiment in a water tank and a full-scale impact in the air. It was noted by Matsutomi that the impact force in the air may be significantly different from that of the waterborne experiment due to the absence of the additional mass effect of the water; this was compensated for, using the data obtained from the small-scale experiment. Based on regression analysis the following impact force equation was proposed:

[3.14] $$\frac{F}{\gamma_w D^2 L} = 1.6 C_M \left(\frac{u}{\sqrt{gD}}\right)^{1.2} \left(\frac{\sigma_f}{\gamma_w L}\right)^{0.4}$$

where γ_w is the specific weight of the driftwood, *D* and *L* are the diameter and length of the log, respectively, $C_M = 1 + C_a$, where C_a is the added mass coefficient based on the displaced fluid volume, *u* is the driftwood velocity at impact and σ_f is the yield stress of the wood. This equation is applicable for driftwood collisions at right-angles with a rigid structure. Unfortunately, this equation is only applicable to driftwood or log debris.

As summarized in FEMA P-646, Ikeno *et al.* [2001, 2003] performed experiments similar to those of Matsutomi [1999] to investigate the impact forces of debris other than driftwood or logs. This study used cylindrical, square and spherically shaped debris which were impacted against an impermeable vertical wall. Based on these experiments an empirical formula was derived in order to calculate the force of the debris impact:

[3.15] $$\frac{F}{gm} = SC_M\left(\frac{u}{\sqrt{g\sqrt{DL}}}\right)^{2.5}$$

where *S* is a constant equal to two (for bores), and *m* is the mass of the drift body. This equation is only valid for impact against an impermeable wall, where the entire flow is reflected back in the offshore direction.

Three basic approaches for estimating the impact forces were compared with experiments performed by Haehnel and Daly [2002] using logs of varying weight impacting a stationary frame placed in the flow, for eight different test setups. The approaches tested were the contact stiffness approach [AASHTO, 1998], impulse-momentum [FEMA, 1995] and the work-energy approach [NAASRA, 1990].

The contact-stiffness approach calculates the maximum impact force of a vessel collision using:

[3.16] $$F_V(kips) = 8.15u\sqrt{DWT}$$

which is based on the dead-weight tonnage of the vessel, *DWT* (long tons), and the vessel velocity, *u* (ft/s). This method only requires the effective contact stiffness of the collision in order to estimate the maximum impact force.

The impulse-momentum approach equates the impulse of the debris impacting the structure with the change in momentum of the debris. The equation for this method is based on the impulse equation:

[3.17] $$I = \int F(t)dt = t_i\overline{F_i} = \int d(u_i m_i)$$

Assuming that the momentum of the debris is reduced to zero as a result of the impact the equation can be reduced to:

[3.18] $$F_i = \frac{u_i m_i}{t_i} = \frac{u_i w_i}{g t_i}$$

The impact duration, t_i, is equal to the duration between the initial debris impact and the maximum impact force. The limitation of this equation is that it calculates the average impact force as opposed to the maximum impact.

The final method, the work-energy approach, is calculated based on the work done on the structure through the kinetic energy of the debris and assuming that the velocity of the debris is reduced to zero upon impact, the solved equation can be reduced to:

[3.19] $$F_{i,max} = \frac{m u_o^2}{S} = \frac{w u_o^2}{g S}$$

The results of the experimental work were compared to the predicted values provided by the three different methods. The results indicated that the contact-stiffness method provided fairly accurate, though slightly conservative predictions of the impact force for all of the tests completed. For the impulse-momentum equation the approach consistently under predicted the impact forces for the reduced-scale models. It was believed that this under prediction was a result of using a constant stopping time rather than a variable one based on the debris mass. The final method, work-energy was found to only be applicable for debris with a kinetic energy greater than 50J. It was found to consistently over predict the impact force due to the use of a constant stopping distance as opposed to one that is a function of the debris mass and velocity.

The impact load of a small and large log was investigated by Nouri *et al.* [2010] for impacts on a cylindrical structure. Two strings were attached to the debris to ensure that the impact was perpendicular to the structure and to ensure the debris did not wash away after impact. This test was performed in order to determine the impact force on the structure, the period in which the force acts and the parameters which would affect the impact force. It was found in the study that the debris produced a second impact as it bounced back for almost all of the experimental runs. This second impact was of lower magnitude than the initial impact in all scenarios.

A coupled drift collision model was proposed by Yeom *et al.* [2009] in order to combine the drifting of water-borne debris with the LS-DYNA collision model. The drift model was based on the immersed boundary method from wave generation to just prior to the collision. This model was verified through comparison with laboratory experiments in order to determine the models accuracy. Additional testing was completed using a full-scale test of a freight container model, shown in Figure 3.24. For this study the coupled drift collision model proved feasible for modeling wave level, wave force and container drift behavior.

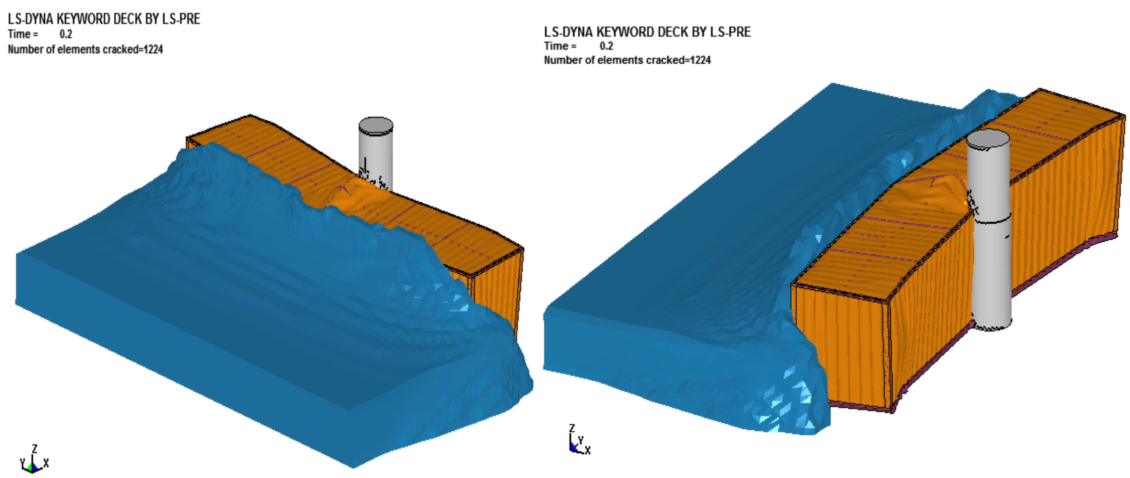

Figure 3.24- Full-scale drift collision test [Yeom *et al.*, 2009]

A method for estimating the maximum superimposed force due to simultaneous impacts of driftwood debris was examined by Matsutomi [2009] taking into account the probability of the impact occurrence. For a single debris impact at time t = τ, the time-history of the collision force can be obtained using:

[3.20]

$$F_\tau(t) = \frac{F_m}{\Delta t_p}(t-\tau) \qquad (\tau \le t \le \tau + \Delta t_p)$$
$$= \frac{F_m}{\Delta t - \Delta t_p}(\tau + \Delta t - t) \qquad (\tau + \Delta t_p < t \le \tau + \Delta t)$$

When the impact involves multiple debris impacts at t = τ and t_1 the maximum collision force can be obtained by:

[3.21] $$F_c(x, y, t) = \left|F_\tau(t) + F_{t_1}(t)\right|$$

No experimental validation exists for the collision force for simultaneous or near-simultaneous debris impact.

Research by Naito *et al.* [2011] is currently looking at ameliorating the disadvantages of the current methods of calculating the maximum impact force based on the design codes, which includes the flexibility of the debris, the variability in the maximum forces obtained by the codes and the fact that the codes are based on static loads for a dynamic event. The current contribution from the University of Hawaii focuses on the use of a single-degree freedom model to analyze the structural elements impacted by debris based on the simplified equation for impact into a rigid support:

[3.22] $$F = \sqrt{E\rho}uA$$

where E is the elastic modulus of the debris. The preliminary analysis of this simplified method is shown in Figure 3.25.

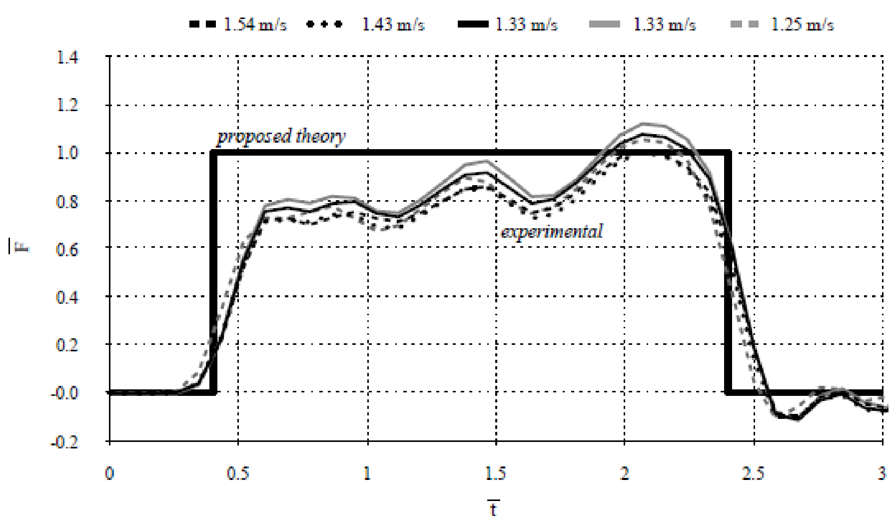

Figure 3.25 - 2m projectile impact [Naito *et al.*, 2011]

Another study which examined the use of flexible debris impact was performed by Kobayashi *et al.* [2012]. In this study the impact of a water-borne steel tube, wood poles and shipping containers was considered. The use of a Hertzian-type contact stiffness allowed for the gradual rise in the impact force due to the deformation of the debris as opposed to the sharp increase that occurs with rigid impact. It was found in this study that the fluid did not increase the impact force of the solid tube and pole projectiles but that the fluid may increase the maximum impact force of hollow structures such as the shipping container.

As observed in Figure 3.25 and the equations for the force calculation, the velocity of the debris plays a large role in the debris impact force. Wesley [2012] examined the impact forces for small scale shipping containers using LS-DYNA, which was compared with a force estimation equation. The impact forces for different velocities, shown in Table 3.1, indicate that there is a large increase in the force for objects traveling at higher velocities, and it can also be seen that the numerical model slightly overestimated the forces obtained from the estimation equation. The relationship between the force and the velocities was seen to be linear at lower velocities, while becoming non-linear once the velocity exceeded 5 m/s.

Table 3.1 – In-air test for different velocities [Wesley, 2012]

v (m/s)	Force (N)	Est. Force (N)	Δt (sec)
1.0	39895	38989	0.0029
2.0	79840	77978	0.0029
3.0	119840	116967	0.0029
4.0	162640	155955	0.0029
5.0	229800	194944	0.0029
6.0	271000	233933	0.0029

A second study examining the impact of idealized shipping containers was performed by Ko [2013]. This study utilized both aluminum and acrylic specimens which were tested in two different orientations, longitudinal and transverse. The tests were completed at 1:5 scaled versions for in-air impact tests and hydraulic experiments. For the longitudinal and transverse in-air tests it was found that there was a linear relation between the impact force and the velocity for both the aluminum and acrylic samples. It was found that the largest forces were caused by the longitudinal aluminum impacts. For the in-water tests the flow speed and the impact velocity of the different specimens was analyzed. It was found for this study that the debris velocities appeared to nearly reach the speed of the maximum measured flow velocities and that the debris velocity decreased with the addition of nonstructural mass. Additionally, it was found that the peak contact forces increased linearly with the increasing debris velocity.

As mentioned previously in this section, the hydrodynamic force acts on the entire structure while impact forces act on a single member. The location of the impact on the structure was found to have an effect on the shear force, momentum and displacement by Kharade *et al.* [2013], using the same impact force. The structure was modeled in *SAP2000* where the impact load from the debris was applied only to a single element on the structure as a point load.

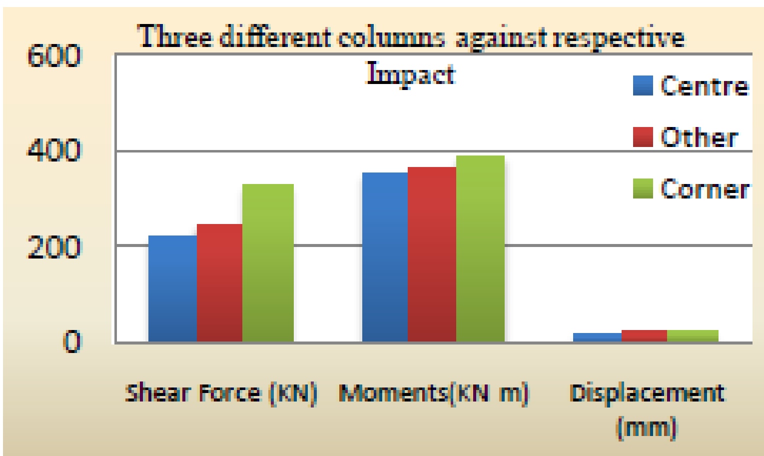

Figure 3.26 - Forces in different columns for constant impact force [Kharade *et al.*, 2013]

The findings of this study indicated that the debris impact on the first floor of a building would result in a significant increase in the axial force, bending moment and shear force though only a small increase in the displacement. It was also found that corner columns were more vulnerable to the impact forces then central column.

3.5 Discussion

The attenuation of hydraulic bores and waves by coastal forests has been studied in depth as shown in literature. It was found in these studies that the different parameters may individually result in an increase in the forest belts efficiency in reducing the tsunami bore, and that the different parameters are interrelated. However, very few studies have examined the effect of different initial water depths on the attenuation effect due to the change in the location of the breaking wave. In general, the observations of these studies indicated that the relationship between the forest belt width and the reduction in inundation exhibits an exponential tendency and that an increase in density results in an increase in reduction. Important observations included the need for variable tree density in the model, flexible debris and the benefits of a moving bed experiment as opposed to a fixed bed model.

When examining debris impact forces many of the studies examined theoretical equations in order to define the maximum impact force of the debris. It was found that there was a discrepancy between the suggested FEMA design equations and the actual forces obtained from experimental studies. This discrepancy may be caused by the fact that the impact of the debris is dependent on more than just the debris velocity but will also be impacted by how long the debris takes to stop and the angle at which it impacts the structure. Similar to the coastal forest attenuation, this literature highlights the need for flexible debris and structures in order to accurately represent the collision. In addition, it can be seen through these studies that the velocity of the debris can have a significant effect on the debris impact force.

4 Description of Physical and Numerical Experiments

This chapter includes a description of the physical experiment used for the impact force comparisons, and the numerical models used for the sensitivity analysis, impact forces and wave runup simulations. Included in this chapter is a description of the numerical formulations used to obtain post-processing results from the simulations.

4.1 Physical Experiment

In order to test the accuracy of the DualSPHysics model, numerical simulations were completed based on the physical experiments performed by Al-Faesly *et al.* [2013]. These physical experiments were carried out at the National Research Council (NRC) in Ottawa, Canada using a partitioned high discharge flume. A hydraulic bore was generated by the sudden release of water from behind a swinging hinged gate into a channel that was 1.3 m wide and 7.3 m long. Figure 4.1 shows the flume with the gate in the open position and the generation of a turbulent hydraulic bore. The gate impounded a 5.6m long and 2.7 m wide reservoir as seen in the figure. The total height of the flume was 1.4 m; however impoundment depths of only 0.55m and 0.85m were used for the experiments. As the bore reached the downstream end of the flume the water was evacuated through the use of a vertical floor drain. A schematic of the flume can be seen in Figure 4.2.

Figure 4.1- Experimental setup of Al-Faesly *et al.* [2013] showing the generation of a turbulent hydraulic bore [Al-Faesly *et al*, 2012]

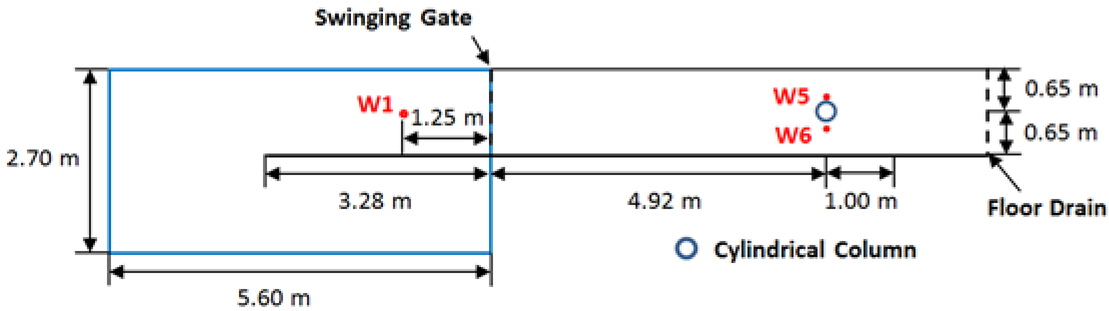

Figure 4.2 - Plan view of the experimental setup for the floating debris tests performed by Al-Faesly *et al.* [2013]

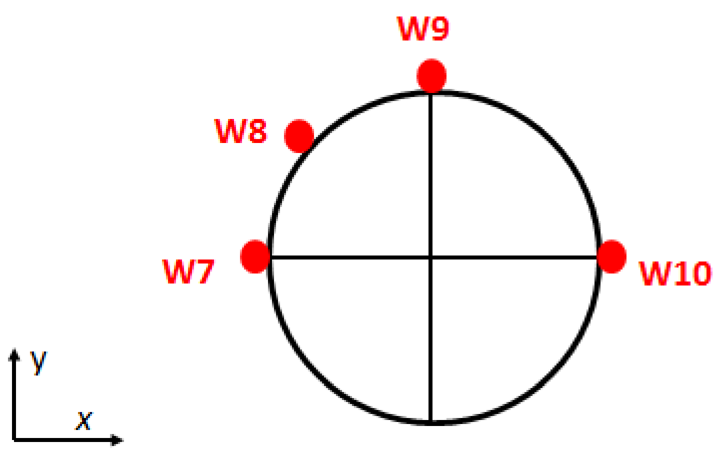

Figure 4.3 - Plan view of the wave gauges located around the cylinder for Al-Faesly *et al.* [2013]

The experiments used a hollow structural model with a cylindrical cross-section made from acrylic, which has an outside diameter of 0.305 m and a wall thickness of 9 mm, see Figure 4.4. This structure was mounted on a six-degree-of-freedom dynamometer which was fixed to the floor of the flume. Additional to the dynamometer was an accelerometer and a linear variable displacement transducer which were placed on top of the model in order to assess the movement of the cylindrical model in the flow. The cylinder was also fitted with four capacitance water level gauges, while three other gauges were located in the flume in order to measure the water elevation as shown in Figure 4.2 and 4.3.

Figure 4.4- Hollow cylindrical structural model [Al-Faesly *et al*., 2012]

Three different wooden samples of different size and mass were used to examine the debris impact loading for the two different water elevations. The dimensions of the wooden debris were: 76.2mm x 76.2mm x 490mm, 76.2mm x 152.4mm x 490mm and 76.2mm x 76.2mm x 916mm, with masses of 1.088kg, 2.258kg and 2.191kg respectively, as shown in Figure 4.5. These debris models were located at a distance of 1.67 m from the swinging gate. The debris was attached to the side of the flume using strings in order to prevent the log from being washed away after the bore impact.

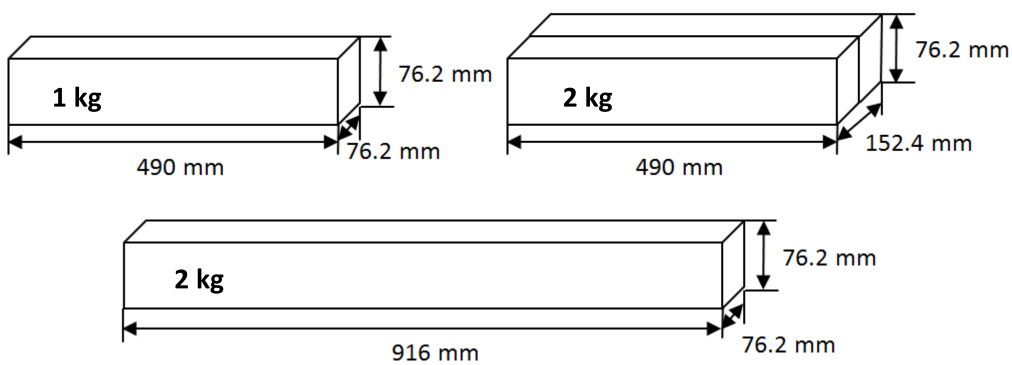

Figure 4.5- Waterborne wooden debris measurements for Al-Faesly *et al.* [2013]

4.2 Numerical Domains

Two domains were used for the numerical experiments performed for this study, one based on the physical model for the sensitivity analysis and debris impact validation and the second for the analysis of the tsunami attenuation by a coastal forest and the impact of the coastal forest on debris. Details on the numerical setup of these models is provided in the following sub-sections

4.2.1 Al-Faesly *et al.* [2013]

The experiments performed by Al-Faesly *et al*., shown in Section 4.1 were modeled numerically. This model was three-dimensional and used the same water reservoir dimensions as in the physical model shown in Figure 4.2. The flume width was also kept the same for the numerical model; however, the domain length was increased to insure that the floating debris was kept inside the domain for the entire simulation. The full physical flume was modeled for this scenario in order to limit the impact on the fluid particles by the flume floor; the partitioned model configuration of the computational domain can be seen in Figure 4.6 before the release of the bore, where the debris is located at 1.67m from the water to the center of the debris. This figure shows the location and size of the 1.088kg waterborne debris. In all cases, but the 1.088kg 0.55m test, the debris was placed directly on the model flume floor; in the 1.088kg test it was elevated off the floor by the particle spacing, 0.025m, in order to remove a model error.

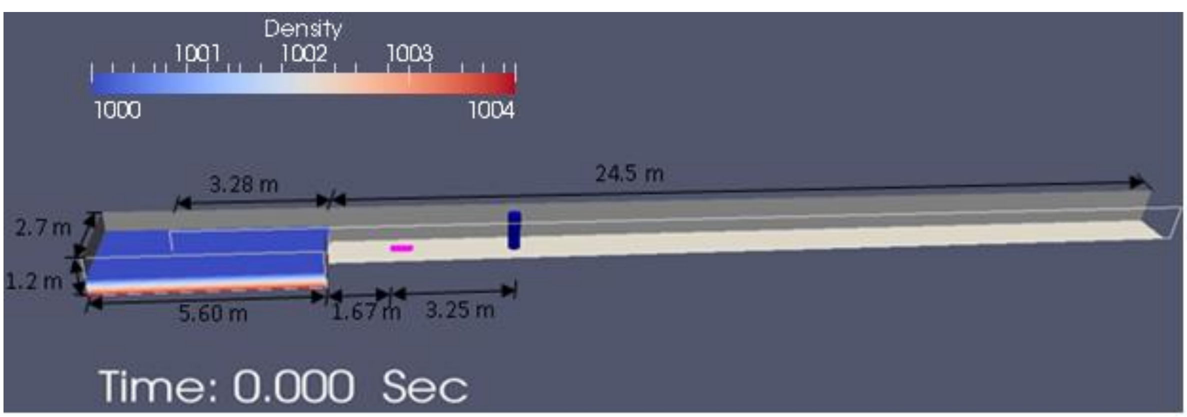

Figure 4.6 - Numerical domain for al-faesly *et al.* [2013] for 0.55m water depth

4.2.2 Coastal Forest

The coastal forest model was utilized for two sets of analyses. The initial analysis examined the effect of the coastal forest on tsunami waves generated in varying water levels. The second analysis examined the effect of debris propagation for one of the aforementioned scenarios and examined the effect of the debris location on its impact force and propagation.

The model was a three-dimensional model which had theoretical initial water depths of 2.25m, 2.4m and 3m (ending in front, at, and behind the coastal forest); however the numerical model slightly underestimated the water depth as shown for the 2.25m water depth in Figure 4.7. The flume length was varied for the different water depths in order to accommodate the variable amount of runup that would occur. The flume lengths were 70m for the 2.25m and 2.4m water depths and 80m for the 3m water depth. The flume contained a simulated wave-maker at the downstream end in order to generate the solitary wave and a beach profile with a slope of 1: 10. The solitary wave generated in all scenarios was based on Hughes [1993] and Goring and Raichlen [1980] and had a wave height of 2.5m. The plan and side view of the designed domain can be seen in Figure 4.8.

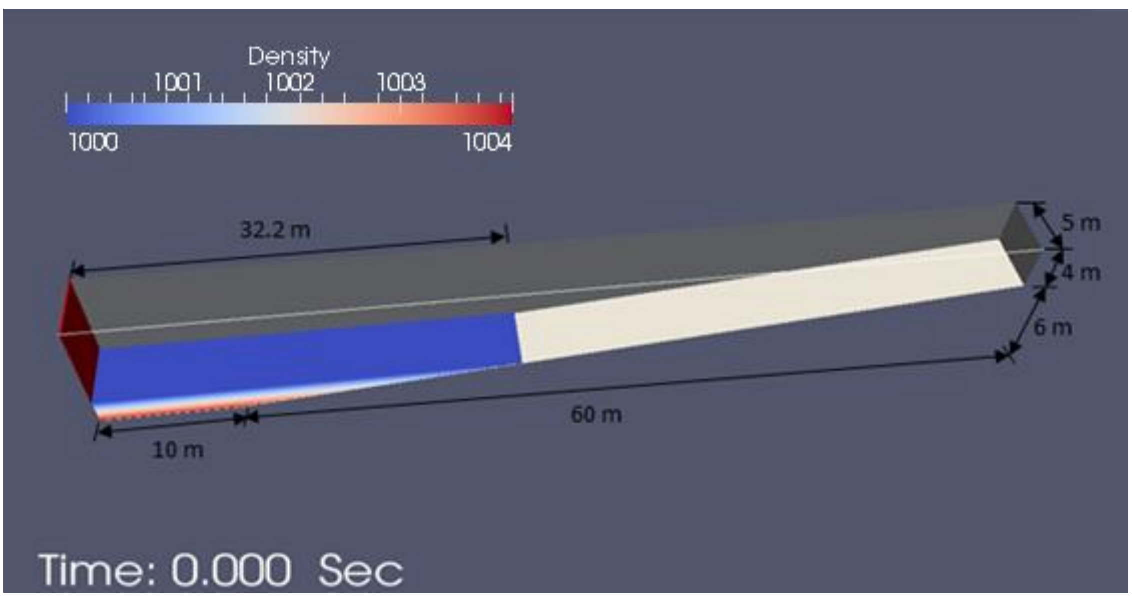

Figure 4.7 - Computational domain for the coastal attenuation analysis for the 2.25m water depth

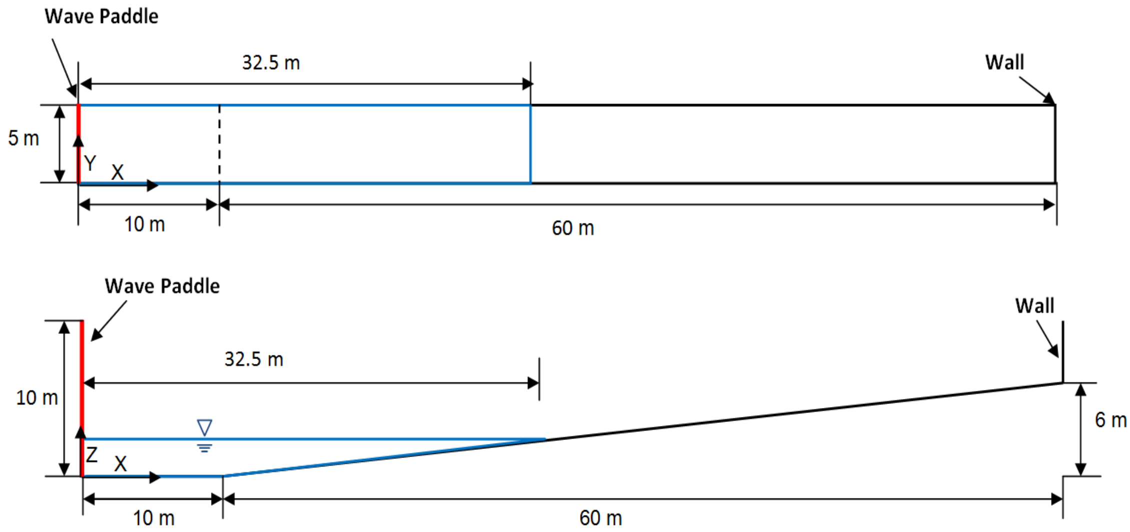

Figure 4.8 – Plan view and side view of the design numerical domain for the coastal attenuation analysis for 2.25m water depth

The trees in the model were located starting at a distance of 34m from the x-axis, the tree configurations can be seen in Table 4.1 and Figure 4.9. These trees were modeled as stationary rigid structures which would not be displaced or bent by the incoming tsunami bore. The rectilinear formation contains trees in rectangular rows with identical spacing in the I_x and I_y directions. The L_x and L_y values are dependent on the number of trees and amount of rows used in the simulation. The staggered formation uses trees in offset rows, with the distance I_x being equal to the spacing between the trees in each row, which is twice the distance between the trees, I_y. The distance C varied based on the initial still-water depths, the values were 1.5m (2.25m still-water depth), 0m (2.4m still water depth) and -6m (3m still-water depth). The tree height was set at 10m in order to avoid any influence on the bore propagation for different forest configurations and water depths

Table 4.1 – Coastal forest configuration and set-up

Formation	Number of Trees per Row	Number of Rows	Tree Diameter (m)	I_y (m)	I_x (m)
No Trees	0	0	N/A	N/A	N/A
Rectilinear	1 - 5	1 - 3	0.25	0.88 - 2.625	0.88 - 2.625
Staggered	2 - 4	2 - 3	0.25	0.583 - 1.05	1.166 - 2.1

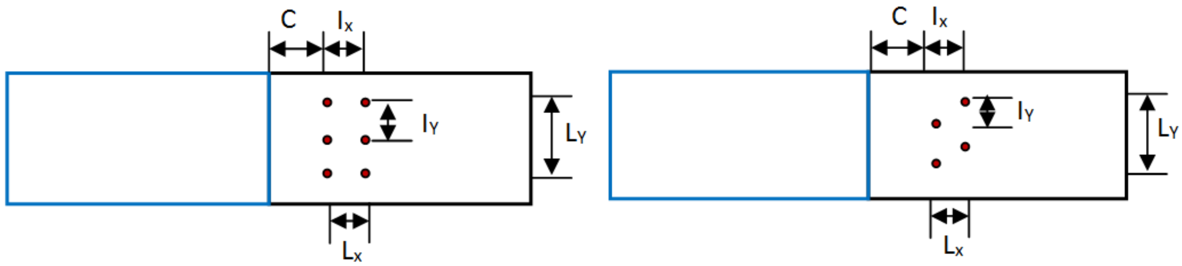

Figure 4.9- Coastal forest for rectilinear (left) and staggered (right) configurations

The scenario which examined the debris impact for a log in different initial positions was examined for the water depth of 2.25m with a tree configuration using 2 rows of 2 trees, with a rectilinear configuration. The log was modeled in both the upright and horizontal position for positions on land and in the water. The dimensions of the log were 0.25m in diameter and 1.5m in length with a mass of 68 kg, roughly 30.5 lbs/ft. The initial debris set-up can be seen in Figure 4.10 which uses the same domain as that shown in Figure 4.7.

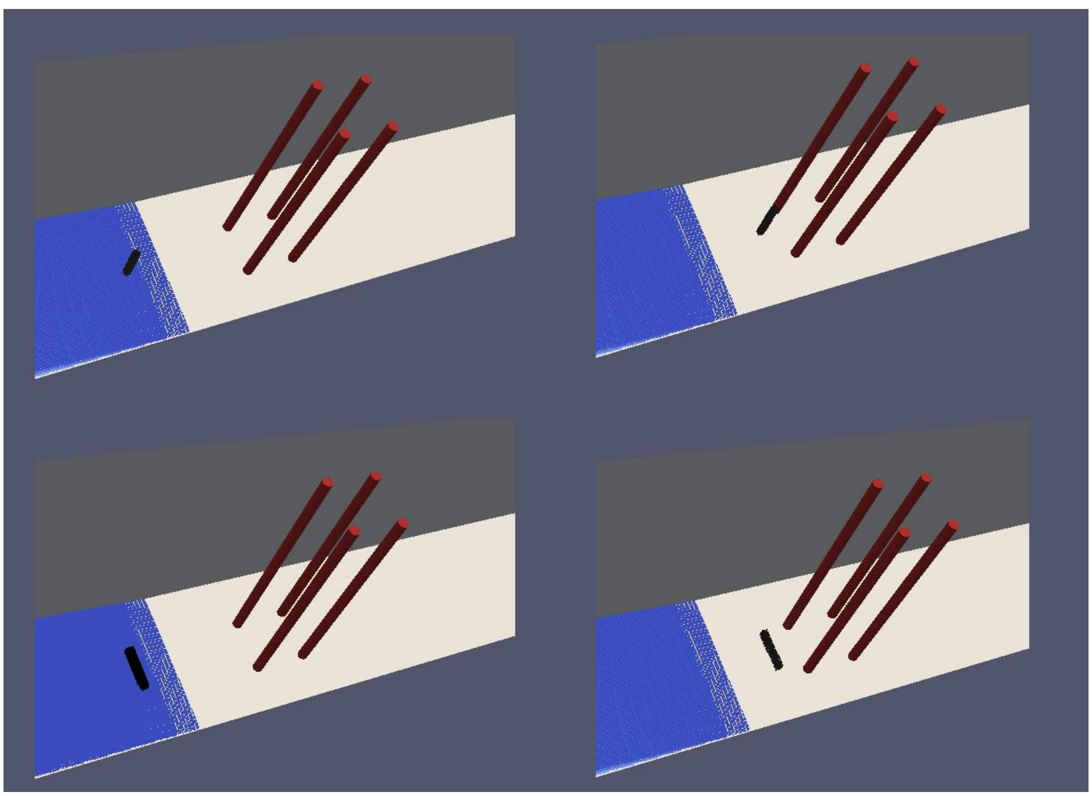

Figure 4.10 - Debris location for coastal forest model

The model outputs obtained for the analysis of the bore attenuation included eight water velocity measurements, the locations are shown in Figure 4.11, as well as the maximum wave attenuation. Both sets of analysis examined the forces acting on the modeled coastal forest. Measurements for the attenuation of the tsunami bore were based on the horizontal inundation of the water and measurements were obtained to an accuracy of ± 0.05m.

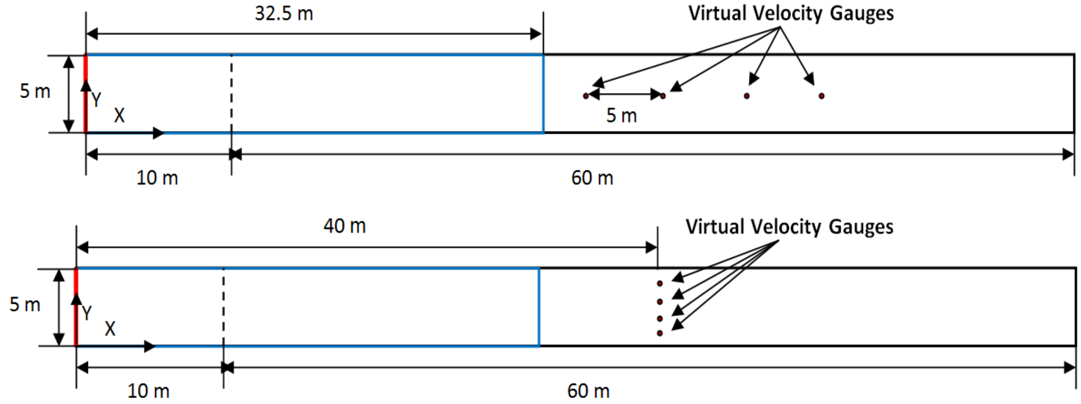

Figure 4.11 - Virtual velocity gauge locations

4.3 Post-Processing Formulation

The forces, maximum water elevation and velocity for this study were obtained using code provided by St-Germain [2012]. This section will provide a basic explanation of the methods used to obtain these values as well as that of the debris impact force which was developed from the modified code of St-Germain [2012].

4.3.1 Fluid Force

The net horizontal force acting streamwise on a column or pier can be calculated by integrating the pressure of the fluid particles around the surface area of the pier. This is accomplished by dividing the area around the pier into tributary areas; see Figure 4.12, which are equidistant from each other and the center of the pier and have a radius of *2h*.

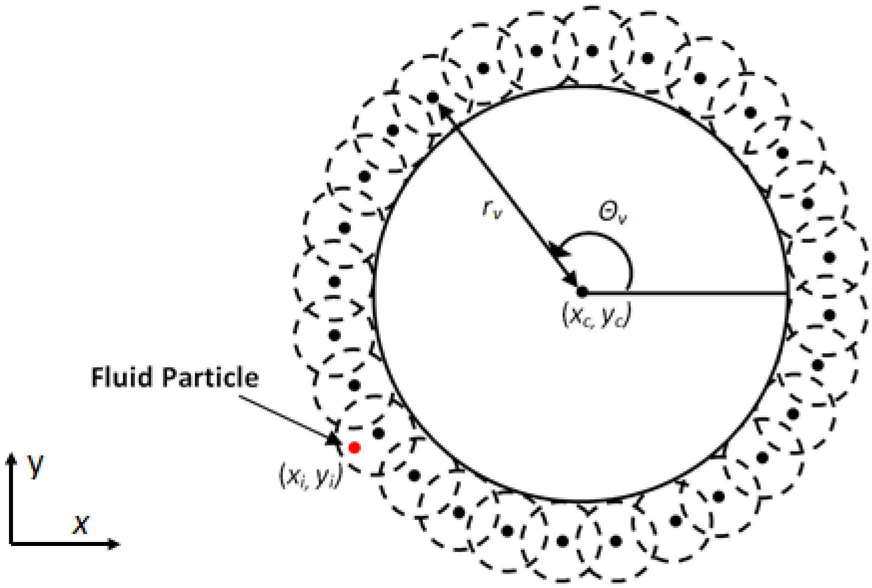

Figure 4.12 - Plan view of the hydrodynamic force sampling volumes for a cylindrical column [adapted from St-Germain, 2013]

Once the particles within the tributary area have been sampled, the approximated pressure within the sampling volume is calculated using the average density of the particles and the equation of state, Eq. 2.61. Finally the streamwise resultant force, F_x, acting on the pier can be calculated using:

[4.1] $$F_x = \int_A \bar{P} \cos\theta_F dA$$

[4.2] $$dA = \Delta\theta_v r_c \Delta z_v$$

[4.3] $$\theta_F = \theta_v - \pi$$

Where r_c is the radius of the circular column, Δz_v is the elevation difference for the centers of the sampling volumes and $\Delta\theta_v$ is the angle corresponding to the arc of the tributary area, see Figure 4.12.

4.3.2 Fluid Velocity

The fluid velocity is calculated by completing a kernel approximation within a single sampling volume. The velocity within a water column can be approximated by using multiple sampling volumes along the column. The sample volume is represented by a sphere of radius 2h in order to be comparable to the smoothing kernel depicted in Figure 2.1. The velocity within the sampling volume can be obtained using:

[4.4] $$\bar{\boldsymbol{u}} = \sum_{i=1}^{N_{Vol}} \frac{m_i}{\rho_i} \boldsymbol{u}_i W(\boldsymbol{x}_i - \boldsymbol{x}_v, h)$$

where N_{vol} is the number of fluid particles located in the sampling volume, v, and $\boldsymbol{x}_v$ is the position vector of the center of the sampling volume.

4.3.3 Water Elevation

The water surface elevation of the model can be obtained using the placement of virtual wave gauges in the domain. These gauges are represented as a sampling volume elongated along its height, Figure 4.13. For this gauge it is assumed that the elevation of the highest water particle is equal to that of the water surface elevation at that point. This may cause issues when evaluating locations with a breaking wave or wave splashing.

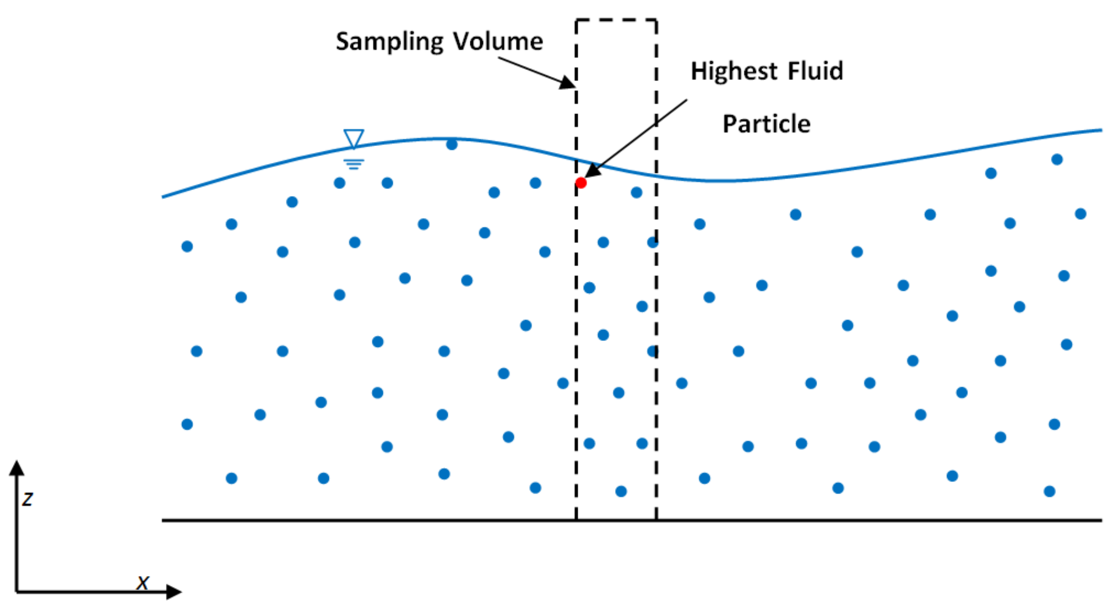

Figure 4.13 - Particle sampling volume for water surface elevation [adapted from St-Germain, 2013]

4.3.4 Debris Impact Force

Similar to the fluid particles in the model, the floating object particles carry their physical properties with them as they propagate through the domain. This is advantageous when calculating the debris impact force as it allows for the calculation of the debris velocity moving through the water.

[4.5] $$Debris\ Velocity = \boldsymbol{u} = \frac{1}{N}\sum_{i=1}^{N}\sqrt{u^2 + v^2 + w^2}$$

The debris velocity can be approximated through the summation of all floating object particles, *N*, for the time step. Using this velocity, the momentum principle can be applied in order to obtain the impulse force acting on the debris:

[4.6] $$\dot{m} = m(\boldsymbol{u_f} - \boldsymbol{u_i})$$

[4.7] $$F_{debris} = {}^{\dot{m}}/_{\Delta t}$$

where $\dot{m}$ is the momentum of the debris and m is the mass. The change in time should be equal to the time that the impact occurs in, unfortunately it is not plausible to run the model at such a small time step. This equation calculates the force acting on the debris. In order to calculate the impact force acting on the structure, the force values were multiplied by -1 and the values below zero were ignored as they are acting on the debris.

[4.8] $$F_i = -F_{debris}$$

It is important to note that this method calculates the impact force for all impacts that occur in the model, this includes impacts with the sidewalls. In order to ensure that the correct impact values are obtained for the impact on a structure the results must be compared with the visuals of the simulation.

4.4 Sensitivity Analysis

The parameters selected for the numerical model were determined based on previous studies as well as on the sensitivity analysis shown in this section. This sensitivity analysis examined variations in the time-histories of the water surface elevation and force based on changes in the inter-particle spacing, the smoothing length, the speed of sound and the artificial viscosity which was used for the floating object simulations. The sensitivity analysis was performed using the setup of Al-Feasly *et al.* [2013] as it was the simulation utilized in the impact force debris tests. The time-history of the water surface elevation was taken immediately in front of the cylindrical pier at gauge 7.

4.4.1 Speed of Sound

The initial parameter tested was the speed of sound, c_0, which is varied based on changes to the speed of sound coefficient, α_{sound} which typically ranges in value from 10 to 40. This parameter directly impacts the force measurements obtained in the post-processing code as it is used in the calculation of the pressure constant, B. For the sensitivity analysis the speed of sound was varied from 26.5m/s to 44.3m/s.

The results of this analysis, shown in Figures 4.14 indicate that the differences in the speed of sound have very little effect on the water surface elevation in the model, but do have an impact on the hydrodynamic force values. In general, it can be seen that the maximum impact force increases as the speed of sound increases, however its effect on the residual hydrodynamic force values is small. The hydrodynamic force for the smallest speed of sound was found to contain large fluctuations indicating that the model was not fully stable. The variations in the speed of sound were found to have an impact on the computational time; an increase in the coefficient value resulted in an increase the computational time as well.

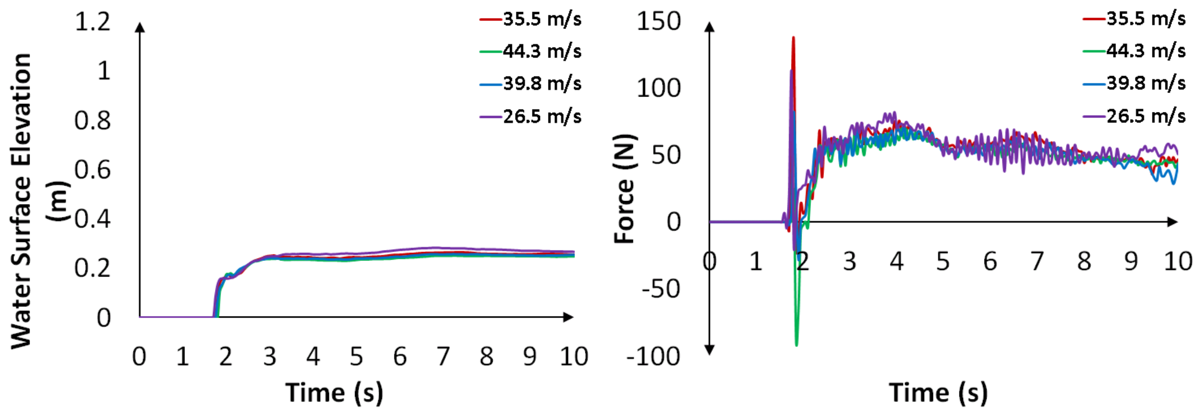

Figure 4.14 - Comparison of the water surface elevation in front of the cylinder and the force time-history for different speed of sound values

Table 4.2 - Computational times for different speed of sound values

Speed of Sound (m/s)	Computational Time (hrs)
35.5	4.25
44.3	4.98
39.8	4.25
26.5	3.24

4.4.2 Viscosity

This model utilizes the artificial viscosity function as this is the only option available due to the presence of the floating object. The viscosity treatment is included in the momentum equation and functions to dissipate energy and prevent collisions of the particles. The artificial viscosity coefficient, $\alpha_{visc,}$ is a user defined function that can vary greatly based on the specific numerical problem, for the sensitivity analysis values ranging from 0.15 to 0.3 were tested.

The time-history of the water surface elevation and the hydrodynamic forces are shown in Figure 4.15. The variations in the artificial viscosity coefficient indicate a time lag in the arrival of the bore to the front of the pier, with the bore arriving earlier for lower coefficient values. Additionally, the water surface elevation is slightly higher for the lower coefficient values. When examining the impact of the coefficient on the force it can be seen that the stability of the model decreases for the lower coefficient values but that the resultant force increases.

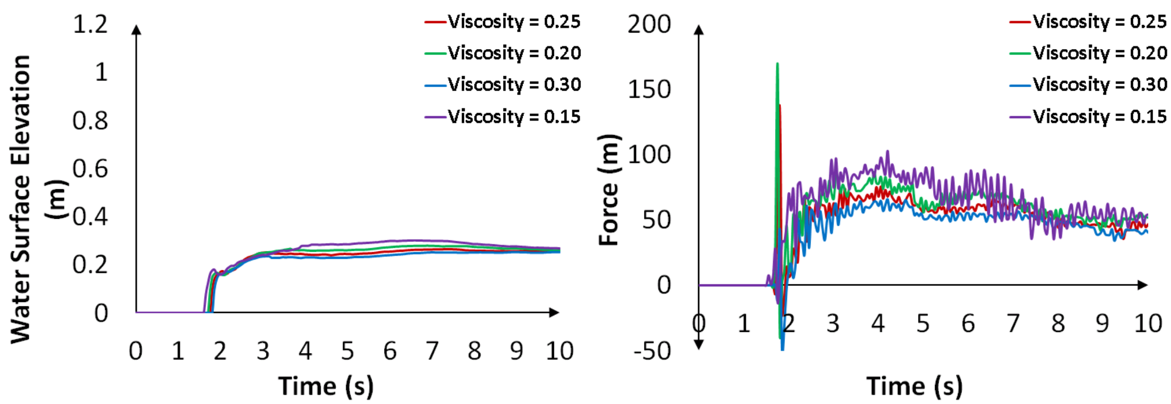

Figure 4.154 - Comparison of the water surface elevation in front of the cylinder and the force time-history for different artificial viscosity values

While variations in the computational time are present for the model there does not seen to be a correlation when relating it to the value of the artificial viscosity coefficient.

Table 4.3 - Computational times for different artificial viscosity values

Artificial Viscosity	Computational Time (hrs)
0.20	3.93
0.25	4.25
0.15	3.93
0.30	3.86

4.4.3 Smoothing Length

The smoothing length chosen for the model has a large impact as it directly influences the kernel approximations. The values chosen for this analysis ranged from 0.0338m to 0.0450m through variation in the smoothing length coefficient, $\alpha_{smoothing}$. Shown in Figure 4.16, it can be seen that the smoothing length has minimal impact on the water surface elevation except for the location of the initial bore impact. When examining the hydrodynamic forces the size of the smoothing length can be seen to have a large impact. The smallest smoothing length results in a large fluctuation in the force measurements around impact and an instability starting at 8s. However, for the larger smoothing lengths the variations in the force values are fairly small. Increases in the smoothing length were found to result in an increase in the computational time of the model as shown in Table 4.4.

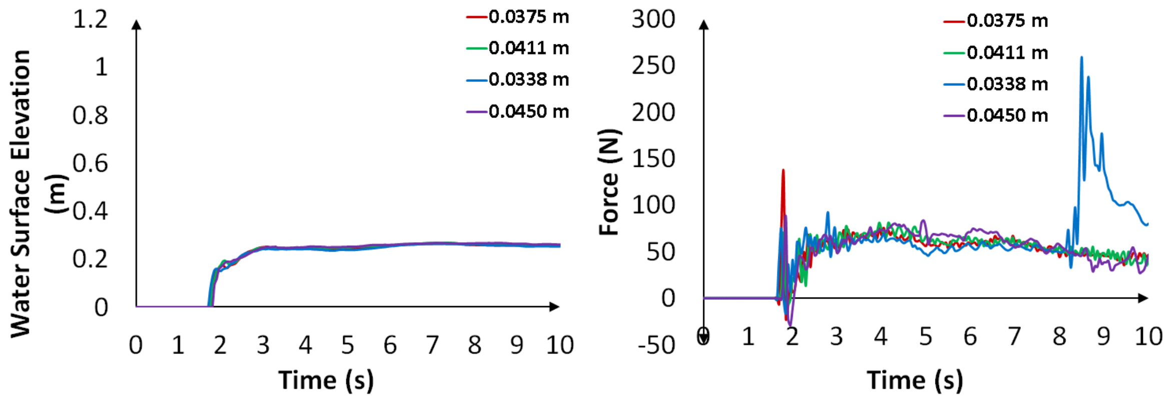

Figure 4.16 - Comparison of the water surface elevation in front of the cylinder and the force time-history for different smoothing length values

Table 4.4 - Computational times for different smoothing length values

Smoothing Length (m)	Computational Time (hrs)
0.0375	4.25
0.0411	4.15
0.0338	4.11
0.0450	4.70

4.4.4 Inter-Particle Spacing

The inter-particle spacing is integral in the proper representation of the fluid movement and denotes the initial spacing between the particles in the model. In this case as the model is three-dimensional the values indicate the distance in the x, y and z planes. The initial inter-particle spacing has a large impact on the time of arrival of the bore front as can be seen in the water surface elevation profile and on the initial water elevation at the bore front. It also has a significant impact on the hydrodynamic force where the stability of the model decreases as the particle spacing increases.

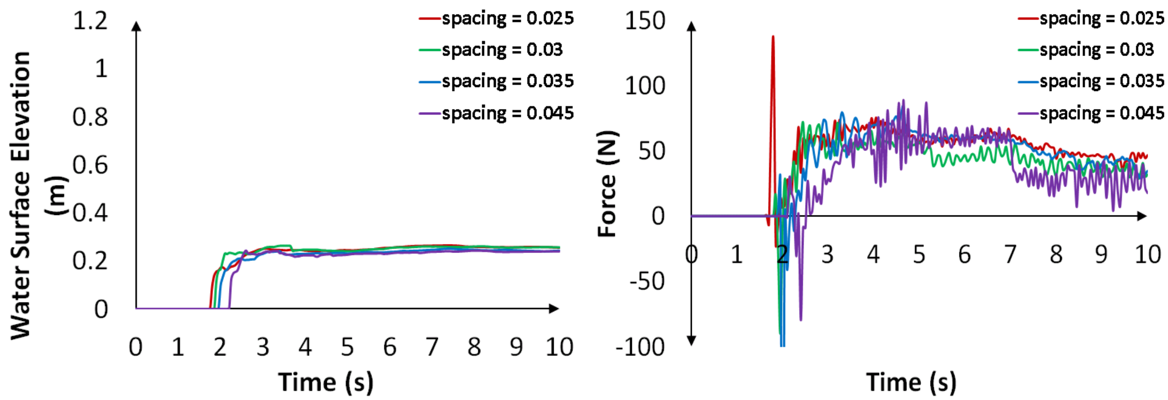

Figure 4.17 - Comparison of the water surface elevation in front of the cylinder and the force time-history for different inter-particle spacing values

Variations in the inter-particle spacing were found to have a direct influence on the time of computation. As the inter-particle spacing decreased the computational time was found to increase as the amount of particles in the model was increased significantly.

Table 4.5 - Computational times for different inter-particle spacing values

Inter-Particle Spacing (m)	Number of Particles	Computational Time (hrs)
0.025	1,625,722	4.25
0.03	992,368	2.19
0.035	690,472	1.40
0.045	354,320	0.75

4.5 Parameter Selection

Shown in this section are the integral parameters selected for the numerical simulations. The parameters shown are: the inter-particle spacing, the smoothing length, the speed of sound, the smoothing kernel, the time stepping method, and the viscosity treatments.

4.5.1 Coastal Forest Attenuation

The parameters selected for these simulations were chosen based on previous experiments and from the comparison of the results of the sensitivity analysis with experimental data. For this model the selected parameters are shown below in Table 4.6. In order to keep the amount of particles in the simulation to a reasonable amount, a higher inter-particle spacing was required due to the scale of the model.

Table 4.6- Numerical model parameters for the coastal forest attenuation model

Numerical Parameters	Value
Inter-Particle Spacing (m)	0.075
Smoothing Length (m)	0.1125
Smoothing Kernel	Cubic Spline
Coefficient for the Speed of Sound	16
Time Stepping Algorithm	Verlet
Viscosity Treatment	Laminar + SPS
Laminar Viscosity	1.0 E^{-6}

4.5.2 Al-Faesly *et al.* [2013]

The parameters selected for the simulations of Al-Faesly *et al.* used a smaller particle spacing than that of the coastal forest attenuation model due to the smaller domain size. Additionally, due to the presence of the floating object the Laminar + SPS viscosity treatment was not used, as this treatment is not available for these objects. This model does not use a wave-maker as the hydraulic bore is generated based on a dam-break bore.

Table 4.7 - Numerical model parameters for Al-Faesly *et al.* [2013]

Numerical Parameters	Value
Inter-Particle Spacing (m)	0.025
Smoothing Length (m)	0.0375
Smoothing Kernel	Cubic Spline
Coefficient for the Speed of Sound	16
Time Stepping Algorithm	Verlet
Viscosity Treatment	Artificial
Viscosity Coefficient	0.25

When compared with the attenuation model this model required a lower time stepping coefficient due to a pressure instability which formed behind the pier for larger values.

4.5.3 Coastal Forest Debris Impact

This model uses the same domain as the coastal forest attenuation simulations; however, as explained in Section 4.5.2 the model could not be run with the Laminar + SPS viscosity treatment, therefore the parameters used for this model are a combination of those shown in Section 4.5.1 and 4.5.2, they are shown in Table 4.8. The viscosity value used for this model was calibrated based on the results of the attenuation model.

Table 4.8 - Numerical model parameters for the coastal forest debris impact model

Numerical Parameters	Value
Inter-Particle Spacing (m)	0.075
Smoothing Length (m)	0.1125
Smoothing Kernel	Cubic Spline
Coefficient for the Speed of Sound	16
Time Stepping Algorithm	Verlet
Viscosity Treatment	Artificial
Viscosity Coefficient	0.01

When compared with the attenuation model this model required a lower time stepping coefficient due to a pressure instability which formed behind the trees for larger values.

4.6 Experimental Versus Computational Time

This section summarizes the details for the numerical models; as the coastal forest attenuation model utilized a large variety of test scenarios the models shown here will indicate the number of particles and computational time for the reference scenarios only. Similarly, as the coastal forest debris impact and the Al-Faesly [2013] models each contained variations of the debris size and location only a selection of the runs are shown.

Table 4.9 -Computational domain and run-time for the numerical simulations

Simulation	No. of Water Particles	No. of Fixed Particles	No. of Moving Particles	No. of Floating Particles	Physical Model Time (s)	Run-Time (hrs)
Attenuation (2.25m)	1,036,750	528,588	34,320	0	30 s	12.73
Attenuation (2.4m)	1,148,550	528,588	34,320	0	30 s	17.99
Attenuation (3m)	1,619,280	597,364	34,320	0	25 s	18.97
Al-Faesly (0.55m 1kg)	998,574	627,956	0	228	10 s	5.81
Al-Faesly (0.85m 1 kg)	1,569,318	627,956	0	228	10 s	14.57
Debris Impact	1,036,750	535,734	34,320	342	25 s	10.42

The coastal forest attenuation runs were simulated for either 25 or 30s, the longer simulation time was used initially to ensure that the runup of the wave was fully captured. The later runs were simulated for only 25s as this was found to be sufficient in capturing the runup and allowed for some examination of the rundown process.

5 Impact of Initial Water Depth on the Effectiveness of Coastal Forests

This chapter includes a description of the solitary wave model used in this study to generate the waves. Also included is an examination of the effectiveness of coastal forests in reducing the propagation of tsunami-bores and the inland bore velocity based on different forest band widths and densities. The focus of this chapter is on the effect of the forests based on different initial water levels. In addition contained in this chapter is an analysis on the hydrodynamic forces caused by the tsunami bore on the individual trees for the different water levels.

5.1 Solitary Wave Model

As mentioned in Chapter 4 the model contained a simulated wave-maker with an imposed motion to allow for the generation of a solitary wave. In all scenarios the modeled wave had a wave height of 2.5m; however the initial water depth, h, was variable.

The solitary wave was generated based on the proposed model of Goring and Raichlen [1980] and Hughes [1993], which is a mathematical model for the generation of solitary waves by a laboratory wave paddle. The wave profile, η, for a water depth of h is calculated based on:

[5.1] $$\eta = Hsech^2[\kappa(Ct - X_o)] + h$$

Where the wave number, κ is:

[5.2] $$\kappa = \left(\frac{3H}{4h^3}\right)^{1/2}$$

and the wave celerity, C, can be obtained using:

[5.3] $$C = [g(h + H)]^{1/2}$$

In order to generate this wave profile the movement and velocity of the wave maker can be obtained based on an iterative process to calculate the position of the wave paddle at:

[5.4] $$X_0^{(i+1)} = X_0^{(i)} - \frac{\left[X_0^{(i)} - \frac{H}{\kappa h}\tanh\kappa\left(Ct - X_0^{(i)}\right)\right]}{\left[1 + \frac{H}{h}\left(\mathrm{sech}\left[\kappa\left(Ct - X_0^{(i)}\right)\right]\right)^2\right]}$$

The stroke of the wave board, S_s, is the distance travelled by the wave board in order to generate the wave, while the stroke duration, t_f, is the time required to complete the wave generation:

[5.5] $$S_s = \sqrt{\frac{16Hh}{3}}$$

[5.6] $$t_f = \frac{2}{\kappa C}\left(3.8 + \frac{H}{h}\right)$$

5.2 Influence of Water Depth

The results contained in this section examine the effect of the different water levels on the propagation of the tsunami-induced hydraulic bore through the coastal forest models, as shown in Table 4.1. The reduction in the bores' inland runup and inundation were examined for each of the configurations; whereas, the bore velocity and forces were examined for a selection of the configurations for each of the water depths.

5.2.1 Propagation

In order to accurately model the attenuation, velocity and impact forces of the tsunami bore it is integral that the breaking and propagation processes are properly modeled and that there are no instabilities in the model. The visuals in Figures 5.1 to 5.3 illustrate these processes as the bore travels up the domain and through the forest for still-water depths of 2.25m, 2.4m and 3m, respectively for a rectilinear configuration of 2 trees/row and 2 rows. These water depths were intended to show the impact of the water ending in front, at and behind the coastal forest. Figure 5.2 shows clearly that the initial water surface elevation in the model was lower than that of the design value, as mentioned in Section 4.2.2.

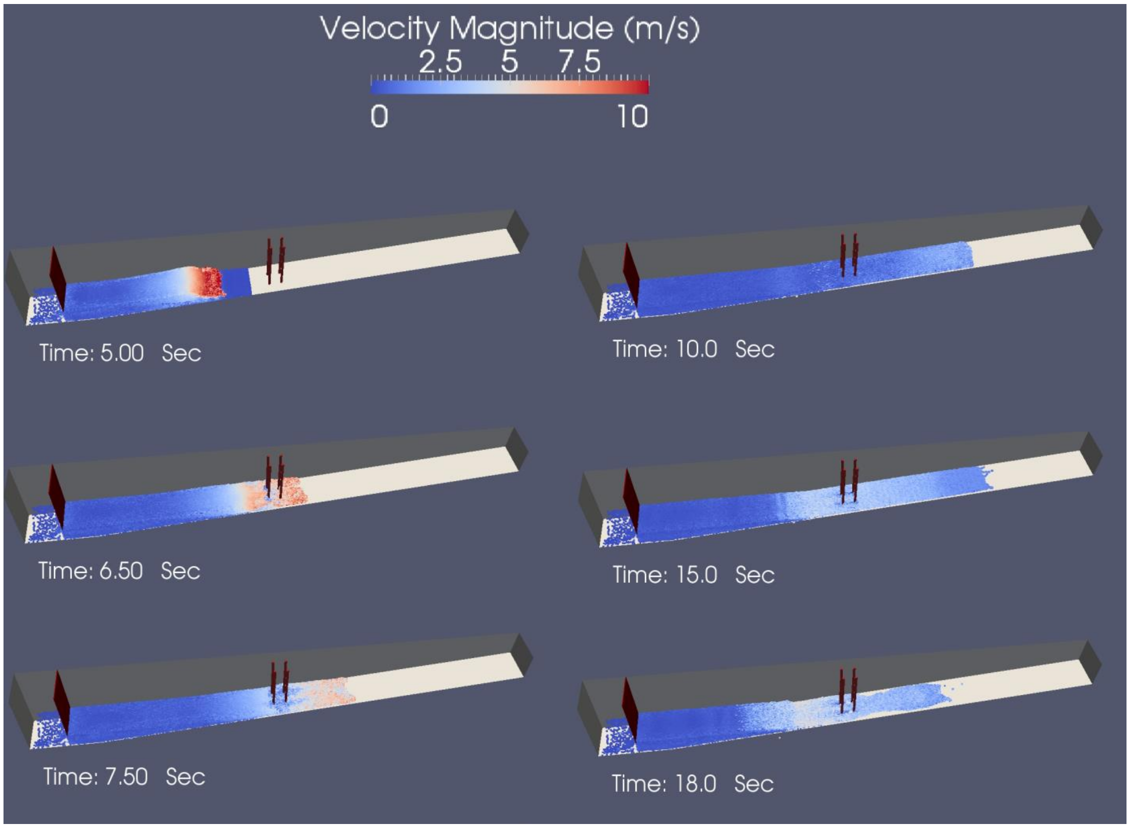

Figure 5.1 - 2.25m water depth (C = 1.5m). Wave propagation over time through a rectilinear coastal forest configuration

For both the 2.25m and 2.4m the bore can be seen to break as a plunging breaker and then propagates through the forest as a hydraulic bore. While for the 3m water depth the tsunami wave breaks just as the bore reaches the forest, resulting in an extremely turbulent bore. The model was able to represent the movement of the bore through the forest for the runup of the wave; however it can be seen at a time of 18s that the bore rundown is not well represented by the model. This was shown by the separation of particles from the bore and the development of gaps along the side of the domain. The problems in the rundown can also be seen in the results of the bore velocity and impact forces for the rundown; however, as the focus of the study was on the maximum inundation of the bore and runup process this was not deemed problematic.

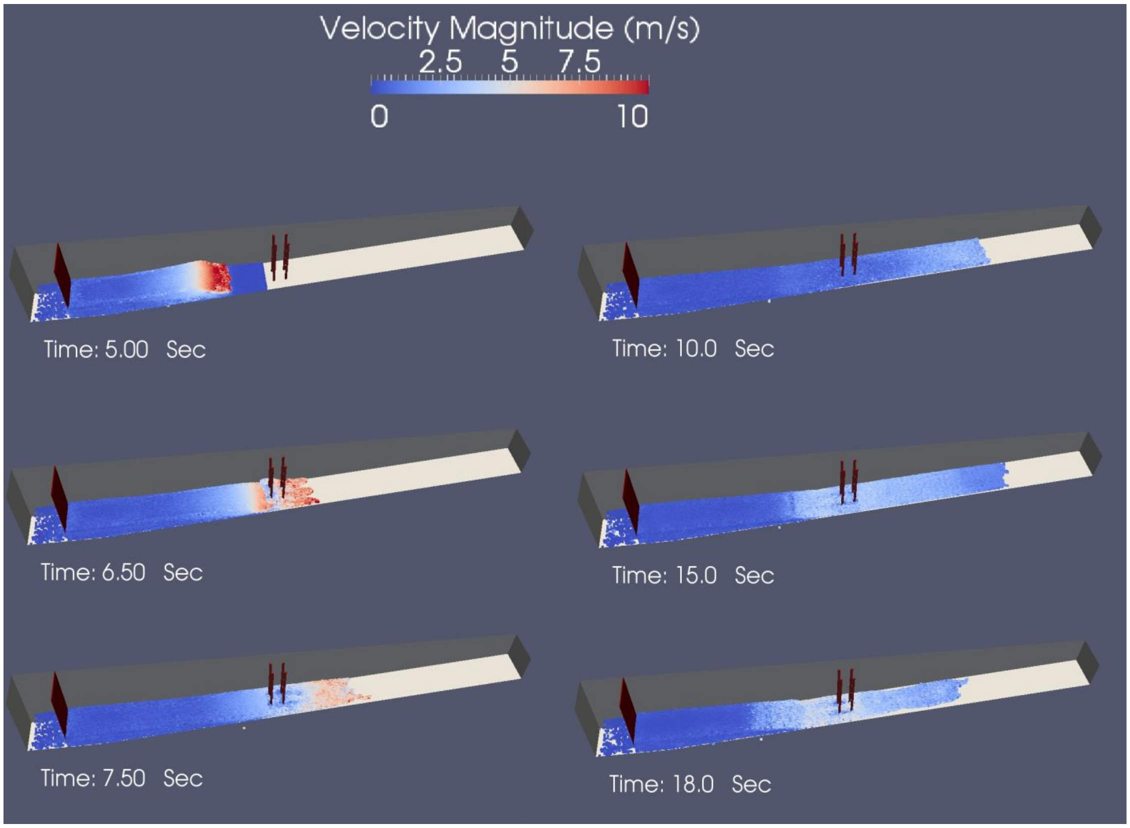

Figure 5.2 - 2.4m water depth (C = 0m). Wave propagation over time through a rectilinear coastal forest configuration

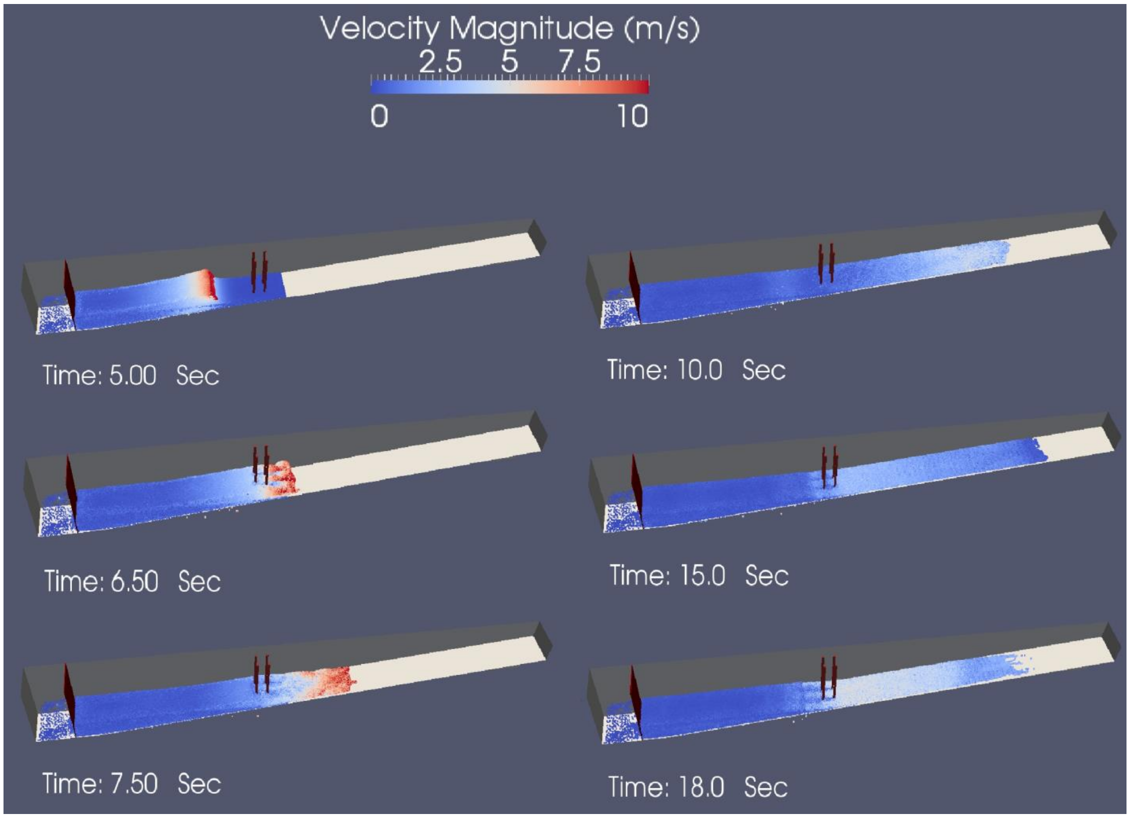

Figure 5.3 - 3m water depth (C = -6m). Wave propagation over time through a rectilinear coastal forest configuration

Due to the difference in initial still-water level the location of the breaker varied for the three different models, which would have an impact on the forests' ability to attenuate the flow. The location of the breaker is shown in Figure 5.4, the actual location of the wave breaking occurs over a distance in the model as the wave propagates forward, the figure shows the event near the end of the breaking process. This figure shows that the wave breaking process occurred from a distance of 11m to 22m from the x-axis, for the 2.24m still-water depth, Fig 5.4(2) the wave was found to break from a distance of 15m to 24m from the x-axis. The final still-water depth of 3m had the wave break at a distance of 23m to 34m from the x-axis, which was directly in front of the forest.

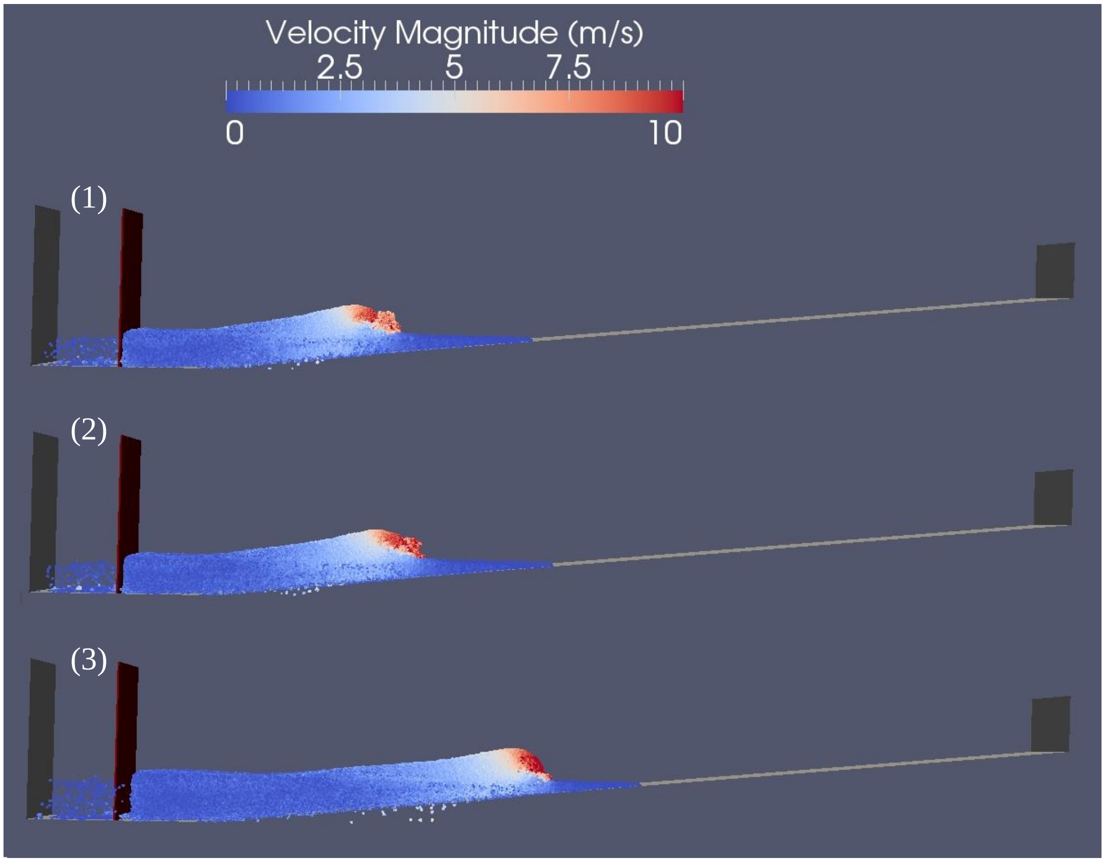

Figure 5.4 - Wave breaking location for (1) 2.25m, (2) 2.4m, (3) 3m water depths

As mentioned in Section 3.3 the coastal forests attenuate the flow based on two mechanisms, the reflection of the bore from the trees and the dissipation of the wave energy as it propagates through the trees. While difficult to quantify the amount of reflection which occurred, the runup of the bore on the trees was compared for the three different water depths for a time of 7.5s, shown in 5.6, which is after the initial bore impact. When compared to the reference scenario with no coastal forest, Figure 5.5, it can be seen that there is a noticeable runup on the tree fronts which causes the reflection of the bore. The amount of runup for the three water depths in reference to the normal water level at the location of the first rows of trees is included in Table 5.1.

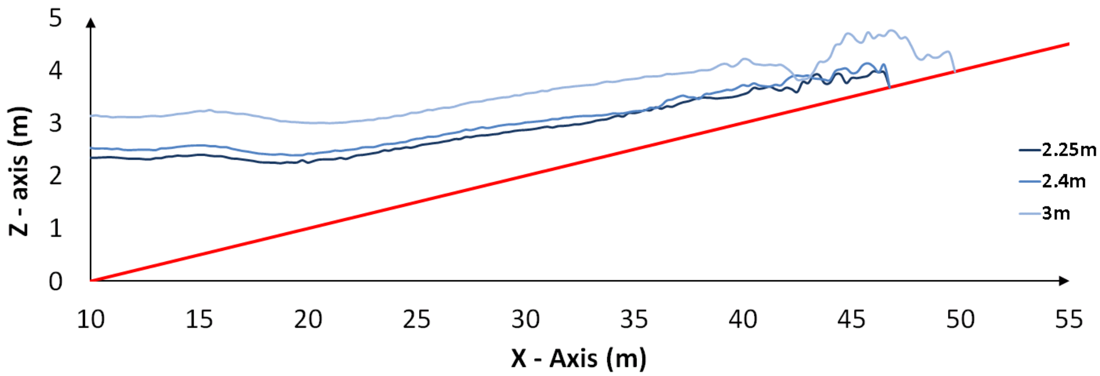

Figure 5.5 - Bore elevation for reference case for different initial still-water depths at 7.5s

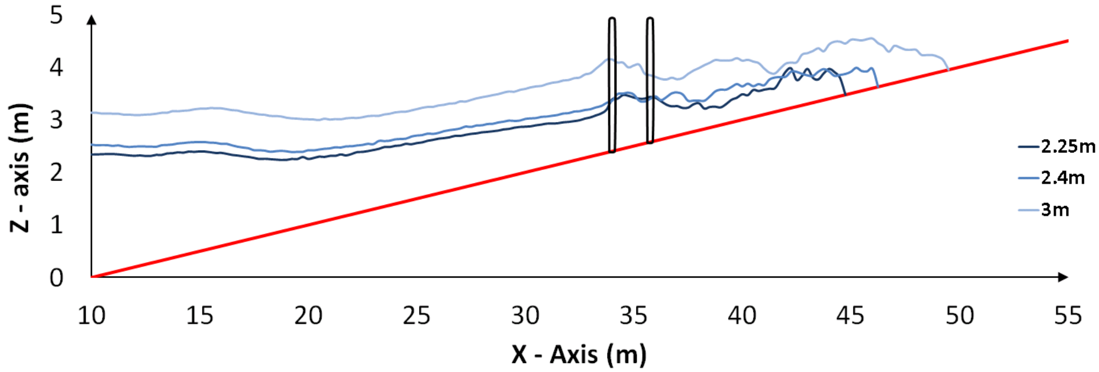

Figure 5.6 - Bore runup on the coastal forests for different initial still-water depths at 7.5s for a rectilinear layout of 2 rows of 2 trees

Table 5.1- Wave runup on the coastal forest

	Water Depth at Tree Location		
	2.25m Water Depth	2.4m Water Depth	3m Water Depth
Reference	3.11	3.18	3.78
2 Trees/Row, 2 Rows	3.38	3.36	4.15

The water depth at the tree location shows an increase of 0.18m to 0.40m from the reference case for the three water depths at a time of 7.5s. The variations in water depth when comparing the 2.25m and 2.4m water depth is fairly similar as the waves break in similar manners and locations. The larger runup for the 3m water depth is caused by the wave breaking immediately before the trees.

5.2.2 Attenuation

Due to the slope of the shoreline the inundation distance is 10 times larger than that of the runup height; therefore this analysis only presents the runup elevation for the runs. The vertical runup heights for the three different scenarios are shown in Figure 5.7 to Figure 5.9, which contain the rectilinear and staggered runup values. The vertical runup values were obtained with respect to the modeled still-water level as opposed to the design still-water level. Two of the scenarios (3m rectilinear with 2 trees/row using 2 rows and the 2.4m staggered with 2 trees/row using 3 rows) were completed using a smaller time step coefficient due to errors in the bore propagation which resulted in the incorrect vertical runup.

When comparing the attenuation of the staggered and rectilinear tree configurations it is evident that the staggered configuration provided significantly more reduction regardless of the initial water surface elevation. It is difficult to determine the trend in the runup for increasing forest widths due to the relatively small amount of widths tested, however it does appear that the change in the runup is typically larger as the amount of rows increases for the rectilinear tests. The change in runup for an increase in forest density for a constant amount of rows is linear for both 2.25m and 2.4m, but shows a logarithmic decrease for the 3m water depth. Figure 5.9 indicates that the reduction in the runup caused by increases in the forest density and width is not as significant when compared to the initial reduction caused by the presence of one tree for the 3m water depth.

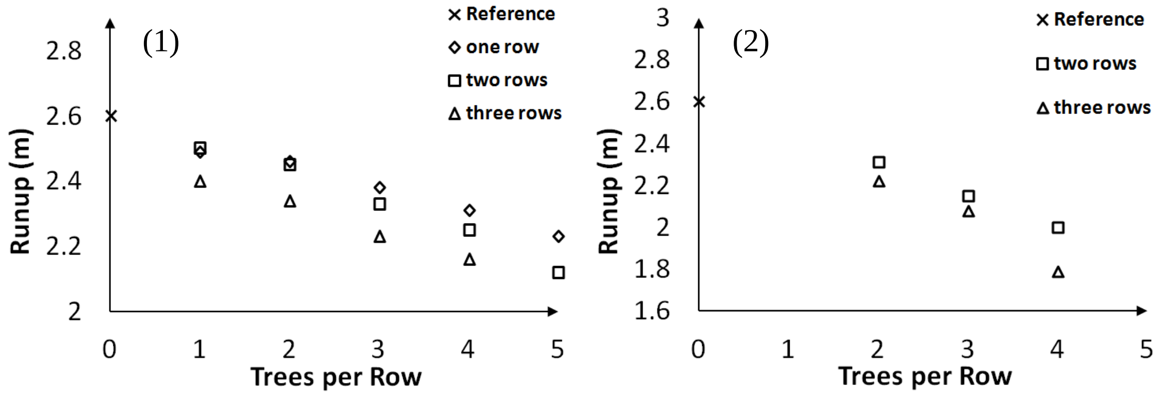

Figure 5.7 - Vertical runup for a water depth of 2.25m (C = 1.5m) for (1) rectilinear, and (2) staggered forest layouts

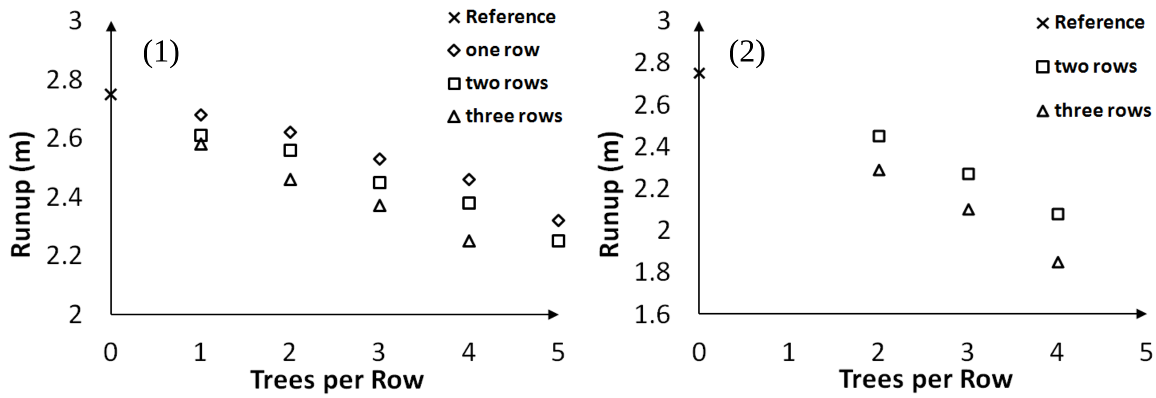

Figure 5.8 - Vertical runup for a water depth of 2.4m (C = 0m) for (1) rectilinear, and (2) staggered forest layouts

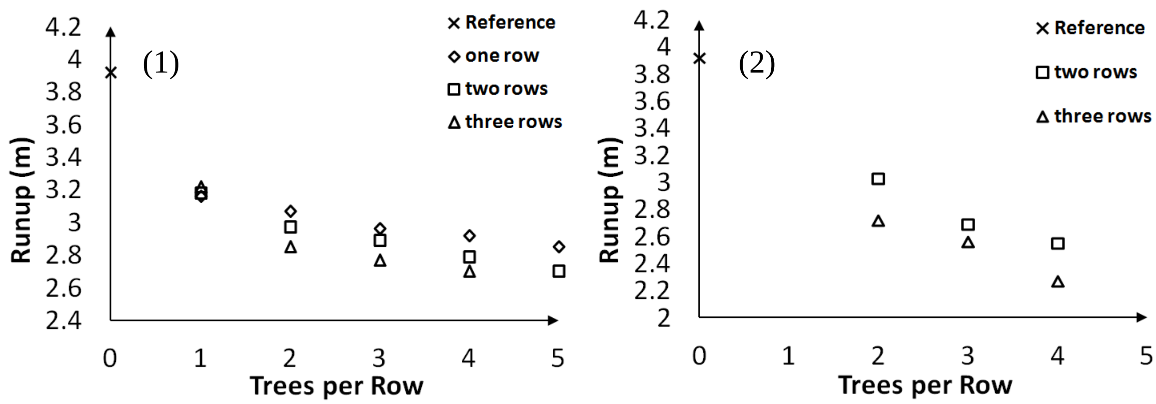

Figure 5.9 - Vertical runup for a water depth of 3m (C = -6m) for (1) rectilinear, and (2) staggered forest layouts

The percent reduction of the runup allows for a direct comparison of the effectiveness of the forest and can be calculated based on:

[5.1] $$Percentage\ Reduction\ = \frac{(without\ vegetation - with\ vegetation)}{without\ vegetation}\%$$

Table 5.2 - Percent reduction of the runup for the rectilinear layout

Trees /Row	2.25 m Water Depth (%)			2.4 m Water Depth (%)			3 m Water Depth (%)		
	1 Row	2 Row	3 Rows	1 Row	2 Row	3 Rows	1 Row	2 Row	3 Rows
1	4.23	3.84	7.70	2.55	5.10	6.18	19.39	18.88	17.86
2	5.38	5.77	10.00	4.73	6.91	10.55	21.68	24.23	27.30
3	8.46	10.39	14.23	8.00	10.91	13.82	24.49	26.28	29.34
4	11.15	13.46	16.92	10.55	13.46	18.18	25.51	28.83	31.12
5	14.23	18.46		15.64	18.18		27.30	31.12	

Table 5.3 - Percent reduction of the runup for the staggered layout

Trees /Row	2.25 m Water Depth (%)		2.4 m Water Depth (%)		3 m Water Depth (%)	
	2 Rows	3 Rows	2 Rows	3 Rows	2 Rows	3 Rows
2	11.15	14.62	10.91	16.73	22.70	30.61
3	17.31	20.00	17.46	23.64	31.38	34.69
4	23.08	31.15	24.36	32.73	34.95	42.09

These tables show that the difference in attenuation for the 2.25m water depth and that of the 2.4m water depth are comparable. However, when the initial water depth is at 3m, the reduction is more significant due to the location of the bore formation.

From these figures and tables it is clear that the location of the bore formation has a significant effect on the coastal forests' ability to reduce the runup height of the bore. While the physical runup is increased as the water level increases, the percent reduction in runup of the waves which break far in front of the forest is significantly less than that of the wave which breaks directly in front of the forest. This may be caused by the increased amount of runup seen on the trees, as shown in Table 5.1, which results in a larger reflection of the bore back offshore.

5.2.3 Velocity

This section examines the reduction in velocity caused by the presence of the coastal forest during the runup of the tsunami bore. A selection of the results is presented here as the velocity was obtained for all of the forest scenarios. The velocity measurements were obtained at a lower frequency of 10 Hz due of the size of the model; as such the bore front velocity was not always captured by the measurements. The values shown are the depth-averaged velocities.

Velocity across the Domain Width

The measurements obtained across the domain width were used to ensure that the tsunami bore propagated uniformly across the domain after passing through the coastal forest. These results are presented for the three still-water elevations in Figure 5.10 for the reference scenario containing no trees. These results confirm that the propagation of the bore is uniform across the domain and that there are no inconsistencies in the runup of the model. For the rundown of the bore, as discussed in Section 5.2.2 variations were present due to the clumping of the water particles in the center of the domain. The variation in the rundown velocities is especially evident for the 3m still-water depth.

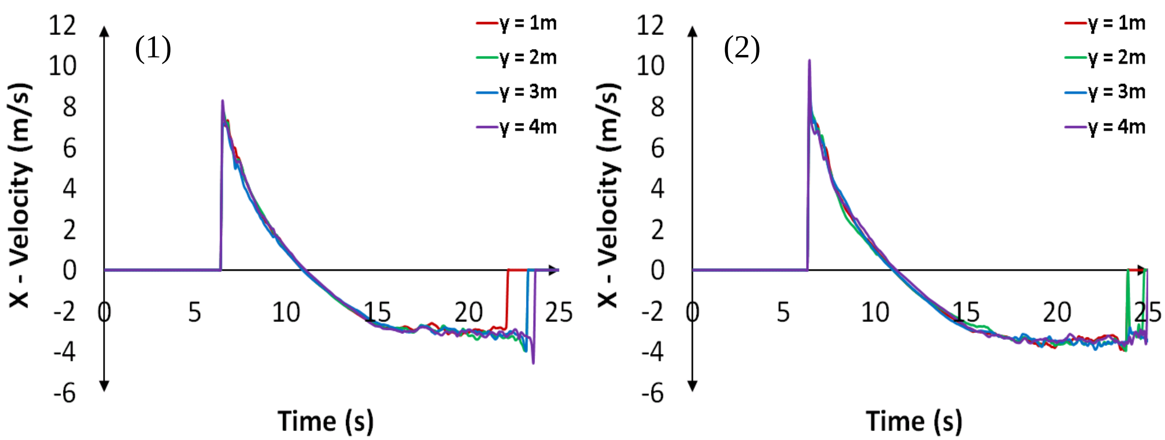

For caption see following page.

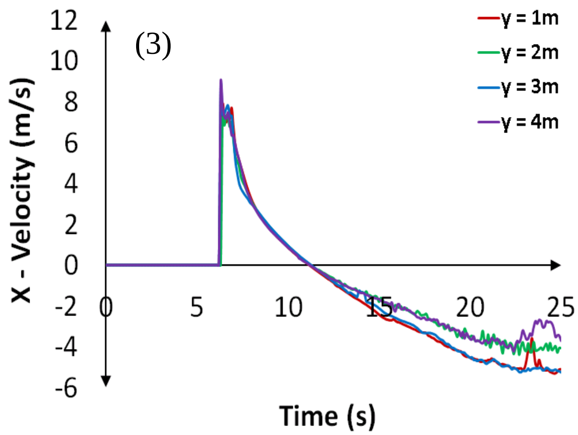

Figure 5.10 - Velocity measurements across the domain width for (1) 2.25m, (2) 2.4m, and (3) 3m still-water levels for reference case

Velocity across the Domain Length

Of more interest for the propagation of the tsunami bore is the velocity profile as the bore travels through the domain. Shown in Figure 5.11 is a comparison of the reference velocities for the different water depths. For both the 2.25m and 2.4m water depths, the bore velocity is reduced as the bore propagates through the domain; however, as the bore breaks much later for the 3m water depth, the velocity of the bore increases as it propagates through the 35m to 50m measurement locations. When comparing the water velocities for the 2.25m and 2.4m models it can be seen that the time of arrival of the bore at the measurement locations is comparable and that the 2.4m water depth has marginally higher water velocities.

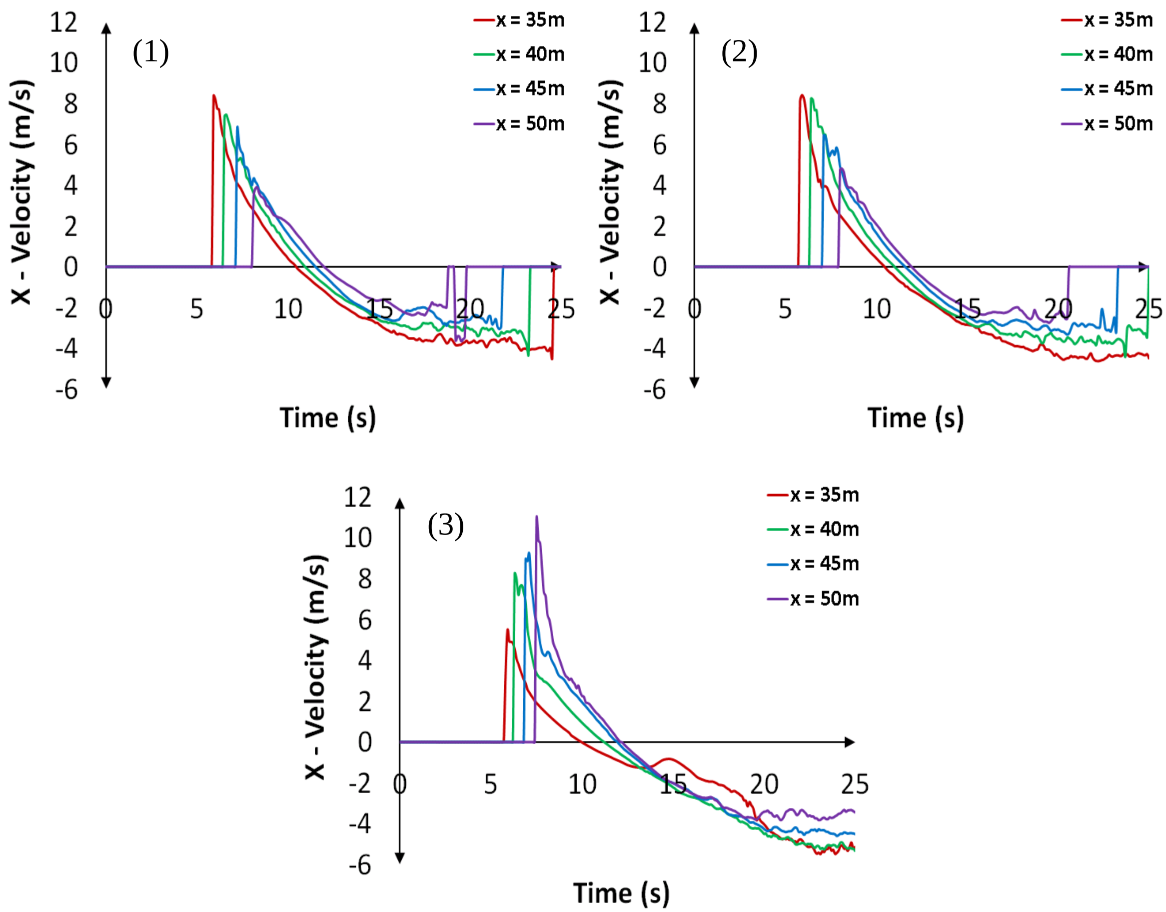

Figure 5.11 - Velocity measurements along the domain length at (1) 2.25m, (2) 2.4m, and (3) 3m for the reference scenario

Increase in Forest Band Width

To examine the reduction in velocity caused by the presence of the coastal forest it was necessary to examine the velocity profiles for both the staggered and rectilinear tree configurations. Shown in Figure 5.12 to 5.17 are the bore velocity profiles for the initial water depths for different forest band widths. Due to space limitations the results shown are for two trees per row only.

Figures 5.12 and 5.13 show the variation in water velocity for a still-water depth of 2.25m at 35m, 40m, 45m and 50m along the domain length. The results show relatively no variation at the 35m location as this is directly behind the first row or trees which all configurations were subjected to. When examining the velocities at 40m and 45m for the rectilinear configuration a slight variation in the peak velocity can be seen but no lag in the arrival time of the bore is present. At 50m, for the rectilinear model there is a lag present in the arrival time of the bore, although small and a reduction in the velocity of the bore both at and after the peak. For the staggered configuration at 40m it is evident that the peak of the bore was not captured by the measurements. A noticeable difference in the bore velocities is seen in Figure 5.13(4) at 50m down the flume length as there is a large time lag and difference in the peak bore velocity for the different forest widths. The reduction in velocity is more obvious in that of the staggered layout because that layout is more effective at attenuating the flow and has a larger effect on the tsunami bore.

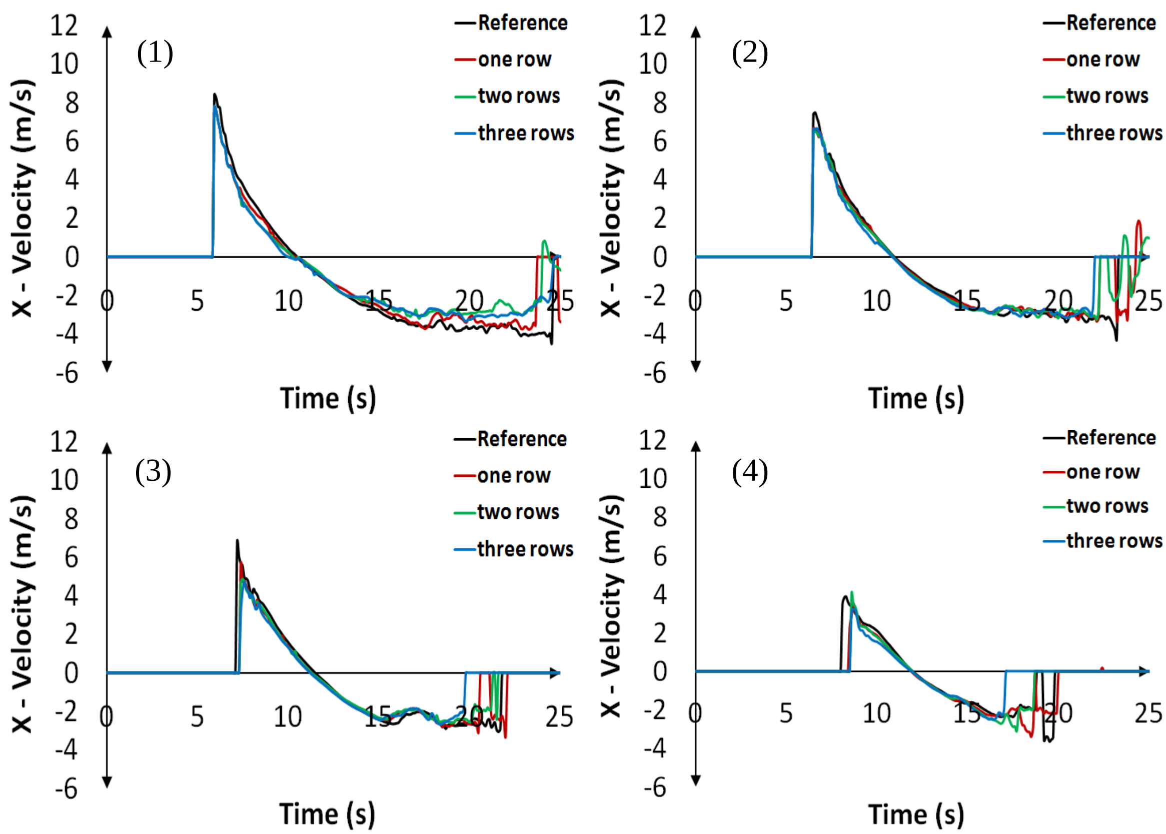

Figure 5.12 - Velocity profiles for the rectilinear layout at a water depth of 2.25m (C = 1.5m) with two trees per row at (1) 35m, (2) 40m, (3) 45m, and (4) 50m

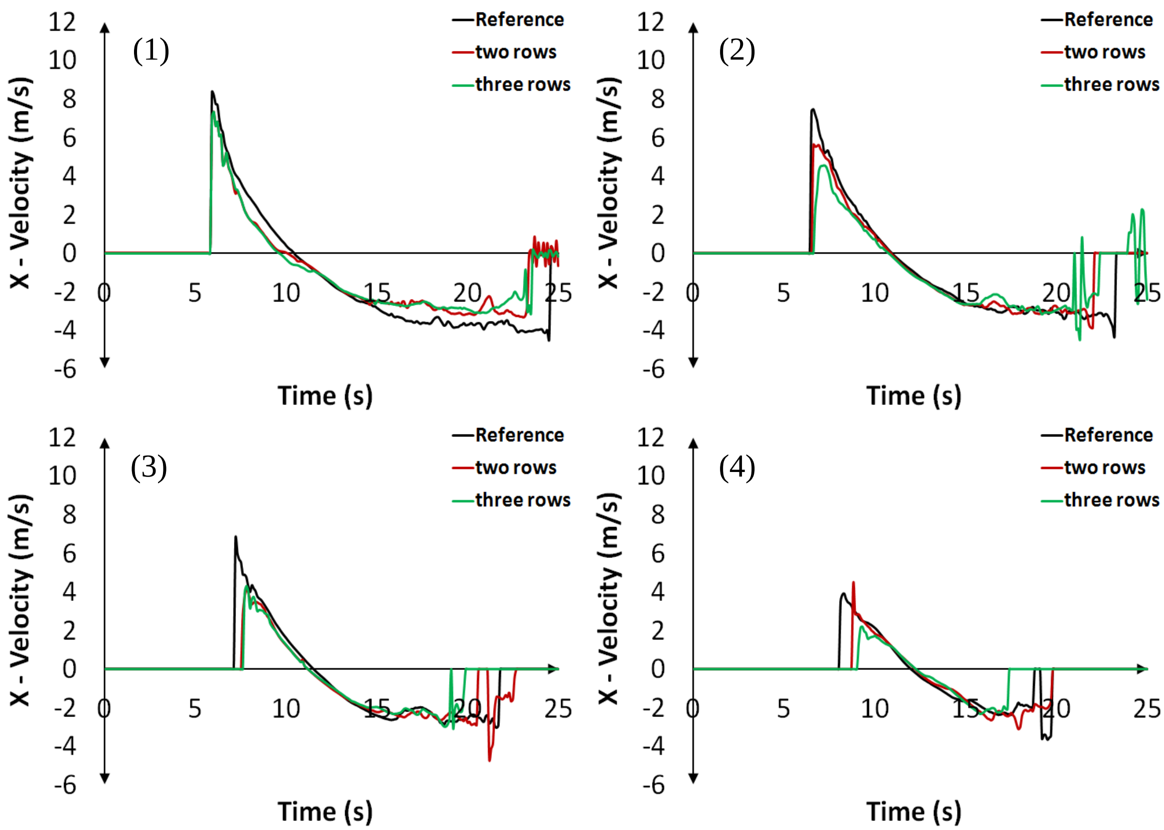

Figure 5.13 - Velocity profiles for the staggered layout at a water depth of 2.25m (C = 1.5m) with two trees per row at (1) 35m, (2) 40m, (3) 45m, and (4) 50m

The results for the 2.4m still-water depth, shown in Figures 5.14 and 5.15 are similar to those of the 2.25m water depth for the rectilinear configuration in that there is minimal variation in the bore velocity for an increasing amount of rows. However, the lag in the bore arrival that was seen in Figure 5.12(4) is not present for this water depth.

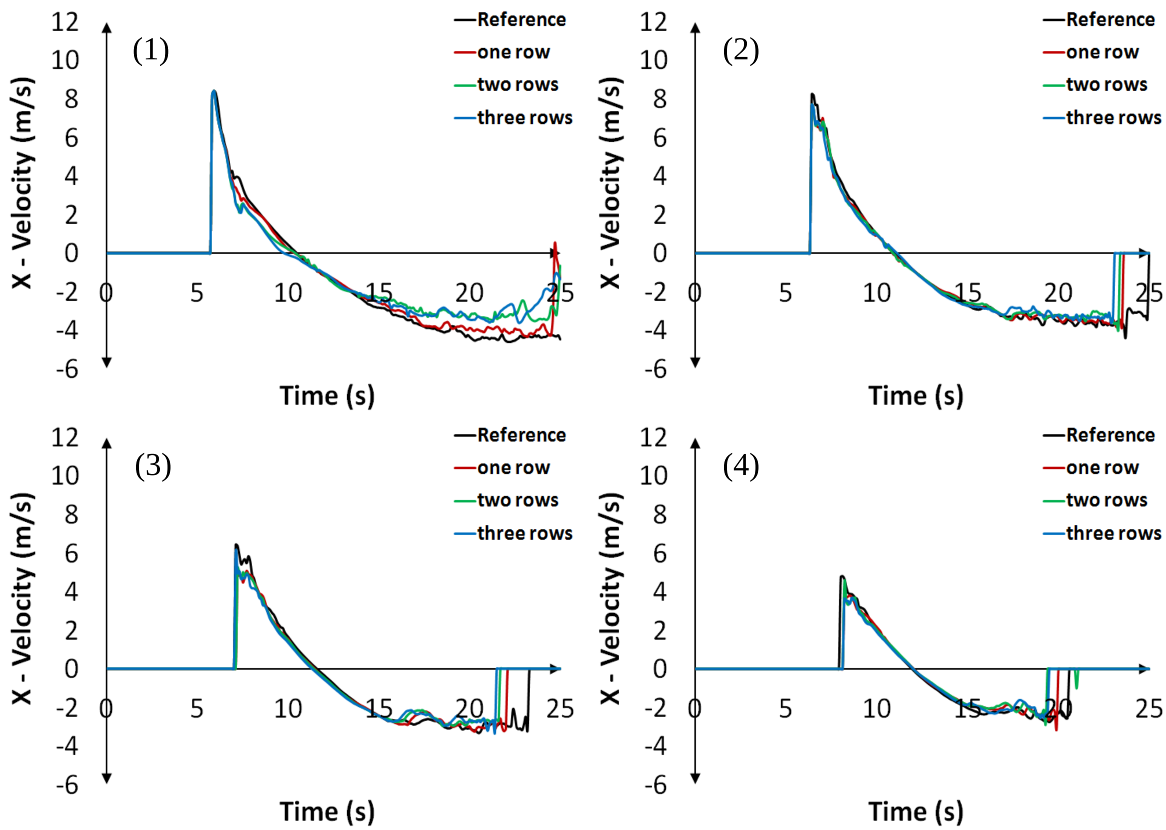

Figure 5.14 - Velocity profiles for the rectilinear layout at a water depth of 2.4m (C = 0m) with two trees per row (1) 35m, (2) 40m, (3) 45m, and (4) 50m

For the staggered layout a reduction in the bore velocity can be seen at 40m with the runup of the bore having a slightly lower peak value. Additionally, at both 45m and 50m, there is a reduction in the peak bore velocity. However, there does not appear to be a lag in the bore arrival at any of the measurement locations.

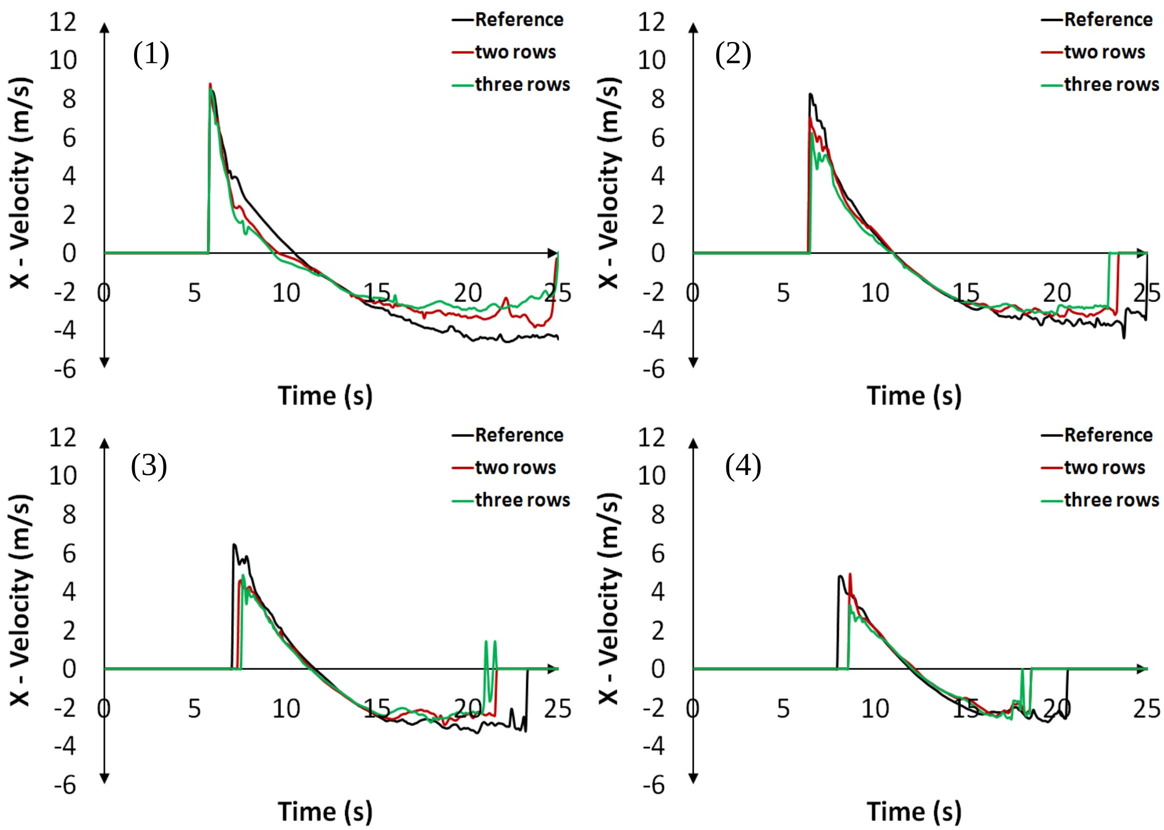

Figure 5.15 - Velocity profiles for the staggered layout at a water depth of 2.4m (C = 0m) with two trees per row (1) 35m, (2) 40m, (3) 45m, and (4) 50m

Finally, Figures 5.16 and 5.17 show the results for the 3m still-water depth. Figure 5.16 for the rectilinear configuration shows that the bore velocities and arrival times are fairly uniform despite increases in the forest belt width. For the staggered layout shown in Figure 5.17, the peak bore velocity is decreased by an increase in the forest width at 40m, 45m and 50m. Additionally, there is a lag in the arrival time of the bore present at 50m, Figure 5.17(4).

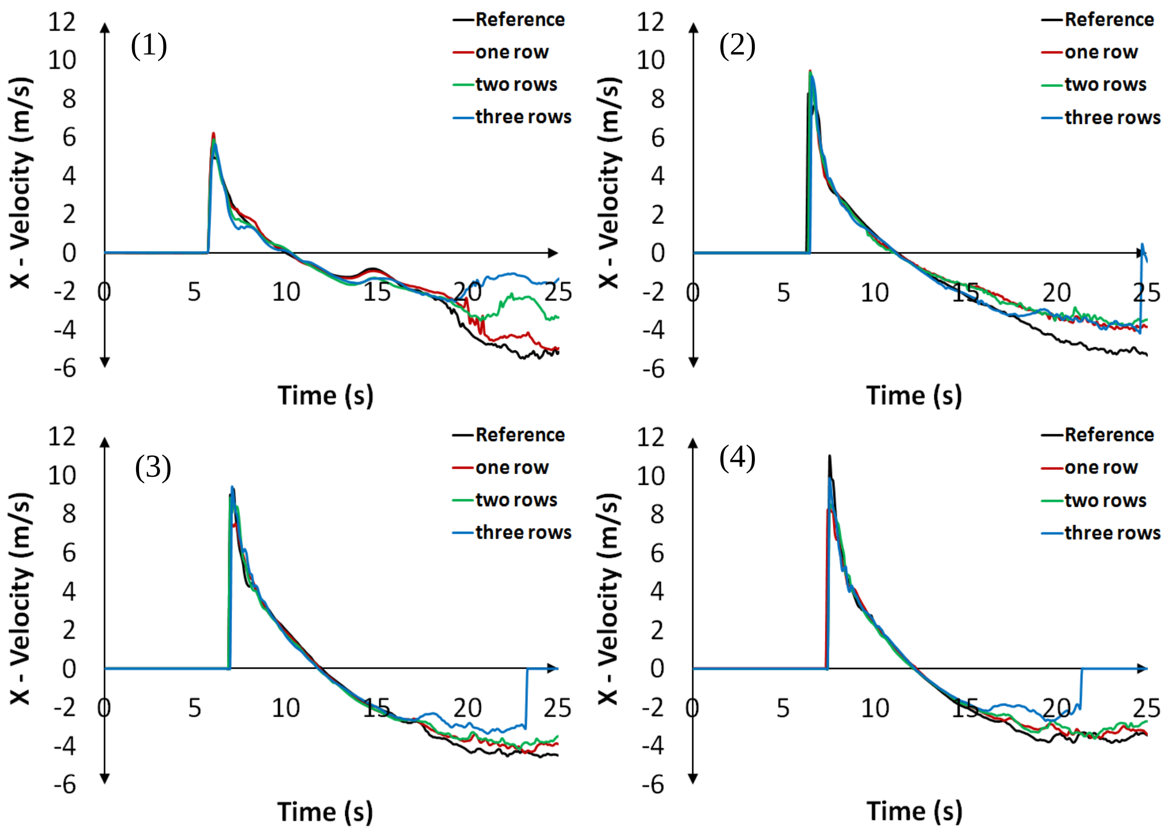

Figure 5.16 - Velocity profiles for the rectilinear layout at a water depth of 3m (C = -6m) with two trees per row (1) 35m, (2) 40m, (3) 45m, and (4) 50m

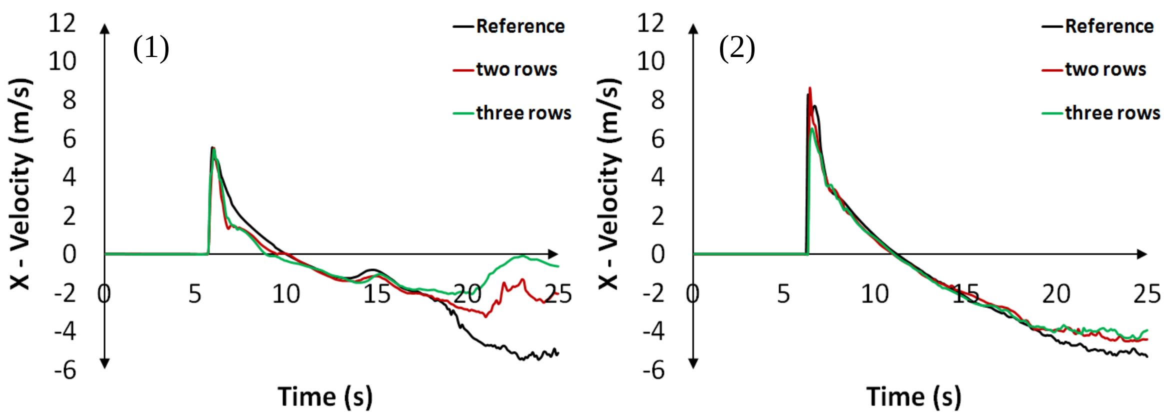

For caption see following page.

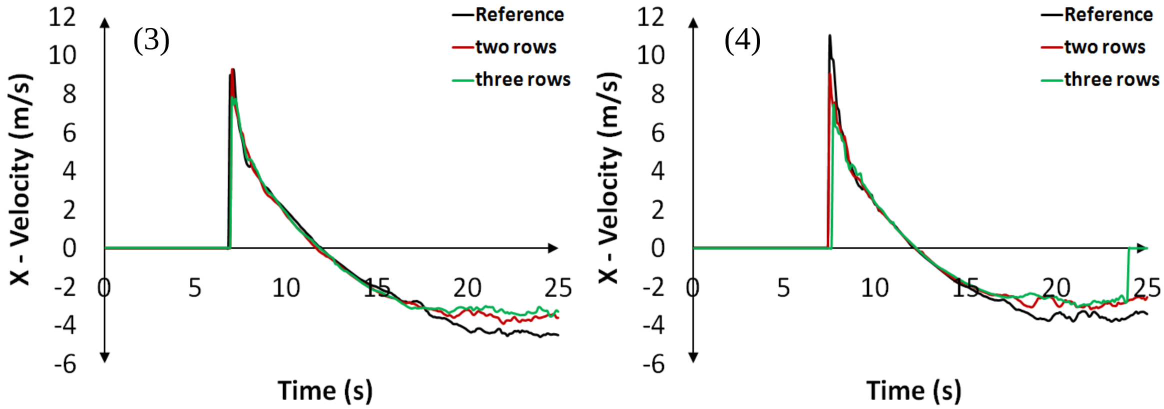

Figure 5.17 - Velocity profiles for the staggered layout at a water depth of 3m (C = -6m) with two trees per row (1) 35m, (2) 40m, (3) 45m, and (4) 50m

When comparing the velocity profiles for the three different still-water levels against those of the reference scenario it is clear that the addition of the trees results in a reduction of the bore velocity, though potentially small. Less clear is the reduction caused by an increasing forest belt width on the velocity in and directly behind the forest; however this may be due to the relatively small increases in width examined. The effect of the forest belt width on the velocity is only evident further upstream in the domain if at all, as the rectilinear configuration showed little to no effect on the velocity.

Increase in the Forest Density

In order to gauge the impact of the forest density on the bore velocity Figures 5.18 to 5.23 present the bore velocity for a set amount of rows and a variable density. Portrayed for the rectilinear layout are the results for one row of trees with different densities, and for the staggered layout the results are for two rows with different densities.

The impact of the tree density for the 2.25m still-water depth is shown in Figure 5.17 and 5.18 for the rectilinear and staggered configurations, respectively. At 35m there is relatively no variation in the velocity for the rectilinear layout, while that of the staggered layout has a large decrease in the bore velocity for the highest density. Further from the forest, at 40m and 45 the effect of the forest becomes increasingly evident as the bore front velocity is decreased and the bore arrival is lagged for higher density scenarios for both layouts. The largest impact is seen at 50m where a large lag is present in the bore arrival time and there is a distinct variation in bore velocity as the density increases.

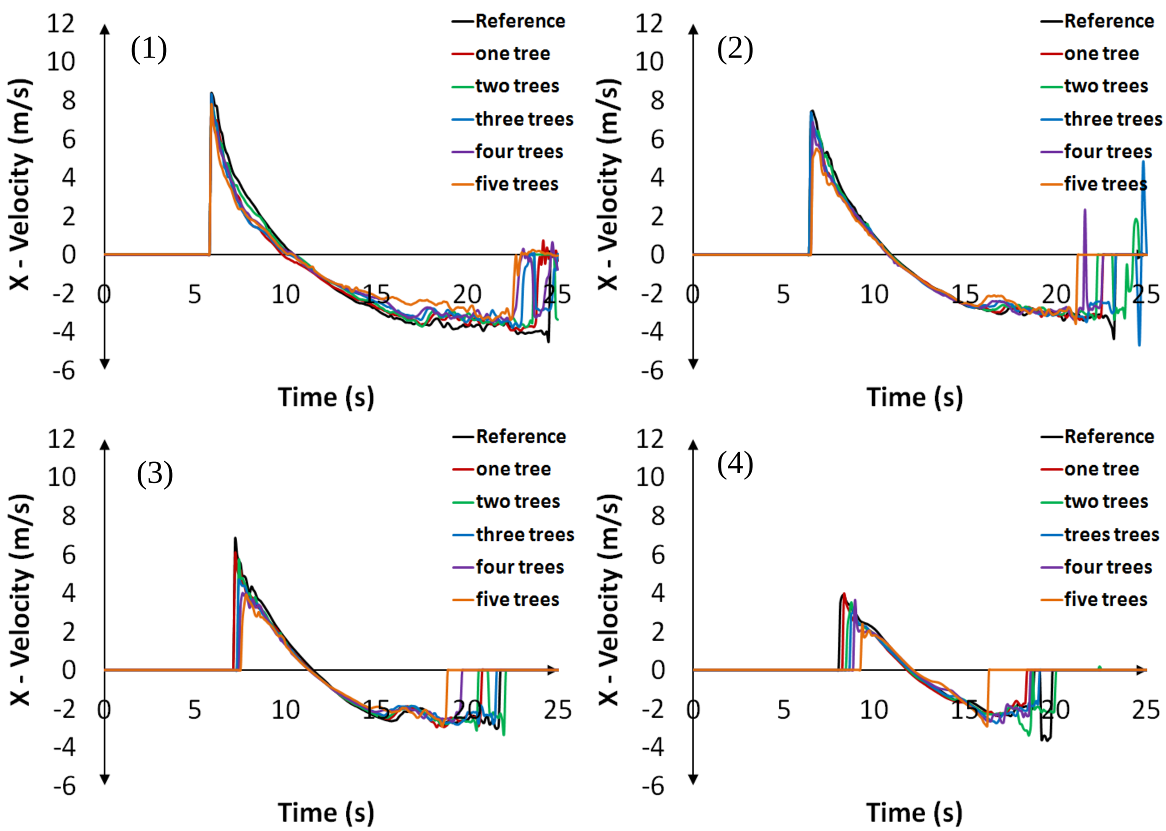

Figure 5.18 - Velocity profiles for the rectilinear layout at a water depth of 2.25m (C = 1.5m) for two rows of trees at (1) 35m, (2) 40m, (3) 45m, and (4) 50m

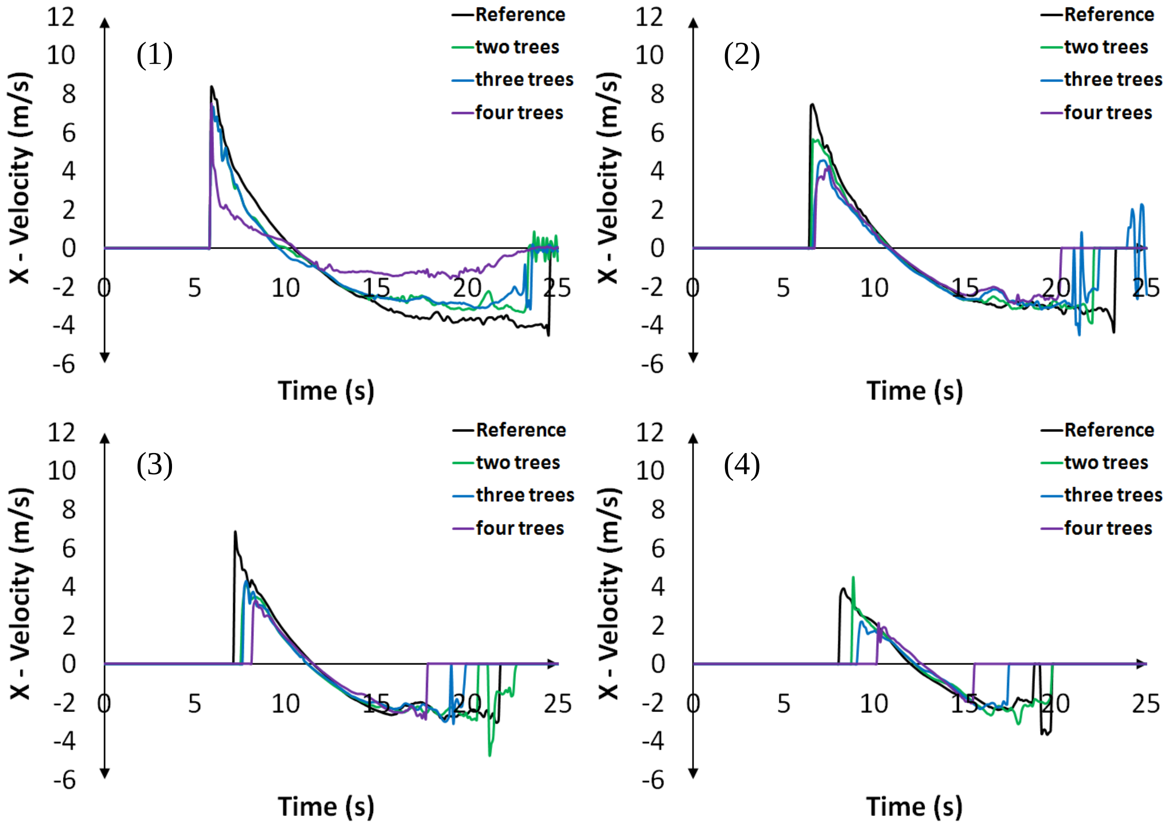

Figure 5.19 - Velocity profiles for the staggered layout at a water depth of 2.25m (C = 1.5m) for one row of trees at (1) 35m, (2) 40m, (3) 45m, and (4) 50m

The results for the rectilinear layout for an initial water depth of 2.4m shows an unusual trend, Fig. 5.20 (2), (3) and (4) all show that the bore propagating through three trees arrives slightly ahead of those propagating through smaller density forests; additionally, for Fig 5.20 (2) and (3) the bore is also propagating with a higher peak velocity. When examining the results of the staggered layout the velocity at 35m is consistent for the peak of the bore, but it can be seen that the velocity decreases more rapidly for the scenarios with increased forest density. Similar to the results for the 2.25m water depth, as the bore propagates down the domain the effect of the higher density forest increases, as the water peak velocity decreases and the arrival of the bore is delayed. Figure 5.21 shows the results for the staggered configuration which indicate a decrease in the peak bore velocity and a delay in the bore arrival as the density of the forest increases.

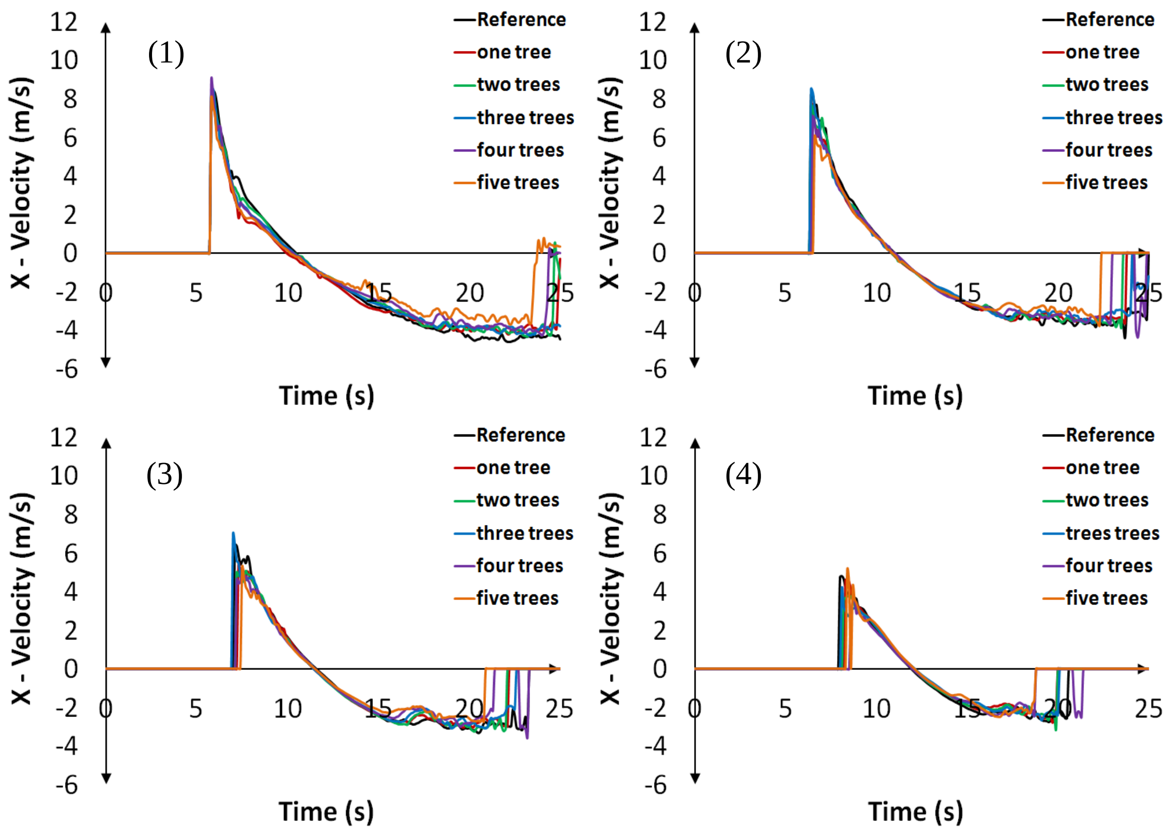

Figure 5.20 - Velocity profiles for the rectilinear layout at a water depth of 2.4m (C = 0m) for two rows of trees at (1) 35m, (2) 40m, (3) 45m, and (4) 50m

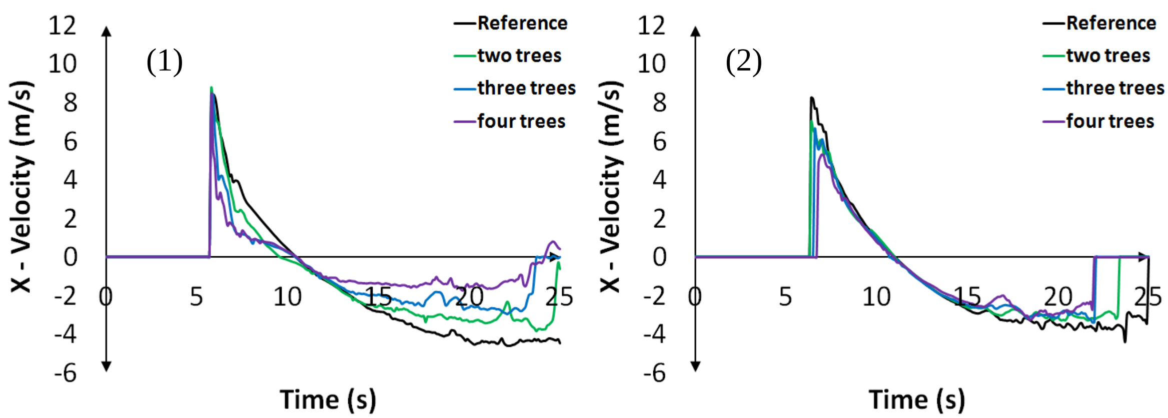

For caption see following page.

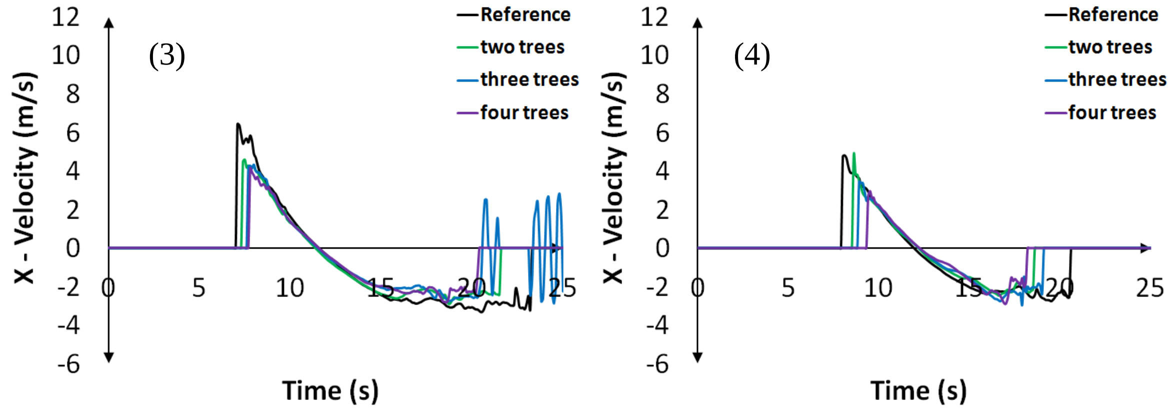

Figure 5.21 **- Velocity profiles for the staggered layout at a water depth of 2.4m (C = 0m) for two rows of trees at (1) 35m, (2) 40m, (3) 45m, and (4) 50m**

The final figures are for the 3m still-water depth. The results of the rectilinear layout, shown in Figure 5.22 indicate that the wave velocity is lower at the location of the trees (35m), then further down the flume at 40m, 45m and 50m. The peak bore velocity has some variation at 45m, which become more apparent further down the flume at 50m where a lag in the arrival time is also present. When compared to the velocities at 40m and 45m there is an overall decrease in the velocity at 50m, however this velocity is still higher than that directly behind the forest.

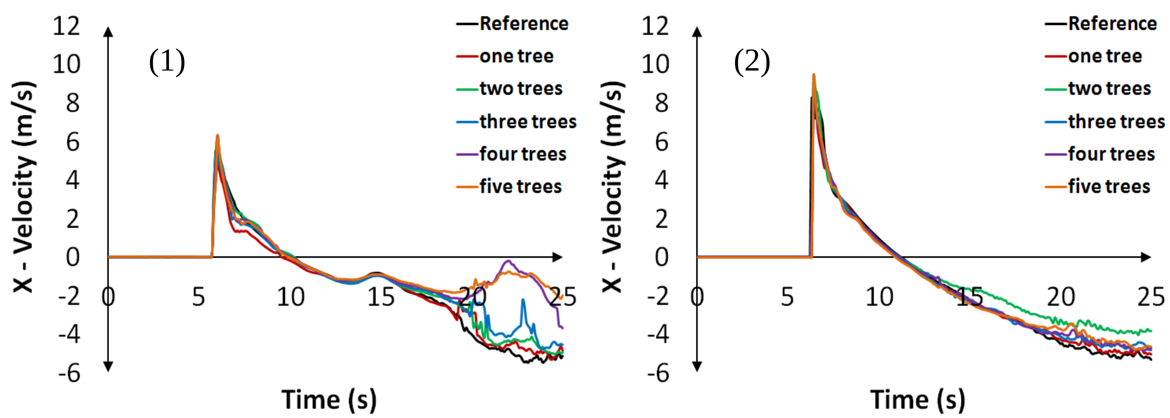

For caption see following page.

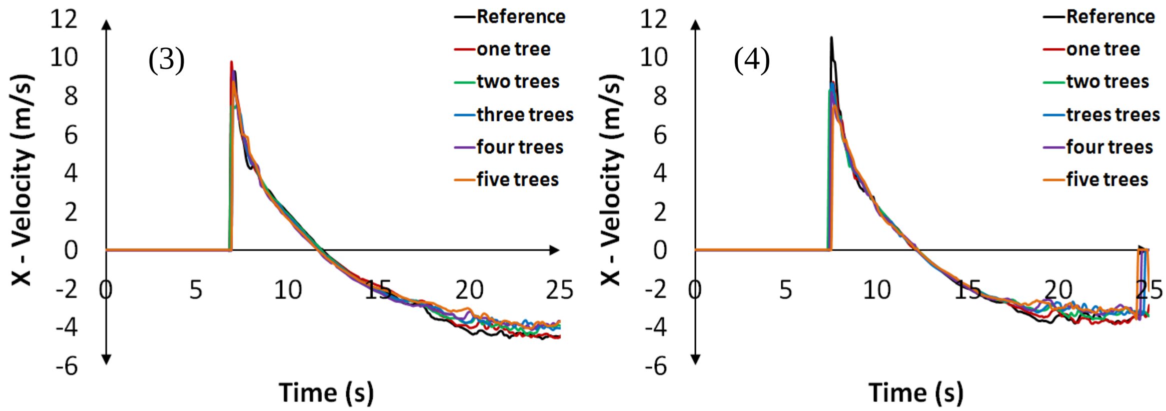

Figure 5.22 - Velocity profiles for the rectilinear layout at a water depth of 3m (C = -6m) for one row of trees at (1) 35m, (2) 40m, (3) 45m, and (4) 50m

For the staggered configuration, Figure 5.23, the increasing forest density results in a decrease in the peak bore velocity and a lag in the bore arrival time which becomes more prevalent as the bore propagates through the domain. Similar to the rectilinear configuration the lowest velocity is found directly behind the forest.

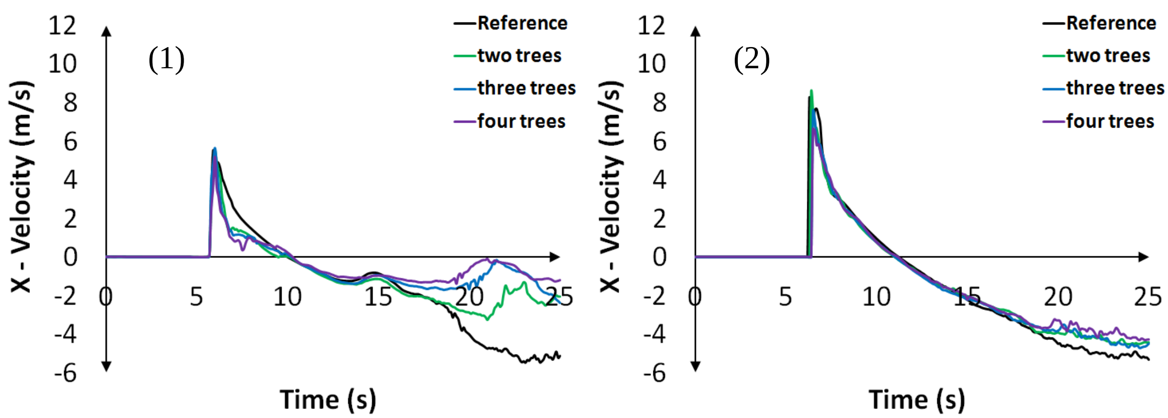

For caption see following page.

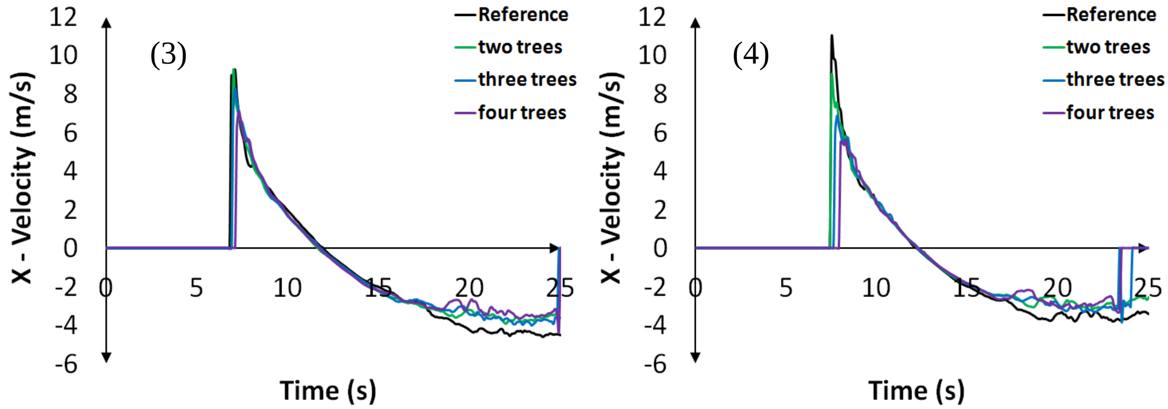

Figure 5.23 - Velocity profiles for the staggered layout at a water depth of 3m (C = -6m) for two rows of trees at (1) 35m, (2) 40m, (3) 45m, and (4) 50m

When examining the effect of increasing the forest density for a constant amount of rows it can be seen that there is a significant effect on the peak velocity and the arrival time of the hydraulic bore.

5.2.4 Hydrodynamic Force

The force measurements were completed for both the staggered and rectilinear layouts with 2 trees per row and two rows. This was done in order to determine whether there was a reduced or increased hydrodynamic forces on the second row of trees due to the location of the first row, the location of the trees are shown in Figure 5.24, and whether the still-water level would influence the hydrodynamic forces acting on the trees.

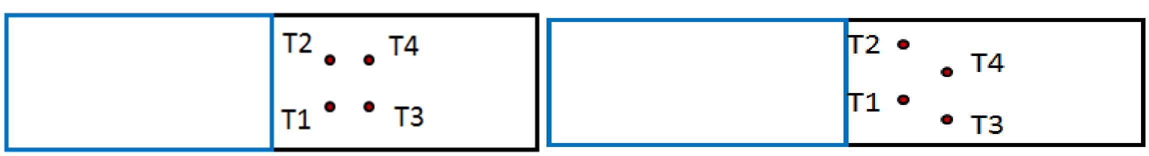

Figure 5.24 - Tree locations for hydrodynamic force measurements

Despite imposing a numerical speed of sound roughly 10 times that of the fluid velocity at the impact, density variations larger than 1% were found to occur at the bore impact (caused by the presence of a few higher density particles). This larger variation in the density may result in greater impact forces acting on the structures caused by an excessive increase in the pressure.

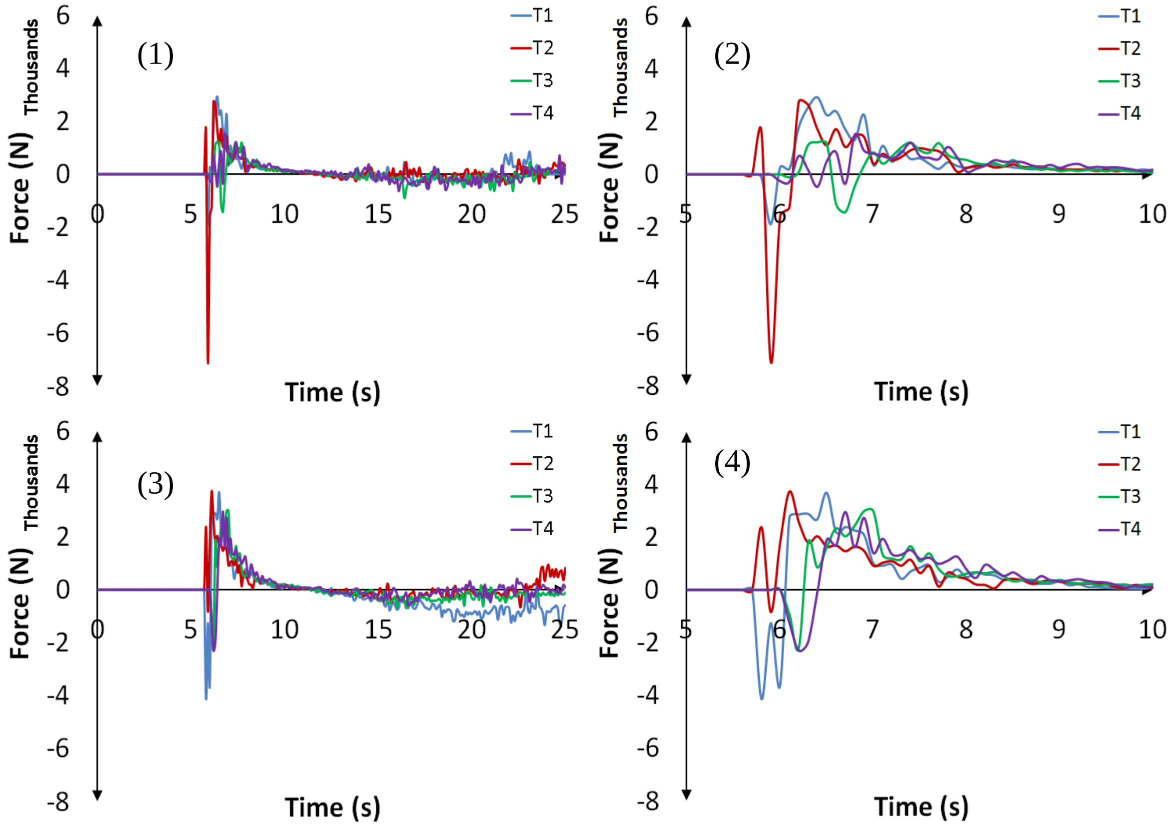

Figure 5.25 - Hydrodynamic impact forces for (1) rectilinear, (2) rectilinear impact, (3) staggered, and (4) staggered impact for the 2.25m water depth (C = 1.5m)

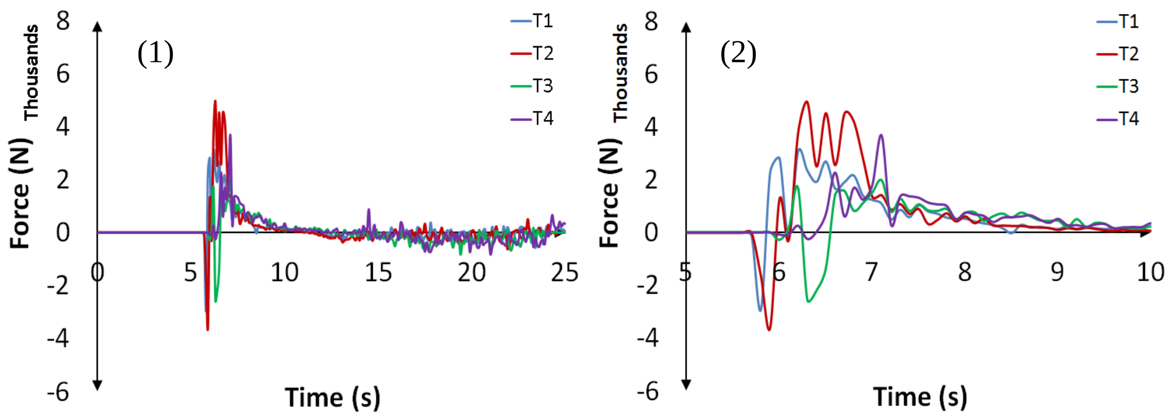

For caption see following page.

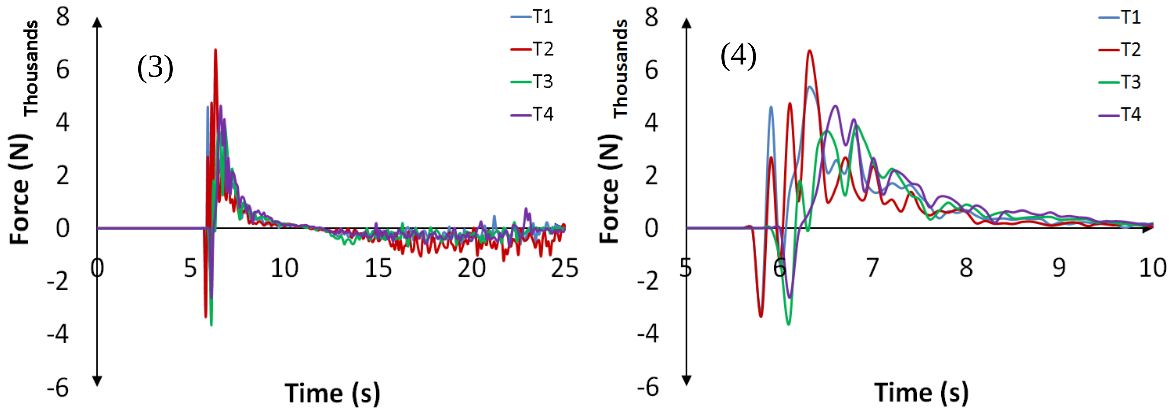

Figure 5.26 - Hydrodynamic impact forces for (1) rectilinear, (2) rectilinear impact, (3) staggered, and (4) staggered impact for the 2.4m water depth (C = 0m)

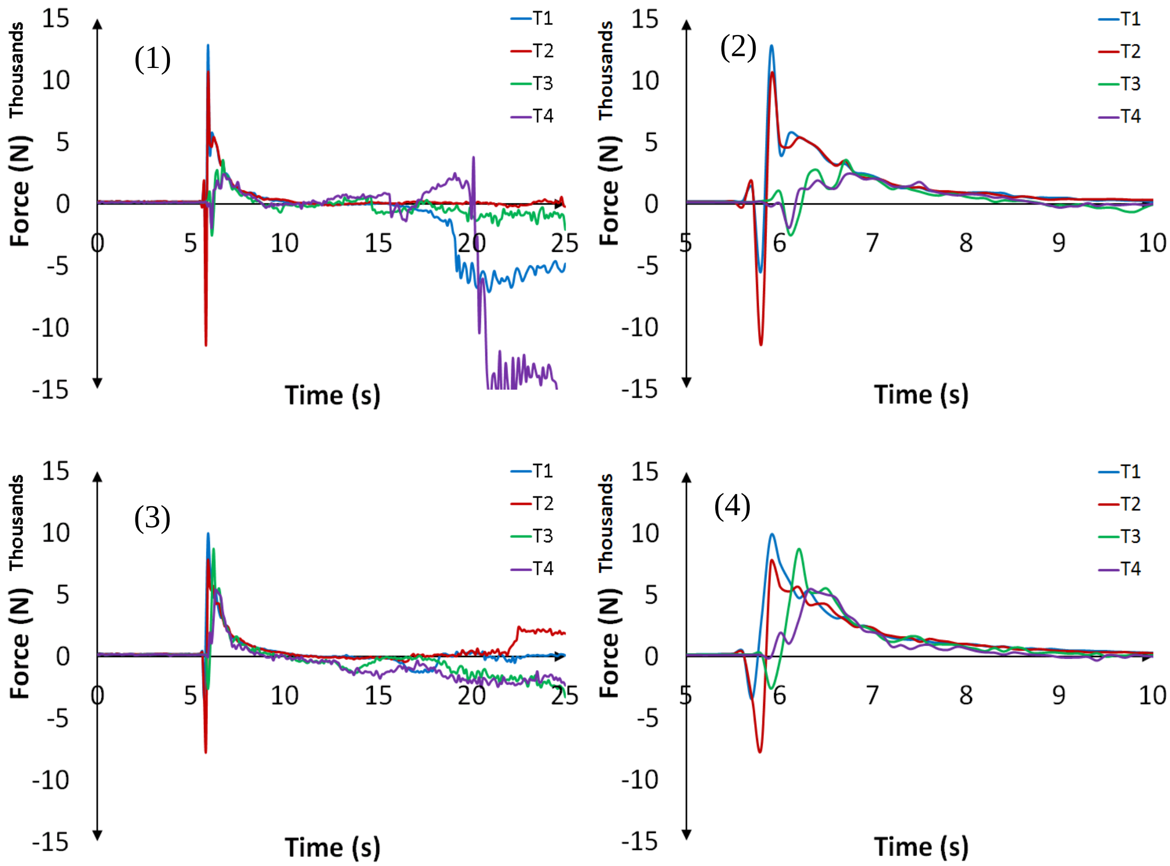

Figure 5.27 - Hydrodynamic impact forces for (1) rectilinear, (2) rectilinear impact, (3) staggered, and (4) staggered impact for the 3m water depth (C = -6m)

Figures 5.25 to 5.27 show the streamwise forces acting on the trees. The forces of the rectilinear configuration show a higher peak force for the first row of trees then for the second, indicating that they shield the second row from direct impact, there is also a delay in the time of the impact which is expected as they are further from the bore. When examining the staggered configuration the initial impact forces are similar for both the first and second rows. There are larger fluctuations in the forces for the rundown of the bore, which can be expected due the issues in modeling the rundown process. This is especially evident in Figure 5.27(1) as the hydrodynamic force on the tree becomes unrealistic during the rundown of the bore in the model, the result shown is for a reduced time stepping coefficient which did not improve the stability of the rundown. The negative forces seen at impact are believed to be caused by the reflection of the bore during runup.

The effect of the initial still-water depth on the hydrodynamic forces can be seen by an increase in the peak hydrodynamic force as the water depth increases. While the difference is small for the 2.25m and 2.4m water depths it is very obvious for the 3m initial still water depth. The forces for the rectilinear configuration at the 3m still water depth were found to be slightly larger than those for the staggered layout; this is believed to be a result of the output time step used. When examining the fluctuations present in the obtained impact forces, the results of the 3m water depth show a defined peak in the force with very little fluctuation when compared to those of the 2.25m and 2.4m still-water depths.

The ability of the tree to resist these impact forces is heavily dependent on the tree species as that will impact its flexibility and the strength of its root system. Possible means of failure include the breaking of the tree branches and/or stem or the overturning/uprooting of the trees. This may also be influenced by the soil properties at the forest location and by the amount of erosion that occurs during the runup of the bore.

5.3 Discussion

In this chapter the impact of different forest configurations and water depths were examined to analyze their effect on the attenuation, velocity, and impact force on a tsunami-induced bore. From this analysis it was found that the reduction in the bores' vertical runup was directly influenced by the layout of the forest, the width of the forest belt and the density of the trees. It was determined that regardless of the still-water level, the staggered layout of the trees provided superior reduction of the runup when compared to that of the rectilinear layout. It was found that increases in the forest belt width would result in a reduction in the runup. Similarly, it was found that increases in the forest density would result in a decrease in the vertical runup. The ability of the coastal forest to attenuate the flow for the different water-surface elevations was found to be comparable for the 2.25m and 2.4m water depths, which had the waves break further in front of the forest. However, the 3m water depth resulted in significantly higher levels of reduction, with the most significant difference in runup occurring between the baseline test and that with one tree.

When examining the reduction in the inland tsunami runup velocity, it was found that the presence of the forest would result in a decrease in the runup velocity, though minor in some cases. Interestingly, variation in the runup velocity for increasing forest belt width was minimal for the rectilinear layout and only present far behind the forest for the staggered layout. As it has been seen from the attenuation that increases in forest belt width decrease the bore runup it may be that the effect of the forest width increase is only seen further behind the forest then was measured. In terms of increasing density there was a clear increasing trend in bore velocity reduction and bore arrival lag as the density of the forest increased. When comparing the magnitude of the bore velocities for the different still-water elevations it is clear that the higher elevation results in significantly higher velocities, even with the attenuation by the coastal forest.

Finally, the location of the trees was found to have an impact on the reduction in the tsunami force. As expected the initial row of trees in the rectilinear configuration shielded the second row from direct impact of the bore; as such it was found that a reduction in the initial impact force could be obtained. As the second row of trees in the staggered layout was not protected the impact force was the same as for the first row. Despite the variation in the initial impact force, the remaining hydrodynamic force was consistent between first and second row for all configurations. The impact force acting on the trees was found to increase as the still-water level was increased.

6 Comparison of Numerical and Physical Results for Debris Impact

This chapter compares the results of the numerical and experimental models described in Sections 4.1 and 4.2.1 in order to test the accuracy of the model in reproducing the hydrodynamic forces of the bore on a structure and the impact forces of the tsunami-moved debris. The analysis examined the accuracy of the models water surface elevation and the forces acting on the structure. The movement of the debris as it impacted the structure and its angle of impact were also studied in order to determine if the model was able to reproduce this process accurately.

6.1 Water Elevation

The water surface elevation in the model was obtained at three locations in the flume and at 4 locations along the cylinder for all model runs. The initial assessment of the model was to analyze the impact location and angle of the debris as this would have a large effect on both the impact force and the bore runup on the cylinder. Due to the free movement of the model debris it was deemed unlikely that the impact would be directly comparable to that of the physical experiments, also as the debris was not restrained as in the physical experiment the debris was allowed to continue downstream of the cylinder, reducing the likelihood of multiple impacts on the structure.

The experimental model used had a “virtually” dry bed as it was not possible to fully remove all of the water from the flume before the experiments. As such, the numerical model was modeled with a dry bed, but two tests were run with the minimum possible wet bed in order to determine the impact this would have on both the water surface elevation and the forces on the structure.

6.1.1 1 kg Debris

This section compares the results for the 0.55m and 0.85m impoundment depths for the 1kg debris.

0.55m Impoundment Depth

At the lower impoundment depth of 0.55m, Figures 6.1 and 6.2 show that the debris in the numerical model impacts the cylinder at a larger angle then that of the physical model. On impact the debris was seen to rotate fully. For the initial impact Figure 6.1 shows that the debris was not carried on top of the bore, but rather in front of it. This would result in lower force estimates at the time of impact as it would not include the hydrodynamic forces of the bore. Additionally, the wide initial angle of the debris impact and the rotation which occurred would result in a lowered debris impact forces as the momentum of the debris was not wholly transferred to the cylinder. Due to the rotation of the debris a second impact occurred, which was perpendicular to the flow.

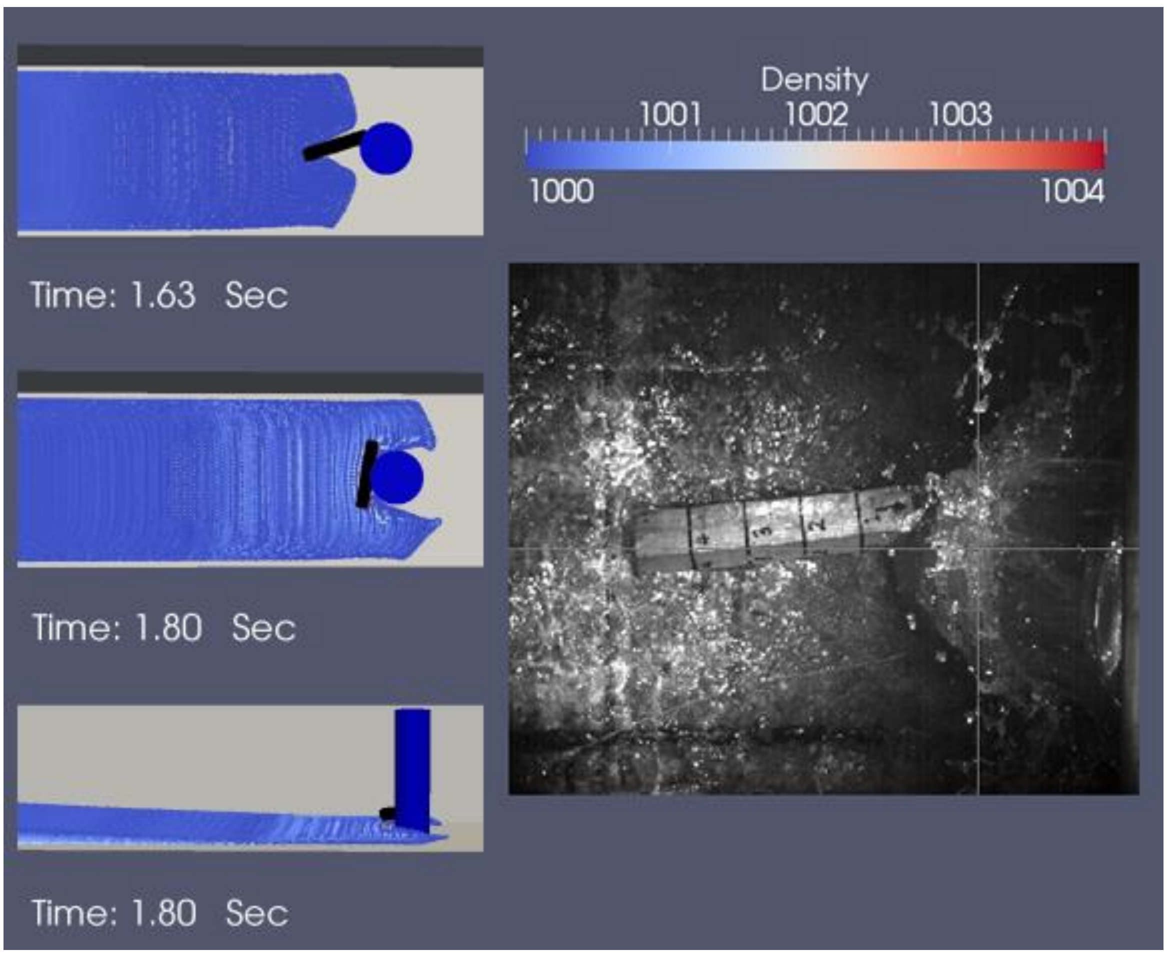

Figure 6.1 - Numerical and physical debris impact for 0.55m impoundment depth and 1kg debris

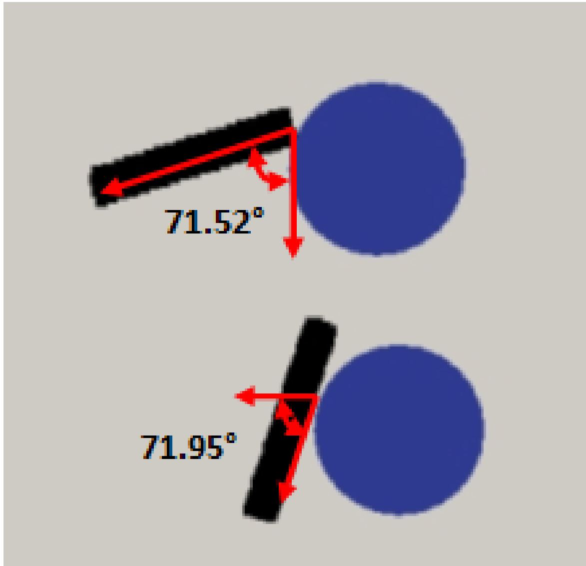

Figure 6.2 – 1kg debris impact angles for 0.55m impoundment depth

The angle of impact for the initial impact on the structure was 71.52° perpendicular to the structure; or 18.48° in relation to the flow direction. From Figure 6.1 it can be seen that the debris in the physical experiment also struck the structure at a slight angle, though more direct than that seen in the numerical experiment. Due to the location of the impact and the angle of impact rotation of the debris occurred. This resulted in a secondary peak force at a time of approximately 1.78s when the debris was at an angle of 71.95° parallel to the flow or 18.05° perpendicular to the structure. In both cases the impact on the structure was not direct which would result in a reduction of the debris impacting forces acting on the structure.

The water surface elevation time-histories are shown in Figure 6.3. Good agreement with the experimental results was found for the initial release of the water from the impoundment reservoir, Fig. 6.3(1). This is opposite of what was found at the water surface elevation at W6 which shows an underestimation of the numerical elevation at the initial impact of the bore and then good agreement as the time continued. From this figure it is evident that the numerical model was not capable of replicating the turbulent nature of the bore, which was expected as the model is single phase only. At the front of the cylinder (W7 and W8) the numerical model greatly underestimated the water surface elevation which may be due to the obstruction caused by the debris. The difference at the front of the cylinder was approximately 0.14m after the initial runup of the bore. At the side of the cylinder, W9, there is good agreement between the data. Finally, the physical experiment indicates that water was initially present behind the cylinder and was drained as the time-history continued contrary to the results of the numerical model which indicated that the cylinder became surrounded by water at a time of 4.5s. Unfortunately, no data was available for gauge W5 along the side of the cylinder.

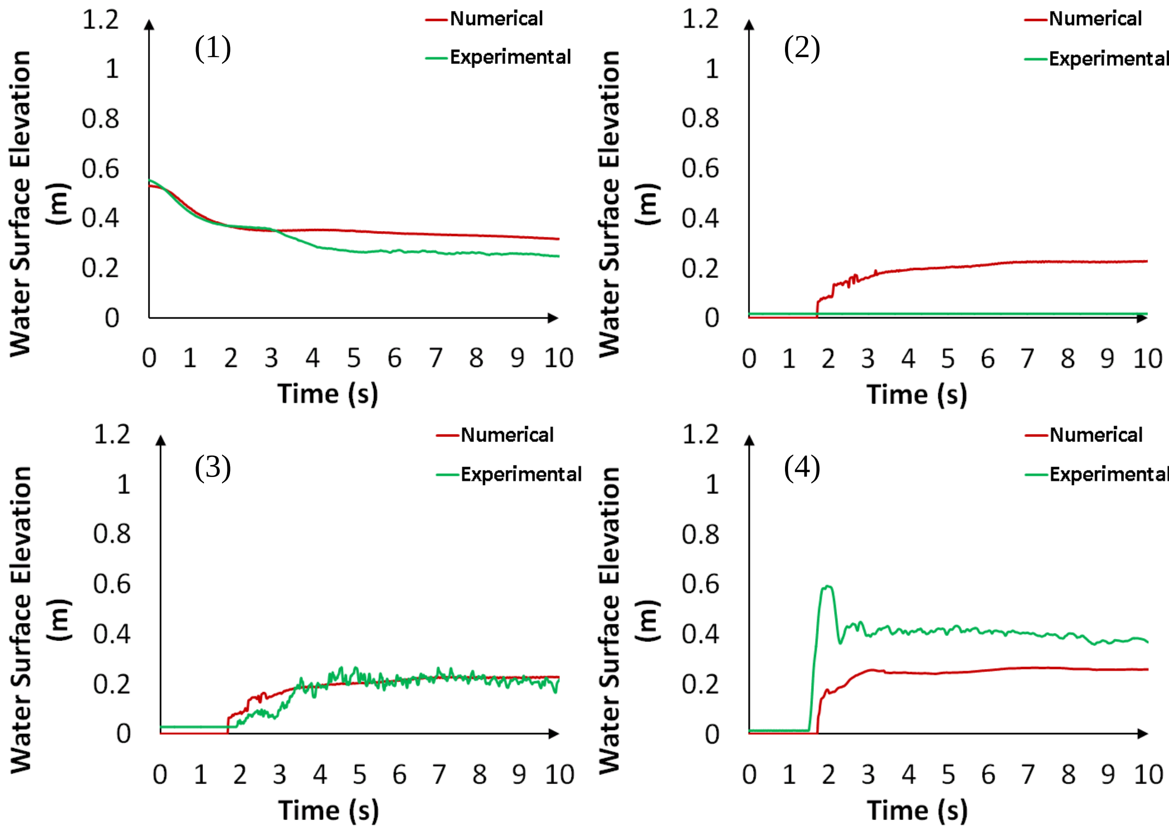

For caption see following page.

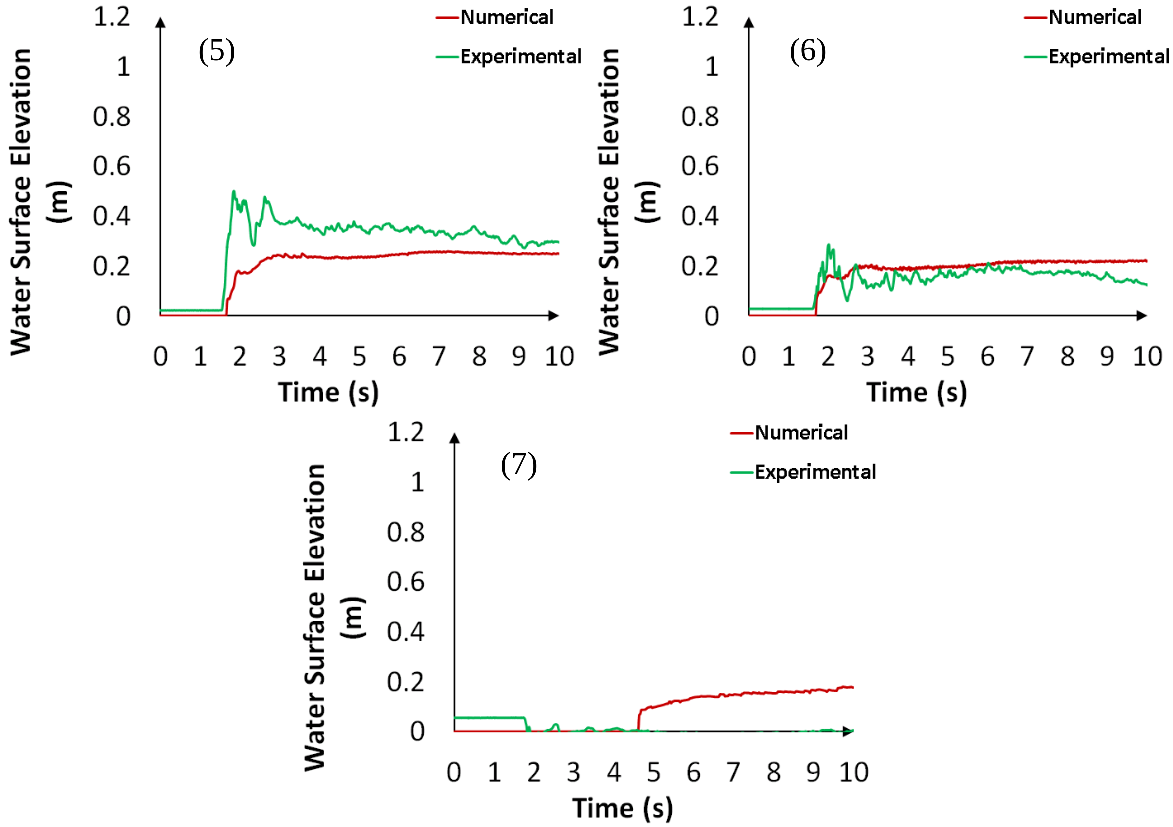

Figure 6.3 - Water surface elevation comparison for 0.55m impoundment depth at (1) W1, (2) W5, (3) W6, (4) W7, (5) W8, (6) W9, and (7) W10

The arrival time of the bore in the numerical model was aligned based on the initial draw-down of the water in the reservoir for the experimental model. This was necessary as the time-history of the measurements was initiated before the initial release of the bore from the gate.

0.85m Impoundment Depth

The results for the 0.85m impoundment depth are shown in Figure 6.4 to Figure 6.6. The debris impact for this test differs from that of the 0.55m debris as the debris did not rotate as significantly upon impact. As in the previous case the main runup of the bore occurred after the initial debris impact.

The angle of impact of the debris is shown in Figure 6.5; the impact angle of the debris was found to be 68.82° perpendicular to the structure, or 21.18° in relation to the flow direction. This angle is wider then that seen in the physical experiment, which experienced a near direct impact. Additionally, the debris impact in the numerical model impacted the structure off center when compared with the physical impact. Due to the angle and the location of impact, the debris was found to rotate slightly on impact and did not maintain contact with the structure for a long period of time. This would result in a reduction in the model impact force. A second impact was noted at a time of 1.23s with the debris striking at a larger angle.

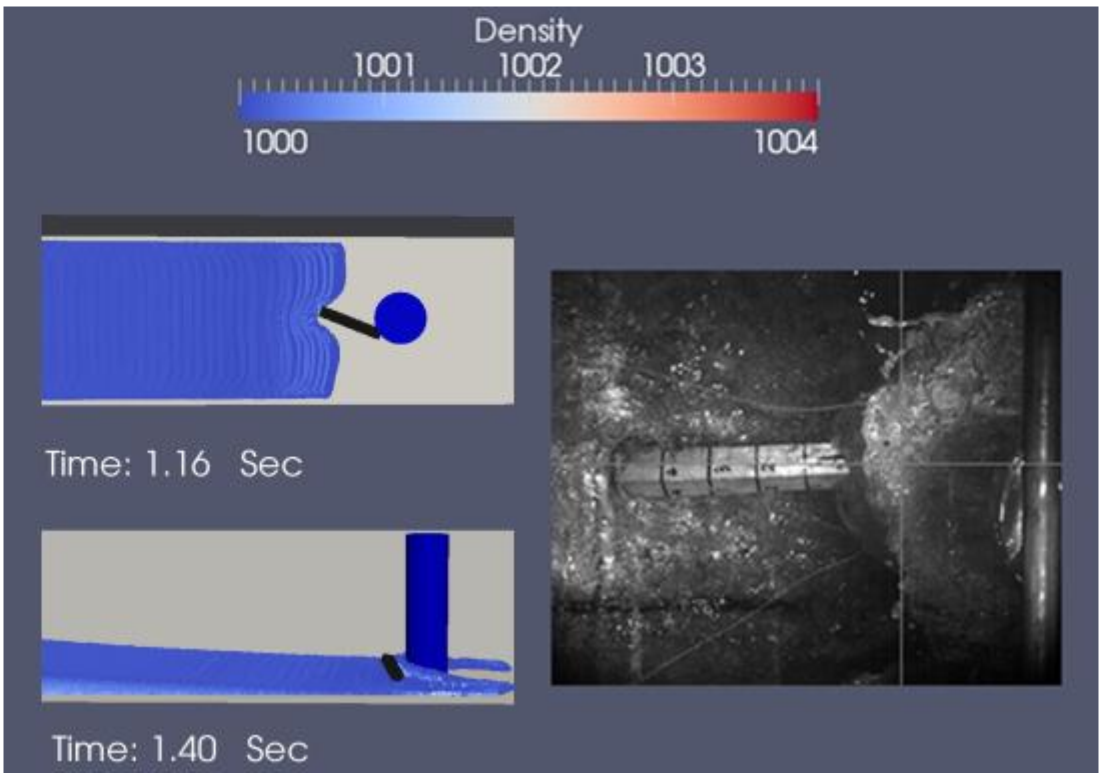

Figure 6.4 - Numerical and physical debris impact for 0.85m impoundment depth and 1kg debris

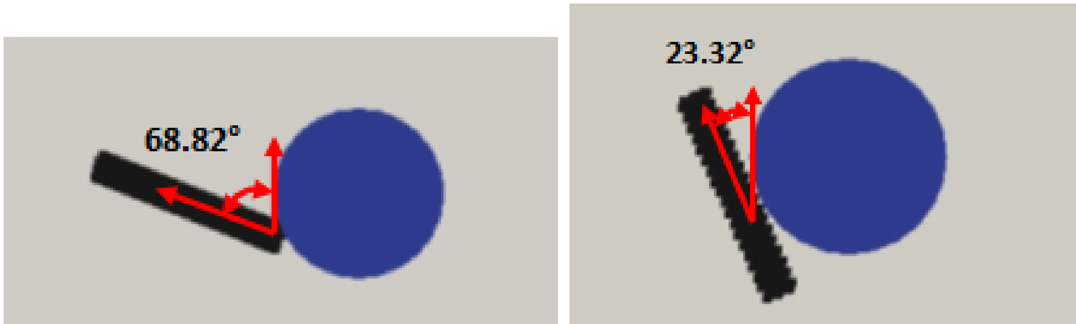

Figure 6.5 - 1kg debris impact angle for 0.85m impoundment depth

The time-histories of the water surface elevation for an impoundment depth of 0.85 are shown in Figure 6.6. Overall the trends found for the 0.55m are similar to those shown in this figure. The water surface elevation in the reservoir at W1 was found to be well modeled for the initial release of the bore, but over modeled the elevation after the initial release. The model was also found to overestimate the elevation at W6 at the side of the flume. Similar to the 0.55m impoundment depth, the initial impact of the bore is not represented in the model at W7 or W8, however, the surface elevation at W7 is consistently underestimated, with a difference of roughly 0.28m after the initial runup, while that of W8 is better modeled after the initial peak. Unfortunately no physical model surface elevations were available for the wave gauge location at the back of the cylinder or at the side of the flume, Fig 6.6 (7) and (5), respectively.

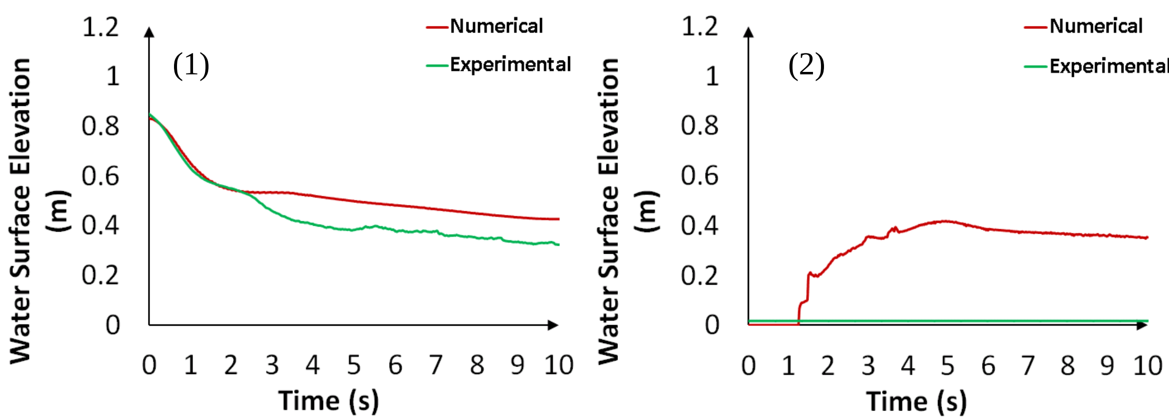

For caption see following page.

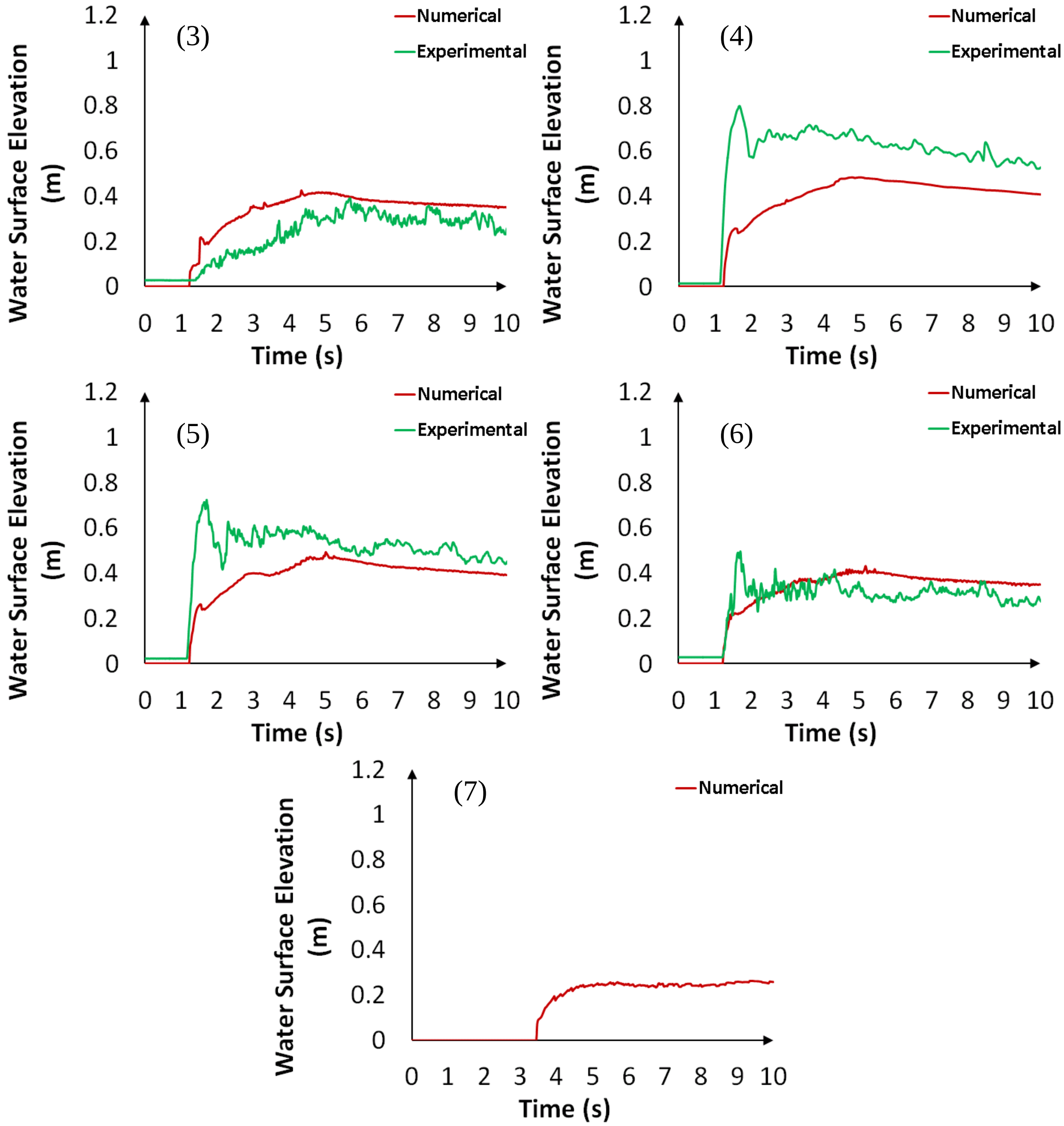

Figure 6.6 - Water surface elevation comparison for 0.85m impoundment depth at (1) W1, (2) W5, (3) W6, (4) W7, (5) W8, (6) W9, and (7) W10

6.1.2 2kg Long Debris

This section shows the results of the debris impact and water surface elevation for the 0.55m and 0.85m impoundment depths for the 2.191kg long debris. For this scenario no experimental water elevation results were available for comparison with the 0.85m impoundment depth.

0.55m Impoundment Depth

The angle of impact for the 0.55m impoundment depth was found to be well modeled as shown in Figures 6.7 and 6.8. The debris was found to impact the cylinder at an angle of 88.66°, which is nearly perpendicular to the structure. Unfortunately due to the length of the debris, the delay between the impact of the debris and the runup of the bore was almost half a second, which results in two distinct impacts on the structure. As the debris impact was perpendicular to the structure and along the structure centerline, there was no rotation of the debris upon impact.

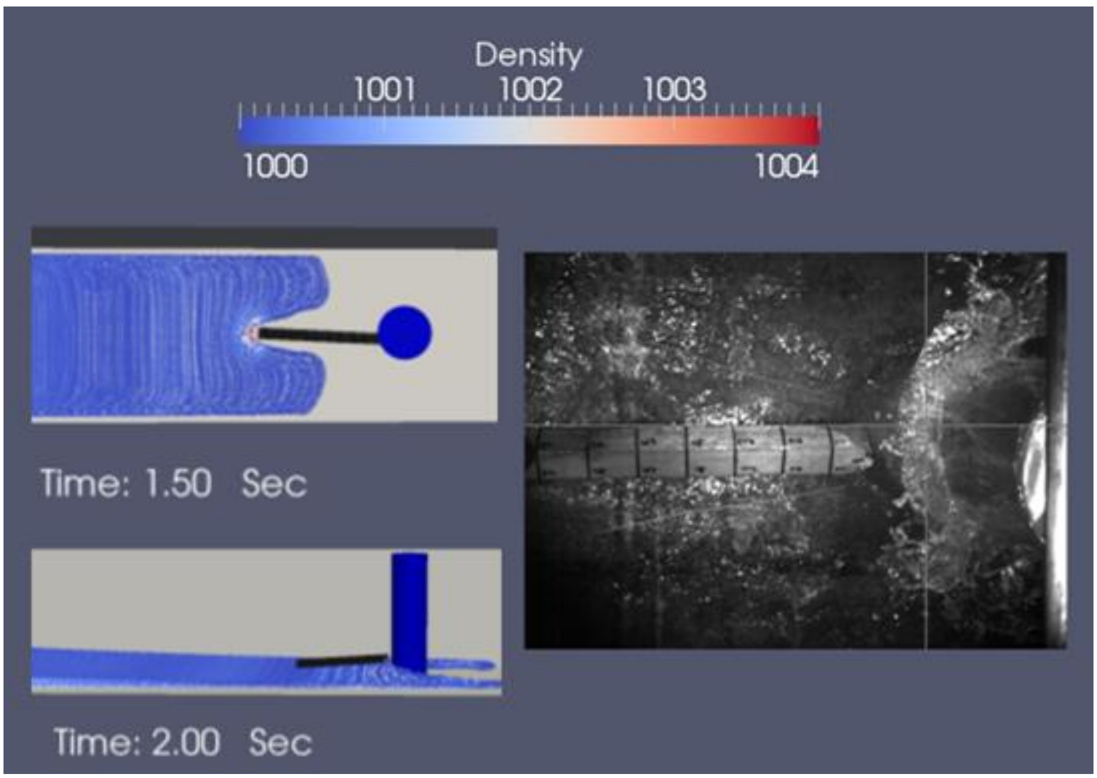

Figure 6.7 - Numerical and physical debris impact for 0.55m impoundment depth and 2kg long debris

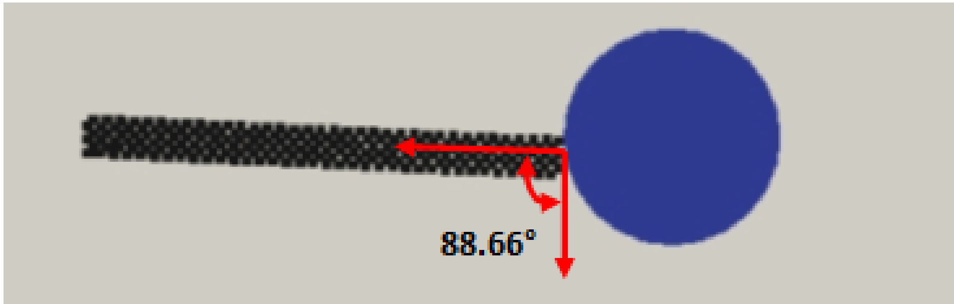

Figure 6.8 - 2kg long debris impact angle for 0.55m impoundment depth

Unfortunately, for this run no experimental water surface elevation measurements were obtained for wave gauges 5 and 10. Additionally the physical model measurements at gauge 6 do not appear to be in accordance to the rest of the model. However, it can be seen from the other gauges that the water surface profile is in good agreement with those of the physical model except at the very front of the cylinder. Wave gauges 7 and 8 show a large peak which was not present for the numerical model, and while the water surface elevation profile is in closer agreement after the initial impact for W7 the model underestimated the water elevation at the very front of the cylinder for the entire simulation, with a difference of 0.19m after the initial runup. As in the previous runs the model underestimated the reduction in the reservoir water elevation after the initial drawdown.

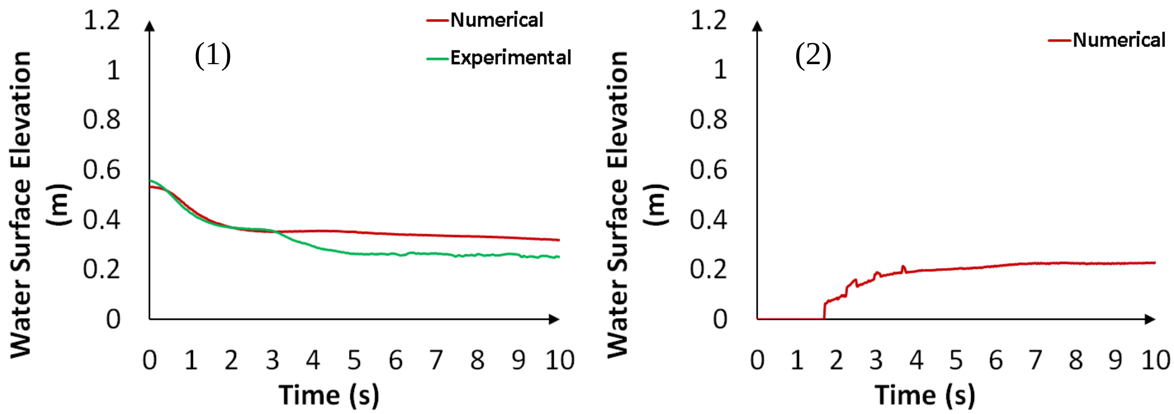

For caption see following page.

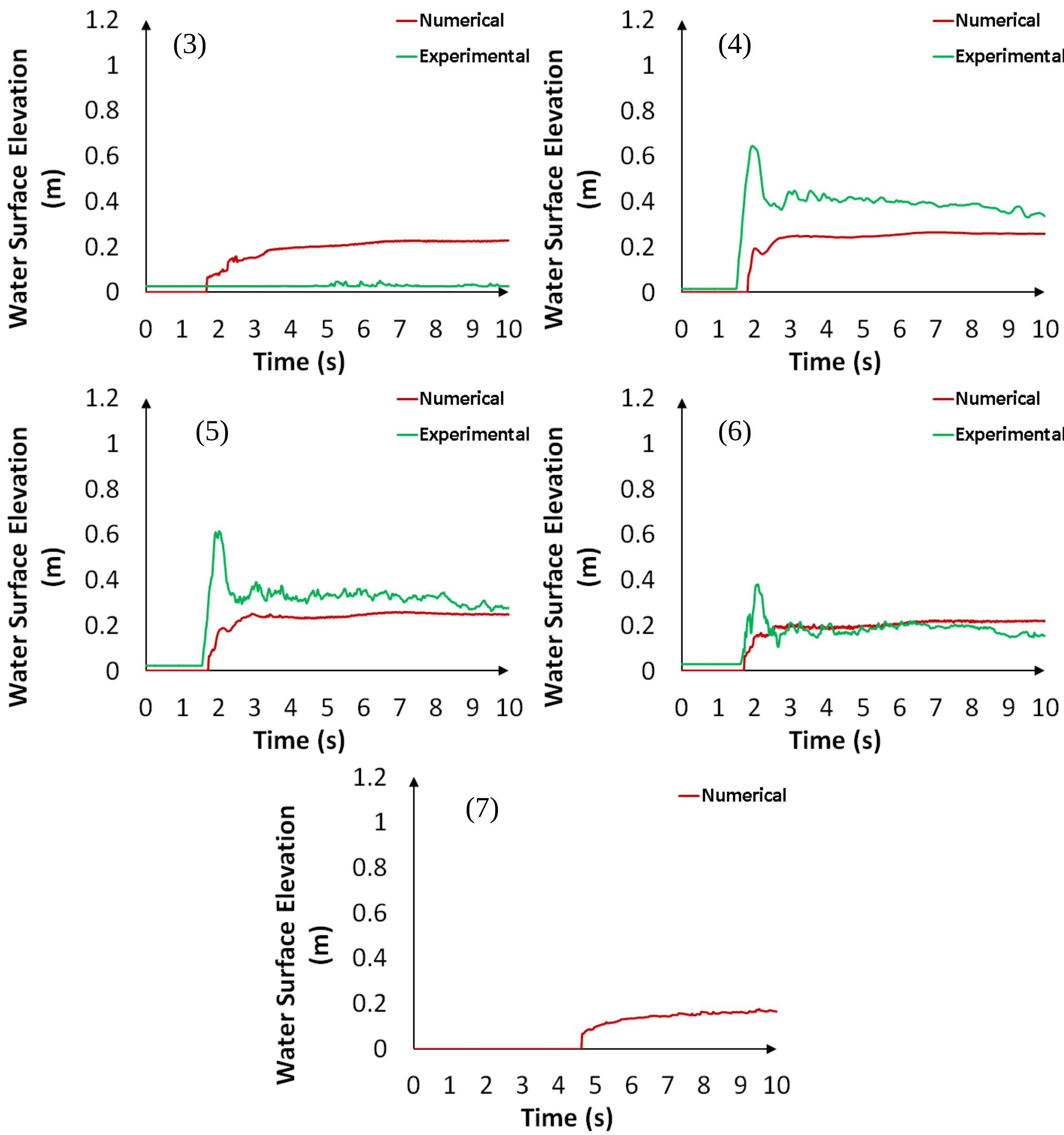

Figure 6.9 - Water surface elevation comparison for 0.55m impoundment depth at (1) W1, (2) W5, (3) W6, (4) W7, (5) W8, (6) W9, and (7) W10

0.85m Impoundment Depth

The debris used for this 0.85m impoundment depth was seen to impact close to the edge of the cylinder, shown in Figures 6.10 and 6.11. The angle of impact for the numerical experiment was found to be 78.12° perpendicular to the structure, however due to the location of its impact there was a slight rotation of the debris which result in a reduction in the runup force. When examining the physical debris impact it can be seen that the debris impacts the cylinder at a right angle and that it also is off-center, however due to the slight inward angle of the debris any rotation would be unlikely. As seen in the 0.55m impoundment test, the debris impacts the structure ahead of the water as it is pushed in front of the bore instead of on top.

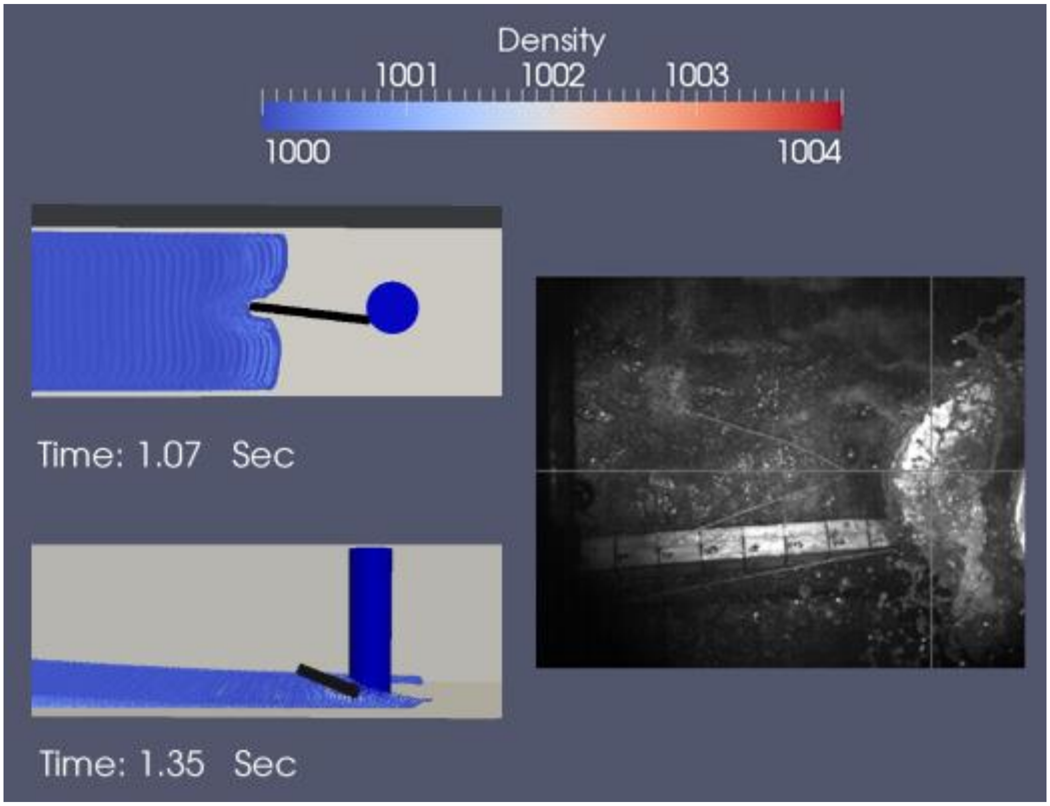

Figure 6.10- Numerical debris impact for 0.85m impoundment depth and 2kg long debris

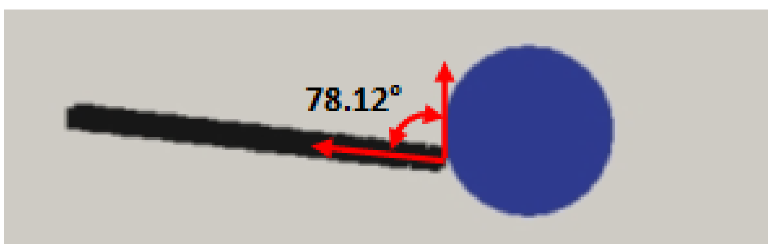

Figure 6.11 - 2kg long debris impact angle for 0.85m impoundment depth

Unfortunately, no data was currently available for the comparison of the 0.85m water depth for the 2kg long debris. The numerical water elevation results are presented in Figure 6.12.

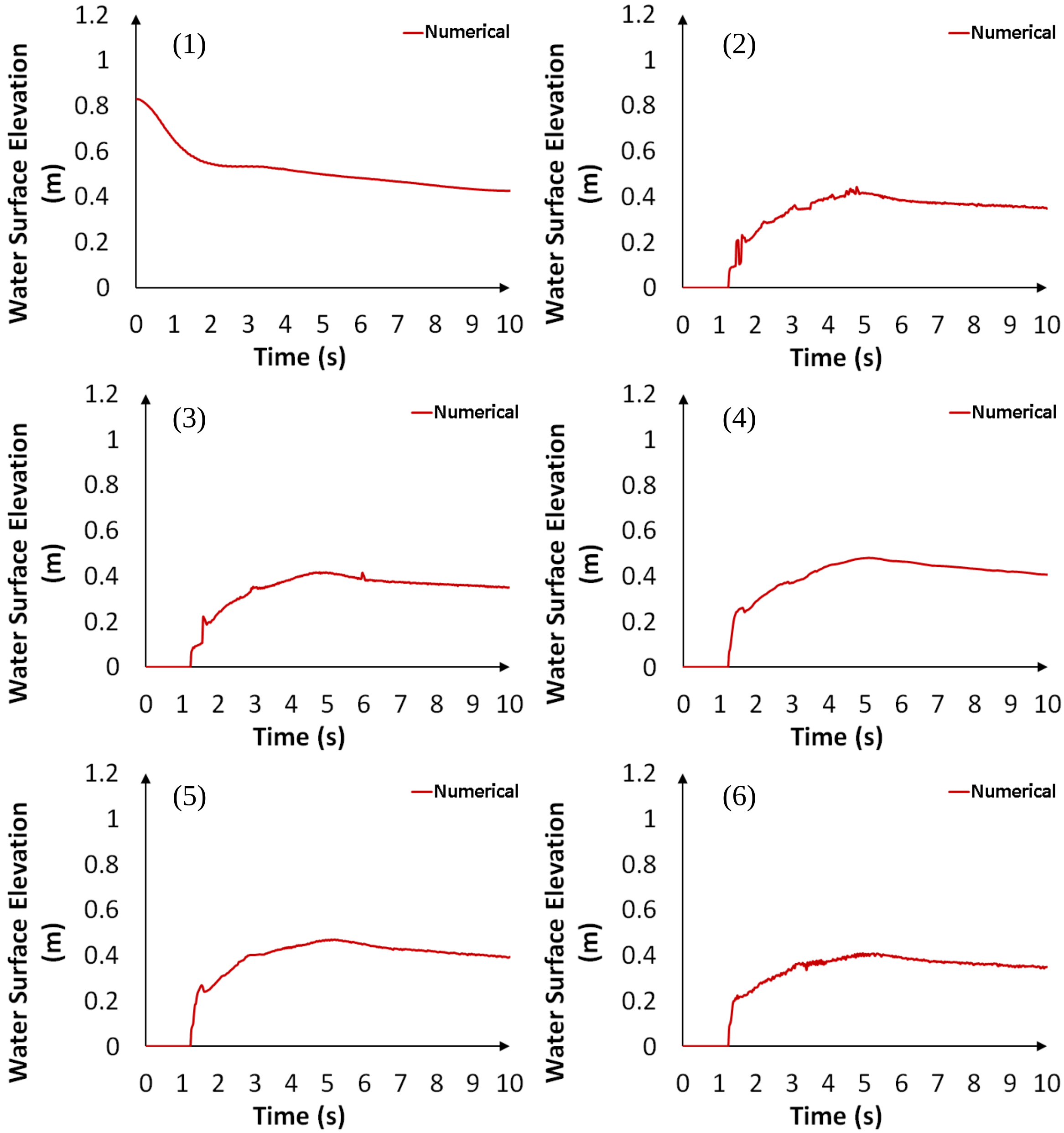

For caption see following page.

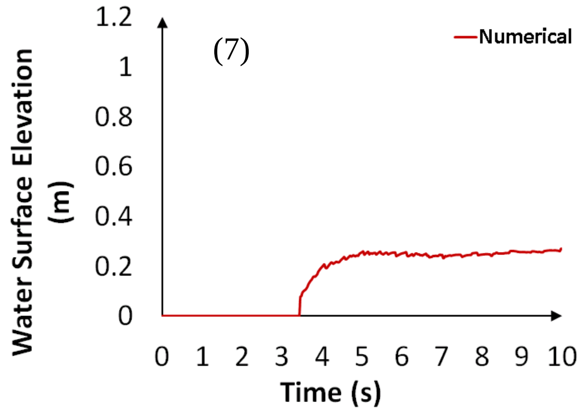

Figure 6.12 - Water surface elevation for 0.85m impoundment depth at (1) W1, (2) W5, (3) W6, (4) W7, (5) W8, (6) W9, and (7) W10

6.1.3 2 kg Wide Debris

This section shows the results of the debris impact and water surface elevation for the 0.55m and 0.85m impoundment depths for the 2kg wide debris. For this scenario no experimental results were available for comparison for the 0.85m impoundment depth and no visuals were available for either test.

0.55m Impoundment Depth

The results for the 2kg wide debris for an impoundment depth of 0.55m shows an impact angle of 81.07° in relation to the cylinder, or 8.93° from the flow direction. The time difference between the bore arrival time and the bore runup on the structure was found to be roughly 0.3s. Both the difference in the impact time of the bore and the debris and the angle of impact would have an effect on the water surface elevation profile at the structure, and would affect the impact force acting on the cylinder. No rotation of the debris occurred upon impact. As mentioned previously no visuals were available from comparison from the physical experiment.

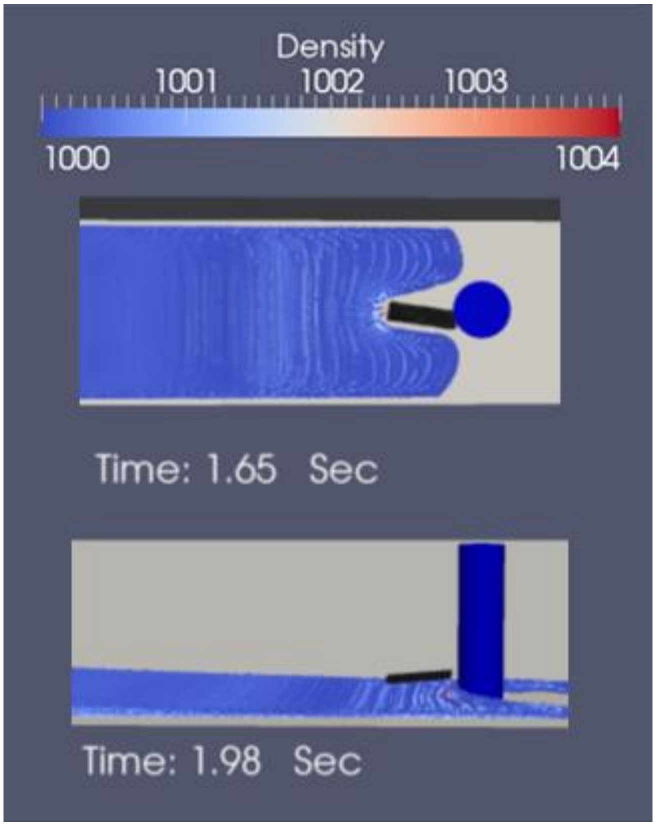

Figure 6.13 - Numerical debris impact for 0.55m impoundment depth and 2kg wide debris

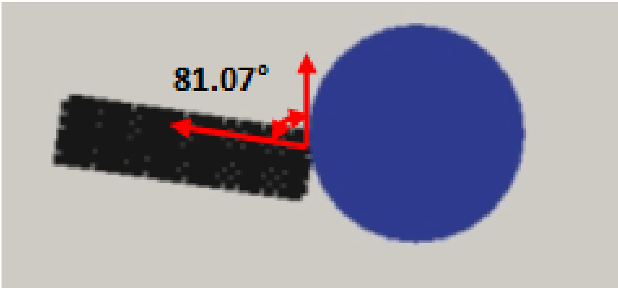

Figure 6.14 - 2kg wide debris impact angle for 0.55m impoundment depth

Similar to Section 6.1.2 no water surface elevation measurements were obtained for wave gauges 5 and 10. However it can be seen from the other gauges that the water surface profile is in good agreement with those of the physical model except at the front of the cylinder. Wave gauges 7, 8 and 9 show large peaks which was not present for the numerical model, and while the water surface elevation profile is in closer agreement after the initial impact for gauges 8 and 9 the model underestimates the water elevation at the very front of the cylinder for the entire simulation (Fig. 6.15(4)). As in the previous scenarios, the model over estimates the reduction in the reservoir water elevation after the initial drawdown.

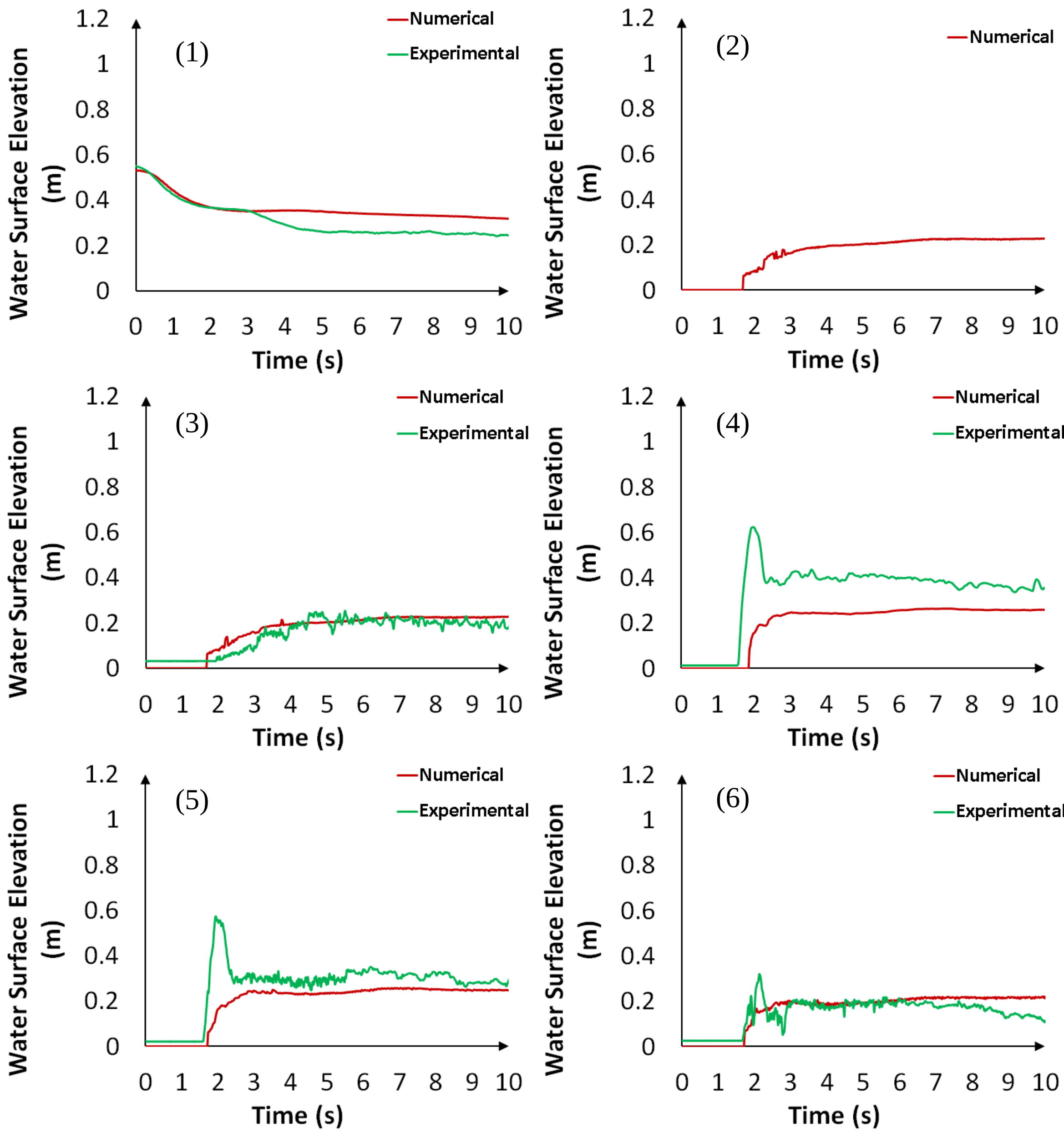

For caption see following page.

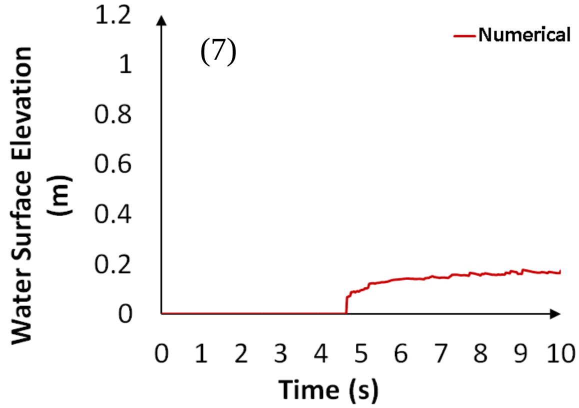

Figure 6.15 - Water surface elevation comparison for 0.55m impoundment depth at (1) W1, (2) W5, (3) W6, (4) W7, (5) W8, (6) W9, AND (7) W10

0.85m Impoundment Depth

No visual results were available for the 0.85m impoundment depth for the comparison of the debris impact location and angle. The 2kg wide numerically modeled debris impacted the cylinder at an angle of 80.71° in relation to the cylinder. The time difference between the impact of the debris and the runup of the bore on the structure, shown in Figure 6.16, was found to be roughly 0.2s. The location of the debris impact was off-center on the cylinder, however the impact time was very short and no rotation of the debris occurred.

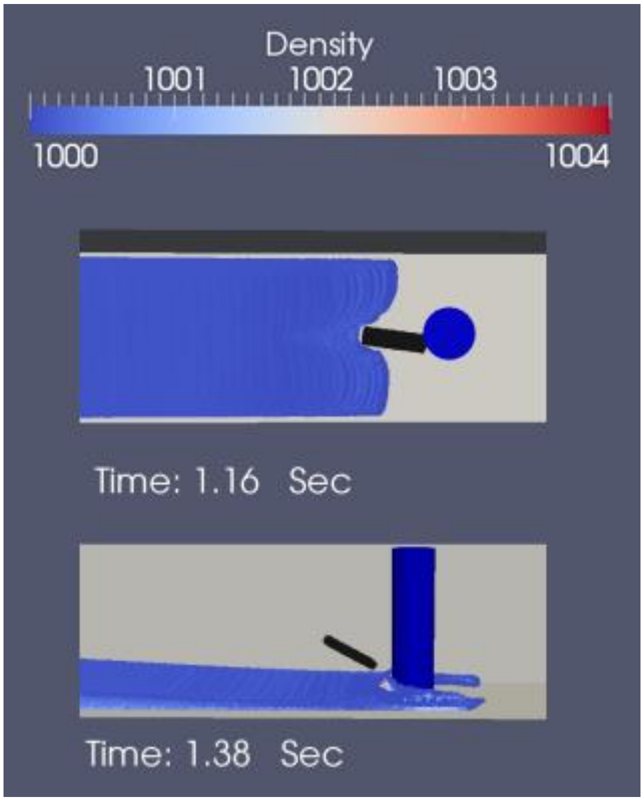

Figure 6.16 - Numerical debris impact for 0.85m impoundment depth and 2kg wide debris

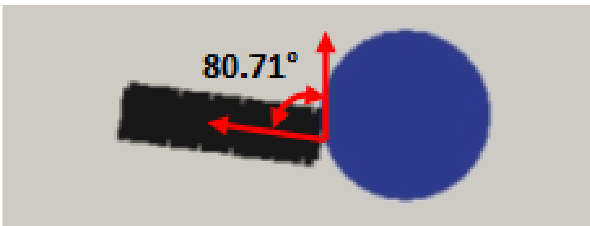

Figure 6.17 - 2kg wide debris impact angle for 0.85m impoundment depth

No data was currently available for the comparison of the 0.85m water depth for the 2kg wide debris. The numerical results are presented in Figure 6.18.

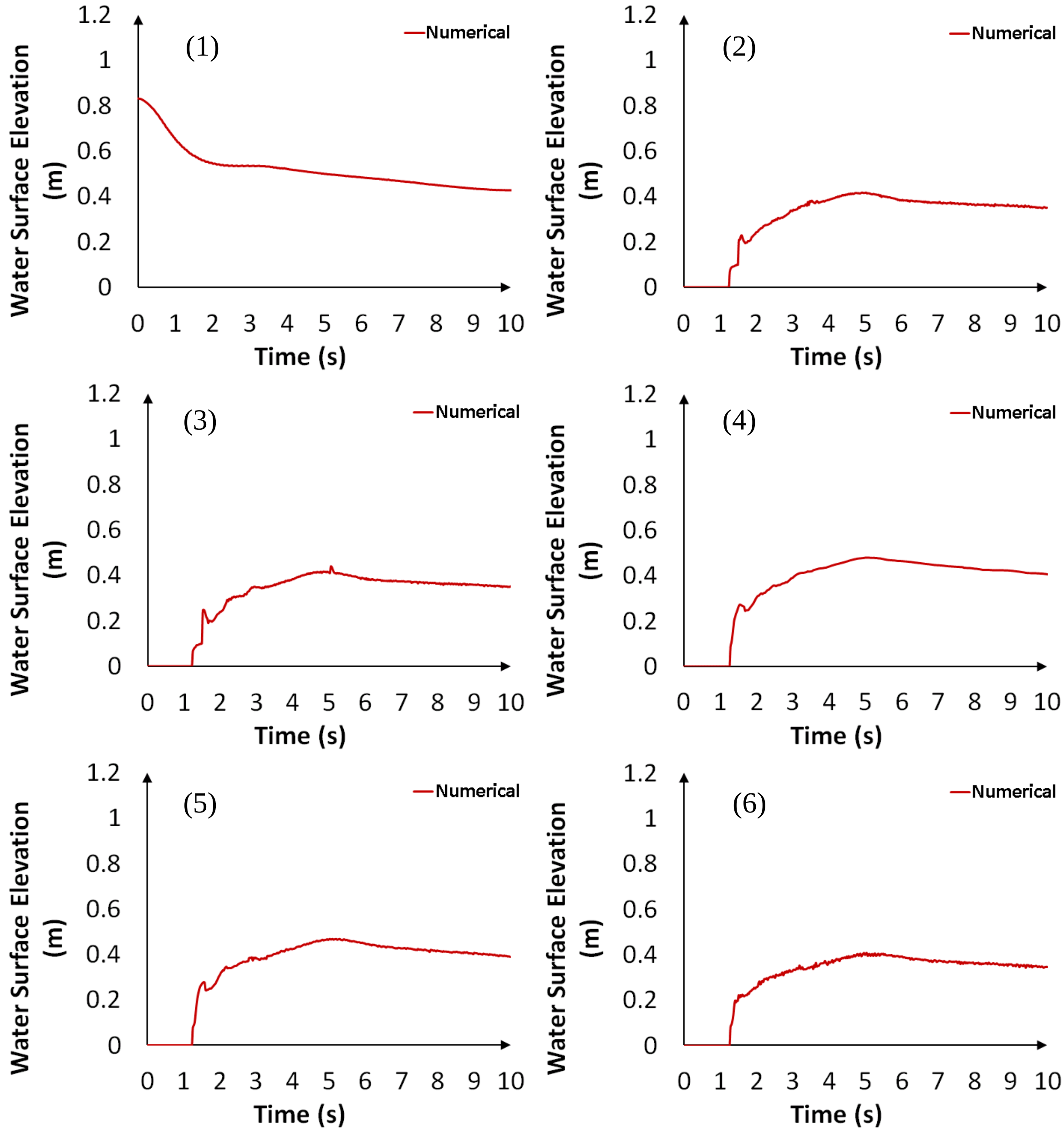

For caption see following page.

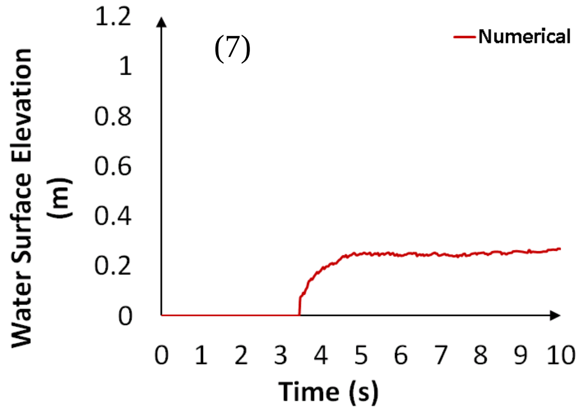

Figure 6.18 - Water surface elevation comparison for 0.85m impoundment depth at (1) W1, (2) W5, (3) W6, (4) W7, (5) W8, (6) W9, and (7) W10

6.2 Impact Force

The hydrodynamic impact force of the bore and the debris impact force were calculated separately for the numerical model and then combined for comparison with the impact force of the physical experiment. In order to accurately assess the impact force of the debris a comparison with the model visuals was completed in order to remove any impact forces caused by the walls or bottom of the numerical domain.

6.2.1 Debris Impact Approximation

The post-processing code used to determine the impact forces acting on the structure is based on the impulse-momentum principle as mentioned in Section 4.3.4 In order to achieve a good approximation using this method an accurate estimation on the stopping time of the debris is necessary. This estimation represents the amount of time required for the debris to impact the structure and come to a complete stop which is denoted by a peak in the impact force, this is also called the rise time of the force. The experimental results provided a rise time of 0.004s to 0.005s for all experimental runs. Unfortunately, the numerical model was run using an output time step of 0.025s which would result in artificially lowered forces acting on the structure, should this be used as the rise time.

In order to assess the impact of the rise time on obtaining accurate debris force estimations the model was run using different output time steps for 2s for the 0.55m impoundment depth with 1.088kg debris. An analysis was completed to determine the sensitivity of the impact force to different numerical output time steps (s) should this time step be used as the impact force rise time. Another analysis was completed to determine if the impact force could be obtained for a model with a larger output time step, by artificially lowering the rise time in the post-processing code, see Figure 6.20.

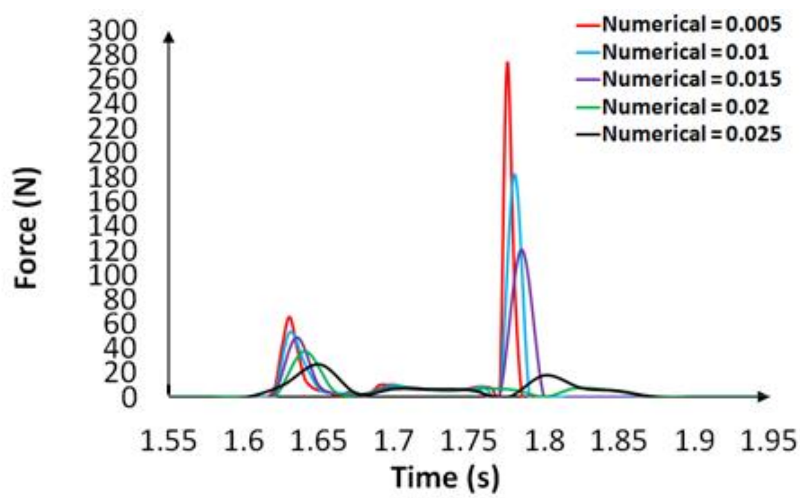

Figure 6.19 – Sampling frequency impact on the debris force

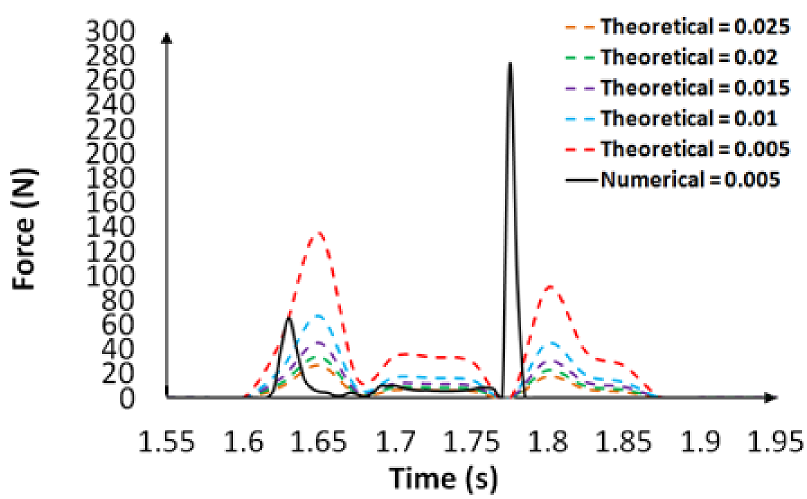

Figure 6.20- Impact of artificially lowered debris stopping time on the debris impact force

This run was selected due to the prolonged debris impact time which included two peak forces acting on the structure. From Figure 6.19 it can be seen for the initial impact that the larger sampling frequencies did not result in a large change in the impact force; however, for the secondary impact there is a large difference in the impact force when using smaller sampling frequencies. Ideally, to obtain the most accurate results a very high sampling frequency would be required which is not always feasible. Figure 6.20 indicates that the impact force results obtained for the higher output frequency may be reproduced if the correct debris stopping time is known. For the initial impact of the debris a stopping time of 0.01s corresponds well with the forces obtained in the high frequency model; however for the second impact it can be seen that all of the models miss the peak impact. The value obtained corresponds very well to the tail end of the impact force; however it appears that the impact occurred too fast for the lower frequency model to obtain the correct estimation of the force.

The results from this analysis indicate that the only method for consistently obtaining accurate estimations of the debris impact forces for the model would be to use a very small output time step as this model does not support variable time steps. This is not plausible for large-scale models or for models which run for a long duration as it would result in an unreasonable amount of output files and would increase the simulation time, as shown in Table 6.1. It also indicates that it is possible to approximate the impact force from a model with a smaller output frequency, but that this requires the knowledge of the force rise time which will vary based on the location and angle of impact and on the mass of the debris.

Table 6.1 - Simulation time based on output frequency for 2 second simulation time (0.55m 1.088kg debris)

Simulation Output Time Step (s)	Simulation Run Time (hrs)
0.025	1.13
0.02	1.70
0.015	1.63
0.01	1.85
0.005	5.20

The numerical model was run for the debris impact for each of the simulations presented in this section at an output time step of 0.005s. The approximated forces from the model with a larger output time step and numerical impact forces for the smaller time step are presented in Table 6.2. The rise time used for the theoretical impact forces were based on those obtained from the visual results when available; these appeared to correspond fairly well with those of the numerically estimated rise times.

The results in Table 6.2 show that there is relatively good agreement for the tests between the theoretically calculated impact forces for the model with a larger output time step and the model impact forces with a smaller time step. This indicates that should the rise time of the debris impact be known it would be possible to obtain the impact force based on the post-processing code without being required to reduce the model output time step. It can be difficult to determine an accurate stopping time from the data as the start of the impact may be slightly subjective, and error in the estimation can result in large changes in the approximated force. Since the rise times were approximated to an interval of 0.005s some error is present as the actual rise time may be in between. In general the difference in the calculated forces was typically around 50N or less; however, two cases did show significantly higher values which indicates that either the difference in the rise time was too large, or only the tail end of the impact was captured as the impact duration was too quick. Improvement could be made by increasing the rise time by a smaller interval as this would give more accurate estimations. It is also possible that the high frequency model impact force did not capture the true peak force due to the output interval.

Table 6.2 - Model forces and errors in the approximation of the impact forces for an artificially reduced time step

Run	Model Impact Force (N)	Numerical/ Visual Rise Time (s)	Theoretical Impact Force (N)	Absolute Error (%)	Force Difference (N)
0.55m 1kg (Impact 1)	65.59	0.01/ 0.01	67.47	2.87	1.88
0.55m 1kg (Impact 2)	272.81	0.005 / unknown	90.44	66.85	182.37
0.55m 2kg long	279.93	0.01/ 0.015	229.67	17.95	50.26
0.55 2kg wide	251.7	0.015 / 0.01	301.058	19.61	49.36
0.85 1kg (Impact 1)	187.71	0.005 / 0.005	186.56	0.62	1.15
0.85 1kg (Impact 2)	175.15	0.01/ 0.01	188.62	7.69	13.47
0.85m 2kg long	314.12	0.01 / 0.01	283.66	9.70	30.46
0.85m 2kg wide	788.07	0.01/ 0.005	1187.09	50.49	398.283

6.2.2 1 kg Debris

The debris impact force for the 0.55m impoundment depth for the first 5 seconds of the model as it traveled through the domain is shown in Figure 6.21 along with visuals corresponding to the debris impact forces. In order to assess the actual impact on the cylinder and the impacts on the bottom and sides of the domain an analysis was performed and the extraneous data was removed. The final debris impact force can be seen in Figure 6.22, where the different stopping time for the impacts was accounted for. As previously mentioned, multiple spikes in the impact force were observed indicating that the debris contact with the structure was not maintained between the impacts. It is shown in the forces that the second impact is larger than the initial impact force on the cylinder. The debris impact forces were based on the theoretical impact method shown in Section 6.2.1, using rise time approximation shown in Table 6.2

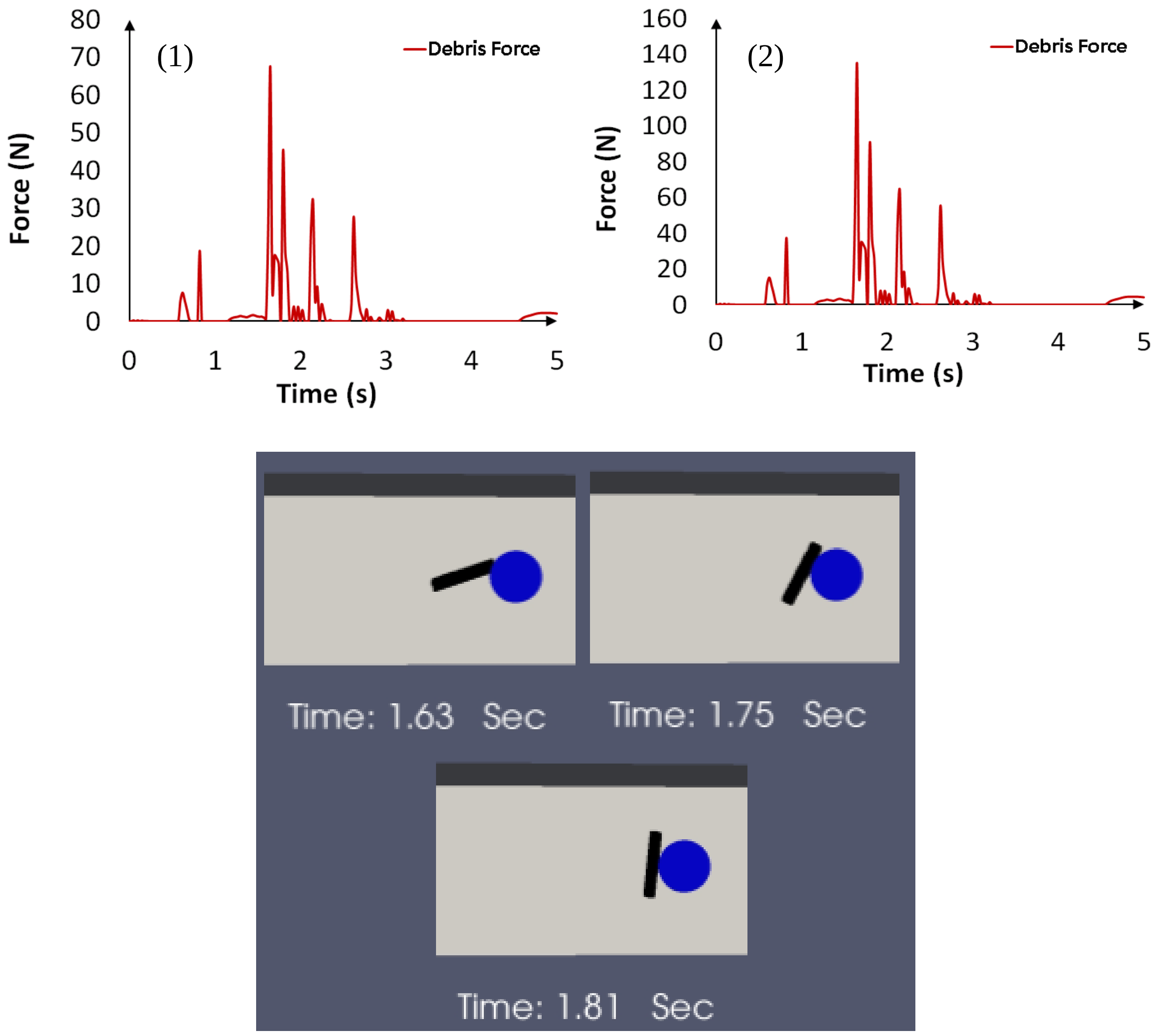

Figure 6.21 - Initial debris impact force results for the 0.55m impoundment depth for a stopping time of (1) 0.01s and (2) 0.005s

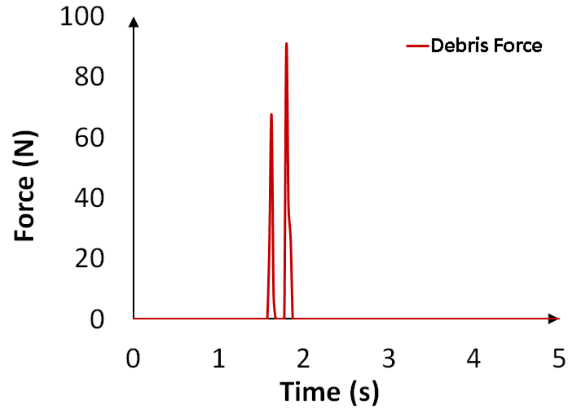

Figure 6.22 - Corrected debris impact force for the 0.55m impoundment depth

From Figure 6.23 it can be seen that the largest contribution to the impact force is from the bore impact as opposed to the debris.

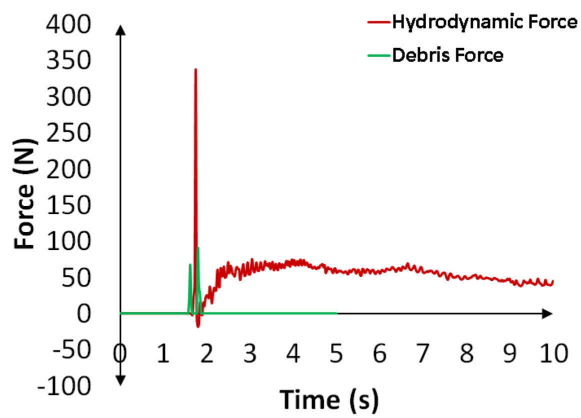

Figure 6.23 - Hydrodynamic and debris impact loading on the cylinder for the 0.55m impoundment depth

The combination of the corrected debris impact force and the hydrodynamic force gives the total forces acting on the structure, which can then be compared to that of the physical experiments. The comparison between the physical and numerical impact loads indicates that the numerical model was not able to reproduce the large initial impact force found in the physical model. However, it was found to model the remaining bore force with better accuracy, but can be seen to underestimate the force as the time-history continues.

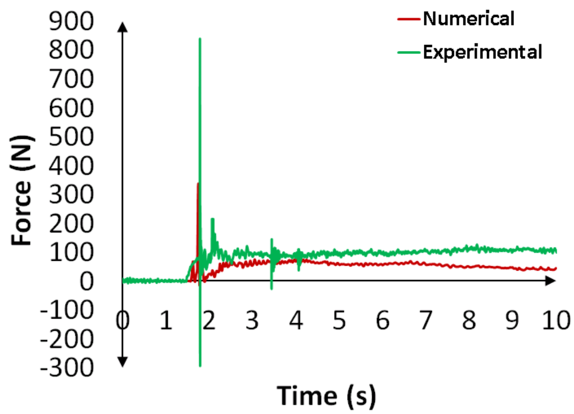

Figure 6.24 - Numerical and experimental comparison of the impact loading on the cylinder for the 0.55m impoundment depth

The discrepancy between the numerical and experimental peak impact forces may be caused by the location of impact on the structure as well as the rotation it undergoes in the numerical model. The increasing difference in the impact force beginning at a time of 4.5s is believed to correspond with the presence of water behind the pier, shown in Fig. 6.3(7), which was not present in the physical experiments.

The corrected debris impact and the hydrodynamic force for the 0.85m impoundment depth are shown in Figure 6.25. When compared to the model forces determined by Al-Faesly *et al.*, shown in Figure 6.26, it can be seen that the numerically modeled force is in much better agreement with the experimental force when compared to the 0.55m impoundment depth. The initial impact force was underestimated; however, the bore hydrodynamic force for the remainder of the model is in fairly good agreement with the experimental data.

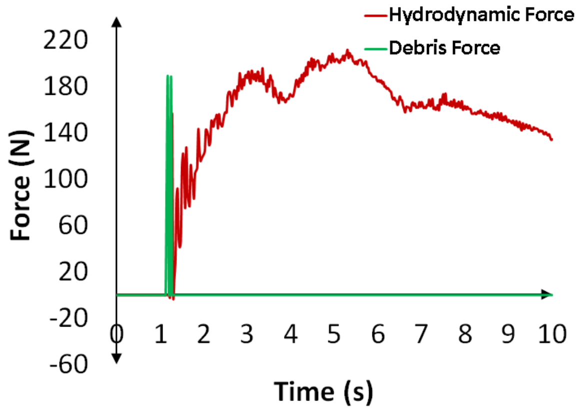

Figure 6.25 - Debris impact and hydrodynamic force for a 0.85m impoundment depth

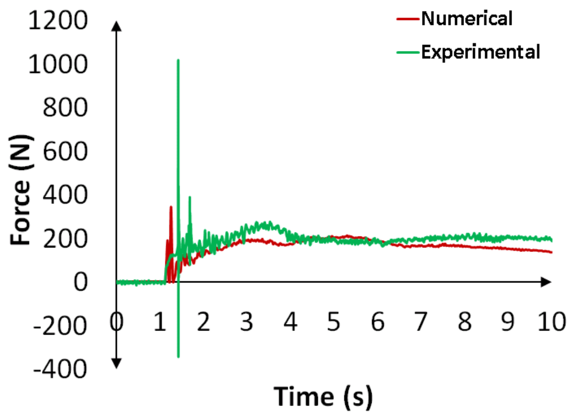

Figure 6.26 - Numerical and experimental comparison of the impact loading on the cylinder for a 0.85m impoundment depth

Similar to the 0.55m water depth scenario, the second impact of the numerical model debris did not impact the cylinder at a right angle which would reduce the impact force.

The cylinder used in the numerical models was a rigid structure which was not able to deform from the impact of the debris, the same can be said about the debris used in the model. However, the cylinder in the physical model experienced acceleration in the flow direction upon being impacted with the debris and the hydraulic bore. The acceleration of the cylinder, shown in Figure 6.27 would result in the absorption of some of the impact force.

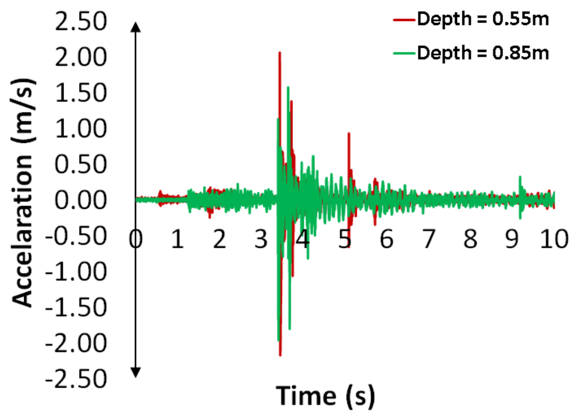

Figure 6.27 - Acceleration of the cylinder for the 0.55m and 0.85m impoundment depths

6.2.3 2kg Long Debris

The corrected debris impact and the hydrodynamic force for the 0.55m impoundment depth are shown in Figure 6.28. The debris impact force occurred almost a full 0.2s before the bore impact which means that the peak impact force on the cylinder is separated into two separate peaks. When compared to the experimental force on the cylinder the peak impact force is significantly lower. The remaining hydrodynamic force of the bore is similar to that of the 1.088kg debris with the numerical model underestimating the bore force progressively more as the time-history continues with a maximum difference in the order of 70 N. As mentioned in Section 6.2.2 this is believed to be due to the presence of the water behind the cylinder, which does appear to have been there for the physical experiment, as they correspond in time.

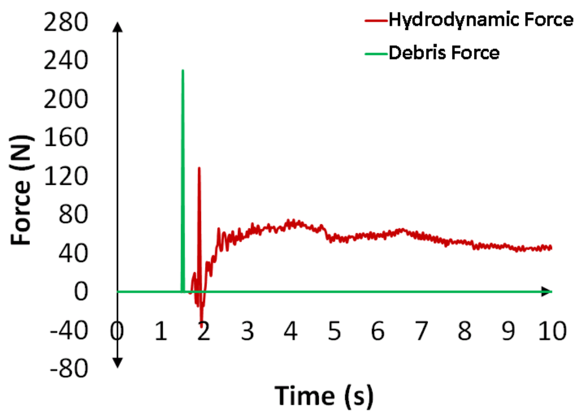

Figure 6.28 - Debris impact and hydrodynamic force for an impoundment depth of 0.55m

The rise time of the impact force on the structure was 0.015s compared with the much smaller rise time of the physical model. Accounting for the difference in the debris stopping time would result in threefold increase in the impact force. However, even with this accommodation the numerical model would still underestimate the impact force by over 500N.

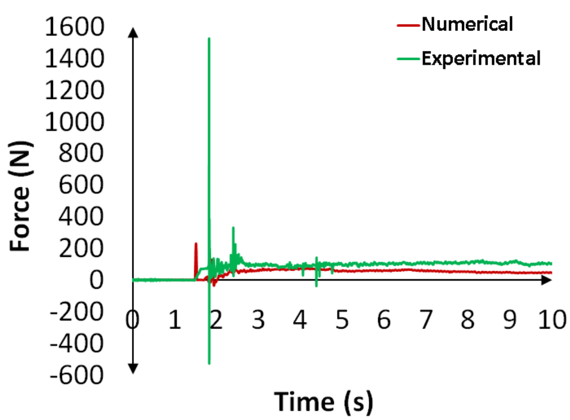

Figure 6.29 - Numerical and experimental comparison of the impact loading on the cylinder for a 0.55m impoundment depth

The corrected debris impact and the hydrodynamic force for the 0.85m impoundment depth are shown in Figure 6.30. For this run the debris impact force was higher than for the previous runs, however the impact still occurred before the bore impacts the cylinder.

Unfortunately, the forces on the structure could not be compared with experimental results as those were not available at this time.

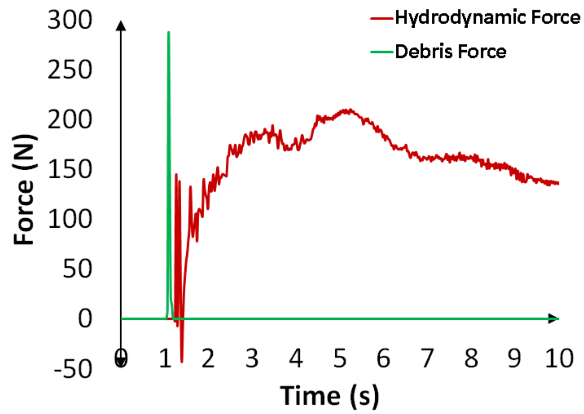

Figure 6.30 - Debris impact and hydrodynamic force for an impoundment depth of 0.85m

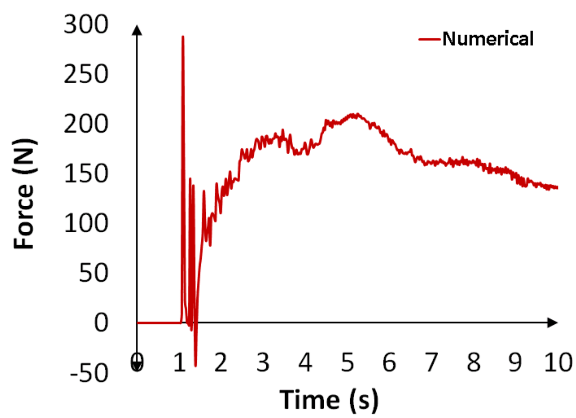

Figure 6.31 - Numerical impact loading on the cylinder for a 0.85m impoundment depth

6.2.4 2 kg Wide Debris

The corrected debris impact and the hydrodynamic force for the 0.55m impoundment depth are shown in Figure 6.32. When compared to the model forces determined by Al-Faesly *et al.*, shown in Figure 6.33, it can be seen that the debris impact force is underestimated and that the model initially gives good agreement for the hydrodynamic force but then underestimates the force as the time-history continues.

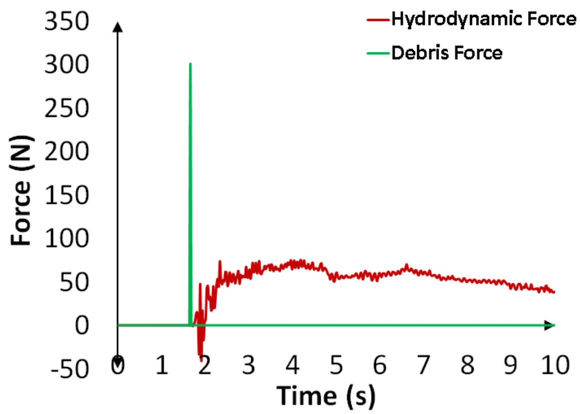

Figure 6.32 - Debris impact and hydrodynamic force for an impoundment depth of 0.55m

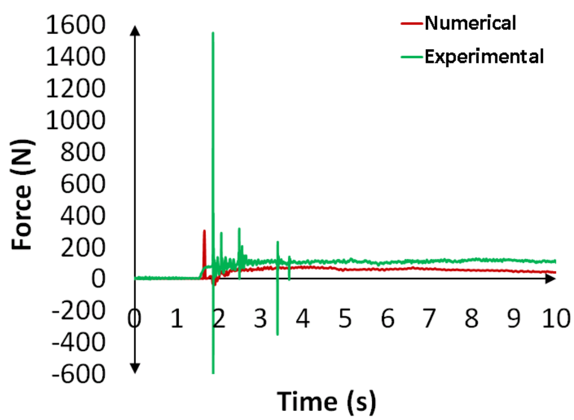

Figure 6.33 - Numerical and physical comparison of the impact loading on the cylinder for a 0.55m impoundment depth

The corrected debris impact and the hydrodynamic force for the 0.85m impoundment depth are shown in Figure 6.34. Unfortunately, the forces on the cylinder could not be compared with experimental results as those were not available at this time.

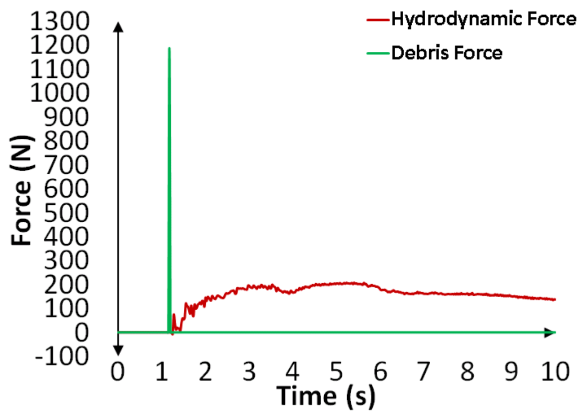

Figure 6.34 - Debris impact and hydrodynamic force for an impoundment depth of 0.85m

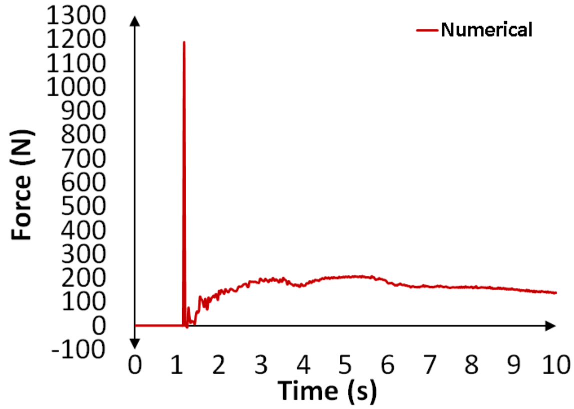

Figure 6.35 - Numerical impact loading on the cylinder for a 0.85m impoundment depth

6.3 Influence of Bed Condition

The influence of the bed condition was tested for two runs; with 2.191kg long debris and impoundment depths of 0.55m and 0.85m. The purpose of this test was to determine the effect of the wet bed on the water surface elevation, the forces on the structure and on the movement of the debris as it impacts the structure as the physical experiments were performed under wet bed conditions. The bed was simulated at the smallest depth possible, which was similar to that seen in some areas of the physical model. However, it should be noted that in the physical model the wet bed was not consistent across the flume as modeled in the numerical simulation.

0.55m Impoundment Depth

The results of the water surface elevation comparison between the wet and dry bed tests indicate that the bed condition has a significant impact on the arrival time of the bore at the different gauges. In all of the cases, excluding the gauge behind the cylinder, the use of a wet bed condition resulted in a delay of the bore arrival of over 1 second. Additionally, from the figures it can be seen that the bore propagating over the wet bed resulted in an increased water surface elevation starting at a time of 5.5s, and that the arrival of the bore in front of the structure was not denoted by a sharp peak in the water surface elevation as with the dry bed condition.

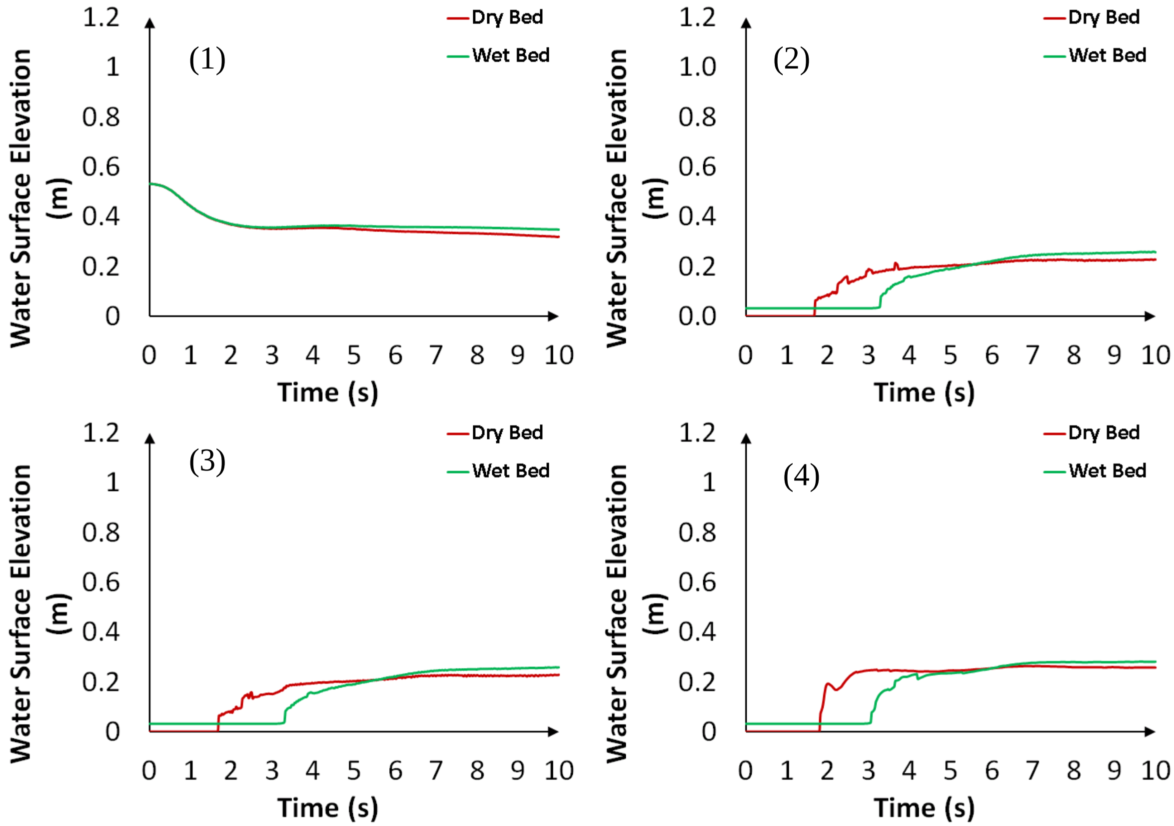

For caption see following page.

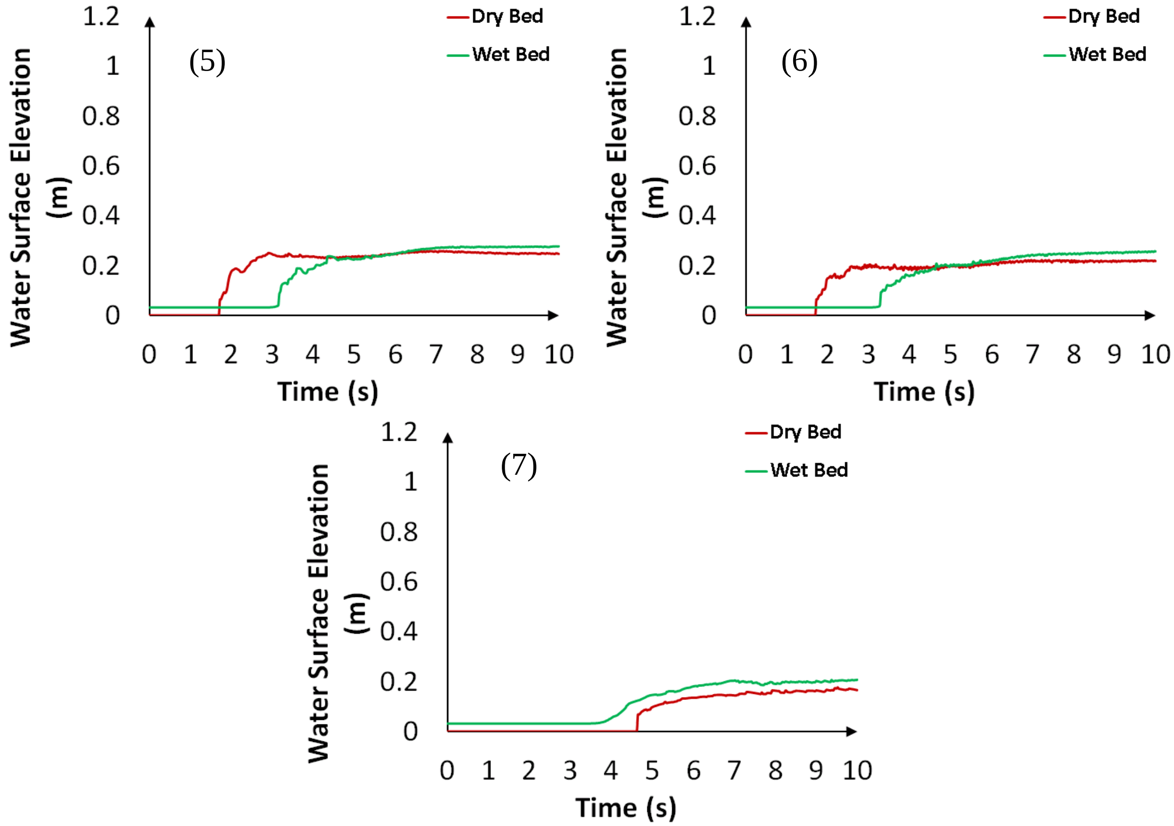

Figure 6.36 - Water surface elevation comparison for the 0.55m impoundment depth at (1) W1, (2) W5, (3) W6, (4) W7, (5) W8, (6) W9, and (7) W10

The debris impact for the wet and dry bed conditions are shown in Figure 6.37. The debris impact for the wet bed condition occured significantly later then that of the dry bed, and actually impacted the cylinder after the initial runup of the bore, as found in the physical model, contrary to the results of the dry bed. As mentioned for Figure 6.36, when examining the amount of runup that occured on the cylinder, it is evident that the wetbed did not produce the same volume of runup as with the dry bed.

The impact angle of the debris, shown in Figure 6.37, indicates a significant difference in the model debris impact location and angle. Additionally, it was found that rotation of the debris on impact occurred for the wetbed scenario which would result in a reduction on the impact forces acting the structure.

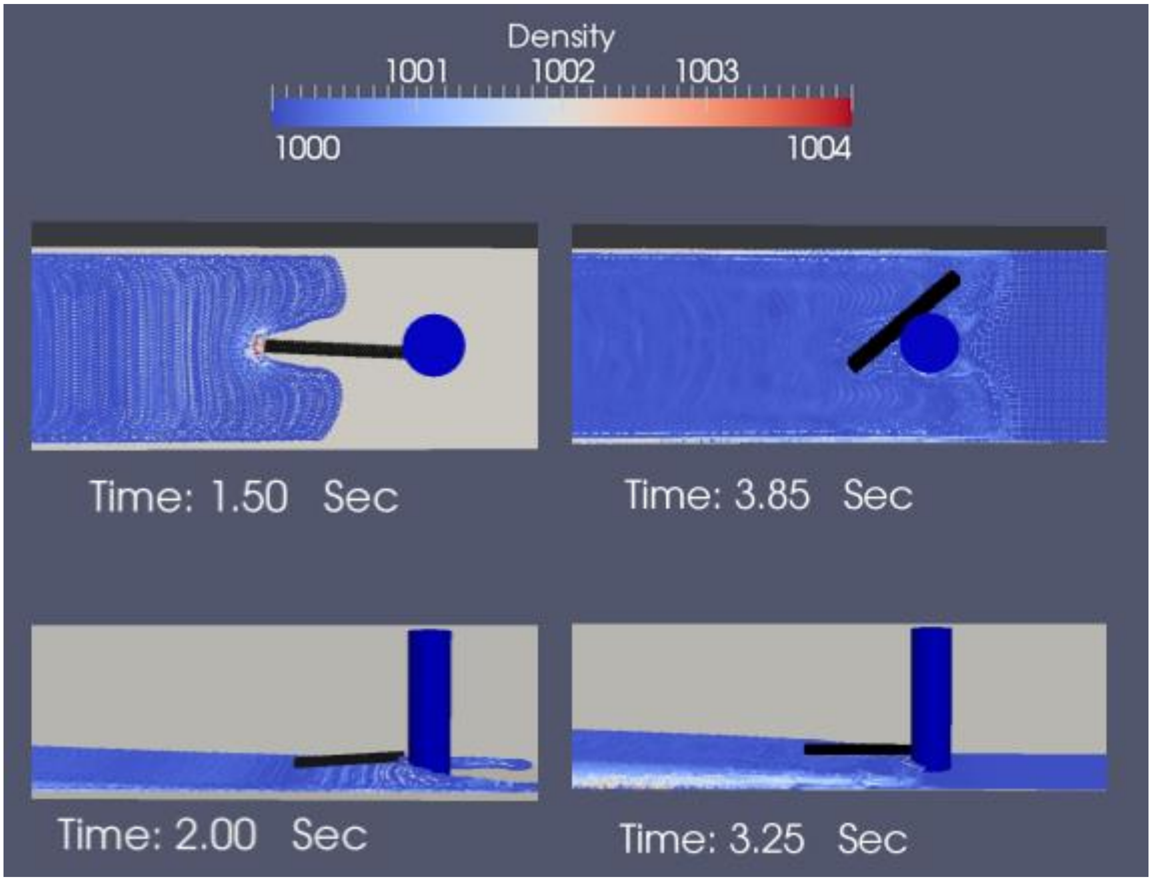

Figure 6.37- Comparison of debris impact for dry (left) and wet (right) bed conditions for 0.55m impoundment depth

The force on the structure shows an interesting trend for the wet bed test scenario. While the initial impact force is much smaller than that seen for the dry bed, the runup force on the structure is similar. The "dip" in the force, seen in both the dry and wet bed scenario at a time of 5s is much more significant for the wet bed model. Larger fluctuations in the hydrodynamic force are also present for the wet bed model following a time of 7s.

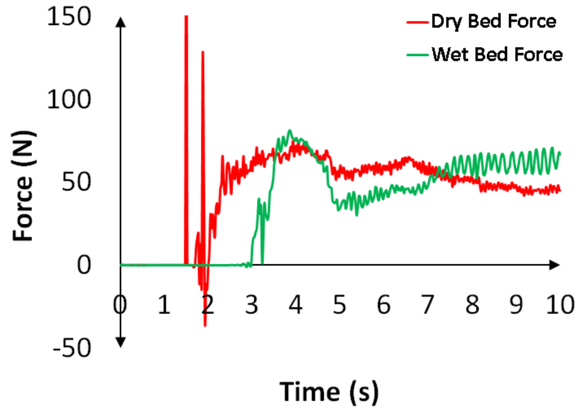

Figure 6.38 - Numerical dry and wet bed comparison of the forces on the cylinder for the 0.55m water depth

0.85m Impoundment Depth

The trends seen in for the 0.55m impoundment depth bed condition comparison were also found for the 0.85m comparison. In all cases the wet bed condition resulted in a delay in the bore arrival time, except behind the cylinder, and higher water surface elevations when compared to the dry bed condition. In contrast to the 0.55m comparison, peaks in the water surface elevation were seen for the arrival of the bore at the cylinder in all gauge locations.

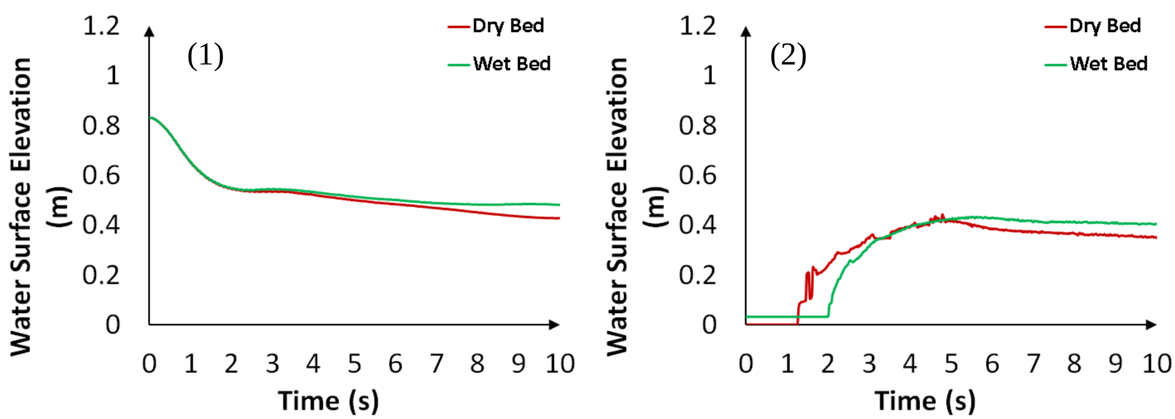

For caption see following page.

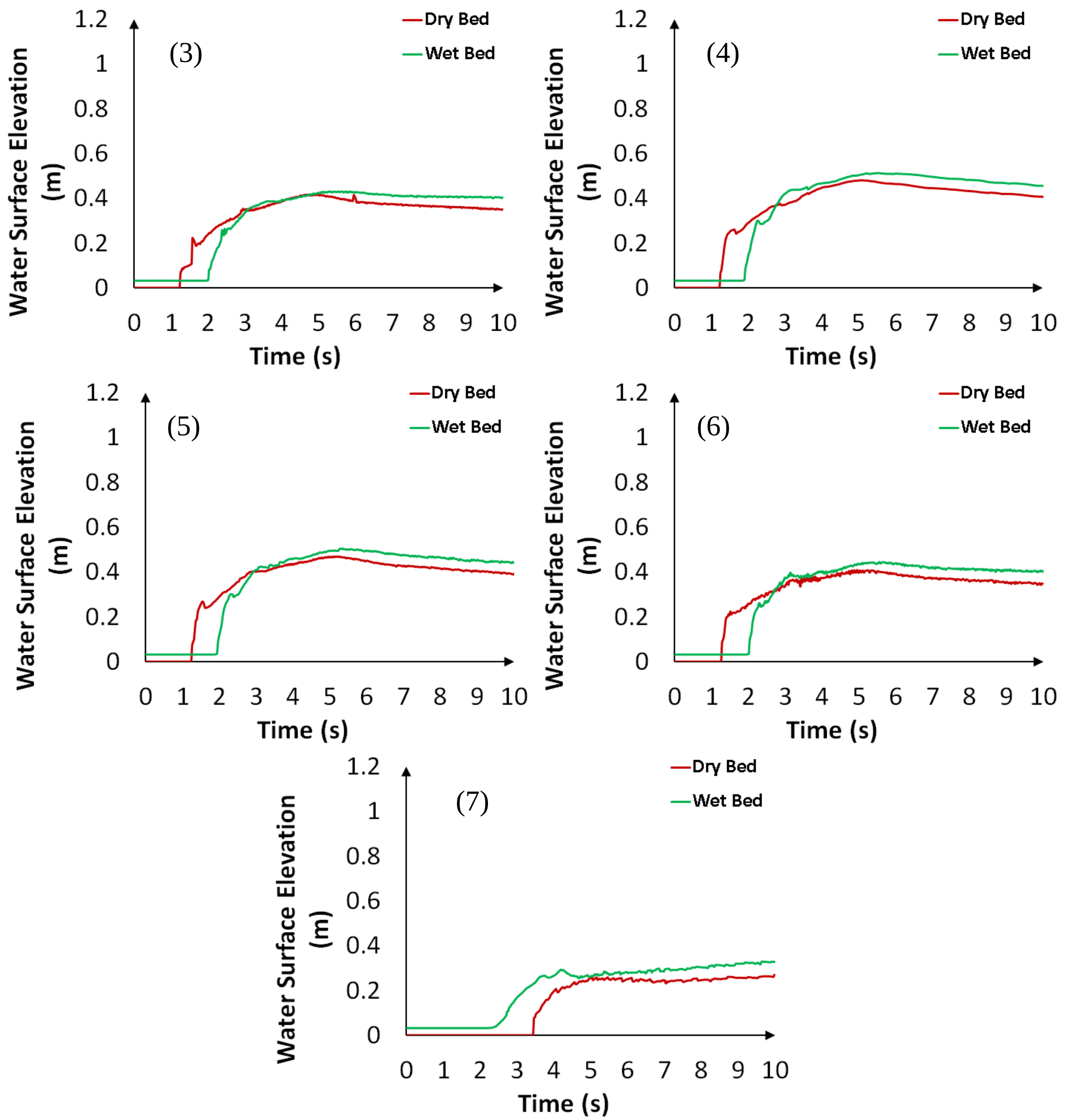

Figure 6.39 - Water surface elevation comparison for the 0.85m impoundment depth at (1) W1, (2) W5, (3) W6, (4) W7, (5) W8, (6) W9, and (7) W10

Figure 6.40 shows the comparison between the debris impact for both the wet bed and dry bed scenarios. The wet bed condition shows the debris propagating under the bore as opposed to on the bore as in the case of the lighter debris, Figure 6.37, indicating that the boundary conditions restricted the fluid from getting underneath the debris. Very little rotation occurred upon impact for the wet bed test.

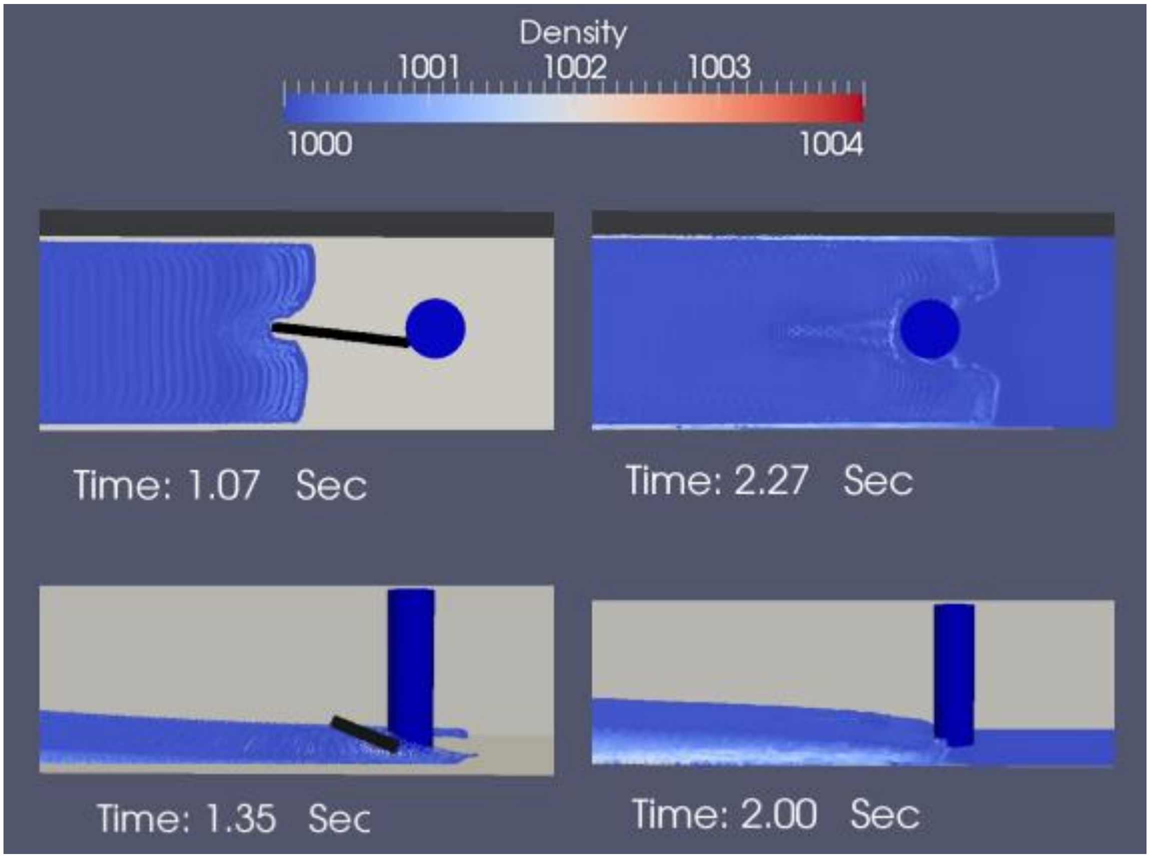

Figure 6.40- Comparison of debris impact for dry (left) and wet (right) bed conditions for the 0.85m impoundment depth

The profile of the impact forces on the structure are fairly similar for the two bed conditions, the main difference being that there is a lag in the bore arrival. When comparing the debris impact forces it can be seen that both forces are comparable, but that the wet bed force occurs after the arrival of the bore unlike the for the dry bed test. The total hydrodynamic force acting on the structure is also larger after impact.

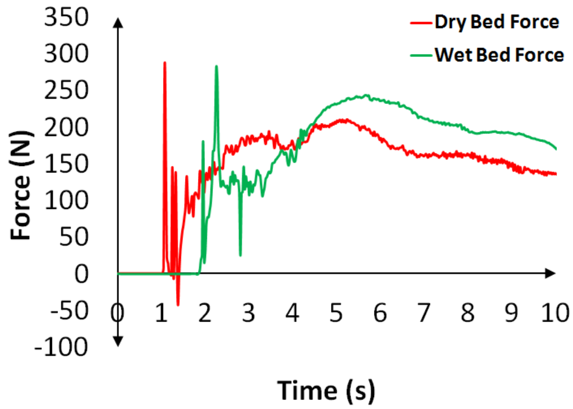

Figure 6.41 - Numerical dry and wet bed comparison of the forces on the cylinder for the 0.85m water depth

6.4 Analytical Comparison

This section shows a comparison between the analytical forces obtained from FEMA P-646 and FEMA P-55, Equations 3.12 and 3.13, respectively, with the debris forces obtained from the physical and numerical experimental studies. Based on FEMA P-55 under the assumption of zone V and no upstream screening, the coefficients C_D and C_B were both taken as 1.0. The building structure coefficient was selected to be 0.8 to represent reinforced concrete foundation walls, alternative values would have been 0.4 or 0.2 for concrete pile and timber pile/masonry columns, respectively. The estimated force was based on the measured debris velocity which ranged from 2.35m/s to 4.41m/s, which has a larger range of velocities when compared to those of Al-Faesly.

For FEMA P-646 the hydrodynamic mass coefficient, *c* which represents the effect of the fluid in motion with the debris was taken to be 0 based on Haehnal and Daly [2002]. The effectives combined stiffness of the debris and structure was based on those obtained in the physical experiment for Al-Faesly. The results for this method are similar to those obtained in the physical experiment but are significantly larger than those obtained in the numerical model.

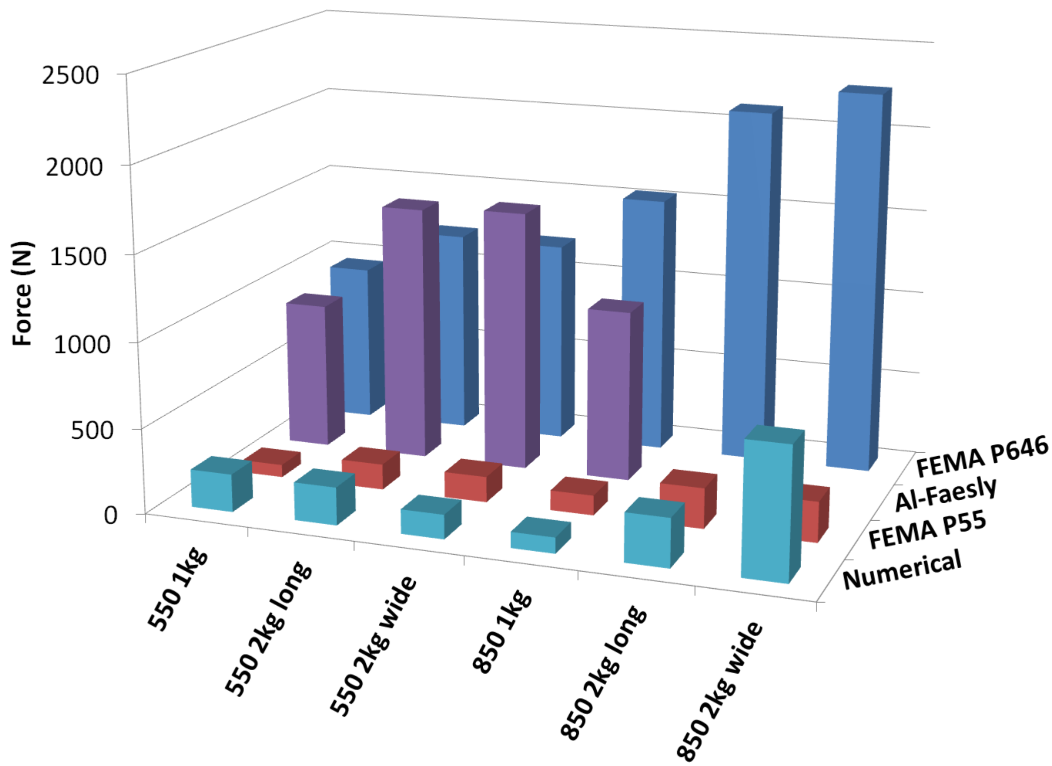

Figure 6.42- Analytical comparison of debris impact force

The large difference between the physical and numerical experiments was noted in previous sections, the results in Figure 6.42 show only the debris impact for the numerical results while the physical impact forces also take into consideration the bore impact on the structure. This does not account for the large difference between the FEMA estimations however.

6.5 Discussion

This chapter examined the validation of the numerical model against the physical experiments performed by Al-Faesly [2013] for the propagation and impact of debris on a free-standing cylindrical structure. The purpose of this chapter was to examine the numerical models ability to replicate the water surface elevation, hydrodynamic forces and debris impact forces obtained in the experiment, and to determine if the model is able to replicate the movement of the debris. It was found that the model was able to reproduce the water surface elevation of the bore with some accuracy except at the front of the cylinder, which may have been caused by the presence of the debris, and at the moment of impact. The model was able to reproduce the impact location and angle of the debris on the cylinder fairly well, but it was found that the debris was pushed in front of the bore as opposed to on the bore as in the physical experiment. Adjustment in the initial placement of the debris did not fix this problem, however the use of a wet bed condition did. This was believed to be caused by the boundary condition which forces the bore to travel around the debris instead of lifting it up, and by the lack of inertia in the initial debris movement for the dry bed runs.

It was evident from the results that the peak debris impact force was smaller than that found in the physical experiments. Some of the differences in the peak impact force can be attributed to the rise time of the force on the structure. It was noted that for the physical model the rise time was constant at roughly 0.004s to 0.005s, while for the numerical model the rise time was typically closer to 0.01s or 0.015s due to the rotation of the debris. The arrival of the debris before the bore would affect the impact force as well; the physical model impact force included both the hydrodynamic force already acting on the structure which was not present for the numerical model. However, even with these differences the numerical model may not unable to capture the full impact force of the debris on the structure.

When comparing the impact of a wet bed condition on the propagation of both the debris and the bore it was clear that the presence of the wet bed results in the delay of the bore arrival at the cylinder. Additionally it was found that the initial peak impact force was smaller for the wet bed condition for the 0.55m impoundment depth and the runup force on the model was higher; similarly the water surface elevation was also higher after the bore front had passed. From the analytical comparison it was found that the results of FEMA P-55 appeared to agree with the debris impact forces found in the numerical model, while the results of FEMA P-646 were in better agreement with those of the physical model.

7 Effect of Position on Debris Movement and Impact Forces

This chapter examines the movement and impacts of a wooden log as it travels through a coastal forest during the runup of a tsunami-induced bore as seen in Chapter 5. This setup was examined for an initial still-water elevation of 2.25m only and was tested for both vertical and horizontal debris. While debris would naturally be orientated in the horizontal position along the ground the objective of this test was also to examine the movement of a tree should it be uprooted or broken by the tsunami bore. Unfortunately, as shown in the following sections, the modeled floating object was unable to remain upright due to the sloped bed of the model. In addition to the impact of the debris on the coastal forest, the movement of the debris through the forest and up the beach slope was examined in order to determine its interaction with the bore and forest during both the runup and rundown of the bore.

7.1 Wave Propagation

This section compares the propagation of the wave with and without the floating debris. As the numerical formulation for laminar + SPS viscosity does not allow for the use of floating objects, the artificial viscosity function had to be used. This comparison also allowed for the examination of the difference in velocity and bore propagation for the different viscosity formulations used in this study.

As the coefficient for artificial viscosity is variable depending on the specific problem a small sensitivity analysis was performed in order to calibrate the model to that of Chapter 5 which used the laminar + SPS viscosity term. The calibration runs were completed for 15s only, as opposed to the 25s used for the full run. It was found that an artificial viscosity coefficient of 0.01 was able to approximate the runup achieved for the reference scenario with 2 trees / row and 2 rows. The runup shown in Figure 7.1 indicates that the artificial viscosity coefficient was able to replicate the runup obtained for the simulations completed using the Laminar + SPS viscosity formulation. When examining whether the presence of the debris had an impact on the runup of the bore it became clear that there was some variation, though minimal in the vertical runup values. Both scenarios using vertical debris resulted in lower runups, while the scenario using the vertical offshore debris resulted in a higher runup value. The runup for the vertical offshore debris shows a different trend then the other model scenarios.

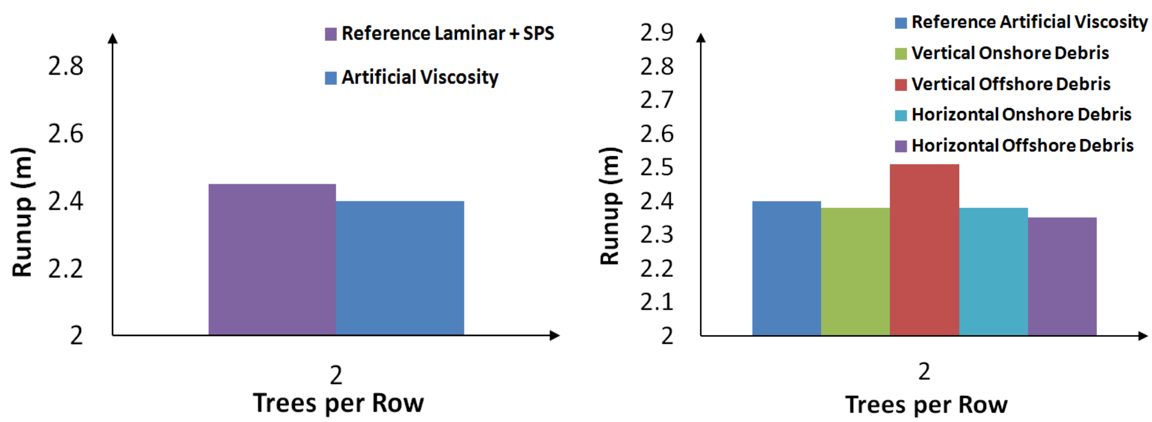

Figure 7.1 - Tsunami run-up for laminar viscosity and artificial viscosity with and without model debris

The tsunami-bore velocity for both the laminar + SPS and artificial viscosity was also compared for the runup of the model. As mentioned previously the artificial viscosity sensitivity simulation were only run for 15s, so a comparison of the rundown is not possible. When comparing the velocities for the different viscosity formulations, the velocity of the bore was found to be fairly consistent even though the velocity measured at the bore front was found to have slight variations due to the measurement frequency. The arrival time of the bore at the measurement location was consistent in the model as well.

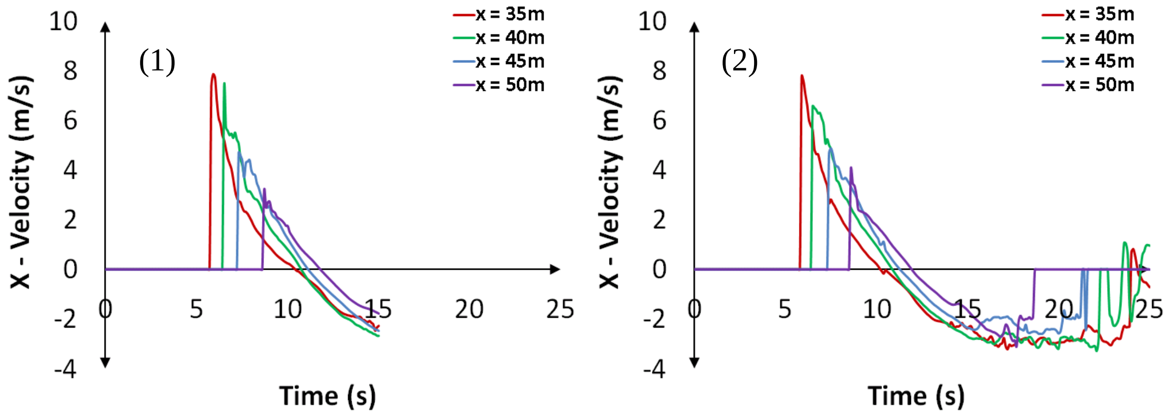

Figure 7.2 - Tsunami velocity for (1) artificial, and (2) laminar viscosity

The velocity of the tsunami-induced bore was compared for each of the debris simulations in order to determine whether the debris location had any impact on the bores' velocity. From Figure 7.3 it can be seen that slight differences in the bore arrival are present at the first gauge location, however no large difference in the bore velocity is present until 45m and 50m. At 45m and 50m the bore for the offshore horizontal debris scenario was found to arrive at the gauges faster and had a larger peak velocity then the other debris scenarios. In all other scenarios the bore was found to propagate similarly. These results indicate that the debris location would not typically have a significant impact on the propagation of the bore for debris of this size.

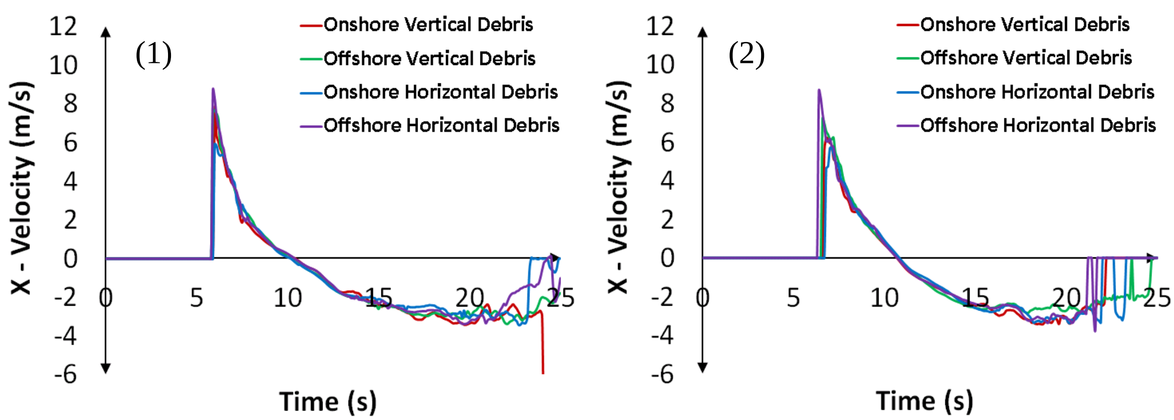

For caption see following page.

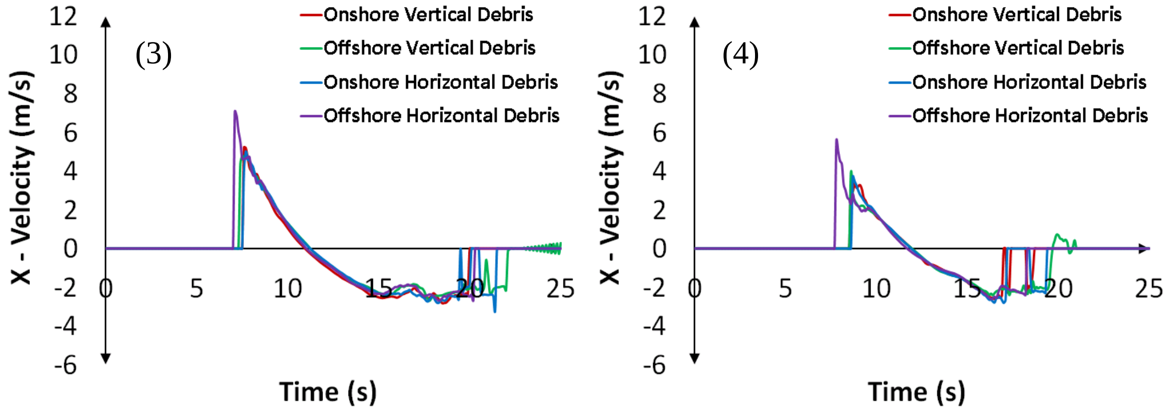

Figure 7.3 - Tsunami velocity for debris at (1) 35m, (2) 40m, (3) 45m, and (5) 50m

7.2 Debris Movement

While the initial debris location did not have a large impact on the runup of the bore or the bores' velocity, it was found to have an influence on the movement of the debris through the coastal forest and through the domain. As the debris was often submerged under the tsunami bore surface the Figures 7.4 to 7.7 show the results of the simulations with a partially transparent bore in order to allow for the proper analysis of the bore movement. The first two figures, 7.4 and 7.5, shows the results for the horizontal debris located onshore and offshore, respectively.

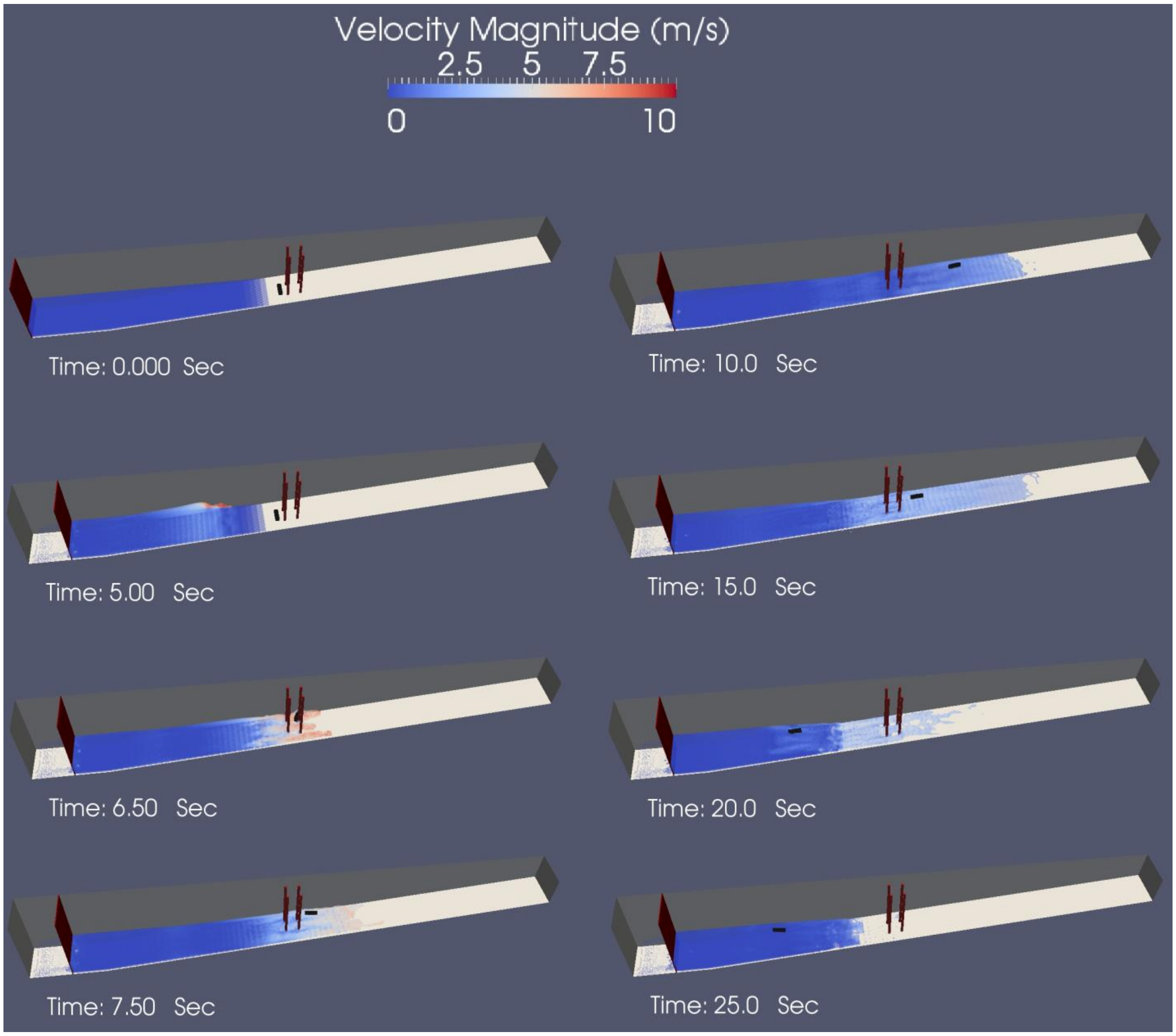

Figure 7.4 – Time-history of debris propagation for horizontal debris located onshore

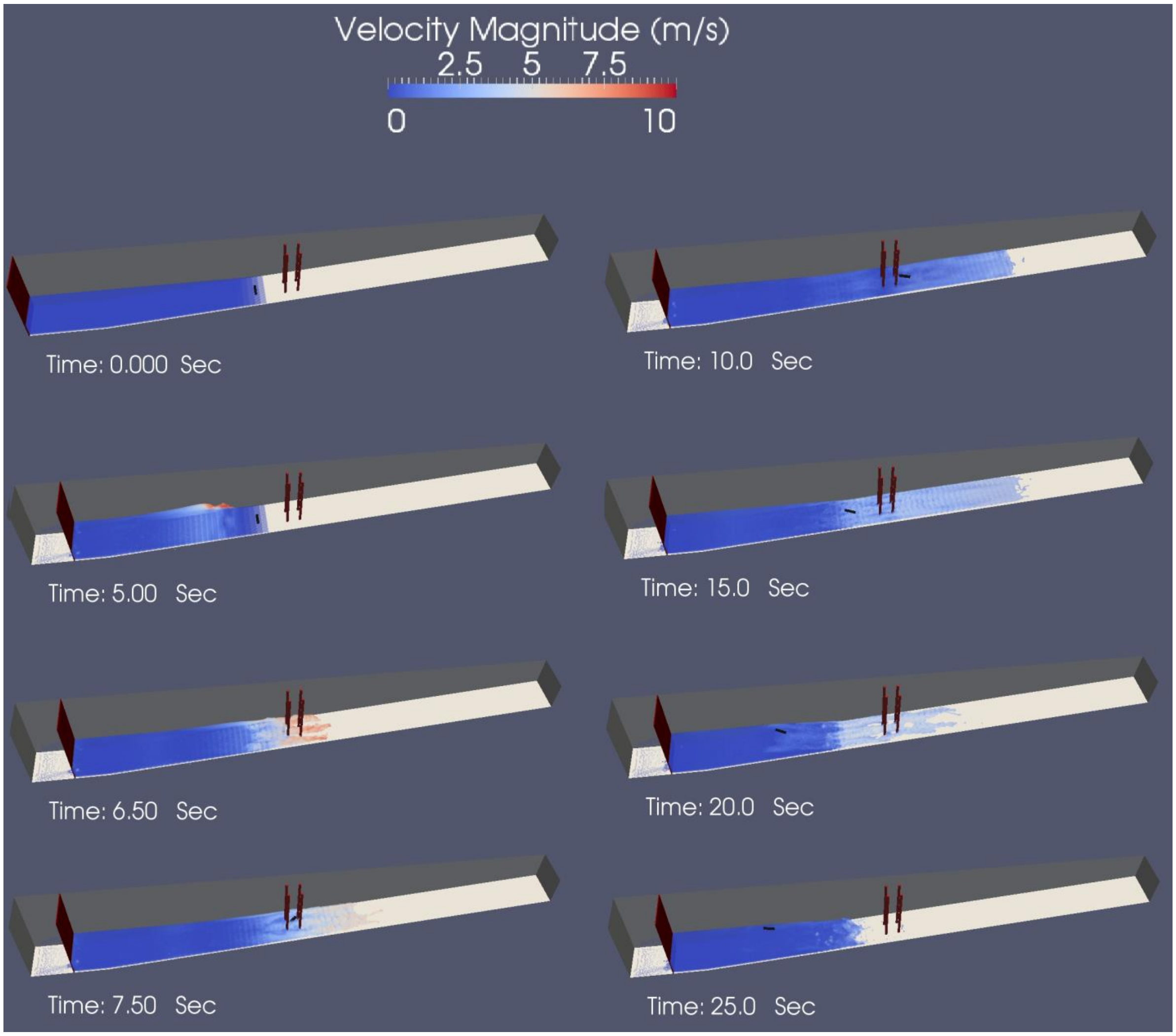

Figure 7.5 – Time-history of debris propagation for horizontal debris located offshore

The debris shown in Figure 7.5 was found to directly impact one of the trees causing it to get temporarily stuck; this resulted in a reduced propagation distance compared to that shown in Figure 7.4, where the debris impacted the trees with glancing blows. In both cases the debris was able to propagate through the forest and continue running up the shoreline, however as Figure 7.5 shows it is possible for the trees to temporarily halt the progression of the debris and can have an impact on how far it travels onshore.

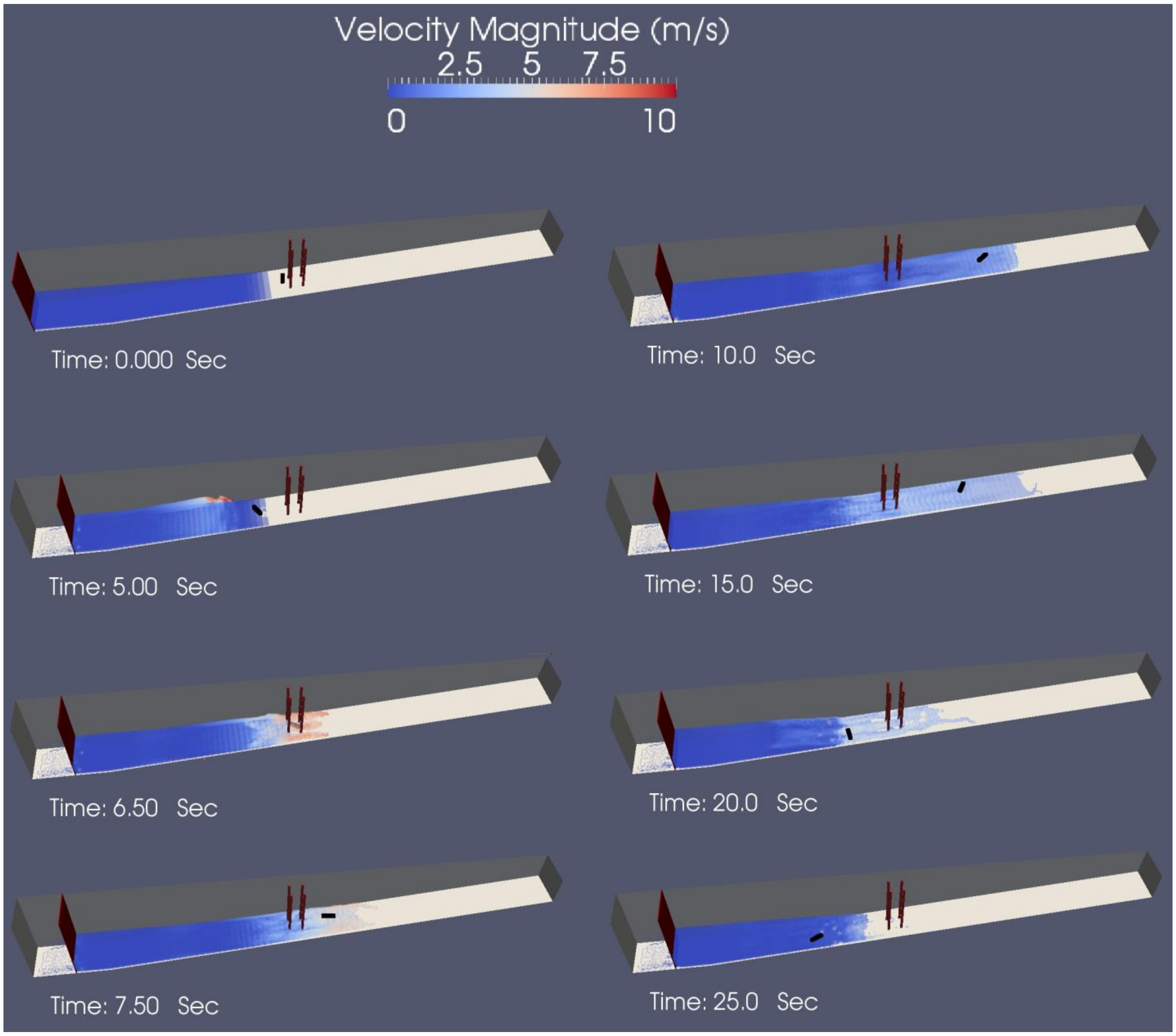

Figure 7.6 – Time-history of debris propagation for vertical debris located onshore

The debris oriented vertically was found to fall over before the approach of the bore. When examining the movement of the debris through the coastal forest the debris which was originally located offshore (Figure 7.7) was found to travel through the forest faster and overall travelled further than that which was originally onshore (Figure 7.6). This was due to the face that the debris did not impact any of the trees during the runup of the bore. As the debris did not rest in its intended position it becomes difficult to make conclusions based on its location.

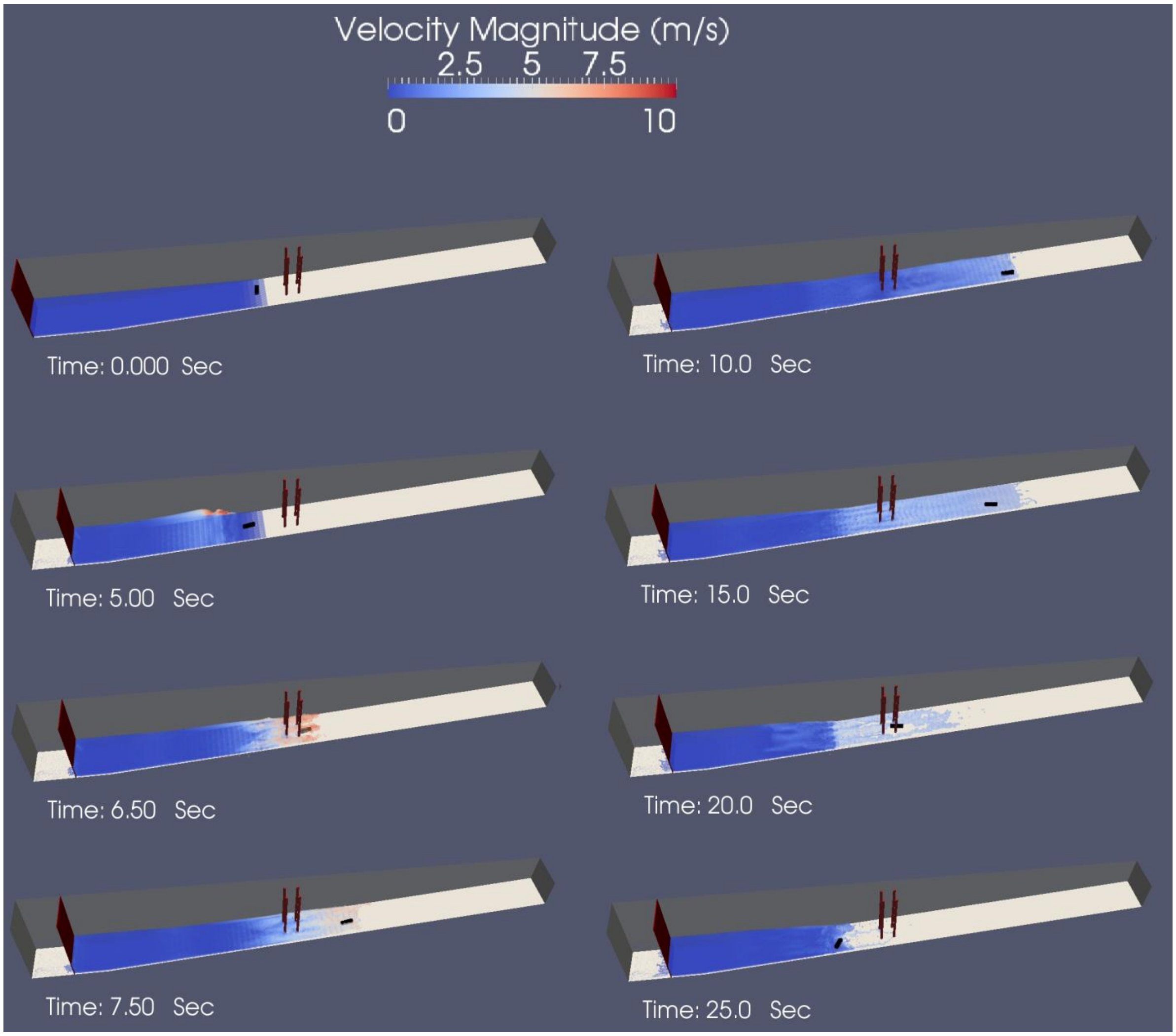

Figure 7.7 – Time-history of debris propagation for vertical debris located offshore

7.3 Impact Forces

The impact forces acting on the individual trees can be separated into the impact force of the debris and the hydrodynamic force of the bore. The analysis required for this section was more complicated than that performed in Chapter 6 as the interest was on the forces acting on the specific trees, while the debris impact is calculated for any impacts caused by the debris. Therefore, the propagation of the debris was carefully examined in order to determine the location of the debris impact force. The hydrodynamic force acting on the individual trees and the general debris impact force is shown in Figure 7.8 for the different debris orientations. As the validation of the models ability to replicate the debris impact forces acting on the structure indicated that the numerical model underestimated the forces, it can be assumed that the numerical forces modeled in this section are lower than those that would be found in a physical model. Despite this it is still possible to get an assessment on the timing of the debris impacts as well as the scale of the debris impact forces which could occur. The rise time of the force was estimated based on the model visualization which introduces some uncertainty into the approximations due to the larger output time step.

The debris impact force acting on the trees was found to have a large range of values dependent on the how direct the impact was on the tree. As can be seen in Figure 7.8 (1) and (2) the impact force was larger than those of the actual bore acting on the structure, while in Figure 7.8 (3) and (4) the debris impact force is quite small. The rundown of the bore resulted in some unreasonable estimations of the bore force for both the horizontal onshore model and the vertical onshore model, this instability in the force was not associated to the propagation of the bore, but rather to the problems which occurred in modeling the rundown of the bore properly. An unrealistic estimation of the bore impact force for the vertical offshore debris scenario was also obtained and was caused by the presence of a few low pressure particles directly in front of the cylinder; modifications to the time stepping coefficient were unable to rectify this problem.

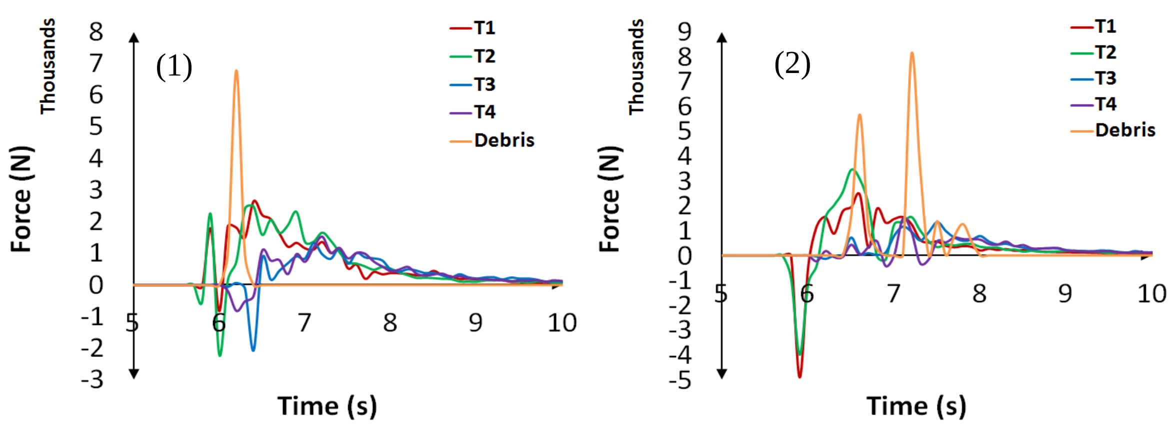

For caption see following page.

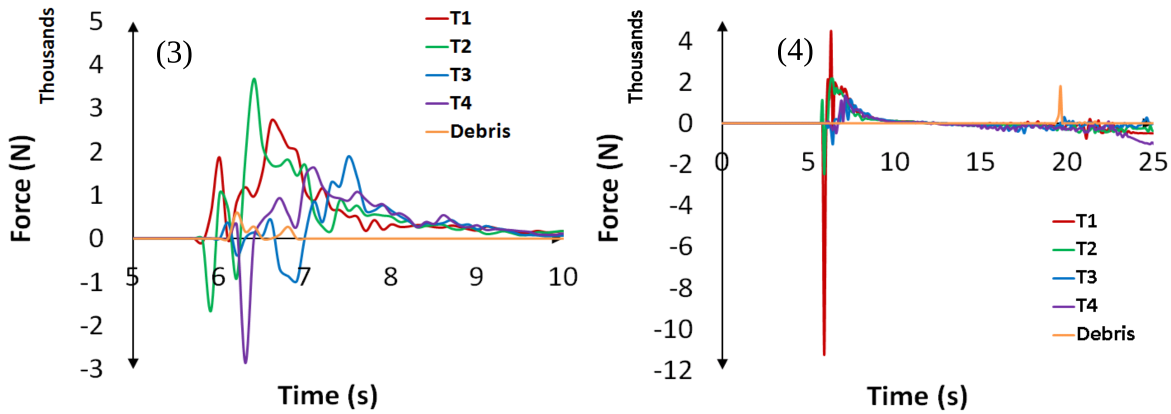

Figure 7.8 - Debris impact forces and hydrodynamic forces for (1) horizontal onshore, (2) horizontal offshore, (3) vertical onshore, and (4) vertical offshore debris at the time of the bore and debris impacts

The debris and hydrodynamic forces acting on the individual trees in the forest were combined and are shown in Figure 7.9. The forces acting on the trees are comparable in magnitude to those seen in Section 5.2.4 for the 2.25m still-water level. When comparing the hydrodynamic and debris impact forces on the individual trees it is clear that the position of the debris does not have an effect on the overall acting forces as all of the forces are in the same level of magnitude.

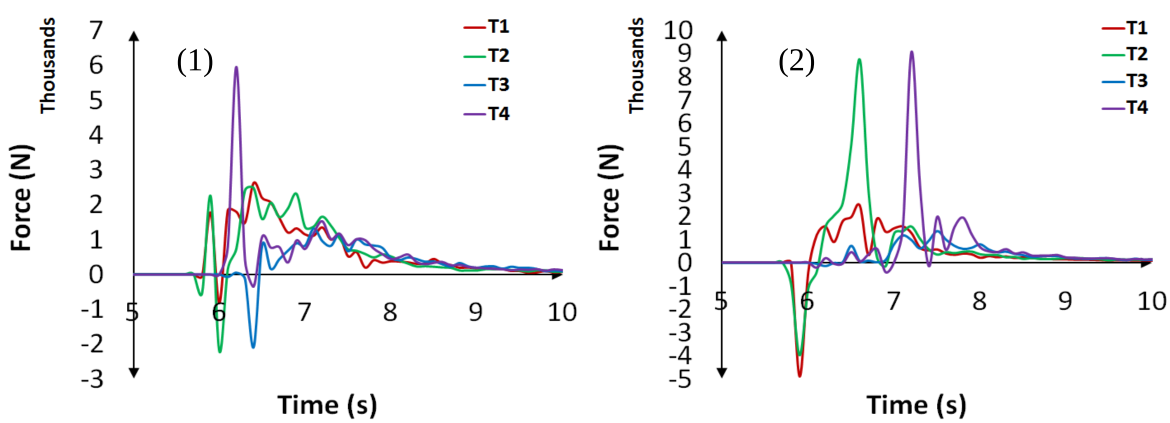

For caption see following page.

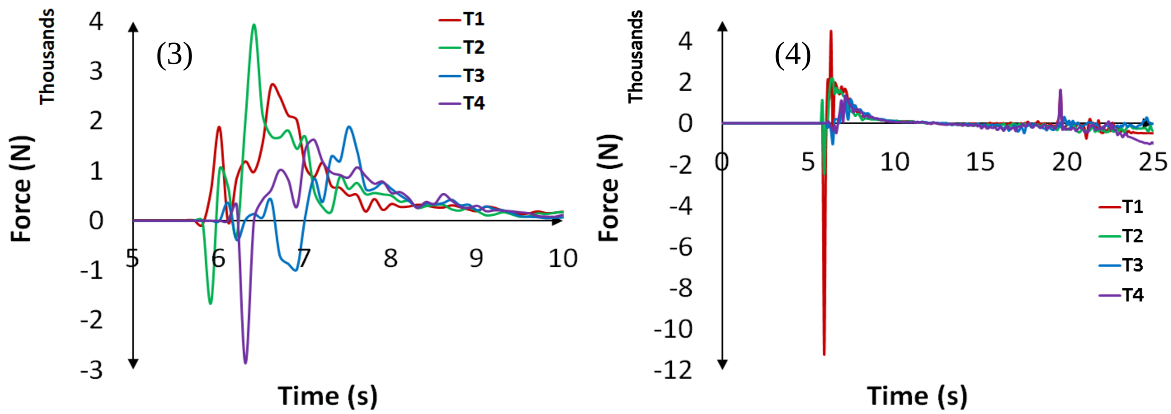

Figure 7.9 - Combined impact force on coastal forest for (1) horizontal onshore, (2) horizontal offshore, (3) vertical onshore, and (4) vertical offshore debris at the time of the bore and debris impacts

7.4 Discussion

This section examined the influence of debris location and orientation on its propagation through the coastal forest, its runup velocity and the forces acting on the trees in order to determine the models capability of performing the large scale impact runs. From this analysis it became evident that the location of the debris had a minimal impact on the runup velocities or the forces, as was expected. However, it was found that the forest could have a significant impact on the debris propagation. In the test modeling the debris in the horizontal offshore position the debris directly impacted one of the trees and therefore propagated less far then the debris in all of the other tests. Alternatively, the debris located vertically offshore did not impact any trees on the runup of the bore and therefore propagated furthest. As expected, one can conclude that the coastal forest has the potential to protect from coastal debris should the debris impact the forest trees directly, and the trees withstand the impact. This potential would be largely affected by the size of the debris and the density and width of the forest.

When examining the model's capability of reproducing large-scale tests, it was found that the use of the artificial viscosity, which is required to simulate the floating debris results in higher instability in the time-history of the bore force. When compared to the simulations shown in Chapter 6, it appeared that the current model was better able to realistically replicate the debris motion as it was picked up by the advancing bore.

8 Conclusion and Future Work

8.1 Conclusions

Based on the analysis of the numerical results presented in Chapters 5 and 7 and on the quantitative comparison of the numerical results with the physical experiments shown in Chapter 6, this section presents the conclusions of this research.

Chapter 5 focused on the assessment of coastal forests' ability to attenuate tsunami-induced bore flow and to reduce its velocity during the runup process. The assessment focused on the variability of the forests effectiveness for different forest widths and densities and various initial still-water levels. The conclusions from this chapter as well as some of the limitations of the model follow:

- The numerical model was able to replicate the runup process of the tsunami-induced bore, including its runup through the modeled coastal forest. However, the rundown of the bore, was found to be poorly represented by the present model.
- The layout of the forest trees, either placed rectilinear or staggered, was found to affect the reduction in the bore runup, the bore velocity, as well as the hydrodynamic impact forces. The staggered configuration was found to be superior in reducing the bore runup and velocity for all still-water levels investigated. However, the layout did not shield the second row of trees from the large impact forces as observed in the case of the rectilinear layout. This increased the exposure of the trees to the full force of the tsunami-induced bore.
- The coastal forest belt was found to have the ability to attenuate the flow and reduce the velocity of the bore when compared to a baseline scenario with no protection. The forest belt width was found to result in a reduction in the runup of the bore as the width increased but did not have a large impact on the bore velocity. The increased forest density was found to reduce the runup of bore linearly and reduce the bore velocity.
- The still-water level impacted the ability of the coastal forest to attenuate the tsunami-induced bore as it would alter the location of the bore formation. The two

scenarios with the bore forming before reaching the forest were found to have similar inundation reduction rates despite different still-water levels, while the bore that formed directly in front of the forest was found to have a significant increase in the rates of reduction. As expected, it was also found that the initial still-water level affects the hydrodynamic impact forces experienced by the trees.

Chapter 6 and 7 focused on the analysis of debris impacts on free-standing structures. This was completed in order to assess the SPH model's ability to replicate debris movement and impact forces. The conclusions drawn from the results presented in Chapter 6 are as follows:

- The numerical SPH model was capable of replicating the water surface levels for different impoundment depths when compared to the results of the physical experiment, except at the instant of impact of the bore which was slightly underestimated and along the front of the cylinder.
- The hydrodynamic forces on the free-standing structure were modeled with varying degrees of accuracy, with higher agreement found for the case of higher impoundment depths. Large discrepancy in the results occurred near the end of the time-series due to the presence of the bore behind the structure, which was not observed with the same intensity in the physical experiments. The presence of an increased bore impact force in the results of the numerical model was due to the use of a dry bed condition instead of the wet-bed condition seen in the model.
- The propagation of the debris was not modeled realistically for the dry bed condition: it was found that the bore pushed the debris in front of the bore front as opposed to carrying the debris with it. As such, the bore did not impact the column first as observed in the physical model. With the wet bed condition, it was found that the movement of the debris was more realistically modeled as the debris traveled with the advancing bore. The bore impact angle was replicated fairly accurately in most cases.
- The impact force on the free-standing structure was significantly underestimated in the numerical model; this was partially due to the rotation of the debris upon impact and the longer stopping time which acted to reduce the impact force.

Chapter 7 examined the propagation of tsunami-borne debris through a coastal forest based on its varying initial location and position. The conclusions found were:

- The initial location of the debris has a significant effect on its propagation through the forest but has minimal effect on the surrounding bore for the size of debris used. It was found that the coastal forest has the ability to delay the propagation of the debris and can reduce the distance to which it travels inland should it directly impact a tree.
- The model was capable of representing the propagation of the debris and the debris was physically picked up by the bore.
- The impact force of the debris on the trees was found to be insignificant in two cases when compared to the large impacts from the bore due to glancing blows on the trees; however, direct impacts were found to result in extremely large forces. The accuracy of the impact forces is uncertain as the validation runs did not provide good comparison.
- Estimation of the impact force rise time was difficult due to the lack of experimental data for comparison. This adds uncertainty to the modeled debris impact forces as the rise time can significantly influence the forces acting on the trees.
- The artificial viscosity resulted in larger amounts of instability comparing to the use of the laminar + SPS viscosity and required several adjustments of the time stepping coefficient in order to reduce the amount of instability occurring in the model.

The differences found in the numerical hydrodynamic and debris impact forces highlight the variability of the impacts which may occur for a tsunami due to the large array of factors such as air entrainment in the bore and the angle and location of the debris impact. The ability of the numerical model to assess the impact forces on the structure was found to be inaccurate based on the validation performed; further validation of this phenomenon is required for this numerical model.

While this study assessed the relationship between the density, width, and layout of the forest for different still-water surface elevations, there are a large number of inter-related parameters which must be considered when assessing the effectiveness of a coastal forest for a specific location. The effectiveness of a coastal forest is highly dependent on its location relative to the shoreline. Therefore, any designs for coastal protection forests must consider the site-specific characteristics.

One of the main limitations of the current SPH model is its inability to incorporate the flexibility of the trees. When impacted by either a tsunami bore or by debris, the trees flexibility has been deemed to have a significant impact on its ability to withstand the high forces. Likewise, the method used in this study for determining the occurrences of debris impact on the free-standing structures was highly subjective and may pose difficulties for more complicated simulations.

8.2 Recommendations for Future Work

Observations from the extensive literature review performed and from the results of the current study have helped identify areas for future consideration in numerical and experimental studies of this issue.

- Research focusing on the ability of the coastal forest to attenuate tsunami bores based on different forest and tsunami parameters is deemed necessary. This includes the development of generalized equations and relations between all of the parameters which would allow for the research to be applied in the design of coastal forests in coastal areas prone to tsunami attack.
- Further validation on the SPH method and existing code for the propagation of coastal flooding and impact of tsunami-borne debris is required in order to assess its ability to replicate the bores' spatial movement and impact under different test conditions.
- Implementation of flexible objects in the current SPH model in order to allow for the proper movement of trees and structures being impact by a bore. Examination into the effect that this would have on the resulting impact and hydrodynamic forces

acting on the structures would be valuable in assessing the true ability of a forest in resisting a tsunami bore.

- Implementation of friction along the flume bed to determine if this would aide in the correct motion of the debris.
- Examining the impact that scouring around the bases of the trees would have on both their ability to withstand tsunami forces and attenuate the flow.
- Examination on the impact of the coastal forest on the rundown characteristics of the tsunami-induced bore.

References

[1] AASHTO. *LRFD Bridge Design Specifications - Second Edition.* American Association of State Highways and Trsnaportation Officials, 1998.

[2] Al-Faesly, Taofiq, Ioan Nistor, Dan Palermo, and Andrew Cornett. "Experimental Study of Structures Subjected to Hydrodynamic and Debris Impact Forces." *Canadian Society of Civil Engineers.* Montreal, 2013.

[3] Asano, Toshiyuki. "Evaluation of Tsunami Attenuation Performance of Coastal Forests Based on Tree Morphology." *Inter. Conf. Coastal Engineering.* World Scientific, 2008a. 1446-1457.

[4] Asano, Toshiyuki. "Time Varying Tsunami Attenutation Ability of Coastal Forests Based on Forest Growth Models." *Coastal Engineering Journal*, 2008b: Vol. 50, 325-348.

[5] Bao, Tran Quang. "Effect of Mangrove Forest Structures on Wave Attenutation in Coastal Vietnam." *Oceanologia*, 2011: Vol 53, 807-818.

[6] Batchelor, G.K. *An Introduction to Fluid Dynamics.* Cambridge: Cambridge University Press, 1967.

[7] Blinn, L., S. Hadjadj, and L. Vervisch. "Large Eddy Simulation of Turbulent FLows in Reversing Systems." In *Selected Proc. of the 1st French Seminar on Turbulence and Space Launchers*, by P. Vuillermoz, P. Comte and Lesieur. Paris: CNES, 2002.

[8] Briggs, Micheal J., Costas E. Synolakis, Gordon S. Harkins, and Debra R. Green. "Laboratory Experiments of Tsunami Runup on a Circular Island." *PAGEOPH*, 1995: vol. 144.

[9] Chan, R. K.-C, and R. L. Street. "A Computer Study of Finite Amplitude Water Waves." *J. Computat. Phys.*, 1970.

[10] Chanson, Hubert, Shin-ichi Aoki, and Mamoru Maruyama. "An Experimental Study of Tsunami Runup on Dry and Wet Horizontal Coastlines." *Science of Tsunami Hazards*, 2003: Vol. 20, 278-293.

[11] Chanson, Hubert, Shin-ichi Aoki, and Mamoru Maruyama. "Experimental Investigation of Wave Runup Downstream of Nappe Impact." Coastal/Ocean Engineering Report, 2000, Vol. 20, No. 5, 278.

[12] Crespo, A. J. C., J. M. Dominguez, A. Barreiro, M. Gomez-Gesteira, and B. D. Rogers. "GPUs, a New Tool of Acceleration in CFD; Efficiency and Reliability on Smoothed Particle Hydrodynamics Method." *PLoS ONE*, 2011.

[13] Crespo, A. J. C., M. Gomez-Gesteira, and R. A. Dalrymple. "Boundary Conditions Generated by Dynamic Particles in SPH Methods." *Computers, Materials and Continua*, 2007: 173-184.

[14] Crespo, A.J.C. *Application of the Smoothed Particle Hydrodynamics Model SPHysics to Free-Surface Hydrodynamics.* PhD Thesis, Vigo, Spain: Universidade de Vigo, 2008.

[15] Dalrymple, R.A., and B.D. Rogers. "Numerical Modeling of Water Waves with the SPH Method." *Coastal Engineering*, 2006: 141-147.

[16] FEMA. *Coastal Construction Manual.* FEMA P55, Federal Emergency Managment Agency, 2011.

[17] FEMA. *Engineering Principles and Practices for Retrofitting Floodprone Residential Buildings.* FEMA Report No. 259, Federal Emergency Management Agency, 1995.

[18] FEMA. *Guidelines for Design of Structures for Vertical Evacuation from Tsunamis - Second Edition.* FEMA P646, Federal Emergency Management Agency, 2012.

[19] FEMA. *Guidelines for Design of Structures for Vertical Evacuation from Tsunamis.* FEMA P646, Federal Emergency Management Agency, 2008.

[20] Forbes, Keith, and Jeremy Broadhead. *The Role of Coastal Forests in the Mitigation of Tsunami Impacts.* Bangkok: Food and Agriculture Organization of the United Nations, 2007.

[21] Gingold, R. A., and J. J. Monaghan. "Smoothed Particle Hydrodynamics: Theory and Application to Non-Spherical Stars." *Monthly Notices of the Royal Astronomical Society*, 1977: 375-389.

[22] Giri, C., Z Zhu, L. L. Tieszen, A. Singh, S. Gillette, and J. A. Kelmelis. "Mangrove forest distributions and dynamics (1975-2005) of the tsunami-affected region of Asia." *Journal of Biogeography*, 2008: Vol. 35, 519-528.

[23] Gomez-Gesteira, M., A. J. C. Crespo, B. D. Rogers, R. A. Dalrymple, J. M. Dominguez, and A. Barreiro. "SPHysics - Development of a Free-Surface Fluid Solver - Part 2: Efficiency and Test Cases." *Computers and Geoscience*, 2012b.

[24] Gomez-Gesteira, M., B. D. Rogers, A. J. C. Crespo, R. A. Dalrymple, M. Narayanaswamy, and J. M. Dominguez. "SPHysics - Development of a free-surface fluid solver - Part 1: Theory and Formulations." *Computers and Geosciences*, 2012a.

[25] Gomez-Gesteira, M., B. D. Rogers, R. A. Dalrymple, A. J. C. Crespo, and M. Narayanaswamy. "User Guide for the SPHysics Code." 2010.

[26] Goring, D., and F. Raichlen. "The Generation of Long Waves in the Laboratory." *Proceedings of the 17th Coastal Engineering Conference.* American Society of Civil Engineers, 1980. Vol. 1, 763-783.

[27] Gotoh, H., T. Shibihara, and T. Sakai. "Sub-Particle-Scale Model for the MPS Method - Lagrangian Flow Model for Hydraulic Engineering." *Computational Fluid Dynamics Journal*, 2001: Vol. 9, 339-347.

[28] Haehnel, Robert B., and Steven F. Daly. *Maximum Impact Force of Woody Debris on Floodplain Structures.* ERDC/CRREL TR-02-2, US Army Corps of Engineers, 2002.

[29] Henderson, F. M. *Open Channel Flow.* New York, USA: McGraw-Hill, 1966.

[30] Hiraishi T., Harada K. "Greenbelt Tsunami Prevention in South-Pacific Region." Vol. 42, 202-213. Port and Airport Research Institute, 2003.

[31] Hughes, S.A. "Physical Models and Laboratory Techniques in Coastal Engineering." In *Advanced Series on Ocean Engineering - Volume 7*. World Scientific, 1993.

[32] Iimura, Kosuke, and Norio Tanaka. "Numerical Simulation Estimating Effects of Tree Density Distribution in Coastal Forest on Tsnuami Mitigation." *Ocean Engineering*, 2012: Vol. 54, 223-232.

[33] Ikeno, M., and Y. Tanaka. "Experimental Study on Impulse Force of Drift Body and Tsunami Running Up to Land." *Proceedings of Coastal Engineering.* Japan Society of Civil Engineering, 2003. Vol. 50, 721-725.

[34] Ikeno, M., N. Mori, and Y. Tanaka. "Experimental Study on Tsunami Force and Impulsive Force by a Drifter under Breaking Bore like Tsunamis." *Proceedings of Coastal Engineering.* Japan Society of Civil Engineering, 2001. Vol. 48, 846-850.

[35] Iribarren, C. R., and C. Nogales. "Protection des Ports II." *17th International Navigation Congress.* Lisbon, Portugal: PIANC, 1949.

[36] Irtem, Emel, Nuray Gedik, M. Sedat Kabdasli, and Nilay E. Yasa. "Coastal Forest Effects on Tsunami Run-Up Heights." *Ocean Engineering*, 2009: Vol. 36, 313-320.

[37] Kharade, Amit S., Atul K. Desai, and Sandip V. Kapadiya. "Criticality of a Structural Column When Subjected to An Impact Load from Water Born Debris in Tsunami Event." *International Journal of Engineering Research and Applications*, 2013: Vol. 3, 2015-2023.

[38] Ko, Harrison T. *Hydraulic Experiments on Impact Forces from Tsunami-Driven Debris.* Masters Thesis, Oregon: Oregon State University, 2013.

[39] Kobayashi, Marcelo H., R. Genest, H. Riggs, and K. Paczkowski. "Simple Hydroelastic Impact Models for Water-Borne Debris." *Proceedings of the Institution of Mechanical Engineers Part M Journal of Engineering for the Maritime Environment*, 2012: 170-179.

[40] Leimkuhler, B. J., S. Reich, and R. D. Skeel. "Integration Methods for Molecular Dynamics." In *Mathematical Approaches to Biomolecuar Structure and Dynamics, IMA Volumes in Mathematics and its Applications*, by K. Schulten, D. W. Sumners and J. P. Mesirov, 161-185. Springer, 1196.

[41] Liu, Philip L. -F., Yong-Sik Cho, Micheal J. Briggs, Utku Kanoglu, and Costas Emmanuel Synolakis. "Runup of Solitary Waves on a Circular Island." *J. Fluid Mech.*, 1995: vol. 302, 259-285.

[42] Lo, E. Y. M., and S. Shao. "Simulation of Near-Shore Solitary Wave Mechanics by an Incompressible SPH Method." *Applied Ocean Research*, 2002: 275-286.

[43] Lucy, L. B. "A Numerical Approach to the Testing of the Fission Hypothesis." *The Astronomical Journal*, 1977: 1013-1024.

[44] Matsutomi, H. "A Practical Formula for Estimating Impulsive Force Due to Driftwoods and Variation Features of the Impulsive Force." *Proceedings of the Japan Society of Civil Engineers.* 1999. Vol 621. 111-127.

[45] Matsutomi, Hideo. "Method for Estimating Collision Force of Driftwood Accompanying Tsunami Inundation Flow." *Journal of Disaster Research,* 2009: Vol. 4, 435-440.

[46] McCord, D. "Aerial of Sukuiso, Japan." *NOAA* . 2011. http://www.ngdc.noaa.gov/hazardimages/picture/show/1482.

[47] Monaghan, J. J. "Gravity Currents and Solitary Waves." *Physica S*, 1996: 523-533.

[48] Monaghan, J. J. "On the Problem of Penetration in Particle Methods." *Journal of Cimputational Physics*, 1989: 1-15.

[49] Monaghan, J. J. "Simulating Free Surface Flows with SPH." *Journal of Computational Physics,* 1994: 399 - 405.

[50] Monaghan, J. J. "Smoothed Particle Hydrodynamics." *Reports on Progress in Physics*, 2005: 1703-1759.

[51] Monaghan, J. J., and A. Kos. "Solitary Waves on a Cretan Beach." *Journal of Waterway, Port, Coastal and Ocean Engineering*, 1999: 145-154.

[52] Monaghan, J.J. "Simulating Free Surface Flows with SPH." *Journal of Computational Physics*, 1994: 399-405.

[53] Monaghan, J.J. "Smoothed Particle Hydrodynamics." *Annual Review of Astronomy and Astrophysics*, 1992: 543-74.

[54] Monaghan, J.J., and J.C. Lattanzio. "A Refined Particle Method for Astrophysical Problems." *Astronomy and Astrophysics*, 1985: 135-143.

[55] Montes, J. S. *Hydraulic of Open Channel Flow*. New York, USA: ASCE Press, 1998.

[56] Morris, J. P. *Analysis of Smoothed Particle Hydrodynamics with Applications.* Victoria Australia: PhD Thesis, Monah University, 1996.

[57] Morris, J. P., P. J. Foz, and Y. Zhu. "Modeling Low Reynold Number Incompressible Flows using SPH." *Journal of Computational Physics*, 1997: 214-226.

[58] NAASRA. *Highway Bridge Design Specification.* National Association of Australian State Road Authorities, 1990.

[59] Naito, Clay, Ron Riggs, Marcelo Kobayashi, and Dan Cox. "Impact Forces from Tsunami-Driven Debris (In-Air Impact Study)." 2011.

[60] NOAA. *Tsunami Data and Information.* 2013. http://www.ngdc.noaa.gov/hazard/tsu.shtml.

[61] Noarayanan, L., K. Murali, and V. Sundar. "Role of Vegetation on Beach Run-Up due to Regular and Cnoidal Waves." *Journal of Coastal Research*, 2012: Vol. 28, 123-130.

[62] Nouri, Younes, Ioan Nistor, and Dan Palermo. "Experimental Investigation of Tsunami Impact on Free Standing Structures." *Coastal Engineering Journal*, 2010: Vol. 52, 43-70.

[63] Panizzo, A. *Physical and Numerical Modelling of Subaerial Landslide Generated Waves.* PhD Thesis, L'Aquila: Universita degli studi di L'Aquila, 2004.

[64] Pelinovsky, E., B. H. Choi, D. C. Kim, I. Didenkulova, and S. -B. Woo. "Two- and Three-Dimensional Computation of Solitary Wave Runup on Non-Plane Beaches." *Nonlinear Processes in Geophysics*, 2008: Vol. 15, 489-502.

[65] Sasaki, K. *The New York Times: Japan Revives a Sea Barrier that Failed to Hold, edited by Onishi, N.* November 2, 2011. http://www.nytimes.com/2011/11/03/world/asia/japan-revives-a-sea-barrier-that-failed-to-hold.html?pagewanted=all.

[66] Shimbun, M. *The New York Times: Seawalls Offered Little Protection Against Tsunami's Crushing Wave, edited by: Onishi, N.* March 13, 2011. http://www.nytimes.com/2011/03/14/world/.

[67] Shugan, Igor, Hwung-Hweng Hwung, and Ray-Yeng Yang. "Tsunami Run-Up on the Horizontal Beach."

[68] Smagorinsky, J. "General Circulation Experiments with the Primitive Equations: I. The Basic Experiment." *Monthly Weather Review*, 1963: Vol 91,. 99-164.

[69] St-Germain, Philippe. *Numerical Modeling of Tsunami-Induced Hydrodynamic Forces on Free-Standing Structures using the SPH Method.* Masters Thesis, Ottawa, Canada: University of Ottawa, 2012.

[70] Stoker, J. J. *Water Waves - The Mathematical Theory with Applications*. New York: Interscience Publishers , 1957.

[71] Strusinska-Correia, A., S. Husrin, and H. Oumeraci. "Tsunami Damping by Mangrove Forest: a Laboratory Study using Parameterized Trees." *Natural Hazards and Earth System Sciences*, 2013: Vol. 13, 453-503.

[72] Synolakis, Costas Emmanuel. "The Runup of Solitary Waves." *J. Fluid Mech.*, 1987: vol. 185, 523-545.

[73] Trainor, J. "Velankanni/ Napagattinam District/ Tamil Nadu/ India." *NOAA*. 2004. http://www.ngdc.noaa.gov/hazardimages/picture/show/996.

[74] —. "Velankanni/Napagattinam District/ Tamil Nadu/ India." *NOAA*. 2004. http://www.ngdc.noaa.gov/hazardimages/picture/show/992.

[75] Verlet, L. "Computer "Experiments" on Classical Fluids. I. Thermodynamical Properties of Lennard-Jones Molecules." *Physical Review*, 1967: Vol. 159, No. 1, 98 - 103.

[76] Ward, Steven N. "Tsunamis." In *The Encyclopedia of Physical Science and Technology*, by R. A. Meyers, Vol. 17, 175-191. Academic Press, 2002.

[77] Wendland, H. "Piecewise Polynomial, Positive Definite and Compactly Supported Radial Functions of Minimal Degree." *Advances in Computational Mathmatics*, 1995: 389-396.

[78] Wesley, Matt. *Impact Forces from Tsunami-Driven Debris: Small Scale Shipping Container*. Thesis, Manoa, Hawaii: University of Hawaii, 2012.

[79] Yeom, Gyeong-Seon, Tomoaki Nakamura, and Norimi Mitzutani. "Collision Analysis of Container Drifted by Runup Tsunami Using Drift Collision Coupled Model." *Journal of Disaster Research*, 2009: Vol. 4, 441-449.

[80] Zhou, S., and R. Dalrymple. "Sediment Suspension Simulation under Oscillatory Flow by SPH - SPS Method." *Proc. 30th International Conference on Coastal Engineering*. San Diego, California: USA: World Scientific, 2006.

[81] Zhu, Y., P. J. Fox, and J. P. Morris. "A Pore-Scale Numerical Model for Flow Through Porous Media." *International Journal for Numerical and Analytical Methods in Geomechanics*, 1999: 881-904.

Appendix A Post-Processing Code

This appendix includes the source code developed for the analysis of debris impact forces on structures and the modified virtual wave gauge. All other codes used in this study were obtained from St-Germain [2012]. Guidance for the use of these programs is included in addition to the source code. It should be noted that the output, called PART files, for the DualSPHysics models were set to ASCII and were generated at a specified frequency.

Virtual Wave Gauge

The only modification to the code allowed for the program *wave_gauge_parameters.exe* allowed it to be an iterative measurement where the location of the measurement varied. This was implemented based on the code developed by St. Germain for the *kernel approximation of Vertical Distribution* and allowed for the location of maximum runup to be determined with ease. The code is included for reference, but is based entirely on that of St-Germain [2012]. For further information on this function of the program see Section 4.3.3.

The input file containing the post-processing parameters are required to be an ASCII file called *wave_gauge_parameters.txt*, and example of the input file is shown in Figure A.1. The first line (1) of the file corresponds to the PART file from which the analysis will be started (integer only), while line (2) indicates the last PART file to be read. The third line (3) corresponds to the total number of particles in the simulation (type integer) and line four (4) indicates the number of boundary particles in the model (type integer). This allows for the model to only consider particles which are non-boundary in the calculation of the maximum water level. Lines (5) to (7) correspond to the location of the center of the rectangular sampling volume (type double), while lines (8) to (10) indicate the dimensions of the sampling volume in the x, y and z directions. The next line (11) indicates the number of iterations that will occur, (12) indicates the direction of the iteration movement and (13) indicates the distance that the measurement location will change. If line (11) is left at one then no additional iterations will occur.

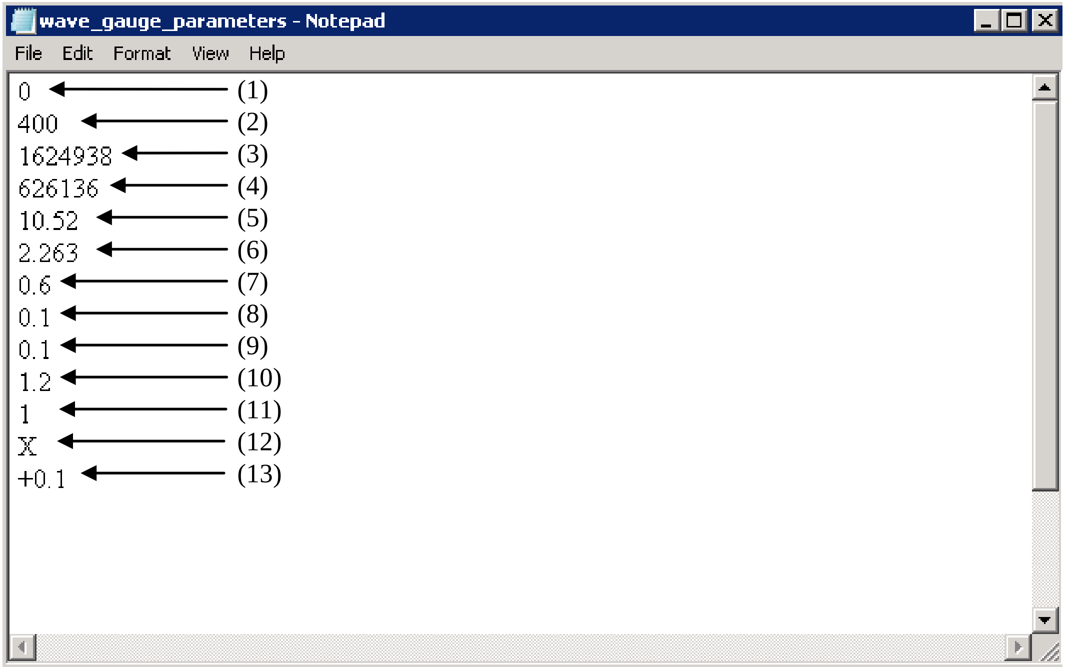

A.1- Example of the Input File For The Post-Processing Program *virtual_wave_gauge.exe*

Once the program has finished its calculations it creates and ASCII output file titled "*Water elevation at Cx=10.52 Cy=2.263.txt". The name of the file indicates the center coordinates in the x-y plane. The file contains a single column of data which corresponds to the calculated maximum water surface level over the specified range of PART files. Should no particles be located within the sampling volume for a PART file then the value will be left as *-1.#IND*, indicating that no value was found.

The program uses the following source files, it should be noted that the main subroutine is located in the file *virtual_wave_gauge.cpp* and that the header files *particle.h* and *sampling_volume.h* are used by multiple programs.

virtual_wave_gauge.cpp

```
/************************************************************
Code by Philippe St-Germain, University of Ottawa, 2012,
modified by Steffanie Piche, University of Ottawa, 2013
The author makes no warranty or guarantee, expressed or
implied, as to the accuracy and reliability of the results
derived from the use of this code. Its free distribution
does not constitute any such warranty or guarantee. No
responsibility or liability is assumed by the author.
************************************************************/
#ifndef WAVE_GAUGE
#define WAVE_GAUGE

#include "particle.h"
#include "sampling_volume.h"

#include <math.h>
#include <string.h>
#include <vector>
#include <iostream>
#include <string>
#include <sstream>
#include <fstream>
#include <cstdlib>

namespace post_processing {

  using namespace std;

  void sampleParticle(int np,int nb ,char* filename,
                      SamplingVolume &sampling_volume){

    //Limits of the rectangular sampling volume
    double x_min=sampling_volume.center_x-
                 sampling_volume.x_dim/2;
      double x_max=sampling_volume.center_x+
                 sampling_volume.x_dim/2;
      double y_min=sampling_volume.center_y-
                 sampling_volume.y_dim/2;
      double y_max=sampling_volume.center_y+
                 sampling_volume.y_dim/2;
      double z_min=sampling_volume.center_z-
                 sampling_volume.z_dim/2;
      double z_max=sampling_volume.center_z+
                 sampling_volume.z_dim/2;

      //Current particle being sampled
      Particle currentParticle;
      //Single line of the PART file
      string line;
      char *charLine;
      //Position of the current particle
      double x_pos;
```

```
double y_pos;
double z_pos;

//Opening the PART file for reading
ifstream infile;
infile.open(filename);

//Looping over all lines of the PART file
int nn=0;
while(nn<np){

  //Making sure that the end of the PART file
  //is not reached
  if(!infile.eof()){

    //Reading a line
    getline(infile,line);

      //Adding a dummy token at the end of the string
      //inorder to avoid an error with the atof function
      //when an empty line is read
      line =line + " 1";

      //If not an empty line
      if(!(line==" 1")){

        //Only sampling water particles and not
        //boundary partilces
      if(nn>nb){

            //Decomposing the line into an array of
            //characters
            charLine = new char[line.length()];
            for(unsigned int i=0;i< line.length();i++){
              charLine[i] = line[i];
            }

            //Determination of the fluid particle position
            x_pos=atof(strtok (charLine," "));
            y_pos=atof(strtok (NULL," "));
            z_pos=atof(strtok (NULL," "));

            //Checking if the particle is inside the
            //retangular sampling volume
            if(((x_min<x_pos)&&(x_pos<x_max))&&
              ((y_min<y_pos)&&(y_pos<y_max))&&
              ((z_min<z_pos)&&(z_pos<z_max))){

              currentParticle.x_pos=x_pos;
            currentParticle.y_pos=y_pos;
            currentParticle.z_pos=z_pos;
              currentParticle.x_vel=atof(strtok (NULL," "));
              currentParticle.y_vel=atof(strtok (NULL," "));
              currentParticle.z_vel=atof(strtok (NULL," "));
              currentParticle.density=atof(strtok (NULL," "));
```

```
                    currentParticle.pressure=atof(strtok (NULL," "));
                    currentParticle.mass=atof(strtok (NULL," "));


sampling_volume.particle_sample.push_back(currentParticle);
                  }

                  //Deleting pointer
                  delete[] charLine;
                  charLine=0;
              }//End of if water particle

            }//end of if not empty line
        }//end of if not end of file

        nn++;

      }//end of loop over all particles

      //Closing the PART file
      infile.close();

  }//End of sampleParticle function

  void printMaxElev(SamplingVolume sampling_volume,
                          vector<string> &elev_time_history,
                                int part_index,int num_part,
                                string outFileName){

    //Determination of the maximum elevation
    double elevation;
      sampling_volume.max_elev(elevation);

      //Converting the maximum elevation into a string
      string elevationString;
      ostringstream ee;
      ee<<elevation;
      elevationString = ee.str();

      //Inserting the maximum elevation at the in the
      //array of the time-history of this one
      elev_time_history.push_back(elevationString);

      //If all the PART files have been processed,
      //the final output file is written
    if(part_index==num_part ){

      //Creating the output file containg the time-history
      //of the water surface elevation
        char* result_filename;
        result_filename=0;
        result_filename = new char[outFileName.length() + 1];
        strcpy(result_filename,outFileName.c_str());
        ofstream outfile(result_filename);
```

```
        //Writing the entire time-history to the output file
        for(int i=0;i<elev_time_history.size();i++){
          outfile<<elev_time_history[i]<<"\n";
        }

        //Closing the output file
        outfile.close();

        //Deleting pointer
        delete [] result_filename;
        result_filename=0;

      }

  }// End of printMaxElev function

}

//*******************************************************
//Main program
//*******************************************************
using namespace post_processing;

int main(int argc,char** argv){

  //Variables for reading the raw PART files
  char* in_filename;
  string in_filenameTemp;
  string indexString;

  //Array for the time-history of the water surface elevation
  vector<string> elevation_time_history;

  //*****************************************************
  //Input parameters
  //*****************************************************

  //Opening file containing input parameters
  ifstream infile;
  infile.open("wave_gauge_parameters.txt");

  //Index of the intial PART file to begin post-processing
  int ini_part;
  //Number of PART files to be processed beyond initial
  //PART file
  int num_part;
  //Total number of particles in the simulation
  int np;
  //Number of boundary particles in the simulation
  int nb;
   //Initial coordinates of the center of sherical sampling
  //volumes
  double ini_center_x;
  double ini_center_y;
  //Coordinates of the center of rectangular
```

```
  //sampling volume
  double center_x;
  double center_y;
  double center_z;
  //Dimansions of the rectangular sampling colume
  double x_dim;
  double y_dim;
  double z_dim;
    //Number of iterations for the procedure
  int numIterations;
  //Direction in which the procedure is repeated
  string direction; // "X" or "Y"
  //Incremental distance between iterations
  double increment;

  //Reading in the inputs
  infile>>ini_part;
  infile>>num_part;
  infile>>np;
  infile>>nb;
  infile>>ini_center_x;
  infile>>ini_center_y;
  infile>>center_z;
  infile>>x_dim;
  infile>>y_dim;
  infile>>z_dim;
  infile>>numIterations;
  infile>>direction;
  infile>>increment;

  //Closing the input file
  infile.close();

  //Writing the inputs to the command promt window
  cout<<ini_part<<" : Intial PART file to begin post-processing"<<"\n";
  cout<<num_part<<" : Number of PART files to process"<<"\n";
  cout<<np<<" : Total number of particles"<<"\n";
  cout<<nb<<" : Number of boundary particles"<<"\n";
  cout<<ini_center_x<<" : Center of sampling volume in the X
direction"<<"\n";
  cout<<ini_center_y<<" : Center of sampling volume in the Y
direction"<<"\n";
  cout<<center_z<<" : Center of sampling volume in the Z direction"<<"\n";
  cout<<x_dim<<" : X dimension of sampling volume"<<"\n";
  cout<<y_dim<<" : Y dimension of sampling volume"<<"\n";
  cout<<z_dim<<" : Z dimension of sampling volume"<<"\n";
  cout<<numIterations<<" : # of iterations for the procedure at different
locations along the specified direction"<<"\n";
  cout<<direction<<" : Direction in which the procedure is repeated (X or
Y)"<<"\n";
  cout<<increment<<" : Incremental distance between iterations"<<"\n";
  //***********************************************************

  //Looping for each iteration of the procedure
  for(int j=0;j<numIterations;j++){
```

```
  //Name of the output file containing the post-processing
  //results
  string outFileName;
  ostringstream cx;
  ostringstream cy;


      if(direction=="X"){
        center_x=ini_center_x+j*increment;
        center_y=ini_center_y;
      }
      else if(direction=="Y"){
        center_x=ini_center_x;
        center_y=ini_center_y+j*increment;
}

    cx<<center_x;
      cy<<center_y;


  outFileName="Water elevation at Cx="
              + cx.str() + " Cy="+cy.str()+ ".txt";

  //SamplingVolume object
  SamplingVolume samplingVolume;

  //Initializing the properties of the SamplingVolume
  //object
  samplingVolume.center_x=center_x;
  samplingVolume.center_y=center_y;
  samplingVolume.center_z=center_z;
  samplingVolume.x_dim =x_dim;
  samplingVolume.y_dim=y_dim;
  samplingVolume.z_dim=z_dim;

  //Looping over PART files
  for (int i=ini_part;i<=num_part;i++){

      //********************************************************
      //Generation of the string corresponding to the current
      //PART file to be processed
      //********************************************************
      ostringstream ii;
      ii<<i;
      indexString=ii.str();

      if (i <10){
        in_filenameTemp="PART_000"+indexString;
        in_filename=new char[in_filenameTemp.length()+1];
        strcpy(in_filename,in_filenameTemp.c_str());
      }
      else if (i<100){
        in_filenameTemp="PART_00"+indexString;
```

```
        in_filename = new char[in_filenameTemp.length()+1];
        strcpy(in_filename,in_filenameTemp.c_str());
      }
      else if (i<1000){
        in_filenameTemp ="PART_0" +indexString;
        in_filename = new char[in_filenameTemp.length()+1];
        strcpy(in_filename,in_filenameTemp.c_str());
    }
      else{
        in_filenameTemp="PART_" +indexString;
        in_filename=new char[in_filenameTemp.length()+1];
        strcpy(in_filename,in_filenameTemp.c_str());
      }
      //*******************************************************

      //Calling the function that will search the current PART
      //file and construct the list of particle located inside
      //the sampling volume
      sampleParticle(np,nb,in_filename,samplingVolume);

    //Calling the function that will write the results to
      //the output file
      printMaxElev(samplingVolume,elevation_time_history,i,
                     num_part,outFileName);

    //Progress feedback on the command prompt window
      cout<<"->Processing file "<<in_filenameTemp<<" for
"<<outFileName<<"\n";

      //Clearing the sampled particles
      samplingVolume.particle_sample.clear();

      //Deleting pointer
      delete [] in_filename;
      in_filename=0;

  }//End of looping over PART files

    //Emptying the time-history vector for the next iteration
    elevation_time_history.clear();


  }//End of iterations

  return 0;

}//End of main program
//************************************************************

#endif
```

Particle.h

```
/*********************************************************
Code by Philippe St-Germain, University of Ottawa, 2012
The author makes no warranty or guarantee, expressed or
implied, as to the accuracy and reliability of the results
derived from the use of this code. Its free distribution
does not constitute any such warranty or guarantee. No
responsibility or liability is assumed by the author.
*********************************************************/
#ifndef PARTICLE_H
#define PARTICLE_H

namespace post_processing {

  class Particle {

    public:
        //Attributes associated to a water particle
        double x_pos;
        double y_pos;
        double z_pos;
        double x_vel;
        double y_vel;
        double z_vel;
        double density;
        double pressure;
        double mass;

  };//End of class Particle

}

#endif
```

Sampling_volume.h

```
/*********************************************************
Code by Philippe St-Germain, University of Ottawa, 2012
The author makes no warranty or guarantee, expressed or
implied, as to the accuracy and reliability of the results
derived from the use of this code. Its free distribution
does not constitute any such warranty or guarantee. No
responsibility or liability is assumed by the author.
*********************************************************/
#ifndef SAMPLING_VOLUME_H
#define SAMPLING_VOLUME_H

#ifndef PI
#define PI 3.141592654
#endif

#include "particle.h"
#include <math.h>
#include <iostream>
#include <vector>

namespace post_processing{

  using namespace std;

  class SamplingVolume{

    public:

        //Array of particles inside the sampling volume
        std::vector <Particle> particle_sample;

        //*****************************************************
        //Variable related to a spherical sampling volume
        //for the kernel approximation of a flow property
        //*****************************************************
        //Center coordinates of sampling volume
        double center_x;
        double center_y;
        double center_z;
        //Smoothing length of sampling volume
        double h;
        //Variable for the equation of state (Eq. 2.65):
        //B= (c0)^2 * rho0 / gamma
        double B;
        //*****************************************************


        //*****************************************************
        //Dimensions of rectangular sampling volume
        //for the determination of the water surface elevation
        //                    OR
        //Dimensions of rectangular tributary area on a
```

```
//rectangular solid object for the determination of
//the resulting for by pressure integration
//*****************************************************
double x_dim;
double y_dim;
double z_dim;
//*****************************************************


//*****************************************************
//Variable for sampling volumes involved in the
//determination of the resulting for by pressure
//integration
//*****************************************************
//Start angle of radial tributary area
double theta1;
//End angle of radial tributary area
double theta2;
//Distance from the center of the circular column to
//the center of the sampling volume
//               OR
//Distance from a center axis of a square column to t
//the center of the sampling volume
double rv;
//*****************************************************

//Function for the kernel approximation of the velocity
//in the X direction
double avg_x_vel(){
  //For the correction of Bonet and Lok (Eq. 2.92)
    double sum1=0;
    double sum2=0;
    //Distance seperating a fluid particle from the
    //center of the sampling volume
    double d;
    //Looping over all fluid particles inside the
    //sampling volume
    for(int i=0;i<particle_sample.size();i++){

      d=sqrt(pow(particle_sample[i].x_pos-center_x,2)+
                 pow(particle_sample[i].y_pos-center_y,2)+
             pow(particle_sample[i].z_pos-center_z,2));

      sum1+=particle_sample[i].x_vel*
                particle_sample[i].mass*
                kernel(d)/
                particle_sample[i].density;

      sum2+=particle_sample[i].mass*
                kernel(d)/
                particle_sample[i].density;

    }//End of loop over all fluid particles
    return sum1/sum2;
}//End of function avg_x_vel
```

```
//Function for the kernel approximation of the velocity
  //in the Y direction (similar as function avg_x_vel)
  double avg_y_vel(){
    double sum1=0;
      double sum2=0;
      double d;
      for(int i=0;i<particle_sample.size();i++){

        d=sqrt(pow(particle_sample[i].x_pos-center_x,2)+
                 pow(particle_sample[i].y_pos-center_y,2)+
                   pow(particle_sample[i].z_pos-center_z,2));

        sum1+=particle_sample[i].y_vel*
                  particle_sample[i].mass*
                  kernel(d)/
                  particle_sample[i].density;

        sum2+=particle_sample[i].mass *
                  kernel(d)/
                  particle_sample[i].density;

      }
      return sum1/sum2;
  }//End of function avg_y_vel

  //Function for the kernel approximation of the velocity
  //in the Z direction (similar as function avg_x_vel)
  double avg_z_vel(){
      double sum1=0;
      double sum2=0;
      double d;
      for(int i=0;i<particle_sample.size();i++){

        d=sqrt(pow(particle_sample[i].x_pos-center_x,2)+
                 pow(particle_sample[i].y_pos-center_y,2)+
                   pow(particle_sample[i].z_pos-center_z,2));

        sum1+=particle_sample[i].z_vel*
                particle_sample[i].mass*
                  kernel(d)/
                  particle_sample[i].density;

        sum2+=particle_sample[i].mass*
                  kernel(d) /
                  particle_sample[i].density;

  }
      return sum1/sum2;
  }//End of function avg_z_vel

  //Function for the calculation of the pressure
  //assumed to be acting at the center of the
  //sampling volume
  double avg_pressure(){
```

```
//Equation of state (Eq. 2.65)
  return B*(pow(avg_density()/1000.0,7)-1);
}

//Function for the kernel approximation of the density
double avg_density(){
  //For the correction of Bonet and Lok (Eq. 2.92)
    double sum1=0;
    double sum2=0;
    //Distance seperating a fluid particle from the
    //center of the sampling volume
    double d;
    //Looping over all fluid particles inside the
    //sampling volume
    for(int i=0;i<particle_sample.size();i++){

        d=sqrt(pow(particle_sample[i].x_pos-center_x,2)+
                 pow(particle_sample[i].y_pos-center_y,2)+
                 pow(particle_sample[i].z_pos-center_z,2));

       sum1+=particle_sample[i].mass*kernel(d);

       sum2+=particle_sample[i].mass/
               particle_sample[i].density*
                 kernel(d);

    }//End of loop over all fluid particles
    return sum1/sum2;
}//End of function avg_density

//Quadratic kernel function (Eq. 2.64)
//Takes as parameter the distance from of the
//water particle from the center of the sampling volume
double kernel(double d){
    double r;
    r=d/h;
    double alpha_d;
alpha_d=5/(4*PI*pow(h,3));
if(0<=r&& r<= 2){
  return alpha_d*
               (3.0/16.0*pow(r,2)-3.0/4.0*r+3.0/4.0);
    }
    else{
      return 0;
    }
}//End of function kernel

//Function for the determination of the elevation of the
//highest water particle inside the sampling volume
//Note that the function parameters are passed by
//reference
void max_elev(double &elev){
    //Setting the maximum elevation to zero
    //initially
    elev=0;
```

```
            //Looping over all water particles inside the
            //sampling volume. If a higher elevation is
            //found, the elev variable is updated.
            for(int i=0;i<particle_sample.size();i++){
              if(particle_sample[i].z_pos>elev){
                elev=particle_sample[i].z_pos;
              }
            }//End of loop over all fluid particles
        }//End of Function max_elevation

  };//End of class SamplingVolume

}


#endif
```

Impact Debris Force

The program *Impact Force.exe* provides the time-history of the debris impact on structure as outlined in Section 4.3.1.The ASCII file providing the parameters to run the program must be labeled *impact_force_parameters.txt,* example shown in Figure A.2. The development of this code was based on that of St-Germain [2012] and so it retains many features from the original code.

The first line (1) of the file corresponds to the PART file from which the analysis will be started (integer only), while line (2) indicates the last PART file to be read. The third line (3) corresponds to the total number of particles in the simulation (type integer) to ensure that the calculations do not exceed the total number of particles in the simulation. Lines (4) to (6) are the amount of fixed, moving and floating boundary particles, respectively. Line (7) indicates the mass of the debris (type integer) and Line (8) indicates the output time step of the model (type double)

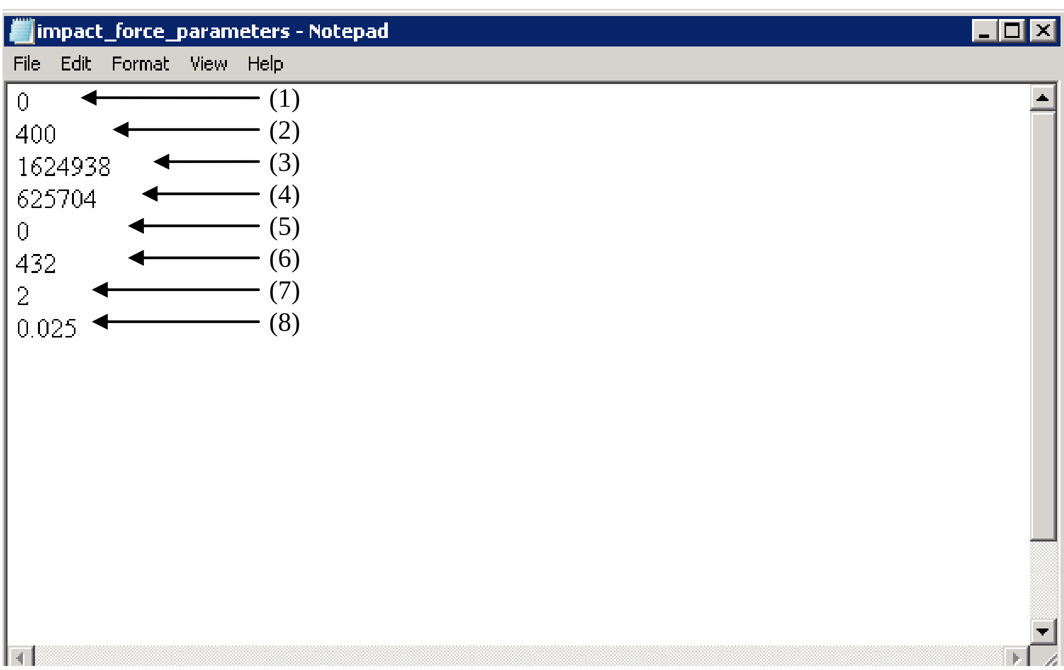

A.2- Example of the Input File For The Post-Processing Program *Impact Force.exe*

Once the program has finished its calculations it creates and ASCII output file titled "*impact force for floating particles.txt"*. The file contains a single column of data which corresponds to the calculated impact force for the floating particles over the specified range of PART files.

The program uses the following source files, it should be noted that the main subroutine is located in the file *impact force.cpp* and that the header file *particle.h* (included above) is used by multiple programs. For this program the header file *sampling_volume.h* has been modified for the calculation of the impact force.

impact force.cpp

```
/************************************************************
Modified code by Steffanie Piche, University of Ottawa, 2013
based on Philippe St-Germain, University of Ottawa, 2012
The author makes no warranty or guarantee, expressed or
implied, as to the accuracy and reliability of the results
derived from the use of this code. Its free distribution
does not constitute any such warranty or guarantee. No
responsibility or liability is assumed by the author.
************************************************************/
#ifndef KERNEL_APPROX
#define KERNEL_APPROX

#include "particle.h"
#include "sampling_volume.h"

#include <math.h>
#include <string.h>
#include <vector>
#include <iostream>
#include <string>
#include <sstream>
#include <fstream>
#include <cstdlib>

namespace post_processing {

  using namespace std;

  void sampleParticle(int np,int nb,int nm,int nf, char* filename,
SamplingVolume &samplingVolume){

      //Current particle being sampled
      Particle currentParticle;
      //Single line of the PART file
      string line;
```

```
char *charLine;
//Position of the current particle
double x_vel;
double y_vel;
double z_vel;
double nmin;
double nmax;
double x_pos;
double y_pos;
double z_pos;

nmin=nm+nb+1;
nmax=nm+nb+nf;

//Opening the PART file for reading
ifstream infile;
infile.open(filename);

//Looping over all lines of the PART file
int nn=0;
while(nn<nmax){
  //Making sure that the end of the PART file
  //is not reached
  if(!infile.eof()){

    //Reading a line
    getline(infile,line);
      //Adding a dummy token at the end of the string
      //inorder to avoid an error with the atof function
      //when an empty line is read
      line =line + " 1";
  //If not an empty line
      if(!(line==" 1")){
    //Only sampling water particles and not
        //boundary partilces
        if(nn>nmin){

          //Decomposing the line into an array of
          //characters
          charLine = new char[line.length()];
          for(unsigned int i=0;i<line.length();i++){
            charLine[i] = line[i];
          }

          //Determination of the fluid particle position

            x_pos=atof(strtok (charLine," "));
          y_pos=atof(strtok (NULL," "));
          z_pos=atof(strtok (NULL," "));
          x_vel=atof(strtok (NULL," "));
          y_vel=atof(strtok (NULL," "));
          z_vel=atof(strtok (NULL," "));

            Particle currentParticle;
```

```
                    currentParticle.x_vel=x_vel;
                    currentParticle.y_vel=y_vel;
                    currentParticle.z_vel=z_vel;


samplingVolume.particle_sample.push_back(currentParticle);

            //Deleting pointer
                  delete[] charLine;
                  charLine=0;
              }//End of if water particle
          }//end of if not empty line
        }//end of if not end of file

        nn++;

      }//end of loop over all particles

      //Closing the PART file
      infile.close();

  }//End of sampleParticle function

  void printTimeHistory(SamplingVolume &samplingVolume,
                                  vector<string> &time_history,
                                  int part_index,int num_part,
                                  string outFileName,int nf, double
mass, double time_step, double& measurement1){

    //Approximation of the flow property
    double measurement;
      double force;


    string forceString;
    ostringstream pp;

      measurement=samplingVolume.avg_velocity(nf);
      force
=samplingVolume.force(measurement,mass,time_step,part_index,measurement1);


    pp<<force;
      forceString=pp.str();
      time_history.push_back(forceString);

    //If all the PART files have been processed,
      //the final output file is written
    if (part_index==num_part){

      //Creating the output file containing the time-history
      //of the water surface elevation
      char* result_filename;
```

```
      result_filename=0;
      result_filename = new char[outFileName.length() + 1];
      strcpy(result_filename,outFileName.c_str());
      ofstream outfile(result_filename);

      //Writing the entire time-history to the output file
      for (int i=0;i<time_history.size();i++){
        outfile<<time_history[i]<<"\n";
      }

        //Closing the output file
        outfile.close();

        //Deleting pointer
        delete [] result_filename;
        result_filename=0;
    }
  }// End of printTimeHistory function

}
//*********************************************************
//Main program
//*********************************************************
using namespace post_processing;

int main(int argc,char** argv){

  //Variables for reading the raw PART files
  char* in_filename;
  string in_filenameTemp;
  string indexString;
  double measurement1;


  //Array for the time-history of the measurement
  vector <string> time_history;

  //*******************************************************
  //Input parameters
  //*******************************************************

  //Opening file containing input parameters
  ifstream infile;
  infile.open("impact_force_parameters.txt");

  //Index of the intial PART file to begin post-processing
  int ini_part;
  //Number of PART files to be processed beyond initial
  //PART file
  int num_part;
  //Total number of particles in the simulation
  int np;
  //Number of boundary particles in the simulation
  int nb;
  //Number of moving particles in the simulation
```

```
int nm;
//Number of floating particles in the simulation
int nf;
    //mass of the object
double mass;
//model output time step
double time_step;

//Reading in the inputs
infile>>ini_part;
infile>>num_part;
infile>>np;
infile>>nb;
infile>>nm;
infile>>nf;
  infile>>mass;
infile>>time_step;


//Closing the input file
infile.close();

//Writing the inputs to the command promt window
cout<<ini_part<<" : Intial PART file to begin post-processing"<<"\n";
cout<<num_part<<" : Number of PART files to process"<<"\n";
cout<<np<<" : Total number of particles"<<"\n";
cout<<nb<<" : Number of boundary particles"<<"\n";
cout<<nm<<" : Number of moving particles"<<"\n";
cout<<nf<<" : Number of floating particles"<<"\n";
cout<<mass<<" : Mass of object"<<"\n";
cout<<time_step<<" : Model output time step"<<"\n";


//************************************************************
//Name of the output file containing the post-processing
//results
string outFileName;

ostringstream floating;
floating << nf;

  outFileName="impact force for floating particles.txt";


//SamplingVolume object
SamplingVolume samplingVolume;

 //Looping over PART files
for (int i=ini_part; i<= num_part; i++){


  //************************************************************
  //Generation of the string corresponding to the current
  //PART file to be processed
    //************************************************************
```

```
      ostringstream ii;
      ii<<i;
      indexString=ii.str();

      if (i<10){
        in_filenameTemp="PART_000"+indexString;
        in_filename=new char[in_filenameTemp.length()+1];
        strcpy(in_filename,in_filenameTemp.c_str());
      }
      else if (i<100){
        in_filenameTemp = "PART_00"+indexString;
        in_filename=new char[in_filenameTemp.length()+1];
        strcpy(in_filename,in_filenameTemp.c_str());
      }
      else if (i<1000){
        in_filenameTemp="PART_0" +indexString;
        in_filename=new char[in_filenameTemp.length()+1];
        strcpy(in_filename,in_filenameTemp.c_str());
      }
      else{
        in_filenameTemp="PART_" +indexString;
        in_filename=new char[in_filenameTemp.length()+1];
        strcpy(in_filename,in_filenameTemp.c_str());
    }
      //*******************************************************

    //Calling the function that will search the current PART
      //file and construct the list of particle located inside
      //the sampling volume
      sampleParticle(np,nb,nm,nf,in_filename,samplingVolume);


      printTimeHistory(samplingVolume,time_history,i,num_part,outFileName,
nf,mass,time_step,measurement1);


      //Progress feedback
      cout<<"Processing file "<<in_filenameTemp<<" for " << outFileName<<
"\n";

      //Clearing the sampling volume
      samplingVolume.particle_sample.clear();

      //Delete pointer
      delete [] in_filename;
      in_filename=0;

  }//End of loop over PART files

  return 0;
}//End of main program
//************************************************************


#endif
```

Sampling_volume.h

```
/**************************************************************
Modified code by Steffanie Piche, University of Ottawa, 2013
based on Philippe St-Germain, University of Ottawa, 2012
The author makes no warranty or guarantee, expressed or
implied, as to the accuracy and reliability of the results
derived from the use of this code. Its free distribution
does not constitute any such warranty or guarantee. No
responsibility or liability is assumed by the author.
**************************************************************/
#ifndef SAMPLING_VOLUME_H
#define SAMPLING_VOLUME_H

#ifndef PI
#define PI 3.141592654
#endif

#include "particle.h"
#include <math.h>
#include <iostream>
#include <vector>

namespace post_processing{

  using namespace std;

  class SamplingVolume{

    public:

        //Array of particles inside the sampling volume
        std::vector <Particle> particle_sample;



        //****************************************************

        //Function for the magnitude of the velocity in the x, y and z
direction
        double avg_velocity(int nf){

            double average_velocity=0;
            double avg=0;



            //Looping over all fluid particles inside the
            //sampling volume
            for(int i=0;i<particle_sample.size();i++){

              avg=sqrt(particle_sample[i].x_vel*particle_sample[i].x_vel
              +particle_sample[i].y_vel*particle_sample[i].y_vel
              +particle_sample[i].z_vel*particle_sample[i].z_vel);
```

```
                average_velocity=average_velocity+avg;



            }//End of loop over all fluid particles
            return average_velocity/nf;
        }//End of function average velocity


        //Function for the magnitude of the force
        double force(double measurement,double mass,double time_step,int
part_index,double& measurement1){

            double force;

            if(part_index==0) {

                        force=0;
                        measurement1=0;
            }
            else if(part_index>=1){

                        force=mass*(measurement-measurement1)/time_step;
                        measurement1=measurement;

                        if(force>=0) {

                              force = 0;
                        }
                        else if(force < 0){
                              force = -force;
                        }

            }
      return force;
        }//End of function  force


  };//End of class SamplingVolume

}

#endif
```